Extending Frequency Modulation Spectroscopy: Sensitive and Selective High Resolution Laser Absorption in the Visible and Ultraviolet

by

Jonathan C. Bloch

B.A., Chemistry, Cum Laude
Cornell University, 1989

Submitted to the Department of Chemistry
in Partial Fulfillment of the Requirements for the Degree of

Doctor of Philosophy

at the

Massachusetts Institute of Technology

June 1996

© 1996 Massachusetts Institute of Technology
All rights reserved

Signature of Author _____
Department of Chemistry
May 15, 1996

Certified by _____
Robert W. Field
Thesis Supervisor

Accepted by _____
Dietmar Seyferth
Chairman, Departmental Committee on Graduate Students

ARCHIVES

MASSACHUSETTS INSTITUTE
OF TECHNOLOGY

JUN 12 1996

LIBRARIES

Extending Frequency Modulation Spectroscopy: Sensitive and Selective High Resolution Laser Absorption in the Visible and Ultraviolet

by
Jonathan C. Bloch

Submitted to the Department of Chemistry
on May 15, 1996, in Partial Fulfillment of the
Requirements for the Degree of
Doctor of Philosophy in Chemistry

ABSTRACT

Initial experimental results and detailed theoretical models for two absorption-based laser techniques, Frequency Modulation enhanced Magnetic Rotation Spectroscopy (FM-MRS) and Pulsed-Frequency Modulation Spectroscopy (Pulsed-FMS) are presented. These new techniques overcome several serious deficiencies of high resolution laser absorption spectroscopies: poor sensitivity, limited wavelength range, and lack of rotational selectivity. FM-MRS provides shot-noise limited sensitivity, selectivity to only paramagnetic species, and spectral simplification. As a demonstration of these advantages, FM-MRS is applied to the detection of trace quantities of NO_2 (an important atmospheric pollutant), and the study of CeF (a free radical at 2000 K). Pulsed-FM, a new method for producing and using transform limited nanosecond pulses of phase-modulated radiation, is discussed. The technique is demonstrated, in both the visible and far UV spectral regions, to provide high sensitivity absorption measurements in spite of large pulse-to-pulse amplitude fluctuations.

Thesis Supervisor: Robert W. Field
Tittle: Professor of Chemistry

This doctoral thesis has been examined by a committee of the Department of Chemistry as follows:

Professor Robert W. Field _____
Thesis Supervisor

Professor Keith A. Nelson _____
Chairman

Professor Moungi G. Bawendi _____
Committee Member

Acknowledgments

To everyone who has helped me complete my graduate studies; to my friends and family; to the all the members of Robert Field's and Jeffrey Steinfeld's research groups, past and present; to Michael McCarthy, Stephani Solina, Jonathan O'Brien, Ilia Dubinsky, Bing Ji, Ivan Lorkovic, and Daryl Williams; to the staff at the chemistry shops and Johnny; to Edward Eyler and his research group (at the University of Delaware); to the Stwalley group at the University of Connecticut; to Trevor Sears and Greg Hall at Brookhaven National Laboratory; to Robert Field, my thesis advisor; to my parents Eric and Civianne:

Thank you.

List of Figures

2.1: Simplified FMS experimental diagram 34

2.2: Generation of the in-phase response 43

2.3: Frequency spectra of sinusoidally phase-modulated fields 47

2.4: Plots of the ordinary Bessel functions $J_a(M)$ and products of Bessel functions $J_a(M)J_b(M)$ 48

2.5: Simplified block diagram of FMS detection electronics 64

2.6: FMS receiver noise for the EG&G FND-100 PIN photodiode as a function of optical power on the detector 72

2.7ab: Plots of the FMS in-phase signal as a function of relative modulation frequency and relative laser tuning 86

3.1: Simplified diagram of the FM-MRS experiment 100

3.2: Generation of FM-MRS in-phase signals for aligned ($\Delta\theta = 0$) polarizers 113

3.3a: Profiles of FM-MRS in-phase lineshapes for (nearly) crossed polarizers ($\Delta\theta = \frac{\pi}{2}$) 115

3.3b: Profiles of FM-MRS quadrature lineshapes for (nearly) crossed polarizers ($\Delta\theta = \frac{\pi}{2}$) assuming that the modulation index is small 116

3.4: Simplified block diagram of the experimental apparatus for FM-MRS trace detection of NO_2 132

3.5: Typical direct absorption and FM-MRS spectra recorded under similar conditions (10 Torr) 137

3.6: FM-MRS signal (peak to peak for strongest Q line in figure 3.5) vs NO_2 pressure and fit of data 138

3.7: FM-MRS spectra as function of NO_2 partial pressure 139

3.8a: Input spectra for correlation analysis to improve sensitivity . . . 142

3.8b: The results of spectral cross-correlations 143

4.1a: Energy level diagram summarizing the LFT calculations for Ce^+. 156

4.1b: Energy level diagram summarizing the LFT calculations for CeF . 157

4.2: Simplified schematic of new high temperature oven 163

4.3: CeF absorption and FM-MRS spectra for the low-J lines of the 5684.2 Å band at 1800 K (set to optimize the absorption signal) 169

4.4: The magnetic rotation spectrum (MRS) for the low-J lines of the [17.6]4.5 $\leftarrow X(1)3.5$ (0,0) band 172

4.5: CeF energy level diagram including results from this work, Azuma 1991, and Clements 1984 175

5.1: Simplified pulsed-FMS experimental diagram 195

5.2: Simplified schematics of a capillary amplifier dye cell 196

5.3: Pulsed-FM and absorption spectra of iodine vapor 206

5.4a: Detector output and Fourier spectrum for excimer pumped pulsed-FMS off-resonance 209

5.4b: Detector output and Fourier spectrum for excimer pumped pulsed-FMS on-resonance 210

5.5: Fast digitizing oscilloscope trace showing the detected laser pulse and a portion of the local oscillator as a frequency reference 215

5.6: Simplified diagram of the UV-pulsed-FMS experiment 217

5.7: Far UV-pulsed-FMS spectra of NO 219

5.8: Fourier spectra of pulsed-FM laser pulses calculated from recorded off-resonance pulses 223

5.9: Optical spectra of the pulsed-FM laser from two amplification stages recorded using a 1.5 GHz FSR etalon 229

5.10: Non-linear transfer function for a saturated amplifier, showing a sinusoidal input field and a distorted output field 234

5.11: Spectra showing how short-pulse optical amplification distorts the input *cw*-FM field 237

5.12a: Calculated pulsed-FM spectra for a fully coupled saturated amplifier driven by a *cw*-FM field with no amplitude modulation 239

5.12b: Calculated pulsed-FM spectra for a fully coupled saturated amplifier driven by a *cw*-FM field with first sideband amplitude and phase errors. 240

5.13a: Off-resonance pulses of phase-modulated radiation generated in a single amplifier cell pumped by a smooth 17 FWHM ns doubled Nd:YAG laser 244

5.13b: On-resonance pulses of phase-modulated radiation generated in a single amplifier cell pumped by a smooth 17 FWHM ns doubled Nd:YAG laser 245

A.1: Energy Levels of a Hund's case (a) molecule in a weak magnetic field 264

A.2: Graphical illustration of MR spectral simulation for the Q(2.5) line of the NiH $B^2\Delta_{5/2}-X^2\Delta_{5/2}(1,0)$ band 270

A.3: Graphical illustration of MR spectral simulation for the Q(3.5) line of the NiH $B^2\Delta_{5/2}-X^2\Delta_{5/2}(1,0)$ band 273

A.4: Graphical illustration of MR spectral simulation for the P(5.5) line of the NiH $B^2\Delta_{5/2}-X^2\Delta_{5/2}(1,0)$ band 276

A.5: Energy level diagram for $N=0$ and $N=1$ of a $^2\Sigma$ state in a magnetic field 290

A.6: Energy level diagram for $N=0$ and $N=1$ of a $^4\Sigma$ state in a magnetic field, with $B_{Rot}=1.0\,cm^{-1}$, $\gamma=0.01\,cm^{-1}$, and the spin-spin constant, $\lambda=0.01\,cm^{-1}$ 292

A.7: Energy level diagram for $N = 0$ and $N = 1$ of a $^4\Sigma$ state in a magnetic field, with $B_{Rot} = 1.0\,cm^{-1}$, $\gamma = 0.01\,cm^{-1}$, and the spin-spin constant, $\lambda = 0.1\,cm^{-1}$ 293

A.8: Calculated MR Spectra for $^2\Sigma$ Hund's case (b) - Hund's case (a) transitions at 100 G with $\gamma = 0.01\,cm^{-1}$: $^RQ_{21}(0.5)$, $^RQ_{21}(1.5)$ 300

A.9: Calculated MR Spectra for $^2\Sigma$ Hund's case (b) - Hund's case (a) transitions at 100 G with $\gamma = 0.01\,cm^{-1}$: $^RR_{11}(0.5)$, $^RR_{11}(1.5)$ 301

A.10: Calculated MR Spectra for $^2\Sigma$ Hund's case (b) - Hund's case (a) transitions at 100 G with $\gamma = 0.01\,cm^{-1}$: $^RR_{22}(0.5)$, $^PP_{11}(0.5)$ 302

A.11: Calculated MR Spectra for $^2\Sigma$ Hund's case (b) - Hund's case (a) transitions at 100 G with $\gamma = 0.01\,cm^{-1}$: $^PQ_{12}(1.5)$ 303

List of Tables

2.1: Useful integrals for calculation of FMS signals 32

2.2: Comparison of FMS and Fluorescence detection limits 90

4.1: Compilation of all CeF Bands 173

4.2: Wavenumbers of Assigned CeF Lines (cm^{-1}) 173

4.3: Molecular Constants of CeF (in cm^{-1}) 176

4.4: Parameters (cm^{-1}) which have been used in the CeF LFT Calculation 181

4.5: Comparison of CeF LFT Level Predictions (v=0) to Experimentally Observed CeF Levels (in cm^{-1}) 182

4.6: Low Lying States of LnF (cm^{-1}) 183

A.1: Relative Zeeman transition energies and transition Intensities and zero-field parameters for a Hund's case (a) Q(2.5) $\Delta\Omega = 0$, $\Omega = 2.5$ transition with electronic, vibrational and rotational energies removed 271

A.2: Relative Zeeman transition energies and transition Intensities and zero-field parameters for a Hund's case (a) Q(3.5) $\Delta\Omega = 0$, $\Omega = 2.5$ transition with electronic, vibrational and rotational energies removed . . . 275

A.3: Results of Hund's case(a) MR simulations for some NiH $B^2\Delta_{5/2} - X^2\Delta_{5/2}(1,0)$ transitions 277

A.4: Hamiltonian Matrix for a Hund's case (b) state in a magnetic field . 286

Contents

Abstract 2
Acknowledgments 4
List of figures 5
List of tables 10
Contents 11

1. Introduction
1.1 The problems: poor sensitivity and poor selectivity 16
1.2 The advantages of absorption spectroscopy 17
1.3 Early solutions and new problems: FM spectroscopy 19
1.4 Extending FMS: FM-MRS 22
1.5 Extending FMS: pulsed-FMS 22
1.6 What's to come 23
1.7 References 24

2. FMS
2.1 Introduction to FMS 26
2.2 FM spectroscopy 30
2.2.1 An Approximate Theory of FM spectroscopy 33
2.2.2 A More Complete Theory of FM spectroscopy 44
2.2.3 Concerns for Computer Simulation of FMS 52
2.3 Signal and Noise and Background 54
2.3.1 Shot noise of a cw-FM laser: The ideal case 59
2.3.2 Overcoming other external noise sources 62
2.3.3 Internal noise 73
2.3.3.1 All FM signals add noise 74
2.3.3.2 Unavoidable undesired signals and laser noise 77
2.3.3.3 The complete *SNR* of FMS 79

2.4 Choosing a technique: FMS, OLAS, or Fluorescence Detection . . 82
2.5 FMS: Conclusion or starting point 91
2.6 References 93

3. FM-MRS
3.1 Introduction to FM-MRS 97
3.2 FM-MRS spectroscopy: The general result 99
3.3 Understanding the general formulation of FM-MRS 107
3.3.1 The suppressed FM-limit of FM-MRS 108
3.3.2 Weak absorbers 110
3.4 Signal magnitude, detection sensitivity, and equipment demands . 114
3.4.1 FM-MRS background intensity, signal ,and implications . . 114
3.4.2 Signal 119
3.4.3 Detection sensitivity of FM-MRS 122
3.4.4 Some FM-MRS improvements 127
3.5 Trace Detection of NO_2 using FM-MRS 130
3.5.1 Experimental 131
3.5.2 Discussion of the basic results 135
3.5.3 Sensitivity improvement from Digital Signal Processing . . 140
3.5.4 FM-MRS Sensitivity and localized selectivity 141
3.5.5 FM-MRS detection of NO_2: Conclusion 146
3.6 References 146

4. Applying FM-MRS to simplify the spectra of CeF at 2000K
4.1 Introduction 151
4.2 Experiment 160
4.2.1 Fluorescence methods: DF and WSFE 161
4.2.2 Magnetically confined experiments: MRS and FM-MRS . . 162
4.3 Results 167
4.3.1 Excitation spectroscopy 174
4.3.2 DIspersed Fluorescence Bands 176

4.4 Summary of Observations 177
4.5 Ligand Field Theory 178
4.6 References 184

5. Pulse-FMS
5.1 Introduction 188
5.1.1 Previous work 189
5.1.2 Primary obstacle for high sensitivity pulsed-FMS 190
5.1.3 High sensitivity pulsed-FMS 192
5.2 Generation of pulsed-FM radiation 194
5.2.1 Frequency chirp and transform limited amplification . . . 201
5.3 Initial pulsed-FMS results in the visible : excimer laser pump . . 203
5.3.1. Noise sources in one excimer pumped dye cell 207
5.3.1.1 Background noise sources in one cell 208
5.3.1.2 On-resonance noise sources in one cell 212
5.4 Tests of pulsed-FMS in the UV region 216
5.4.1. Noise sources in multiple ,Nd:YAG pumped cells 221
5.4.2 Saturation behavior 226
5.4.2.1 Uncoupled Saturation 227
5.4.2.2 Coupled Saturation and FMS background reduction . . 231
5.5. Current developments: custom Nd:YAG pumped pulsed-FMS . . 242
5.6 The limit, future developments 247
5.7 References 249

6. Conclusions and Prospects 255
6.1 References 258

A The MR effect
A.1 Introduction 259
A.2 Molecules in a magnetic field:The Linear Zeeman Effect . . . 260
A.3 Individual Hund's case (a) states 264

A.4 MR transitions between Hund's case (a) states 267
A.5 Simulation of Hund's Case (a) MR spectra 269
A.6 Hund's case (a) analysis 274
A.7 Introduction to Hund's case (b) MR spectrum 281
A.8 Individual Hund's case (b) states 281
A.8.1 Intuitive approach to the Hund's case (b) Zeeman effect . . . 284
A.8.2 Spherical tensor algebraic methods 287
A.8.3 Hund's case (b)-case(b) MR transitions 291
A.8.4 Analysis of Hund's Case (b) MR spectra 295
A.8.5 Simulation of Hund's Case (b)-Case (a) MR spectra and analysis 297
A.9 References 305

B The Hund's case (a) matrix elements of a laboratory fixed operator
B.1 Introduction 308
B.2 From Hund's case (a) to the laboratory 308
B.3 Using equation B.7 312
B.4 References 314

C Computer Programs
C.1 Computer code for chapter 4 315
C.1.1 Program MeshBk.for 315
C.1.2 Program BkCalc.For 319
C.1.2.1 Subroutine Bkn.for 322
C.1.2.2 Output of BkCalc 324
C.2. Computer code for appendix A 324
C.2.1 Function Hrb 324
C.2.2 Function Hsrb 325
C.2.3 Function Hzb 326
C.2.4 Function Mueb 328
C.2.5 Subroutine H8b 329
C.2.6 Subroutine H8a 333

C.2.7 Program ZS 336
C.3 A sampling of utility programs for the Coherent 699-29 laser . . 352
C.3.1 *.SCN loader 352
C.3.2 Load & Print 355

D Author's publications 370

1.1 *The problems: poor sensitivity and poor selectivity*

Since the development of the laser nearly forty years ago, scientists, engineers, and recently the general public have been learning to use laser light to make sensitive measurements on systems as fundamental as atomic hydrogen and as complex as the human body. Many of these measurements rely on the remarkable ability of lasers to detect and identify minute quantities of a substance by its spectroscopic signature.

Perhaps the most general and versatile of these spectroscopic detection methods is absorption spectroscopy, in which the identity and quantity of a substance is determined by measuring the removal of light energy from a laser beam that passes through a sample (Gallagher 1991). The absorption signal from a trace quantity of substance is so small that it appears as a tiny blip on the immense background of the laser. The sensitivity of the absorption method is limited by random noise in the laser that causes the immense background to fluctuate and obscure the tiny blip. Poor sensitivity is the primary disadvantage of laser absorption spectroscopy. (Whittaker 1985).

Laser absorption spectroscopy cannot differentiate between blips generated by different samples occurring at the same wavelength, or from an unwanted signal,

perhaps developing from a dust particle travelling through the laser beam. This poor selectivity further limits the usefulness of laser absorption spectroscopy, even when a substance sample removes sufficient intensity from the laser so that the sample-induced blip would be otherwise identifiable on the immense background.

Most of the research that goes into new detection methods focuses on finding techniques that reduce or circumvent these problems of poor sensitivity and poor selectivity.

1.2 *The advantages of absorption spectroscopy*

With laser absorption spectroscopy so limited, why would one want to use it? Absorption spectroscopy possesses a number of distinct advantages over other spectroscopic techniques. First it is a simple, linear technique. The absorbance, calculated from size of the sample-induced blip, can be directly and linearly related to the concentration or amount of a sample present (Skoog 1982, 491). The relationship between the absorption signal and the sample can be fully described by a single fundamental parameter, the absorption cross section. In other spectroscopic techniques, such as fluorescence based methods, two parameters are often needed, the absorption cross section and the fluorescence quantum yield. And in other techniques such as degenerate four wave mixing,

intra-cavity absorption, and opto-galvanic methods, the signal may depend in a non-linear or otherwise complicated manner on the absorption cross section and the laser intensity[1]. When the relationship between signal and sample depends upon multiple parameters or is non-linear, it is more difficult to quantitatively identify a substance (Gallagher 1981).

The absorption technique is also insensitive to whatever happens to the sample after absorption occurs (Gallagher 1981). If a sample, upon absorbing laser intensity, rapidly dissociates, reacts, or otherwise does not fluoresce, the absorption event may not be detectable by other methods that rely on the occurrence of subsequent phenomena, such as fluorescence. In these cases, absorption spectroscopy may be the only suitable detection method.

The signal in absorption spectroscopy is easily measured because it travels on a collimated, pencil-like laser beam (Tran 1983). It is not spread out over all directions like fluorescence. It can be detected arbitrarily far from the sample, so that absorption spectroscopy can be used for remote sensing applications. In other techniques, such as fluorescence, ionization, acousto-optic, or opto-galvanic methods, the signal is often best measured in proximity to where it was generated[2]. For monitoring combustion processes, environmental pollutants, and other remote samples, absorption spectroscopy may be most appropriate.

---

[1]See Gallagher 1981, Demtröder 1988 and others

[2]See Demtröder 1988 for a general discussion of these techniques. Although both acousto-optic and opto-galvanic spectroscopies are sensitive absorption based methods, they measure the generation of sound waves and ions (respectively) and not the removal of energy from the laser.

Absorption spectroscopy is usually non-intrusive (Tran 1983). It does not destroy the sample. Other techniques, such as ionization, opto-galvanic detection, often destroy the sample, rendering it useless for future analysis. Laser absorption spectroscopy can also provide considerably higher spectral resolution than fluorescence based methods because the resolution is limited by the laser and not the bandpass of the detection device[3] (Demtröder 1988).

1.3 *Early solutions and new problems: FM spectroscopy*

The limits of laser absorption spectroscopy, poor sensitivity and poor selectivity, can be overcome by modification and enhancement of the basic technique. Unfortunately, most potential enhancements are not generally applicable. For example, the absorption signal may be separated from the background and unwanted signals by sample-modulation (Gehrtz 1985). To do so efficiently, the modulation must occur outside the noise bandwidth of the laser, at a frequency where no noise in excess of the shot-noise occurs. This is often impractical, since the excess noise of many lasers extends to MHz frequencies (Hollberg 1983), and most sample absorptions cannot be modulated at high frequencies[4] if at all.

---

[3]This assumes that the ultimate resolution of the absorption and fluorescence based techniques is Doppler limited.

[4]An exception to this occurs in multiple resonance spectroscopies, where the population of the intermediate state (and the absorption from this state) can be rapidly modulated by the pumping laser.

Another possible solution to the sensitivity problem, is to employ some means of noise cancellation or subtraction. Usually this entails comparing the signal detected on a laser beam that passes through the sample to the signal from a reference laser that has not passed through the sample. Signals common to both channels are discarded. This method, however, is not generally applicable because a suitable reference beam that contains all the noise (and no sample-induced signals) cannot always be obtained when the two beams traverse substantially different paths[5]. Even when a suitable reference beam is available, the benefit of dual-beam noise cancellation schemes is limited by optical path disturbances, such as turbulence (Gallagher 1981). Although active amplitude stabilization schemes can substantially reduce the intensity fluctuations of many lasers[6], such a high level of performance is required that it is unlikely that suitable devices will be constructed in the near future (Litfin 1980).

Simple source-*intensity* modulation is not, however, a solution to the sensitivity problem, because such amplitude modulation imparts the same time dependence to both the signal and noise (Gehrtz 1985). By using source *phase* or frequency modulation, the absorption dependant signal can be modulated without modulating the noise. One method that uses source-*phase* modulation to remove the immense fluctuating background, named Frequency Modulation

---

[5]If the two beams travel different paths, they will be steered by different mechanical and optical components, which impose different microphonics (noise from mechanical instabilities) and wavefront aberrations onto each beam.

[6]Typical stability levels are 0.01% . See Miller 1990.

Spectroscopy (FMS)[7] by its developers at IBM[8], promised a scheme for high sensitivity measurements at wavelengths where continuous wave (*cw* and not pulsed) lasers were available. The new absorption based method was simple and elegant, using only a single laser beam (Supplee 1994). The *cw*-laser requirement, however, limited the FMS method to studies in the visible and near IR wavelengths. It could not be performed in the ultraviolet region (Tran 1984) where many interesting species, including atmospheric pollutants, strongly absorb[9].

FMS provides a significant improvement in sensitivity over ordinary laser absorption spectroscopy, perhaps even 5 orders of magnitude. However, FMS falls short of reaching the highest sensitivity theoretically possible, quantum-limited detection, because of its own subtle limitations (Gerhtz 1985,Whittaker 1985). FMS also fails to provide a significant improvement in selectivity (McCarthy 1994). These relatively minor shortcomings prompted the development of several new FMS-based methods with the hope of realizing simple, quantum-limited, and selective laser based substance detection at all optical wavelengths[10]. Two new methods, Frequency Modulation enhanced

---

[7]By using source-frequency modulation, one performs Wavelength Modulation Spectroscopy (WMS). WMS is closely related to FMS. See Supplee 1994.

[8]See G.C. Bjorklund, IBM Invention Disclosure SA 870135 (March 1979) and U.S. Patent 4,297,035 (November 1981).

[9]For example, NO absorbs around 220 nm. See chapter 5.

[10]See chapter 2, the review article of Supplee 1994, and references therein.

Magnetic Rotation Spectroscopy (FM-MRS, a selective quantum-limited method) and FMS with transform limited pulses (pulsed-FMS, a sensitive method for UV absorption studies) are presented in this thesis.

1.4 *Extending FMS: FM-MRS*

Frequency Modulation enhanced Magnetic Rotation Spectroscopy or FM-MRS, is an absorption based *cw*-laser technique that identifies a substance by exploiting its magnetic optical activity. Magnetic optical activity is a change in absorption (or refractive index) that develops for certain species when they are placed in magnetic fields. FM-MRS provides significant selectivity by distinguishing between signals from magnetically active samples and all other signals, including those from dust or any substance that does not possess magnetic optical activity. All paramagnetic molecules, such as free radicals, are magnetically active. FM-MRS achieves quantum-limited sensitivity by overcoming the defects of ordinary FMS. Hence, free radicals can be selectively detected with the highest sensitivity possible. Their tiny blips are picked out in the presence of immense unwanted signals using FM-MRS.

1.5 *Extending FMS: pulsed-FMS*

Another newly developed extension of FMS, Frequency-Modulated spectroscopy using Pulse-Amplified cw lasers (or pulsed-FM spectroscopy),

permits sensitive, high resolution absorption measurements to be made not only in the visible, but also in the ultraviolet and infrared regions with pulsed laser light whose intensity fluctuates 30% or more . The high peak powers attainable with pulsed-FMS make it possible to use nonlinear wavelength conversion techniques to generate these otherwise inaccessible laser wavelengths.

Although the technique is still in the early stages of its development, it will be useful for studying the structure of important transient species and for sensitively detecting many molecules that have no detectable absorption in the visible spectrum. Pulsed-FM spectroscopy is ideally suited to study a wide variety of new problems because of its nanosecond time resolution, near-zero background, and potentially quantum-limited sensitivity.

1.6 *What's to come*

The next chapter presents the FMS technique. The presentation of the two new extensions, FM-MRS and pulsed-FM, proceeds from this introductory material. The fundamentals of the FM-MRS methods and the trace detection of the atmospheric pollutant NO_2 using FM-MRS are discussed in Chapter 3. The results of a study on another free radical, CeF, produced in a high temperature furnace, are in chapter 4.

The development of pulsed-FMS and initial demonstrations of the method in

the visible and ultraviolet regions are presented in Chapter 5, and a short summarizing conclusion is given in Chapter 6.

1.7 *References*

1988 Demtröder, W.,"Laser Spectroscopy: Basic Concepts and Instrumentation," Springer Series in Chemical Physics **5** (Springer-Verlag: New York).

1981 Gallagher, T. F., R. Kachru, F. Gounand, G. C. Bjorklund, and W. Lenth, "Frequency-modulation spectroscopy with a pulsed dye laser," *J. Opt. Soc. Am.*, **7**, 28.

1985 Gerhtz, M., G. C. Bjorklund, E. A. Whittaker, "Quantum-limited laser frequency-modulation spectroscopy," *J. Opt. Soc. B*, **2**, 1510.

1983 Hollberg, L., M. Long-Shen, M. Hohenstatt, and J. L. Hall, "Precision measurements by optical heterodyne technique," SPIE Vol **428**, 91.

1980 Litfin, G., C. R. Polluck, R. F. Curl, and F. K. Tittel, "Sensitivity enhancement of laser absorption spectroscopy by magnetic rotation effect," *J. Chem. Phys.*, **72**, 6602.

1994 McCarthy, M. C., J. C. Bloch, and R. W. Field, "Frequency-modulation enhanced magnetic rotation spectroscopy: A sensitive and selective absorption scheme for paramagnetic molecule," *J. Chem. Phys.*, **100**, 6331.

1990 Miller, P. J., "Methods and Applications for Intensity Stabilization of Pulsed and CW lasers from 257 nm to 10.6 microns," SPIE Vol **1376** Laser Noise, 180.

1982 Skoog, D. A. and D. M. West, "Fundamentals of analytical chemistry," 4ed.,Saunders College Publishing (New York)

1994 Supplee, J. M., E. A. Whittaker, and W. Lenth, "Theoretical description of frequency modulation and wavelength modulation spectroscopy," *Appl. Opt.*, **33**, 6294.

1983 Tran, N. H., R. Kachru, T. F. Gallagher, J. P. Watjen, G. C. Bjorklund, "Pulsed frequency-modulation spectroscopy at 3302 Å,"*J. Opt. Soc. Am.*, **8**, 157.

1984 Tran, N. H., R. Kachru, P. Pillet, H. B. van Linden van den Heuvell, T. F. Gallagher, and J. P. Watjen, "Frequency-modulation spectroscopy with a pulsed dye laser: experimental investigations of sensitivity and useful features," *Appl. Opt.*, **23**, 1353.

1985 Whittaker, E. A., M. Gehrtz, and G.C. Bjorklund, "Residual amplitude modulation in laser electro-optic phase modulation," *J. Opt. Soc. B*, **8**, 1320.

2.1 *Introduction to FMS*

FM Spectroscopy (FMS) is a simple single *cw*-laser technique that measures, with very high sensitivity and spectral resolution, the absorbance and dispersion (imaginary *and* real parts of the refractive index) of a substance as a function of optical frequency (Bjorklund 1980) . FMS was invented[1] to provide essentially the same information as does ordinary high resolution laser absorption spectroscopy (OLAS), but with improved detection sensitivity. Unlike fluorescence-based detection methods, FMS does not depend in any way upon inducing fluorescence in a sample. Likewise, evaluating the sensitivity and usefulness of FMS against OLAS and fluorescence detection is complicated and depends upon the intended application.

This chapter prepares the reader for the presentation of new extensions of FMS. The fundamentals of FMS will be elucidated here through a theoretical treatment of the experimental line shapes, a detailed, but practical, signal to noise ratio analysis, and a comparison to other simple techniques, such as OLAS and

[1]"Method and device for detecting a specific spectral feature," U. S. patent 4,297,035 (27 October 1981), G. C. Bjorklund.

fluorescence detection methods. Understanding the new techniques of Pulsed-FM and FM enhanced magnetic rotation spectroscopy, relies on these fundamentals of FMS.

In FMS, a single, specially prepared phase-modulated laser beam, the "FM-ed laser beam", is directed through a sample. Because phase-modulation rather than amplitude modulation is used, the intensity of the laser before the sample has no oscillating component at the modulation frequency. As it traverses the sample cell[2], absorption and dispersion alter the energy content and optical phase, respectively, of the FM-ed laser beam. These interactions can cause the intensity of the FM-ed laser to become time-*dependent* and periodic, so that a component of the intensity after the sample now oscillates at the original phase-modulation frequency, a radio-frequency (RF) high enough to be outside the noise bandwidth of the original laser. The intensity oscillations at the phase-modulation frequency are easily extracted from the detected photocurrent, demodulated, and converted into the now time-*independent* FM signal, without adding significant detection noise. The detected FM signal simultaneously measures both the sample absorption and dispersion at detection levels approaching the quantum limit.

Since both the FM signal and the OLAS signal depend directly on the interaction of the probe laser with the sample, they are direct methods. The

[2]Or optical cavity, etc.

detected signal in both of these techniques can be characterized by a single parameter that describes the absorption of the sample[3]. This, however, is not true for fluorescence based detection methods, which require two parameters to relate the detected signal to the sample under study (Hirschfeld 1977; Ingle 1982). The first parameter is the same one needed for FMS and OLAS, which describes the absorption event. The second, additional parameter is needed to describe the quantum efficiency of subsequent phenomena such as fluorescence. For brevity, methods that rely on the occurrence of additional phenomena after absorption, such as fluorescence techniques, are termed indirect methods. The applicability of indirect methods is limited compared to the applicability of direct methods, such as FMS. However, indirect methods are often more sensitive.

As mentioned already, the FMS signal is obtained by processing the measured intensity of the FM-ed beam, to extract the high frequency time-dependent component oscillating at the phase-modulation frequency. Contrast this to the situation that occurs in OLAS , probably the simplest direct high resolution technique, where the signal is effectively the *time-independent* or zero-frequency intensity removed (or absorbed) by the sample[4], determined by the

---

[3]For FMS, the Kramers-Kronig relations (Lipson 1995, 398) are used to relate absorption and dispersion

[4]This assumes that the laser's wavelength remains unchanged over the measurement period, that the interactions with the sample are simple and linear, obeying Beer's Law (Castellan 1983, 585; Demtröder 1981, 42), and that noise is not included.

difference in laser intensities before and after the sample. In either experiment, FMS or OLAS , the laser intensity randomly fluctuates about some time-averaged value due to various sources of amplitude and phase noise. The fluctuations can be quite large. For a typical *cw*-dye laser, the fluctuations are often on the order of 1 to 10% of the average optical power, and they occur over a range of time scales, "from dc up to a few megahertz" (Wong 1985). Hence the sensitivity of OLAS, and most other direct methods, is limited by fluctuating background levels, since a small change of the intensity due to the sample interaction can no longer be measured in the face of the larger changes due to the noise of the laser[5]. The smallest signals can only be recovered by long time-averaging[6] or heroic normalization schemes which attempt to remove the excess noise electronically. Methods whose sensitivity is limited by background fluctuations are known as *background limited.* FMS, in contrast to most other direct methods, should be a *background-free* technique, because its phase-modulation/demodulation scheme is designed to cancel the background noise, without external normalization or time-averaging. In FMS, when there is no sample absorption, the special oscillating component of the FM-ed laser's intensity is zero, and there is therefore no FM signal. The sensitivity of FMS is

[5]Unless the sample's interactions can be modulated at frequencies outside the noise bandwidth.

[6]This is true because the signal in ordinary absorption spectroscopy is assumed to be time-independent, while the noise is assumed to time average to zero.

determined by the effectiveness of its noise cancellation scheme, rather than the background intensity fluctuations that limit OLAS.

Most indirect methods, such as laser induced fluorescence spectroscopy [7], are also background free techniques, like FMS. This occurs because the "subsequent" phenomena can usually be separated from the fluctuating background. Using FMS, rather than a background-free indirect method, is the only choice when the sample does not, for example, appreciably fluorescence after absorption. For most applications, the choice of methods depends subtly upon the project goals, the available equipment, and the realizable detection sensitivity of each method. After the FM method is thoroughly discussed, this choice will be analyzed.

2.2 *FM spectroscopy*

In this section an FM experiment is outlined. Based on this sketch, mathematical expressions describing FM spectroscopy are developed. A simplified example that clearly displays all the crucial features of the technique is presented first. Following that, the finer details are considered using a more complete, approximation free treatment.

[7]One exception is the Fluorescence Dip method, where the signal is obtained from a change in the intensity of fluorescence rather than the occurrence of fluorescence. Although it is an indirect method, Fluorescence Dip is background limited, like absorption.

The goal of the mathematical treatment is to describe the time-dependent photocurrent generated by a laser impinging on a suitable "square-law" detector. The *real* electric field (from the laser beam) $\vec{E}_R(t)$, generates a photocurrent $I(t)$ at the detector ,

$$I(t)= Q_{det}\frac{1}{T}\int_{-T/2}^{+T/2} \vec{E}_R(t)\cdot\vec{E}_R(t)dt. \qquad 2.1$$

Q_{det} is a frequency-dependent proportionality constant that describes the quantum efficiency of the specific detector and relates the detected intensity to the optical field units. In equation 2.1, the real $\vec{E}_R(t)$ is used rather than a complex vector, to avoid errors (Yariv 1991, 3) that would otherwise hide any useful FM effect! Until later, $Q_{det} = 1$ for simplicity.

The integration or averaging over optical period T in equation 2.1 accounts for the fact that the detector is considerably too slow to follow the teraHertz optical oscillations. This operation yields the familiar factor of $\frac{1}{2}$ (see table 2.1) usually encountered in the "classical" time independent expression for the average intensity of non-modulated fields, $I = \frac{1}{2}E^2$ (Born 1964).

Although the electric field must be a real vector quantity, it is often desirable during calculations to express it as the real part of a complex vector, $\vec{E}(t)$, (known as the analytical signal of $\vec{E}_R(t)$),

Table 2.1: Useful integrals for calculation of FMS signals

$$\frac{1}{T}\int_0^{+T} cos(\omega t)dt = \frac{1}{T}\int_0^{+T} sin(\omega t)dt = \frac{1}{2}$$

$$\frac{1}{T}\int_0^{+T} cos(\omega t \pm A)dt = \frac{1}{T}\int_0^{+T} sin(\omega t \pm A)dt = \frac{1}{2}$$

$$\frac{1}{T}\int_0^{+T} cos(\omega t)sin(\omega t)dt = 0$$

$$\frac{1}{T}\int_0^{+T} cos(\omega t)cos(\omega t \pm A)dt = \frac{1}{T}\int_0^{+T} sins(\omega t)sin(\omega t \pm A)dt = \frac{1}{2}cos(A)$$

$$\frac{1}{T}\int_0^{+T} cos(\omega t)sin(\omega t \pm A)dt = -\frac{1}{T}\int_0^{+T} sin(\omega t)cos(\omega t \pm A)dt = \pm\frac{1}{2}sin(A)$$

$$\frac{1}{T}\int_0^{+T} cos(\omega t + A)cos(\omega t - A)dt = \frac{1}{T}\int_0^{+T} sin(\omega t + A)sin(\omega t - A)dt = \frac{1}{2}cos(2A)$$

$$\frac{1}{T}\int_0^{+T} cos(\omega t \pm A)sin(\omega t \mp A)dt = \mp\frac{1}{2}sin(2A)$$

$$\frac{1}{T}\int_0^{+T} cos(\omega t \pm A)sin(\omega t \pm A)dt = 0$$

$$\vec{E}_R(t) = Re\left(\vec{E}(t)\right) = \frac{1}{2}\left[\vec{E}(t) + \vec{E}(t)^*\right], \qquad 2.2$$

where the asterisk signifies the complex conjugate. This "save[s] a great deal of manipulation and space" (Yariv 1991, 1, 29). All *vectors* in this chapter are complex valued, unless otherwise noted. The reader should use equation 2.2 to calculate the actual field from a given complex field.

2.2.1 *An Approximate Theory of FM spectroscopy*

Simplified treatments of FMS have appeared in the literature (Bjorklund 1980,1983; Supplee 1994 and therein). They proceed by approximation of a complicated, yet accurate, expression for the electric field of the FM'ed laser beam. The complicated expression is usually presented without motivation, obscuring insight. The following unique and simplified treatment develops its conclusions directly and transparently.

Figure 2.1 shows the essential features of an FMS experiment. In FMS, a single frequency (single longitudinal mode) laser beam is passed through a radio frequency (RF) electro-optic phase modulator (EOM)[8]. The EOM imposes new

[8]EOMs are commercially available for frequencies from DC to many gigahertz from many sources including Quantum Technologies Inc, Con-Optics Inc., and v–Focus. Most EOMs are used from 1-1000 MHz, hence the term Radio Frequency.

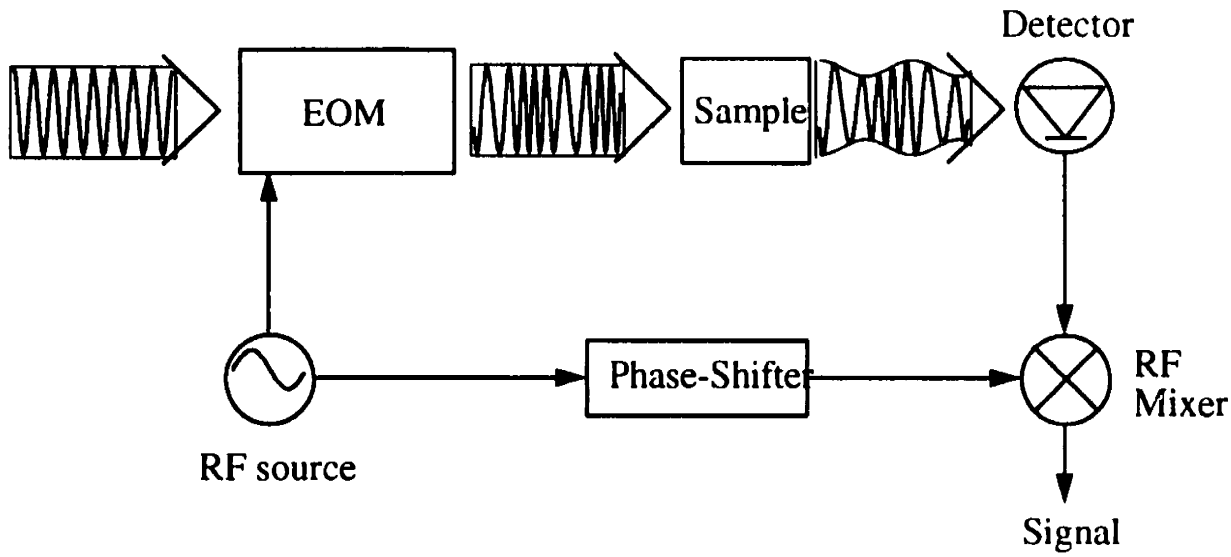

Figure 2.1: Simplified FMS experimental diagram. This figure is described in the text. Essentially, the output of a single longitudinal mode *cw*-laser is passed through an electrooptic phase modulator (EOM), through a sample, and onto a photodetector. The detector's output is demodulated by the mixer, generating the FMS signal.

optical frequency components on the original laser beam. The phase-modulated or FM-ed laser beam is then directed through a sample cell. After the cell, the beam impinges on a suitable photodetector. The output of the photodetector is sent to an RF mixer. The mixer extracts the frequency component of the photocurrent oscillating at the frequency of the phase-modulation, in much the same way a lock-in amplifier demodulates a chopped signal ("A Lock-in Primer" 1986). The FM signal is proportional to[9] the output of the mixer. When no sample is present in the cell, no FM signal develops, but there is certainly optical intensity on the detector. When sample is present, and when this sample absorbs or phase shifts certain optical frequency components differently than others, an FM signal develops. Let us proceed to a mathematical description of this sketch.

In principle, the EOM modulates the phase of the laser without altering its average intensity[10]. The optical electric field entering the EOM is

$$\vec{E}_c(t) = E_c e^{i(\omega_c t + \phi_c)} \hat{p}_c, \qquad 2.3$$

where E_c is the complex field amplitude, $\hat{p}_c$ the complex polarization unit-vector[11], $\omega_c t + \phi_c$, the optical frequency and phase[12]. The optical phase

[9]In practice, the FM signal is usually the low frequency output (difference frequency) of the mixer. The sum frequency output at twice the modulation frequency can also be used.

[10]For a complete treatment of electro-optic modulation see Chapter 9 of Yariv 1991.

[11]This vector is a Jones (Jones, 1940; Kliger 1990) 2 component vector, specifying the

contains the dependence on the wavevector.

Upon exiting the EOM, the *purely phase modulated field* is,

$$\vec{E}_{FM}(t) = E_c e^{i\left[\omega_c t + \phi_c + \phi(t)\right]} \hat{p}_c , \qquad 2.4$$

where $\phi(t) = M \sin\left(\omega_{RF} t + \phi_{RF}\right)$ is the time dependent phase shift imposed by the modulator. M is known as the modulation index[13], and ω_{RF} the modulation frequency. Without loss of generality we set $\phi_c = 0$[14]. The real part of $\vec{E}_{FM}(t)$ can be found easily (at least when E_c and $\hat{p}_c$ are real quantities),

$$\begin{aligned} Re\left(\vec{E}_{FM}(t)\right) &= E_c \hat{p}_c \cos\left(\omega_c t + M \sin \omega_{RF} t\right) \\ &= E_c \hat{p}_c \left[\cos \omega_c t \cos\left(M \sin \omega_{RF} t\right) - \sin \omega_c t \sin\left(M \sin \omega_{RF} t\right)\right] \end{aligned} \qquad 2.5$$

If $M << 1$ (the peak modulation phase deviation is small), we have narrowband (NB) angle modulation[15] (Hsu 1993, 80). Then, using the "small angle approximation",

---

laboratory polarization of the laser. Here, it is superfluous; for FM-MRS, a polarization sensitive technique presented in later chapters, it is essential.

[12]The choice of the subscript *c* to designate the original laser field will be made clear later. It was not chosen to signify a complex quantity.

[13]The modulation index is the peak phase retardation, determined by the applied RF electric field and non-linear response of the crystal (Yariv 1991, 325). The modulation depth is often used describe the energy or power ratio of the sidebands to the carrier (defined later). Caveat Emptor, some authors use the terms exchangably.

[14]For real EOMs, the realized modulation index depends on the wavevector and the optical and electrical phase-velocities (Yariv 1991, 336 and therein). Here, this dependance is ignored.

[15]To appreciate the origin of this phraseology, see figure 2.3.

$$\cos\left(M\sin\omega_{RF}t\right) \approx 1$$
$$\sin\left(M\sin\omega_{RF}t\right) \approx M\sin\omega_{RF}t\,. \qquad 2.6$$

The electric field of the NB FM'ed laser is,

$$Re\left\{\vec{E}_{FM}(t)\right\} = E_c\hat{p}_c\left[\cos\omega_c t + \frac{M}{2}\cos\left(\omega_c + \omega_{RF}\right)t - \frac{M}{2}\cos\left(\omega_c - \omega_{RF}\right)\right]. \qquad 2.7$$

Equation 2.7 contains the optical spectrum of the FM-ed laser for $M << 1$. The spectrum consists of a strong line at ω_c, the original optical frequency, known as the carrier (hence the subscript c) and a pair of weaker components, known as sidebands, at $\omega_c + \omega_{RF}$ and $\omega_c - \omega_{RF}$. The sidebands are new *optical* frequency components created by the RF phase modulation. Each sideband appears with a different sign of M. This is unique to angle (phase or frequency) modulated waveforms; amplitude modulation produces sidebands with the same sign of M (Hsu 1993, 87).

We calculate the intensity of the NB FM-ed laser beam at this point, $I_{NB}^{Null}(t)$. The laser beam has not yet entered the sample cell, so the intensity here is equivalent to the off resonance-- no sample, no absorption, no dispersion-- case. This intensity is the background intensity or null intensity. Using equation 2.1, $I_{NB}^{Null}(t)$ is the sum of six integrals. Since,

$$\omega_{RF} << \omega_c, \qquad 2.8$$

the terms oscillating at ω_{RF} do not change appreciably over a period of ω_c; therefore, they are removed from the integrals. Using the integrals listed in table 2.1, we find,

$$I_{NB}^{Null}(t) = \frac{E_c^2}{2}\left[1 + M\cos\omega_{RF}t - M\cos\omega_{RF}t + M^2\left(\frac{1}{4} + \frac{1}{2}\cos 2\omega_{RF}t\right)\right] \qquad 2.9$$
$$= \frac{E_c^2}{2}\left[1 + M^2\left(\frac{1}{4} + \frac{1}{2}\cos 2\omega_{RF}t\right)\right]$$

The first step in equation 2.9 is shown to emphasize that the two terms oscillating at ω_{RF}, the intensity beat notes arising from cross terms of a sideband with the carrier, cancel perfectly. Since the oscillating terms occur from cross terms of two different electric field components, FMS is known as a heterodyne technique, even though two different lasers are not explicitly combined on the detector.

Note that the average intensity, equation 2.9 integrated over the period of ω_{RF}, is not quite the same as the intensity input to the modulator. When the complete treatment is presented, it will be shown that our approximation for $M << 1$ has introduced an error in the amplitude of the carrier. From equation 2.9, we see that in the absence of a sample, the intensity of the NB FM-ed laser *does not oscillate at* ω_{RF}. The complete treatment extends this result to all values of M.

Now let us consider the effects of a trace amount of a sample, by allowing the NB FM-ed laser beam to pass through a cell, and then impinge on a detector. Beer's law behavior[16] (Demtröder 1981, 42) is expected. The sample then exponentially attenuates (and phase shifts) the optical electric field in proportion to the concentration and sample-cell path length. Each of the three optical frequency components of the NB FM-ed laser must be treated separately. Each is specified independently using the succinct notation,[17]

$$\omega_n = \omega_c + n\omega_{RF} \ . \qquad 2.10$$

The electric *field* attenuation of a single optical frequency component ω_n, is $e^{-\delta_n}$, where δ_n is related to the sample's frequency-dependent absorption coefficient α,

$$\delta_n = \alpha_n L, \qquad 2.11$$

where L is the length of the cell. Likewise, the phase-shift ϕ_n of a single optical frequency component ω_n, is related to sample's frequency-dependent refractive index n',

---

[16]More accurately, Beer-Lambert's law (Levenson 1988, 2).

[17]These symbols and relationships are common (Bjorklund 1980;Supplee 1994), but not universal (Levenson 1988, 74).

$$\phi_n = \frac{n'_n L \omega_n}{c}. \qquad 2.12$$

The overall effect on each frequency component is expressed using an effective sample operator[18] S_n,

$$S_n = e^{-\delta_n} e^{-i\phi_n}, \qquad 2.13$$

so that the NB FM-ed field, after passing through a Beer's Law sample, impinging on the detector is,

$$\begin{aligned} \vec{E}^S_{FM}(t) &= S_n \vec{E}_{FM}(t) \\ &= E_c \hat{p}_c \left[e^{-\delta_0 - i\phi_0 + i\omega_c t} + \frac{M}{2} e^{-\delta_1 - i\phi_1 + i\omega_1 t} - \frac{M}{2} e^{-\delta_{-1} - i\phi_{-1} + i\omega_{-1} t} \right]. \end{aligned} \qquad 2.14$$

The intensity after the sample, $I^S_{NB}(t)$, is calculated using equation 2.1 and the integrals in table 2.2. Suppressing the small terms of order M^2 leads to

$$I^S_{NB}(t) = \frac{E_c^2}{2} e^{-\delta_0} \left[e^{-\delta_0} + M e^{-\delta_1} \cos\left(\omega_{RF} t + \phi_0 - \phi_1\right) - M e^{-\delta_{-1}} \cos\left(\omega_{RF} t - \phi_0 + \phi_{-1}\right) \right]. \qquad 2.15$$

From equation 2.15, we learn that if either the absorption or phase-shifts experienced by the two sidebands differ, the intensity beat notes at ω_{RF} no longer cancel, and a time-dependent, periodic intensity develops.

As described earlier, in FMS, the signal from the photodetector is fed into an RF mixer. The reference frequency input to the mixer, known as the local

[18]The sample operator (a Jones' Matrix) is a convenient construct, akin to a simplified form of the dielectric susceptibility used in Maxwell's formulation of the electromagnetic theory of light.

oscillator or LO, is ω_{RF}, albeit with an arbitrary phase shift ϕ_{RF}, electronically split off (and delayed) from the original driving field of the EOM. The output of the mixer, is $V(t)$, in volts,

$$V(t)= R\, I^{S}_{NB}(t)\, cos\left(\omega_{RF}t + \phi_{RF}\right), \qquad 2.16$$

where R is the resistance of the detection system, usually 50Ω. Since the mixer multiplies the photocurrent and LO, $V(t)$ contains frequency components[19] at DC and harmonics of ω_{RF}. After the mixer, $V(t)$ is low-pass filtered, to remove frequencies of ω_{RF} and higher. This yields the NB FM signal voltage (after some algebra),

$$V_{NB}= RM\frac{E_c^2}{2}e^{-\delta_0}\left[e^{-\delta_1}cos\left(-\phi_0+\phi_1+\phi_{RF}\right)-e^{-\delta_{-1}}cos\left(+\phi_0-\phi_{-1}+\phi_{RF}\right)\right]. \qquad 2.17$$

Equation 2.17 is simplified by recasting it in terms of quadratures,

$V_{NB}= V_{NB}^{Inphase}cos\left(\phi_{RF}\right) + V_{NB}^{Quad}sin\left(\phi_{RF}\right)$, with,

[19]The multiplication of two sinusoids creates only two new frequencies--the sum and difference of the original frequencies. In real mixers, the fields are not ideal sinusoides; there is always some square-wave component to them. This creates other frequencies, harmonics of the original frequencies and their sum and difference frequencies ("A Lock-in Primer" 1986).

$$V_{NB}^{Inphase} = RM\frac{E_c^2}{2}e^{-\delta_0}\left[e^{-\delta_1}cos\left(-\phi_0+\phi_1\right)-e^{-\delta_{-1}}cos\left(+\phi_0-\phi_{-1}\right)\right]$$
$$V_{NB}^{Quad} = RM\frac{E_c^2}{2}e^{-\delta_0}\left[e^{-\delta_1}sin\left(-\phi_0+\phi_1\right)-e^{-\delta_{-1}}sin\left(+\phi_0-\phi_{-1}\right)\right]. \qquad 2.18$$

$V_{NB}^{Inphase}$ is known as the in-phase component, and V_{NB}^{Quad} the quadrature component. The term "in-phase" signifies the component of the FM beat note oscillating in phase with the modulation applied to the EOM, while the term "quadrature" implies a phase difference of $\frac{\pi}{2}$. Note that the FM signal cannot be increased without limit by increasing M, since equation 2.17 is only valid for $M << 1$.

If we are using FMS to detect a very weak signal[20], $\phi_n << 1$ and $\delta_n << 1$. Then using the small angle approximation and

$$e^{-\delta_n} \approx 1-\delta_n, \qquad 2.19$$

equation 2.18 can be simplified. Retaining only the largest contributions to the inphase and quadrature terms, we find, $V'_{NB} = V'^{Inphase}_{NB}cos\left(\phi_{RF}\right) + V'^{Quad}_{NB}sin\left(\phi_{RF}\right)$,

$$V'^{Inphase}_{NB} = Q_{det}RM\frac{E_c^2}{2}\left(\delta_1-\delta_{-1}\right)$$
$$V'^{Quad}_{NB} = Q_{det}RM\frac{E_c^2}{2}\left(\phi_1+\phi_{-1}-2\phi_0\right). \qquad 2.20$$

Equation 2.20 shows that the NB FM signal for weak absorptions and

[20]The actual requirement is that the differences, $\delta_1-\delta_{-1}$ and $\phi_1+\phi_{-1}-2\phi_0$, are small.

dispersions is proportional to the sum of two very *simple*[21] terms, $V'^{Inphase}_{NB}$ and V'^{Quad}_{NB}. The relative contribution to the total signal from each term is set by adjusting the RF phase delay (perhaps by changing the relative RF or optical path length).

In the small signal limit, the in-phase term is proportional to the difference of absorption coefficients at the two sideband frequencies and that the quadrature term is proportional to the second difference of the dispersions[22]. For a sample with well isolated optical resonances of widths large compared to ω_{RF}, the difference of absorptions as a function of ω_c or laser frequency (*e.g.*, the FMS line shape), appears as a first derivative of a Gaussian, while the dispersion term appears as the second derivative of a Doppler-broadened dispersion profile (or similar to a third derivative of a Gaussian profile). Generation of the in-phase (small signal) absorptive response is shown in figure 2.2.

Let us now derive a more complete theory of FM spectroscopy without the restriction that $M << 1$, before delving into the issues of sensitivity.

---

[21]That these terms are simple and thereby more memorable than those in equation 1.18, has led to a number of erroneous conclusions, including the assertion that the FMS signal is *always* linearly (and simply) dependent on the sample differential absorption. Absorption of the carrier, an effect that has been neglected so far, adds a quadratic signal dependence.

[22]The first differences of a series of three numbers, a, b and c, are $(a-b)$ and $(b-c)$, while the second difference is $(a-b)-(b-c)$.

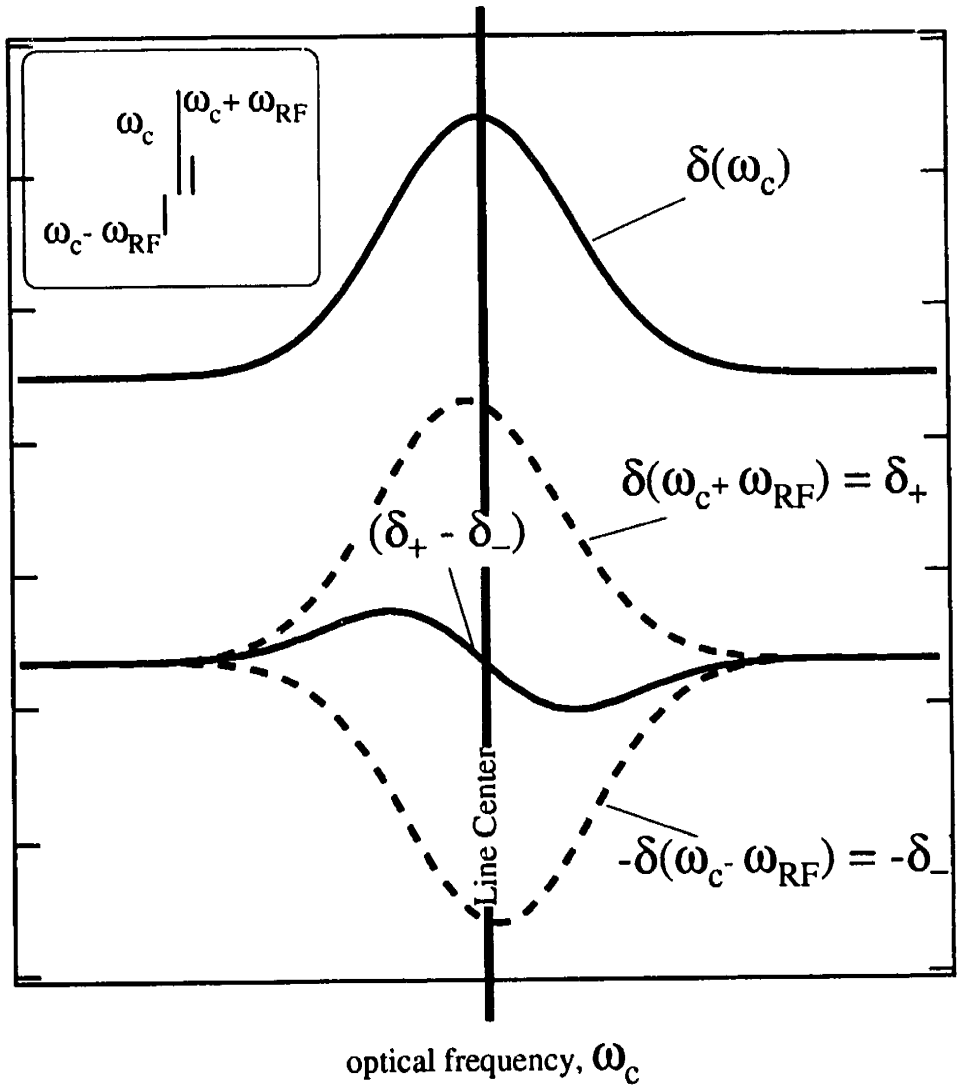

Figure 2.2: Generation of the in-phase response. The frequency spectrum of the FM-ed laser field is shown in the small inset plot. The top bold line is the absorption experienced by the carrier while the dotted lines are for the +1 sideband and the negative of absorption of the -1 sideband. The lower bold line, the signal, is the difference of the two dotted curves.

2.2.2 *A More Complete Theory of FM spectroscopy*

In section 2.2.1, a simplified theory of FMS that described the line shapes for $M << 1$ was developed by employing the small modulation angle approximation. In that case the modulation was known as narrowband FM. For weak absorptions with significant frequency spread compared to the modulation frequency, the NB FM line shapes closely approximate a first or third derivative of a Gaussian, (appropriately) Doppler broadened. Now we relax the restriction $M << 1$ and derive a more complete theory.

Other authors have presented non-approximate theoretical treatments of FMS, but primarily in the context of more complicated FMS experiments (Cooper 1987). Most recent is the review article "Theoretical description of frequency modulation and wavelength modulation spectroscopy" (Supplee 1994). The following treatment is uniquely focused to develop the material necessary for understanding the extensions of FMS covered in the following chapters.

Recall that the electric field after the modulator was expressed,

$$\vec{E}_{FM}(t) = E_c e^{i\omega_c t} e^{iM\sin\omega_{RF} t} \hat{p}_c . \qquad 2.21$$

Our goal now is to find the exact frequency spectrum of $\vec{E}_{FM}(t)$. Since the function $e^{iM\sin\omega_{RF} t}$ is periodic, with period $T_{RF} = \frac{2\pi}{\omega_{RF}}$, its Fourier series

representation[23] (Karu 1995, 102) is,

$$e^{iM\sin\omega_{RF}t} = \sum_{n=-\infty}^{\infty} c_n e^{in\omega_{RF}t}. \qquad 2.22$$

The complex Fourier coefficients c_n are found, setting $\omega_{RF}t = x$, by

$$c_n = \frac{1}{2\pi}\int_{-\pi}^{\pi} e^{iM\sin x} e^{-inx} dx = J_n(M). \qquad 2.23$$

$J_n(M)$ is the Bessel function of the first kind, of order n, argument M, which appears in equation 2.23 *via* its usual generating integral (Lipson 1995, 465). Thus we have an alternative way of expressing $\vec{E}_{FM}(t)$ that transparently contains its optical frequency spectrum ,

$$\vec{E}_{FM}(t) = E_{c_n}\sum_{n=-\infty}^{\infty} J_n(M) e^{i(\omega_c + n\omega_{RF})t}\hat{p}_c. \qquad 2.24$$

Figure 2.3 displays the frequency spectrum of $\vec{E}_{FM}(t)$ for various values of M and figure 2.4 shows some Bessel functions and products of Bessel functions *vs.* M. The figures and equation 2.24, show that phase modulation introduces an infinite comb of sidebands. As M increases, the intensities of the higher order sidebands increase, and the effective frequency spread of the laser moves from narrowband ($M << 1$) to wideband.

---

[23]The Fourier transform (or frequency spectrum) of any periodic signal (period =T) is *always* composed of impulse functions at frequencies that are integer multiples of 1/T .

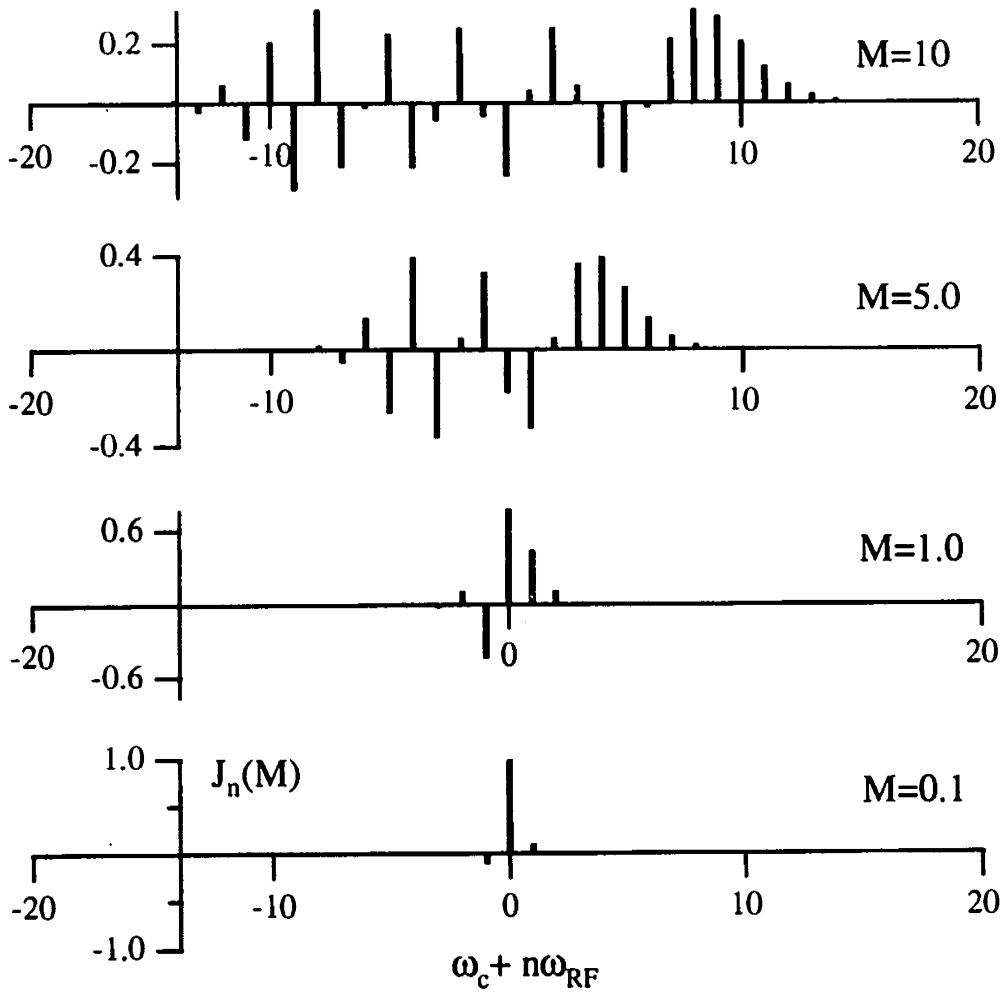

Figure 2.3: Frequency spectra of sinusoidally phase-modulated fields. M is the modulation index or peak phase retardation. For M=0.1, the field is considered narrow-band. For M=10 it is wideband.

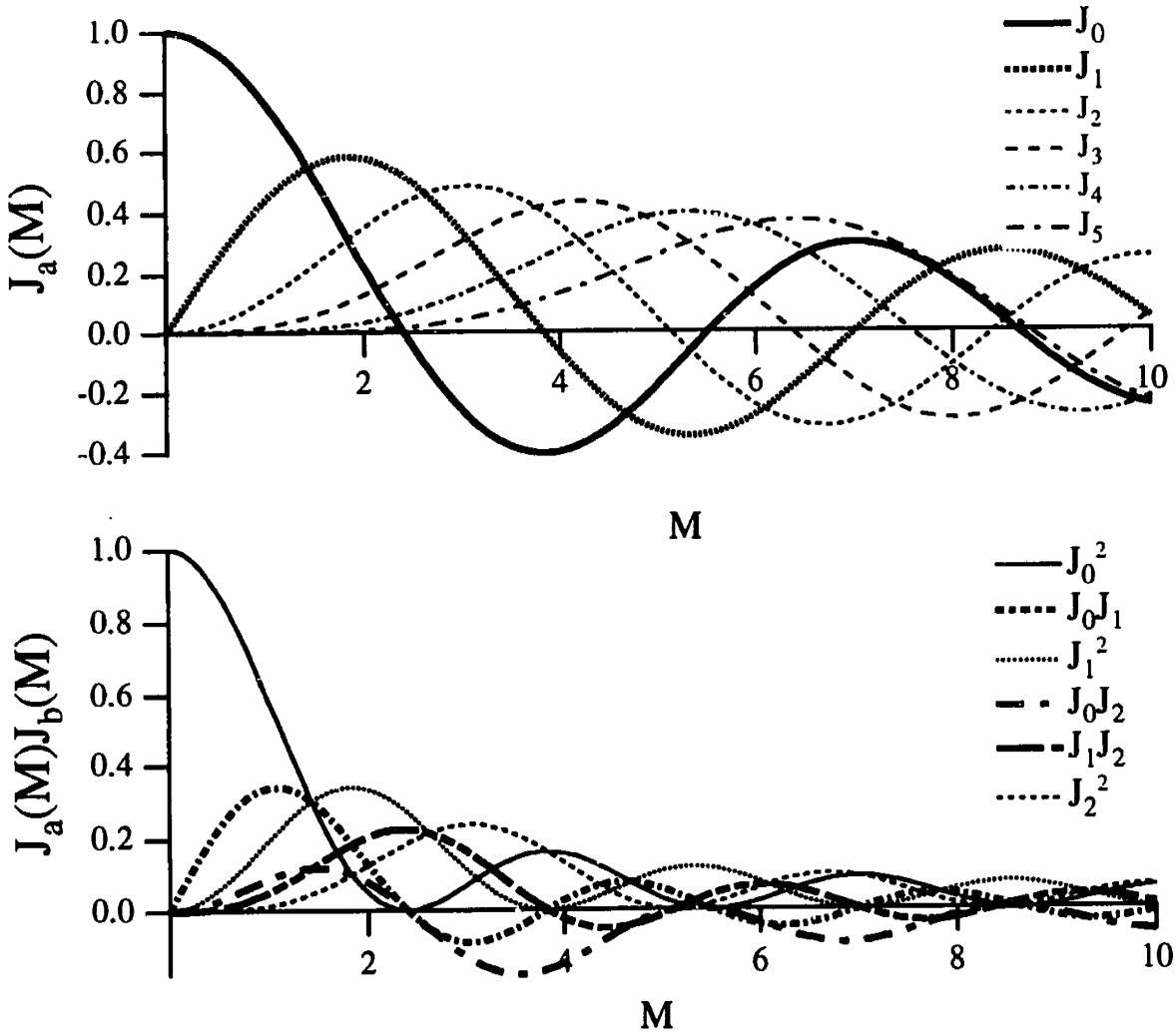

Figure 2.4: Plots of the ordinary Bessel functions $J_a(M)$ in top panel and products of Bessel functions $J_a(M)J_b(M)$ in bottom panel.

Because

$$J_{-n}(M) = (-1)^n J_n(M), \tag{2.25}$$

there is a sign difference between *all* odd $-n$ and $+n$ sidebands. This gave rise to the FM null in our earlier treatment. Using,

$$J_n(M << 1) = (-1)^n \frac{M^n}{2^n n!}, \tag{2.26}$$

the earlier results (see equation 2.7) become a special case of equation 2.24 (Arfken 1985, 675).

As stated previously, pure phase modulation should not alter the *average* intensity of the laser[24]. Yet, the earlier approximate theory failed to show this. Parseval's theorem for Fourier series (Hsu 1993, 4),

$$I = \sum_{n=-\infty}^{\infty} c_n^2, \tag{2.27}$$

states that the average intensity (or power content) of a periodic signal is equal to the sum of the squares of its Fourier coefficients. For FMS, the Fourier coefficients are the Bessel functions (from equation 2.23). The use of the Bessel function series relation (Hsu 1993, 86),

[24]This expression of energy conservation is relevant to noise considerations discussed later.

$$\sum_{n=-\infty}^{\infty} J_n^2(M) = 1 \qquad 2.28$$

and equation 2.27, together show that the (average) energy is conserved in the phase-modulation process.

After exiting the sample cell, the laser beam's field is expressed using equation 2.13 as[25],

$$\vec{E}_{FM}^{S}(t) = E_{c_n} \sum_{n=-\infty}^{\infty} S_n J_n(M) e^{i(\omega_c + n\omega_{RF})t} \hat{p}_c . \qquad 2.29$$

As before, we aim to calculate the component of the intensity oscillating at ω_{RF} arising from the FM-ed field. Each component of the complex valued field in equation 2.29 can be written as the product of an optical oscillation term and a term $\vec{k}$, containing all constants and slowly-varying terms[26]. Considering the field in this way facilitates the calculation of its intensity,

$$\begin{aligned} I(t) &= Q_{det} \frac{1}{T} \int_{-T/2}^{+T/2} \vec{E}_R(t) \cdot \vec{E}_R(t) dt \\ &= Q_{det} \frac{1}{T} \int_{-T/2}^{+T/2} \left[\vec{E}^2(t) + 2\vec{E}(t) \cdot \vec{E}^*(t) + \vec{E}^{*2}(t) \right] dt \\ &= \frac{Q_{det}}{2} \vec{k} \cdot \vec{k}^* = \frac{Q_{det}}{2} \vec{E} \cdot \vec{E}^* \end{aligned} \qquad 2.30$$

because the fast optical oscillations cancel out in the cross term.

---

[25]There is another way (Supplee 1994) to express this which leads to a very different, non intuitive yet equivalent result. First (following Supplee and therein), we could derive a simple expression by allowing only one single sideband to interact with the sample. Next (extending the idea here) the general result could be found by summing over all possible single sidebands.

[26]Slowly varying with respect to the optical period.

Using equation 2.30, the intensity of the FM-ed field in equation 2.29, $I_{FM}(t)$, is,

$$I_{FM}(t) = \frac{Q_{det}}{2} \sum_{a=-\infty}^{\infty} S_a J_a(M) e^{ia\omega_{RF}t} \sum_{b=-\infty}^{\infty} S_b^* J_b(M) e^{-ib\omega_{RF}t}. \qquad 2.31$$

The FM signal (the filtered output of the mixer) V_{FM}, will be the component of $I_{FM}(t)$ oscillating at ω_{RF}, or the sum of all terms in equation 2.31 with $|a-b| = 1$. Using $J_n = J_n(M)$ and $\Lambda = RQ_{det}\frac{E_c^2}{2}$ for brevity,

$$\begin{aligned} V_{FM} &= \Lambda \sum_{a=-\infty}^{\infty} J_a J_{a+1} \left[S_a S_{a+1}^* e^{-i\phi_{RF}} + S_a^* S_{a+1} e^{+i\phi_{RF}} \right] \\ &= \Lambda \sum_{a=0}^{\infty} J_a J_{a+1} \left[\left(S_a S_{a+1}^* - S_{-a}^* S_{-a-1} \right) e^{-i\phi_{RF}} + \left(S_a^* S_{a+1} - S_{-a} S_{-a-1}^* \right) e^{+i\phi_{RF}} \right] \qquad 2.32 \\ &= \Lambda \sum_{a=0}^{\infty} J_a J_{a+1} \left[e^{-\delta_a - \delta_{a+1}} \cos(\phi_{RF} - \phi_{a+1} + \phi_a) - e^{-\delta_{-a} - \delta_{-a-1}} \cos(\phi_{RF} + \phi_{-a-1} - \phi_{-a}) \right]. \end{aligned}$$

The last line in equation 2.32 describes FMS for all modulation depths and Beer's law sample interactions. If need be, it can be recast in terms of an in-phase and quadrature term, and all the previous results of the approximate theory are easily obtained from it. For example, when no sample is present, the two terms within the last brackets cancel, and there is no FM signal. Equation 2.32 is useful for accurate computer simulation of FMS, considered in the next section. The retained accuracy of the simulated FMS signal is limited by the number of terms considered in the sum.

Parameters in equation 2.32 can be set to optimize the FM signal. The optimal

value of the modulation frequency depends on the system under study. As suggested by many authors (for the case of small or moderate modulation depth), the FMS signal increases until the modulation frequency is approximately the line width of the isolated absorption feature (Supplee 1994; Bjorklund 1983). Thus, the many small gas phase molecules that have room temperature line widths in the visible region of *1 GHz* or more (due .o Doppler broadening) require a high modulation frequency.

If the modulation frequency is set roughly on the order of the resonance width or larger (typical for most FMS applications), the optimal value of the modulation index, $M = 1.4$, occurs approximately at the maximum of the product $J_1(M)\left[J_0(M) + J_2(M)\right]$ (see figure 2.4).

When the modulation frequency is smaller than the linewidth, the FMS signal is always reduced from the optimal value due to absorption of the carrier. For weak absorbers, this is a small effect. But, as the absorption of the carrier increases, the FMS signal tends towards zero. This behavior will be explored when OLAS is compared to FMS.

2.2.3 *Concerns for Computer Simulation of FMS*

In the previous two sections of this chapter, equations describing FMS were

presented for various parameter ranges. If the complete optical frequency response of the system under study is known (the absorption and dispersion of the molecule), simulated FMS spectra are easily created. This section outlines an approach to computer simulation of the FMS line shape for the low modulation index, weak absorber case and discusses how the more complete solution (equation 2.30) can be utilized.

Suppose that we wish to simulate an FMS spectrum for arbitrary molecular resonance, over a range of cm^{-1}, at an energy resolution on the order of a fraction of the modulation frequency. At each discrete energy value, we use equation 2.20 to calculate a single point in the FM spectrum. We must do this for every point in the spectrum. Our calculations are simulating the laser scanning in frequency as "sliding" across a molecular resonance. This sliding and a calculation at each point, is equivalent to discrete convolution, an operation ideally suited for computer implementation. Using this approach, the in-phase FM signal is calculated by convolving a two-peak stick spectrum of the sidebands (the frequency spectrum of the laser minus the carrier) with the absorptive part of the molecular response, and the quadrature signal is calculated by the convolution of the dispersive part of the response with a stick spectrum of the sidebands plus twice the carrier[27]. If for example, the FM signal due to a

[27]Both the inphase and quadrature response are calculated simultaneously using complex (real and imaginary) frequency spectra.

molecule in an optical cavity was desired, the frequency response of the cavity/molecule system would be calculated and input to the convolutions in a similar manner.

If the modulation index and or molecule system response is large enough to warrant using equation 2.32, the procedure above must be modified somewhat. Two different paths can be taken. First, the simple procedure can be used iteratively for each term in the sum in equation 2.32, employing the appropriate cosine and exponential operations after each convolution. A second, rather elegant[28] approach would be to recast the entire derivation of the FM signal, in a formal manner, using convolutions (and Fourier transforms) from the onset. That approach would be suitable for highly precise calculations of the FMS signal when the unmodulated laser's frequency spectrum is not simple.

2.3 *Signal and Noise and Background*

In the laboratory, the FM signal is never measured in isolation. Rather,we record simultaneously the FM signal along with an undesirable and unavoidable signal due to noise are recorded. For a single measurement of the total detected signal, the noise and FM signal contributions cannot be separated. The presence

[28]For another even more general approach (useful for chirped resonators) see also Seigman, 1991, 1101 and references therein.

of noise establishes a fundamental limit on the use FMS for quantitative sensitive detection. The noise sets both the lower limit on the smallest detectable signal and the accuracy on every FMS measurement. In FMS, the noise depends on the FM signal magnitude. Obviously, we have intense interest in understanding and controlling the noise contributions to the total detected signal.

This section's analysis of the signal and noise issues of FMS does not simply develop an expression that reveals the ultimate *limiting* sensitivity of the technique. That has been presented by many authors (Bjorklund 1983; Silver 1991). Here, the analysis leads also to an understanding of the observed signal to noise ratio *at all signal levels.* This cleanly separates the signal to noise issues from dynamic range concerns for FMS. The goal is to provide a framework for researchers to easily implement a shot noise limited FMS detection system, analyze new extensions of FMS, and gain insight into the inclusion of background signals as noise sources.

Noise contributions in a laser experiment come in two general types--external and internal. External noise is added by the detection process, while internal noise is inherent to the method itself. Amplifier noise is one such external source, while laser intensity fluctuations are an internal source. Shot-noise can be of both types. The internal sources will be represented by considering the electrical signals they generate once they are externally detected. This approach

provides a unified treatment of the internal and external contributions.

Following the presentation of some background material, shot-noise, external, and internal noise sources will be discussed, in that order. In the next section of this chapter, a simple model for the FM signal is introduced to facilitate comparison with absorption and fluorescence based methods.

As mentioned at the beginning of this section, the recorded signal at any instant is actually the theoretical FM signal plus noise. The signal is expressed conveniently either as a time dependent total current or total voltage,

$$\begin{aligned} V_{Total}(t) &= V_{FM} + V_{Noise}(t) \\ i_{Total}(t) &= i_{FM} + i_{Noise}(t) \end{aligned} \qquad 2.33$$

From now on, however, we consider only the current since the corresponding voltages can be calculated using the impedance of the detection system. The total detected signal is time dependent due only to the presence of noise, since the laser frequency is assumed to be held fixed while the signal is recorded.

The photocurrent from optical sources (internal noise sources plus FM signal) is related to the laser's electric field using equation 2.2. Alternatively, expressing the total power from the laser impinging on the detector's active area in Watts, conveniently yields.

$$Q_{det} = \frac{e\eta}{\hbar\omega} G_{det} = \frac{e\eta\lambda}{hc} G_{det} = G_{det}\rho\,, \qquad 2.34$$

where e is the charge of an electron, η is the quantum efficiency of the detector reflecting the probability that an electron is generated by each incident photon, and ω is the optical frequency and λ the wavelength. Additionally, G_{det} is the current gain of the detector and ρ is the frequency dependent detector responsivity in amps/watt. Since the FM-ed laser beam contains more than one optical frequency, equation 2.34 must be applied carefully.

The noise contribution in equation 2.33 is a time-dependent fluctuating current with a zero time-averaged mean, a signed quantity that may add or subtract to the FM signal at any instant. The possible presence of interfering (non-noise) infinitely stable background signals is ignored so that the true time-independent FM signal (equation 2.32) is obtained by the infinite-time average of the detected signal,

$$i_{FM} = \lim_{T\to\infty} \int_0^T i_{Total}(t)\, dt = \overline{i_{Total}(t)}\,, \qquad 2.35$$

and the total noise power[29] is obtained,

$$\overline{i^2_{Noise}} R = \overline{\left(i_{Total}(t) - i_{FM}\right)^2} R. \qquad 2.36$$

[29]Power is the most convenient unit for noise. Using power units avoids the necessity of taking square roots. Also note that the noise power may actually have a frequency dependence.

A figure (of merit) called the Signal to Noise Ratio, $\frac{S}{N}$ or SNR, is readily used to quantify the level of noise contamination *at a particular signal level.* The units of the signal and noise terms are of crucial importance, and will be indicated by a subscript P for power or i for current when needed,

$$\left(\frac{S}{N}\right)_P = \frac{i^2_{FM}}{i^2_{Noise}} \qquad 2.37$$

This formula is not often applied in the laboratory because of either the long time required to make a single accurate measurement of a noisy signal, or the difficulty involved in recording a tiny noise contribution when the FM signal dominates. Instead, the noise is often estimated as the background level, (when no FM signal occurs), and the FM signal is measured (when it clearly dominates) using as much time-averaging as needed. $\frac{S}{N}$ values that would occur at different FM signal levels are then estimated, often incorrectly assuming that the noise is independent of signal. This experimentally convenient approximation of $\frac{S}{N}$ must be clearly remembered because it obscures the importance of distinguishing the dynamic range from the $\frac{S}{N}$.

Once the smallest $\frac{S}{N}$ that is tolerable is determined by our requirements for signal detection[30], the smallest detectable FM signal can be calculated, and from it, using either Equation 2.16/20 or 2.30 , we can infer the sensitivity of the

[30]Although this may seem to be an arbitrary issue, it is far from a prosaic one and is often debated. See Yariv, 1991, p. 359 for a fact-based treatment.

method in terms of the smallest detectable absorption (or dispersion) and the maximum achievable $\frac{S}{N}$ of the technique. This seems straightforward, yet unless the proper (unapproximated) $\frac{S}{N}$ is used, its value for analyzing laboratory implementations of FMS is lost. Let us now begin to quantify this process for various sources of noise.

2.3.1 *Shot noise of a cw-FM laser: The ideal case*

In this section, the shot-noise of a *cw*-laser is treated. No other noise sources are considered here, even though they are surely present in the laboratory. Therefore, this discussion is an idealized, unrealistic scenario, that specifies a benchmark against which to judge all direct laser spectroscopies.

Consider now FMS performed with a laser, modulator and detection system that have zero *excess* noise. A noise is termed excess noise, if it is, at least in theory, completely removable (without time averaging and normalization), by modification of the experimental apparatus. The only noise in this *perfect* experiment is the unavoidable shot-noise of the photons (or subsequent photo-electrons) that arise due to quantum fluctuations. Shot-noise arises (classically) from the fluctuations in the arrival rates of the particle photons (or electrons) that we are inherently counting in detecting our signal. If we are counting (on

average) n photons, we are actually making n measurements, so that our counting error (for a Poisson distribution[31]) will be $\sqrt{n}$ particles. The shot-noise of the photons themselves can be calculated, yielding an optical noise power, that subsequently impinges on a photodetector and creates a corresponding electronic shot-noise current. Alternatively (and equivalently), by considering only electrons, the shot-noise of the total photoelectrons generated in the photodetector by the entire laser beam (Yariv 1991, 364, 410), can be calculated. To be precise, we are always actually counting electrons[32] (we never count photons). Hence, I choose to consider shot-noise as an external noise added in the detection process (although it surely exists in the laser itself).

Shot Noise is known as "white" noise (Gowar 1984, 405), a term used to signify that its frequency spectrum is flat or constant (from dc to daylight)[33]. This means that the shot noise *power* will be a constant times the frequency interval or bandwidth of detection. This linear dependence on bandwidth *does not* reflect the fact that shot noise is a function of the average number of photons counted, but rather it reflects the "impulsive" arrival of each discrete photon.

---

[31]Shot-Noise follows a Poisson Distribution, not a Gaussian Distribution. Remembering this distinction (when other noise sources are considered concurrently) does not significantly affect the analysis here. (Gowar 1984, 413).

[32]If, we assumed otherwise, the calculated shot-noise power would differ by a factor of the detector's quantum efficiency. If the detector had unit quantum efficiency, there would be no error. Either way, we are free to view the generator of the shot noise as photons or electrons.

[33]Actually, the term "white" implies that the noise spectral density is independent of frequency.

The counting of even a single photon develops white shot-noise -- a result easily comprehended by recalling that the Fourier transform of a delta function is a constant function of frequency (Yariv 1991, 366)!

All this means that the detected signal current shot noise power $\overline{i_{SN}^2}$ due to a *cw*-laser beam of total average laser power (in area A) of P_c is (see Yariv),

$$\overline{i_{SN}^2} = 2e\, G_{det}^{2+x} \sqrt{\overline{i_{Total}^2}}\, \Delta f = 2e\, G_{det}^{2+x} \rho\, P_c\, \Delta f \qquad 2.38$$

where Δf is the detection bandwidth in Hz, and x is an additional small factor needed to precisely explain the "additional" shot-noise in detectors with gain (Yariv 1991, 435). If other current sources (other than optical) were present, they would be included in the total current. Notice that shot noise power is a linear function of Δf but depends upon the optical frequency *via* the responsivity, ρ.

For a $1\ mW$ $600\ nm$ laser beam detected using a photodiode with $\rho = 0.4\ A/W$, $\Delta f = 1\ Hz$, $G_{det} = 1$ and $x = 0$, the shot noise current[34] is $1.1 \times 10^{-11} A$. This is only $4.5 \times 10^{-6}\%$ of the total current from the entire laser, $400\ \mu A$. Because the shot noise current is proportional to the square root of the optical power, when the optical power increases, the fraction of shot-noise of the

[34]For comparison, had we calculated the optical shot-noise as an internal source we would have found $1.8 \times 10^{-8} W$.

total current decreases. Potentially then a *1 mW* laser can provide six orders of magnitude or more dynamic range from the shot-noise noise floor to the total photocurrent. But, in OLAS, the shot-noise current is always swamped by the current from much larger laser power fluctuations. The excess laser noise establishes the noise floor and limits the sensitivity *range* of OLAS. How FMS circumvents this problem will be considered when internal noise sources are presented.

2.3.2 *Overcoming other external noise sources*

As the title of this section suggests, all non shot-noise external noise sources can in principle be overcome, by making them small and negligible relative to the shot-noise. There is no compelling reason to eliminate totally the non shot-noise external sources, since reducing them substantially below the shot-noise will not strongly influence the external noise floor.

The goal of this section is to detail the implementation of an FMS experiment that would be shot-noise limited *if the internal noise sources did not exist.* Thus here, the shot-noise limited *detection system* for FMS is presented. In the next section, we discuss the more complex internal noise issues, involving the FM-ed laser.

If the detection system is to be shot-noise limited, we must reduce *all non-*

shot-noise external sources of noise to ensure that the shot-noise is, by far, the largest source of noise, since the total noise power in the experiment is the sum of all individual noise *powers* that arise[35].

The FMS detection system consists of only a few block-like components, as illustrated figure 2.5. An optical receiver, consisting of a photodetector and preamplifier, converts the laser intensity into an electrical signal; an RF mixer acts as the primary demodulation circuit; and the combination of a mechanical chopper and lock-in detector, or some other similar device, establishes the detection bandwidth. Each block will be considered separately.

A full range of optical receivers has been thoroughly investigated, due to their importance in optical communication (see Gower 1984; Ross 1966; Keiser 1983; Yariv 1991; and references therein). Only receivers suitable for *cw*-FM experiments in the visible and near IR are considered here.

For the $1 - 10\,mW$ or $0 - 10\,dBm$ optical power levels of a *cw*-FM experiment, and typical modulation frequencies of up to $1\,GHz$, the inexpensive and sturdy solid-state photodiode is the most appropriate detector. Photomultiplier tubes cannot usually handle the mW *cw*-optical powers and most are too slow (>1 nanosecond) if they are affordable.

[35]The key idea is that the noise sources are uncorrelated. Also, to be exact, how the noise powers are combined should depend on the noise probability distributions involved (Gaussian, Poisson, etc.).

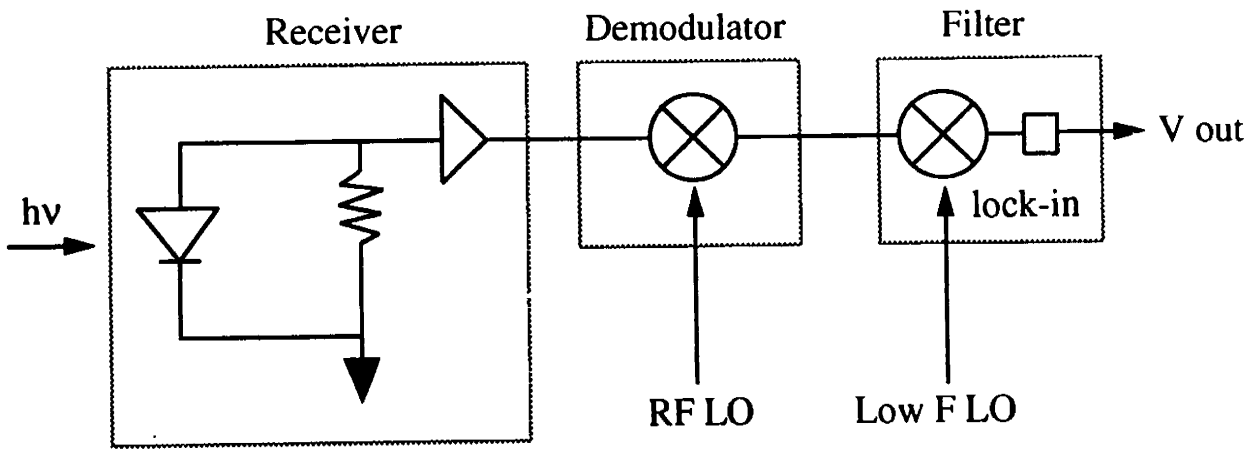

Figure 2.5: Simplified block diagram of FMS detection electronics. The receiver consists of a reverse biased photodiode, a load resistor and low noise preamplifier. The demodulator is an RF mixer and the filter is a lock-in amplifier. LO stands for local oscillator, the frequency reference for the demodulators.

The photodiode must be used in photoconductive mode, rather than photovoltaic mode, in order to have a suitable RF modulation response. A photoconductive diode is a reverse biased diode that operates as a current source, as shown in figure 2.5. In this configuration, the detector has its fastest time response, because the positive reverse bias voltage accelerates the electrons, reducing their transit time across the diode.

The diode-detector's current output is connected across $50\,\Omega$[36] to an RF preamplifier. RF amplifiers with $50\,\Omega$ input impedance are chosen because they are inexpensive, commercially available, broadband, and easy to use, while the other major option, the transimpendace circuit[37], can be difficult to construct, and may have undesirable high-frequency oscillations (Gowar 1984, 424).

When no light is on the photodiode, the detector still produces a current (Yariv 1991,431), known as the dark current, i_d. Thermal generation of free charge carriers in the diode creates the dark current (Palais 1988, 154). It is known to decrease at low temperature, but it is not a noise source as such. Rather, since i_d contributes to the total current (light on or light off) generated at

[36]The 50Ω is a standard value, matching the input impedance of most available RF amplifiers. The effect on response time and noise will be considered later.

[37] When a photo-diode is used in a transimpedance circuit, the photocurrent is converted to a voltage using an opamp, thus providing the potential for very high transimpedance gain with very low noise and unintentional resonances (gain peaking).

the detector, it must also be included when calculating the shot-noise power (see equation 2.38). No other significant (at visible wavelengths) noise sources are inherent in the diode itself.

As shown in figure 2.5, an ordinary resistor is placed across the output of the detector, so that the photocurrent generates a voltage equal to the product of the responsivity, optical power, and load resistance, R_L. The non-zero (statistical) thermal motions of the electrons within the resistor create another noise, i_{Th}, known equivalently as Johnson, Thermal, or Nyquist noise. Since each non-stationary discrete charge carrier (electron) contributes a pulse to the total current, thermal noise (similarly to shot-noise) is also known as white noise. Hence we find,

$$\overline{i_{Th}^2} = \frac{4kT\Delta f}{R_L}, \qquad 2.39$$

where k is the Boltzmann constant and T the temperature in Kelvins.

From equation 2.39 alone, it appears that increasing R_L ought always to increase the $\frac{S}{N}$ of our receiver[38]. We cannot, however, increase R_L without limit. The problem is that as R_L increases, both the time response and the dynamic range of the receiver decreases. The time response and the dynamic

[38]This most not be an altogether obvious result, having been independently "discovered" and reported three times (Gowar 1984 411), perhaps because the thermal noise power $\overline{i_{Th}^2}R_L$ itself is independent from R_L.

range are separate issues.

The time response is often specified in terms of a frequency, $f = 0.35/t_{.1-.9}$, where $t_{.1-.9}$ 10-90% current rise time. The frequency at which the power output of the detector has dropped by half or $3\,dB$ is determined by the load resistance R_L and capacitance C_{Det} of the detector[39],

$$f_{3-db} = \frac{1}{2\pi R_L C_{Det}} \qquad 2.40$$

The dynamic range is also limited by the load resistor, which effectively provides (transresistance) gain of R_L. If R_L is large enough, a small current can generate a voltage that saturates and possibly damages the amplifiers[40].

After the load resistor, the signal is passed through a preamplifier. The amplifier provides gain G_a, but adds noise N_a. Even the best amplifier degrades the $\frac{S}{N}$ somewhat,

$$\frac{(SNR)_{out}}{(SNR)_{in}} = \frac{\frac{G_a S_{in}}{G_a N_{in} + N_a}}{\frac{S_{in}}{N_{in}}} = \frac{G_a N_{in}}{G_a N_{in} + N_a} < 1 \qquad 2.41$$

Obviously the amplifier would be omitted from the circuit if it was not needed for other reasons. In FMS two reasons conspire to necessitate the use of a

[39]This assumes that we have chosen the circuit's time constant as 63% of RC and that RC< the transit time across the diode.

[40]R_L must also be kept small enough so that the maximum voltage would not exceed the diode's reverse bias voltage.

preamplifier. First, the tiny FM signals we wish to record must be large enough for measurement by the ultimate recording device, whatever that is. Some type of amplification is always required, even if it occurs within the recording device itself. Secondly, RF amplification is achievable with much less noise and at much less expense than the low frequency amplification that would be required after demodulation, perhaps within the recording device. Thus, the most inexpensive and lowest noise option is to use an RF preamplifier, before demodulation. The most convenient way to include the amplifier noise is to modify equation 2.39 to use an effective noise temperature, T_e, defined by

$$T_e = T + T_a, \tag{2.42}$$

where T_a is the amplifier noise temperature related to its specified (unitless) noise *factor*, F, or noise *figure* (in dB) NF,

$$F = 1 + \frac{T_a}{290}, \quad NF = 10 \log F. \tag{2.43}$$

After the preamplifier [41], the signal is fed into the mixer for demodulation. The mixer acts somewhat like an attenuator, reducing the signal by at least a factor of two, since we are only interested half of its output, the low-pass filtered

[41]The gain bandwidth of the preamplifier should select only the RF beat signal. Otherwise a filter must be used to remove the unwanted signals at (intense) DC and the even harmonics of the modulation frequency.

difference frequency. This effective mixer attenuation can be accounted for by adjusting the gain parameters of the preamplifier.

After the mixer, a device is used to establish the system bandwidth. One simple method uses a mechanical chopper to *100%* amplitude modulate the laser beam[42] and a lock-in amplifier to recover this low frequency modulation of the signal currant. The lock-in allows various integration times (hence bandwidth selectivity) and additional pre-and post low-frequency demodulation amplification. The small noise added by the lock-in need not be considered[43] and the 50% duty cycle reduction (by the chopper) becomes significant only if effects due to the ambient light become appreciable (including ambient light shot-noise).

Now we can express the external total noise $\overline{i_{Nx}^2}$ added by the detection system (including laser shot-noise),

$$\overline{i_{Nx}^2} = \overline{i_{SN}^2} + \overline{i_{PraAmp}^2} + \overline{i_{Th}^2} = 2e\left(\sqrt{\overline{i_d^2}} + \rho G_{det}^{2+x} P_c\right)\Delta f + \frac{4kT_e\Delta f}{R_L} \qquad 2.44$$

Our goal here, to have a shot noise limited *detection* system, will be met when the $2e\left(\sqrt{\overline{i_d^2}} + \rho G_{det}^{2+x} P_c\right)\Delta f$ term dominates in equation 2.43.

[42]The amplitude modulation does not itself reduce the noise of the laser. For insights into how modulation affects noise, see following section on internal noise.

[43]The noise (added by the preamplifier) is amplified by the lock-in to a level much higher than the noise the lock-in itself contributes. From this, a general rule of thumb is inferred: for a properly designed experiment, the first amplifier (the pre-amplifier) determines the $\frac{S}{N}$.

The dark current is constant and determined by the detector (and temperature) and, since it is small, on the order of $1 - 10\,nA$ (for visible wavelength photodiodes), its contribution to the shot-noise is not of much concern here. Instead, the most important factors determining the dominant external noise source are the optical power and preamplifier noise.

Lets us consider now, some real examples: a typical (large area, 5 mm^2) PIN photodiode (EG&G FND-100), with device characteristics at $600\,nm$,

$$\begin{aligned} &\rho G_{det} = 0.4\,A/W \\ &C_{Det} = 8.5\,pF \\ &i_d = 10nA \\ &\left[R_d > 10^6\Omega,\ R_S = 20\Omega\right] \end{aligned} \qquad 2.45$$

coupled *via* a resistor to a preamplifier. From the data above and equation 2.40, when $R_L = 50\,\Omega$, $f_{3-dB} = 375\,MHz$. The manufacturer recommends using a high $90\,V$ reverse bias to reduce the transit time to less than $1\,nS$ so that the practical $3\,dB$ bandwidth will be typically larger than $350\,MHz$. Then, for $R_L = 50\,\Omega$, the diode's response would be transit time limited. Fluctuation in the bias voltage would then cause fluctuation in the diode's frequency response, and a loss of sensitivity at high frequencies, with little effect on the dc response. Thus the bias voltage must be from a very stable power supply[44].

[44]A battery makes an excellent, stable bias supply. But, when large currents are drawn from the battery, the voltage may droop, reducing the modulation response.

Let us now add a $50\,\Omega$ input impedance preamplifier, one that is either a low noise model with $NF = 1dB$, or a more typical (noisy) one with $NF = 10\,dB$. The low noise model increases the effective thermal noise temperature by $75\,K$[45], while the noisy one increases it by $2610\,K$. The total noise (root mean square current) and the various contributions to it, are plotted in figure 2.6 *vs.* the incident optical power for a narrow[46] detection bandwidth of $\Delta f = 1\,Hz$. To be just at the shot noise limit for this equipment and bandwidth, the optical power on the diode must exceed $1\,mW$ for the low noise amplifier, and $10\,mW$ for the noisy one. Unfortunately, the higher intensity necessary for the $NF = 10\,dB$ amplifier may not be tolerated by the detector, may be unavailable, or may cause unwanted saturation of the optical transition, so that using the noisy amplifier may rule out implementation of shot-noise limited detection. If the available optical power is less than needed for the low noise amplifier, a different photodetector with internal gain, such as an Avalanche Photodiode (APD), is required. The internal gain increases the signal current and the shot-noise, but the shot-noise increase is somewhat faster, because the *excess* shot-noise factor x in equation 2.38 is greater than zero. Therefore, for an APD, the value of the detectors gain should be only as large as needed to be just at the shot-noise limit.

[45]A noiseless amplifier would have $NF = 0\,dB$. To achieve noise figure much lower than $1dB$, the amplifier and load resistor would have to be cooled.

[46]The importance of narrow vs large bandwidth becomes immense once internal noise sources are considered.

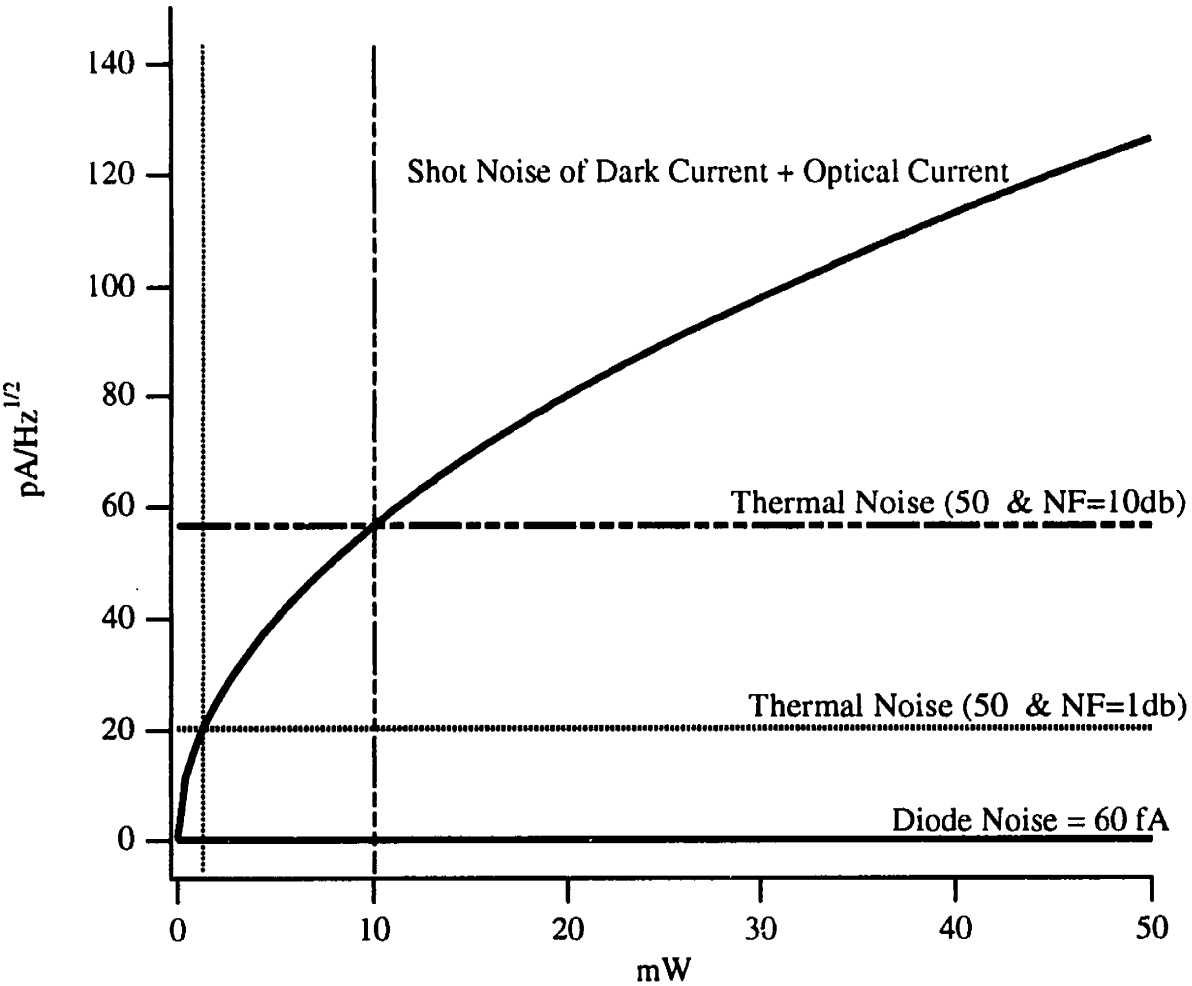

Figure 2.6: FMS receiver noise for the EG&G FND-100 PIN photodiode as a function of optical power on the detector.

2.3.3 *Internal Noise*

Shot-noise, external noise sources, and shot-noise limited *receiver* design was discussed in the previous sections. To implement a shot-noise limited FMS *experiment*, the detected internal noise must less than the shot-noise. Although the total internal laser noise, $\overline{i_L^2}$, is much larger than the shot-noise, an FMS experiment is designed to detect only a portion of $\overline{i_L^2}$. It is then the size of this "portion" that is of crucial importance. Many factors, including the total laser noise, the magnitude of the FMS signal, and the particular EOM used, influence the size of the portion of detected internal noise. Overall, the signal noise ratio of FMS is dominated by contributions from the laser noise, while the dynamic range is limited by the combined effects of laser noise and imperfect phase-modulation.

In the past, the $\frac{S}{N}$ of FMS has been investigated when the signal level is vanishingly small. For small signals, the noise was dominated not by the shot-noise, but rather by a portion of the internal laser noise that unfortunately "leaks" in (Gehrtz 1985). Experimental efforts have attempted to elucidate the fundamental origin of the "leak" with incomplete success (Whittaker 1985). Theoretical reports have modeled its effect on the FM line shape and detection sensitivity for the smallest signals (Gehrtz 1985). And finally, various methods

have been presented to obliterate effects of the "leaks", by modifying and extending the FM technique (Levenson 1983; Whittaker 1984a,b; Wong 1985; Gehrtz 1985; McCarthy 1992; Bloch 1994). Nonetheless, the complete origin of and the parameters that control the leak remain unsatisfactorily known (Gehrtz 1985). Many of the key insights even remain undeveloped, because only effects on vanishingly small signal levels were considered. In the following sections, the "leak" is discussed for all signal levels.

2.3.3.1 *All FM signals add noise*

This section shows how every FM signal increases the detected noise level. The *cw*-laser used in the FMS experiment has a total internal noise level in excess of the optical shot-noise. The average total excess noise power detected on the single-component *cw*-laser beam is $\overline{i_{LN}^2}$. What happens to the noise during phase-modulation in the EOM? Just as the average intensity of the laser was preserved in the phase-modulation process, so is the average noise power.

Consider the carrier before modulation. It has a time-dependent amplitude and phase that contains the noise. In the modulation process, described by equation 2.24, this noise is copied onto every frequency component of the FM-ed laser beam. Thus, phase modulation does not remove any noise[47], and if the EOM

[47]In fact, this is a general result applying to all types of modulation, including amplitude

functions as designed, should not add noise either[48].

FMS should have a zero background level. The zero background develops because of pair-wise cancellation of sideband-carrier beat notes. In mathematical treatments of FMS, the cancellation occurred *via* a subtraction of the parameters describing the sample interaction; recall equation 2.20 for reference. Even though the original laser has excess internal noise, as does each component in the FM'ed laser beam, in the subtraction process that occurs in FMS detection, all of this noise is cancelled when no excess internal noise is present at the modulation frequency. This demonstrates the importance of the modulation frequency being beyond the noise bandwidth of the laser.

When an FM signal occurs, the noise cancellation is no longer *perfect.* Hence, *an FM signal always is accompanied by a noise signal due to detection of a portion of the internal noise.* This basic fact has been absent in most $\frac{S}{N}$ analyses of FMS, yet neglecting this idea makes understanding background noise sources impossible.

To quantify this in a simple manner, we must introduce a parameterized expression for the NB FMS signal, and the total internal laser noise. Let us

---

modulation. Modulation just copies, or moves noise to a different frequency.

[48]If the RF drive to the EOM is noisy, phase-modulation will add some noise. A carefully designed detection system, with matched electrical and optical propagation times, will not detect this noise off-resonance.

assume that the sample interaction is purely absorptive and small, that there are no other losses (background absorptions), and that the width of a particular spectral feature is small compared to the modulation frequency so that it is probed by only one sideband and that the carrier is unaffected. In such a case, the FM experiment is placed on *somewhat* equal footing with OLAS[49], and the FM signal current is,

$$i_{FM} = \frac{G_{det}\rho\delta M P_c}{2}, \qquad 2.46$$

where δ is the (fractional) absorption of the sideband's electric field. This signal causes exactly the fraction δ of the noise associated with one sideband, or the fraction δM of the total internal laser noise, to leak through.

The total internal laser noise before phase-modulation is usefully expressed by the total RMS fractional power fluctuation , N_L, which certainly has frequency and bandwidth dependence that has been omitted here[50]. Then, independent on the particular photodetector used, the carrier to noise ratio or *CNR* in electrical power units is defined,

$$CNR_P = \frac{1}{N_L^2}. \qquad 2.47$$

Hence the portion of the internal noise detected in an FMS experiment due to the

[49]This will be explored when OLAS and FMS are compared.

[50]For example, $N_L = 0.1$ implies that the RMS laser power fluctuates 10%.

FM signal is,

$$\overline{i_{LNFM}^2} = \frac{\left(G_{det}\rho\delta M P_c N_L\right)^2}{4} = \frac{i_{FM}^2}{CNR}. \qquad 2.48$$

This noise portion is non-zero whenever any FMS signal develops. Likewise, if an unwanted FMS signal exists, we must expect that there will be some FMS detected laser noise.

2.3.3.2 *Unavoidable undesired signals and laser noise*

Phase-modulation copies the laser noise onto each optical frequency component of the FM-ed laser. In turn, this is the cause of a non-shot noise FMS noise level whenever an FM signal develops. Unfortunately, even when there is no FM signal, undesirable background signals may occur. These signals can be generated anywhere along the beam path; they also leak noise.

If the undesirable background signal is stable on the timescale of the FM measurement, the background can simply be subtracted from the detected signal, and treated as non-noise interference, but the associated leaked noise must be considered as a noise source. If the undesirable background is unstable, it further contributes to the detected noise.

In the literature, the term Residual Amplitude Modulation or RAM has

referred the non-zero background of FMS itself (stable or otherwise), the detected FM background noise, and even sometimes the effective imbalance of the sidebands that would cause such noise or background. This has obscured the understanding needed for controlling the problem in the laboratory. Hence, except when referring to previous work, use of the term RAM will be avoided.

Previous work has identified two types of RAM that occur with the EOM. RAM displaying optical frequency dependence, probably arising from accidental multipassing within the EOM, and other RAM independent of frequency, arising from an as yet unknown source (Gehrtz 1985). Apparently total RAM on the order of $10^{-5}-10^{-2}$, in units of fractional laser *field* values, are common (Gehrtz 1985, Levenson 1988). Along the beam path, outside of the EOM, weak accidental etalons, perhaps modulated by unstable mechanical optical components, can contribute to the background signal. Regardless of source, the total of all undesirable background signals can be lumped together[51] into a single parameter, a single sideband attenuation factor Δ, defined similarly to the FM signal current in equation 2.46. Δ can be time-dependent if necessary. The total background current (or signal) is,

$$i_{BS} = \frac{G_{det}\rho\Delta M P_c}{2}. \qquad 2.49$$

[51]Since each individual signal is a signed quantity, interferences surely exist.

This current generates a noise source, $\overline{i^2_{BNFM}}$, analogous to equation 2.48,

$$\overline{i^2_{BNFM}} = \frac{\left(G_{det}\rho\Delta M P_c N_L\right)^2}{4} = \frac{\left(\frac{\Delta}{\delta} i_{FM}\right)^2}{CNR} \qquad 2.50$$

Obviously, this noise can be made smaller by reducing the background signal or by reducing the total laser noise. It is unclear why the effect of reducing the total laser noise has been omitted in literature reports of RAM[52]. Now that all relevant noise sources for FMS have been described, the *SNR* of FM can be calculated.

2.3.3.3 *The complete SNR of FMS*

The shot-noise, external and internal noise sources were described, and a simple parameterized model of the FM signal was presented. Assembling the results symbolically, the FMS *SNR* is,

$$\left(\frac{S}{N}\right)_P = \frac{i^2_{FM}}{\overline{i^2_{SN}} + \overline{i^2_{Th}} + \overline{i^2_{LNFM}} + \overline{i^2_{BNFM}}}. \qquad 2.51$$

In a properly designed detection system, thermal noise, dominated by the shot-noise, can be neglected. This yields the simplified result,

[52]Although laser noise has always been mentioned (see Whittaker 1985), it is clear that the possible solution to the RAM problem by reducing laser noise has been omitted. For example, if the RAM is as small as 10^{-5}, and the Shot Noise, 10^{-7} (in fractional optical power units), laser noise of less than 10^{-2} or *1%* is sufficient for shot-noise predominance.

$$\left(\frac{S}{N}\right)_P = \frac{i_{FM}^2}{\overline{i_{SN}^2} + \overline{i_{LNFM}^2} + \overline{i_{BNFM}^2}} = \frac{\delta^2 M^2}{4CQR^{-1} + M^2 CNR^{-1}\left(\delta^2 + \Delta^2\right)}. \qquad 2.52$$

The *CQR* is the carrier to quantum noise power ratio, defined,

$$CQR = \frac{\left(\frac{2}{\delta M} i_{FM}\right)^2}{\overline{i_{SN}^2}} = \frac{\rho P_c}{2e\, G_{det}^x\, \Delta f}, \qquad 2.53$$

if the detector's dark current is also neglected.

Equation 2.52 must be interpreted with care. While three distinct limits exist: shot-noise domination, background/*CNR*, or even signal/*CNR* domination, understanding the entire FMS *SNR* is best gained from considering what is relevant in the laboratory.

In the laboratory, two questions arise. First, what is the smallest detectable absorption, and second, what is the *SNR* of a typical measurement when the absorption is not small?

The smallest detectable absorption, δ_{Min}, is found from equation 2.52 by fixing the minimum acceptable *SNR*. δ_{Min} determines the dynamic range of FMS and quantifies the techniques practical sensitivity. If the minimum acceptable *SNR* is unity, then δ_{Min} becomes,

$$\delta_{Min} = \sqrt{\frac{4CQR^{-1} + \Delta^2 CNR^{-1}}{\left(1 - CNR^{-1}\right)M^2}} = \sqrt{\frac{\frac{8e\, G_{det}^x\, \Delta f}{\rho P_c} + \Delta^2 N_L^2}{\left(1 - N_L^2\right)M^2}}. \qquad 2.54$$

If δ_{Min} is reduced, sensitivity has been improved. Unless the total laser power fluctuations approach unity (100% power fluctuations), δ_{Min} is determined primarily by either the shot-noise or the product of laser noise and background level. If the detection sensitivity is quantum-limited , the product of laser noise and background level must have been made smaller than the shot-noise. Once that is accomplished, (so long as total laser power fluctuations do not approach unity), δ_{Min} is relatively insensitive to *CNR*. In that limit, we can approximate the *SNR* by neglecting the background and laser noise. This yields a simple expression that agrees with previous reports[53], for a unity-gain photodetector, (Bjorklund 1983),

$$\delta_{Min}^{SN} \approx 2\sqrt{\frac{2e\,\Delta f}{\rho P_c M^2}}\,. \qquad 2.55$$

Although shot-noise may be the largest noise source, δ_{Min} may not be optimized. Equation 2.54 suggests that the smaller the bandwidth, the better the sensitivity. Yet, recalling equation 2.54, the bandwidth cannot be decreased without limit and continue to have shot-noise dominated detection. When the bandwidth is too small, not enough shot-noise will be detected to be shot-noise limited. The origin of this issue lies with details of the noise spectra.

[53]Not exactly. Bjorklund 1983 considers detection of the entire beat note at once, which contains twice the number of discrete carriers, and hence, provides a detection limit better by a square root of two.

Shot-noise is white, while laser noise is certainly not; it actually tends towards zero at high frequencies. The optimal δ_{Min}, at any optical power level, occurs when the bandwidth is small enough, that if it is made any smaller, the background laser noise product begins to dominate. A large bandwidth may provide shot-noise limited detection, but alas, with poor sensitivity[54].

The *SNR* for FMS measurements of reasonable signals (signals substantially larger than δ_{Min}) is found from equation 2.5, by neglecting the smallest noise term. This is almost always the shot-noise term. This leads to an effective (laboratory) expression for the *background* limited *SNR* for FMS,

$$\left(\frac{S}{N}\right)_P^{Eff} = \frac{CNR}{1 + \frac{\Delta^2}{\delta^2}}. \qquad 2.56$$

Interestingly, equation 2.56, shows that the *SNR* for FMS is never better than the *CNR*, and when the background levels approach the size of the absorption, the *SNR* may be significantly worse. Equation 2.56 can be used to estimate the background limited detection sensitivity, though it contains no information about the ultimate detection sensitivity of FMS.

[54]Gehrtz 1985 discusses this idea, citing an example (Hollberg 1983), but, following Bjorklund 1983, does not present an unapproximated expression for detection sensitivity.

2.4 *Choosing a technique: Comparing FMS, OLAS, or Fluorescence Detection*

This section compares FMS to OLAS and fluorescence detection in regard to the question, "Which techniques, if any, allow me to make my particular measurement?" Typical real (non-ideal) experimental apparatus are considered, without concern of whether they are actually available. Two choices need to be made: first whether OLAS or FMS provides superior detection sensitivity, and then second, whether the superior absorption based technique or fluorescence detection is more effective.

In the previous section, FMS was placed on equal footing with OLAS by assuming that FMS had simply measured the same single parameter that OLAS did, the absorption of the sample. But, because FMS is a differential heterodyne technique, the signal it measures will often only be a fraction of that measured by OLAS. To compare the use of OLAS and FMS to make the same measurement, a more accurate model of the FMS signal is required. Absorption and fluorescence detection methods can compared by assuming that the fluorescence signal is determined by the product of the OLAS absorption parameter and an effective fluorescence parameter.

Consider now using OLAS to measure the absorption of an isolated molecular resonance. The absorption feature has a energy full width at half maximum of

Γ, and a peak absorption per sample cell length (electric *field* attenuation units) of $\delta_P = \delta(\omega_P)$ at line center ω_P. In OLAS, the optical intensity after the sample on the peak of the resonance is,

$$I_{Out} = e^{-2\delta_P} I_{In} \qquad 2.57$$

where $I_{In} = \frac{E_c^2}{2}$ is the intensity before the sample, neglecting the efficiency of the detector. The absorption parameter (peak absorption) is readily extracted from equation 2.57 *via* normalization. Hence, OLAS measures $-2\delta_P$, because δ_P is the field attenuation,

In FMS, the situation is more complicated because multiple optical frequencies may sample the single feature simultaneously. Determining even the peak FMS signal requires accurate knowledge of the lineshape. For simplicity we consider a Gaussian lineshape with full width at half maximum of Γ,

$$\delta(\omega) = \delta_P exp\left[-(\omega-\omega_P)^2 \frac{4ln\,2}{\Gamma^2}\right] \qquad 2.58$$

For a weak absorber with $\delta_P << 1$, the in-phase component of the NB FM signal, including carrier absorption, is given by an expression similar to equation 2.18,

$$V_{NB}^{Inphase} \approx RM\frac{E_c^2}{2}(1-\delta_0)(\delta_1-\delta_{-1}) \qquad 2.59$$

using $\delta_n = \delta(\omega_c + n\omega_{RF})$. Using the absorption defined in equation 2.58 leads to,

$$V_{NB}^{Inphase} \approx 2RM\delta_P\left(1-\delta_P e^{-\left(\frac{\Delta\omega}{\Gamma}\right)^2 4\ln 2}\right) I_{In} e^{-\left(\frac{\Delta\omega}{\Gamma}\right)^2 4\ln 2} e^{-\left(\frac{\omega_{RF}}{\Gamma}\right)^2 4\ln 2} \sinh\left(\frac{\omega_{RF}\Delta\omega}{\Gamma^2} 8\ln 2\right) \qquad 2.60$$

A plot of equation 2.60 (neglecting the term quadratic in δ_P) is shown in figure 2.7a. In general, the largest FMS signal occurs when $\frac{\omega_{RF}}{\Gamma} = \frac{\omega_0 - \omega_p}{\Gamma}$. Figure 2.7b displays equation 2.60 for a few values of δ_P with the constraint $\omega_0 = \omega_{RF} + \omega_p$ as a function of $\frac{\omega_{RF}}{\Gamma}$. This constraint fixes the frequency of one sideband at line center (so that it always experiences the peak absorption δ_P), while varying $\frac{\omega_{RF}}{\Gamma}$ tunes the carrier and other sideband across the feature.

The plot in figure 2.7b can be divided into three regions: (I) large $\omega_{RF} > \Gamma$, (II) moderate $\frac{\omega_{RF}}{\Gamma}$, and (III) small $\omega_{RF} << \Gamma$. In region (III) all 3 components of the FM-ed laser simultaneously probe the feature, while in region (I) each component samples the feature independently.

In region (I) the signal has saturated and the parameters are optimized. At best, therefore, FMS determines δ_P, not $2\delta_P$. In region (II), the FMS signal scales roughly as $\delta_P\left(\frac{\omega_{RF}}{\Gamma} - \delta_P\right) 4\ln 2$. That is, linearly with $\frac{\omega_{RF}}{\Gamma}$, but both linearly and quadratically with the absorption. Since $\frac{\omega_{RF}}{\Gamma} < 1$, the quadratic term is negligible for small absorptions. For large absorptions in region (II) the carrier is attenuated along with the sideband, reducing the signal. In region (III),

(a)

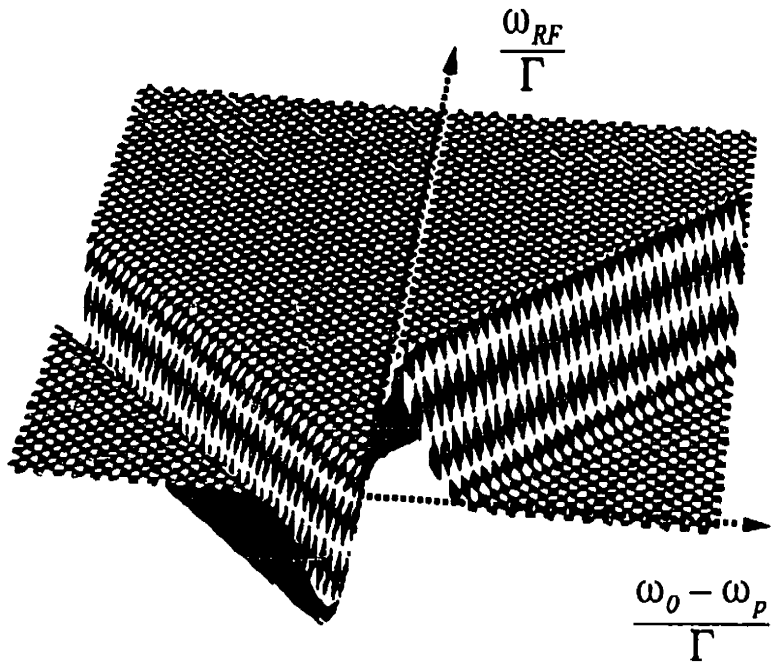

(b)

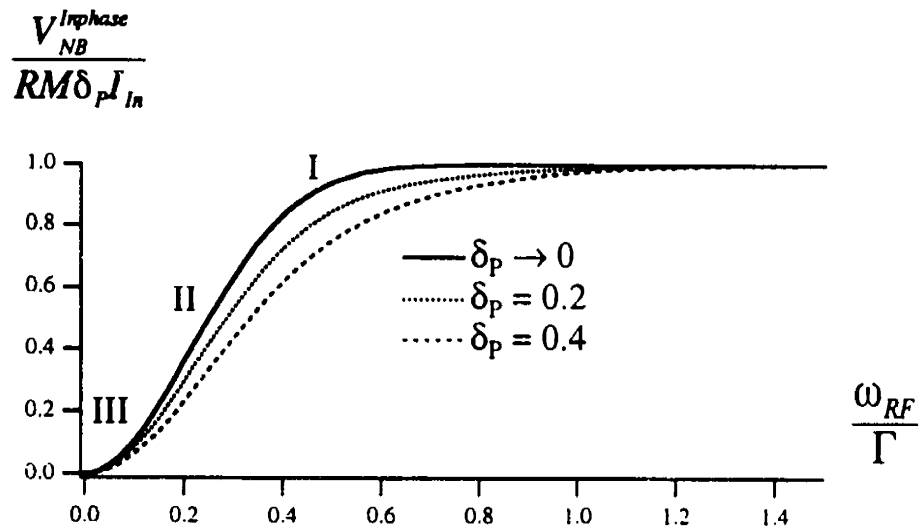

Figure 2.7ab: Plots of the FMS in-phase signal as a function of relative modulation frequency and relative laser tuning. See description in text.

the signal is very sensitive to $\frac{\omega_{RF}}{\Gamma}$. If $\omega_{RF} << \Gamma$, the maximum FMS signal occurs when laser frequency is tuned so that $\frac{\omega_0 - \omega_p}{\Gamma} \approx \pm 1$. This is not evident from figure 2.7 but rather from the fact that when $\omega_{RF} << \Gamma$, the FMS signal closely approximates the first derivative of the absorption lineshape, whose extremes occur at $\frac{\omega_0 - \omega_p}{\Gamma} \approx \pm 1$. For comparison purposes, a single factor can be used for the effect of any FMS signal reduction relative to OLAS,

$$a = \frac{V_{NB}^{Inphase}}{R\delta_P} \leq 0.5M \qquad 2.61$$

For large modulation frequencies (region (I) in figure 2.7b) the factor is closest to unity (no loss) at $0.5M$.

The complete FM *SNR* has already been presented while the OLAS *SNR* is easily found. Recall that *CNR* is the carrier to noise ratio and that the dominant noise source in OLAS is always the laser noise so that,

$$\left(\frac{S}{N}\right)_P^{OLAS} = \frac{4\delta^2}{CNR^{-1}} = 4\delta^2 CNR. \qquad 2.62$$

Then, setting the minimum acceptable *SNR* at unity, the minimum detectable signal in OLAS is half the square root of CNR^{-1}. The minimum detectable signal in FMS depends upon the limiting noise source. For background limited FMS, the worst case (see equation 2.56),

$$\delta_{Min}^{FM,BL} = \frac{\Delta}{a\sqrt{(CNR-1)}}. \qquad 2.63$$

FMS provides superior sensitivity than OLAS does unless the FMS attenuation factor squared[55] is on the order of the $\Delta^{-2}CNR$. In rare cases, a very strong absorption, a very small modulation index , or a very small modulation frequency, in combination or by themselves, can cause OLAS to win out. Most often, FMS will be chosen over OLAS for sensitive detection even for extreme FMS backgrounds ($\Delta \approx 0.1$).

The choice between FMS and a fluorescence based technique is more complicated because it depends upon dominant noise sources for each technique, which may differ, even when the same laser is used for both methods. In theory, four possibilities exist, the combinations of shot-noise or background noise predominance for each method. Since, it would be unusual for FMS to be shot-noise limited and fluorescence to be background limited, this case will be ignored[56] below. For simplicity only weak absorption and weak fluorescence are considered. In that case, the fluorescence shot-noise limited *SNR* is

$$\left(\frac{S}{N}\right)_P^{F,SN} = \frac{\delta F}{CQR^{-1}} = \delta F CQR, \qquad 2.64$$

[55]For a $1\ mW$ laser, $\Delta^{-2}CNR$ is on the order of 1×10^6 in power units.

[56]This would only occur if the detected fluorescence could not be separated from scattered laser radiation because they occur at the same optical frequency.

where F is the overall fluorescence yield reflecting the product of the fluorescence quantum efficiency and the detector's collection efficiency[57], CQR is the carrier to quantum noise ratio. The FM shot-noise limited SNR, entirely neglecting laser noise, from equation 2.52, is

$$\left(\frac{S}{N}\right)_P^{FM,SN} = \frac{1}{4}a^2\delta^2 CQR \ , \qquad 2.65$$

where $\delta_{FM} = a\delta$ with $0 \le a \le 0.5M$, reflecting the fact that the absorption parameter for FMS must be reduced to account for non-optimal FMS.

The fluorescence background limited SNR is,

$$\left(\frac{S}{N}\right)_P^{F,BN} = \frac{CNR}{1 + \frac{\Delta_F^2}{\delta^2 F^2}} \qquad 2.66$$

where Δ_F is a fluorescence background parameter. This SNR has a weak dependence on signal because, in theory, fluorescence methods are background-free techniques. The FMS background limited SNR is given in equation 2.56, by inserting the proper attenuation factor. These results are used to calculate the minimum detectable absorption and are compiled in table 2.2.

From table 2.2, we see that when both techniques are shot-noise limited[58],

[57]The SNR depends linearly of the product δF because the shot noise here is due only to the fluorescence intensity and not the total laser intensity.

[58]and performed on the same sample, with the same laser.

that FMS provides superior detection sensitivity when,

$$a > 2F\sqrt{CQR} \qquad 2.67$$

From the example calculation of the shot noise for a *1 mW cw*-laser presented just after equation 2.38, $\sqrt{CQR}$ is found to be about 2×10^7. For this example, FMS would provide superior sensitivity when the effective fluorescence yield is less than 10^{-7}. Clearly, unless the fluorescence is very weak and poorly detected, FMS will provide *inferior* sensitivity.

Table 2.2: Comparison of FMS and Fluorescence detection limits

δ_{Min} *for* $\left(\frac{S}{N}\right)_P = 1$	Shot-Noise Limited	Background Limited
FMS	$\frac{2}{a\sqrt{CQR}}$	$\frac{\Delta}{a\sqrt{(CNR-1)}}$
Fluorescence	$\frac{1}{F\,CQR}$	$\frac{\Delta_F}{F\sqrt{(CNR-1)}}$

In general, the experimental conditions can be changed to enhance the

performance of either technique. Increasing the power[59], favors fluorescence, yet increasing the path length usually favors FMS, because of difficulties involved in efficiently collecting long path fluorescence. In fact, with a long multipass cell, or a high finesse optical cavity, it is not unreasonable to expect FMS to provide substantially superior sensitivity[60] when both techniques are shot-noise limited. In addition to changing the theoretical sensitivity of the methods, changing the conditions may actually severely limit practical implementation of the techniques.

When both techniques are background limited, FMS would provide superior detection sensitivity when, (from table 2.2),

$$\frac{\Delta}{a} < \frac{\Delta_F}{F}. \qquad 2.68$$

Here, FMS is usually superior, and for a multipass cell, certainly so. The other possibilities from the table 2.2 produce obvious, expected results.

2.4 *FMS: Conclusion or Introduction*

In the preceding section, FMS was shown to provide superior sensitivity to OLAS, and when the conditions were appropriate, even superior sensitivity to

[59]Increasing the optical power considerably above *1 mW* will damage the EOM.

[60]Mathematically, imagine an FMS enhancement factor, rather than attenuation factor, $a >> 1$.

fluorescence based detection methods. An additional benefit of using FMS, perhaps lost sight of in the comparison based on absorption, was FMS's unique ability to measure the dispersion of a sample, which is measured neither by OLAS nor fluorescence methods.

Due to a non-zero product of background signal and laser noise, FMS does not often provide shot-noise limited sensitivity under narrow detection bandwidth conditions. Furthermore, if the shot-noise limited regime were reached, the laser intensity could not be increased substantially (to increase the sensitivity), due to equipment limitations and damage thresholds.

Nonetheless, certain molecular systems, those in which fluorescence is weak or poorly collectable, can only be studied by an absorption-based direct method. For those cases, FMS is ideal, assuming that a suitable laser source is available at the wavelength of the study. Unfortunately, *cw*-lasers are not available throughout the optical spectrum. This limits the applicability of FMS to the visible and near IR regions (Tran 1983).

These two primary defects of FMS-- the non-shot noise limited sensitivity, and the limited wavelength range-- can be overcome by extending the method. Consider this chapter as an introduction to the new extensions of FMS, FM-MRS and pulsed-FMS.

2.5 *References*

1985 Arfken, G., *Mathematical Methods For Physicists*, Boston: Academic Press.

1980 Bjorklund, G. C. ,"Frequency-modulation spectroscopy: a new method for measuring weak absorptions and dispersions", *Opt. Lett.*, **5**, 15.

1983 Bjorklund, G. C., M. D. Levenson, W. Lenth, and C. Ortiz, "Frequency Modulation (FM) Spectroscopy: Theory of Lineshapes and Signal-to-Noise Analysis," *Appl. Phys. B*, **32**, 145.

1994 Bloch, J. C., R. W. Field, G. H. Hall, T. J. Sears, "Time-resolved Frequency Modulation Spectroscopy of Photochemical Transients," J. Chem. Phys., 101, 1717.

1964 Born, M. and E. Wolf, *Principles of Optics*, New York: Macmillian.

1983 Castellan, G. W., *Physical Chemistry*, 3rd edn., Reading: Addison-Wesley Publishing Co.

1987 Cooper, D. E., and R.E. Warren, "Two-tone optical heterodyne spectroscopy with diode lasers: theory of line shapes and experimental results," *J. Opt. Soc. Am. B.*, **4**, 470.

1981 Demtröder, W., *Laser Spectroscopy* (Springer series in chemical

physics; v. 5), Berlin: Springer-Verlag.

1985 Gehrtz, M., G. C. Bjorklund, E. A. Whittaker, "Quantum-limited laser frequency-modulation spectroscopy," *J. Opt. Soc. Am. B.*, **2**, 1510.

1984 Gower, J., *Optical Communication Systems*, Englewood Cliffs, N.J. : Prentice-Hall.

1977 Hirschfeld, T, "The Choice between Absorption and fluorescent Techniques," *Appl. Spectrosc.*, **31**, 245.

1993 Hsu, H. P., *Schaum's outline of theory and problems of analog and digital communications*, New York: McGraw-Hill.

1982 Ingle, J. D.Jr., "Additional Comments Relating to the Choice between Absorption and Fluorescent Techniques," *Appl. Spectrosc.*, **36**, 588.

1941 Jones, R. C., "New Calculus for the treatment of optical systems," *J. Opt. Soc. Am.*, **31**, 488.

1995 Karu, Z. Z., *Signals and Systems Made Ridiculously Simple*, Cambridge, ZiZi Press.

1983 Keiser, G., *Optical Fiber Communications*, New York: McGraw-Hill.

1983 Levenson, M. D., W. E. Moerner, and D. E. Horne, "FM spectroscopy detection of stimulated Raman gain,"*Opt. Lett.*, **8**, 108.

1988 Levenson, M. D. and S. S. Kano, *Introduction to nonlinear laser*

spectroscopy, Boston: Academic Press.

1995 Lipson, S. G., H. Lipson, and D. S.Tannhauser, *Optical Physics*, 3rd edn., Cambridge: Cambridge University Press.

1986 "A Lock-in Primer," *PARC technical Note T-459*, EG&G Princeton Applied Research, Princeton, N.J.

1994 McCarthy, M. C., J. C. Bloch, and R. W. Field, "Frequency-modulation enhanced magnetic rotation spectroscopy: A sensitive and selective absorption scheme for paramagnetic molecules," *J. Chem. Phys.*, **100**, 6331.

1988 Palais, J. C., *Fiber Optic Communications*, 2nd edn., Englewood Cliffs, N.J.: Prentice Hall.

1966 Ross, M., *Laser Receivers: Devices, Techniques, Systems*, New York: John Wiley & Sons.

1991 Silver, J. A., D. S. Bomse, and A. C. Stanton, "Frequency-modulation absorption spectroscopy for trace species detection: theoretical and experimental comparison among methods" in *Optical Methods for Ultrasensitive Detection and Analysis: Techniques and Applications*, Proc. Soc. Photo-Opt. Intrum. **1435**, 64.

1994 Supplee, J. M., E. A. Whittaker, and W. Lenth, "Theoretical description of frequency modulation and wavelength modulation

spectroscopy," *Appl. Opt.*, **33**, 6294.

1984a Whittaker, E. A., B. J. Sullivan, G. C. Bjorklund, H. R. Wendt, and H. E. Hunziker, "ND_4 Schüler band absorption observed by laser FM spectroscopy in a photochemical reaction," *J. Chem . Phys.*, **80**, 961.

1984b Whittaker, E. A., H. R. Wendt, H. E. Hunziker, and G. C. Bjorklund, "Laser FM Spectroscopy with Photochemical Modulation: A Sensitive, High Resolution Technique for Chemical Intermediates," *Appl. Phys. B*, **35**, 105.

1985 Whittaker, E. A., M. Gehrtz, and G. C. Bjorklund, "Residual amplitude modulation in laser electro-optic phase modulation," *J. Opt. Soc. Am B.*, **8**, 1320.

1985 Wong, N. C., and J. L. Hall, "Servo control of amplitude modulation in frequency-modulation spectroscopy: demonstration of shot-noise-limited detection," *J. Opt. Soc. Am. B.*, **9**, 1527.

1991 Yariv, A. , *Optical Electronics*, 4e, Philadelphia: Saunders College Publishing.

3.1 *Introduction to FM-MRS*

Frequency Modulation Enhanced Magnetic Rotation Spectroscopy or FM-MRS, is a double-null, absorption based cw-laser technique that measures the magnetic optical activity (circular birefringence and circular dichroism) of a sample with shot-noise limited detection. FM-MRS is a complementary combination of FM spectroscopy (previously discussed in chapter 2) and Magnetic Rotation Spectroscopy (MRS, see appendix A) that offers a significant improvement in sensitivity and utility over the individual methods (McCarthy 1994).

Whereas FM spectroscopy is applicable to the study of any atom, molecule, or optical cavity system, MRS, based on the Zeeman effect, is applicable to only paramagnetic species such as radicals. Because of the $1/J(J+1)$ intensity dependance of the the linear Hund's case (a) Zeeman effect, both MRS and FM-MRS provide relative enhancement of low-J spectral lines, as well as line shapes that contain branch-dependent phase diagnostics. This additional information, not obtainable with FMS, often simplifies a molecular spectrum and aids in its

interpretation. In addition to being selective to paramagnetic species, FM-MRS provides 2 to 3 orders of magnitude of greater sensitivity than FMS alone.

FM-MRS achieves its high sensitivity by *optically* (as opposed to electronically) suppressing the residual non-shot noise FM background that limits the detection sensitivity of nearly all applications of FMS. Accompanying this improvement is an associated but much smaller reduction of signal, due to FM-MRS's reliance on the MR effect (see Appendix A).

Based on the presentation of FMS in chapter 2, expressions for the unique line shapes FM-MRS produces are developed in the next section. The issues involving the FM-MRS signal reduction, detection sensitivity, and equipment will also be discussed.

Next, the high sensitivity of FM-MRS will be illustrated by an experiment involving detection of NO_2 (Smith 1995). Detection of trace levels of NO_2 is critical in atmospheric pollution monitoring and also in forensic applications, because NO_2 is an expected decomposition product of many explosive materials. FM-MRS will be shown to provide NO_2 detection levels of 20 parts in 10^9 in one well-defined region, while being relatively insensitive to higher ambient laboratory concentrations along the entire beam path. Simple digital signal processing techniques, that exploit the unique FM-MRS line shapes, will be shown to improve the detection sensitivity by 2 orders of magnitude or more.

Following the demonstration of detection sensitivity, the ability of FM-MRS to enhance low-J spectral lines (compared to higher-J lines) will be demonstrated by describing an experiment on Cerium Monofluoride(CeF) in the next chapter. CeF is produced in a high temperature oven at $2000K$ and its optical spectra are therefore exceeding complex and weak, owing to the dispersed thermal population and the open-shell, "radical" nature of the molecule. FM-MRS will be shown to reduce the effective temperature of the gas while providing adequate sensitivity to facilitate identification and assignment of the most important spectral features.

3 .2 *FM-MR spectroscopy: The general result*

Figure 3.1 displays a simplified schematic of the essential FM-MRS experimental equipment. The arrangement is very similar to that of FMS, shown in figure 2.1 with, however, two major differences. First ,the sample is now contained in a homogeneous d.c. magnetic field, whose axis is parallel to the laser beam's propagation axis. Second, a pair of optical polarizers are inserted into the beam path and aligned in a "crossed" configuration, so that second polarizer provide maximum extinction of the laser beam intensity. A mathematical description of the experiment follows. It is assumed that the reader already has

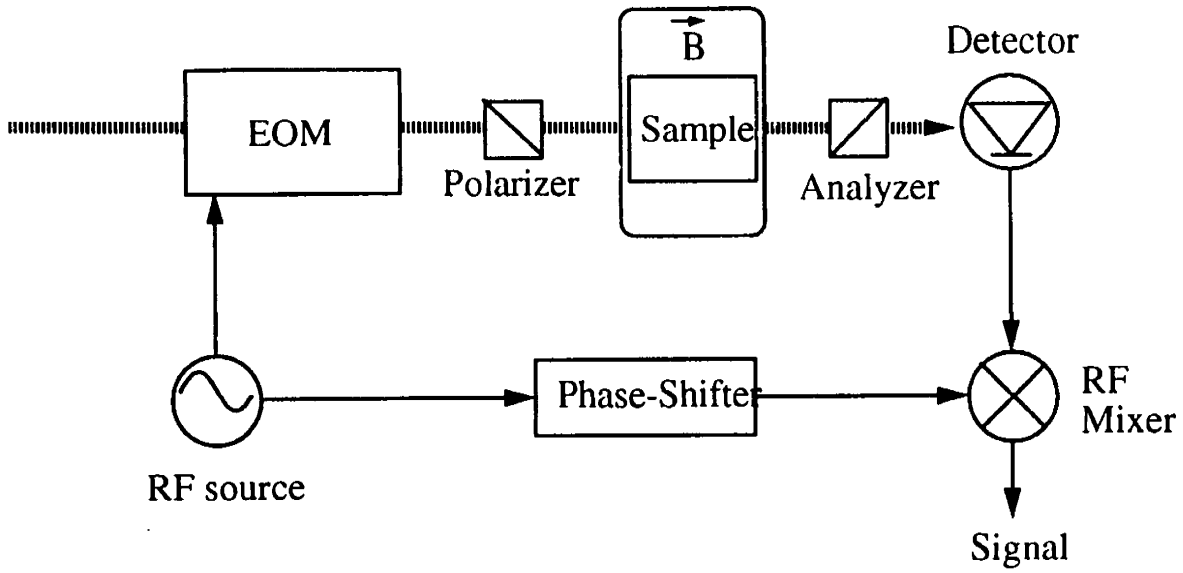

Figure 3.1: Simplified diagram of the FM-MRS experiment. The arrangement of equipment is very similar to figure 2.1 for FMS, except that for FM-MRS, the sample has been placed in an axial (relative to the laser beam, shown as a doted line) magnetic field and two polarizers have been inserted into the beam path. The entrance polarizer is aligned to transmit the maximum laser intensity while the exit polarizer, the analyzer, is aligned for full extinction of the laser intensity off-resonance. See also figure 3.4.

substantial familiarity with the description of FMS as presented in chapter 2.

The output of a single longitudinal mode *cw*-laser is passed through an electro-optic modulator (EOM), an ideal optical linear polarizer, and then enters a sample cell. The laser beam propagates along the laboratory $\hat{z}$- axis so that its polarization vector lies in the $\hat{x},\hat{y}$ plane. Following the presentation in chapter 2, the electric field entering the sample cell is described as,

$$\vec{E}_{FM-MRS}(t) = E_{c_n} \sum_{n=-\infty}^{\infty} J_n(M) e^{i(\omega_c + n\omega_{RF})t} (\hat{p}_c \cdot \hat{p}_{in}) \hat{p}_{in} \qquad 3.1$$

where $\hat{p}_{in}$ is the polarization axis of the laser beam (here determined by the entrance polarizer), and $\hat{p}_c$ is the linear polarization axis of the laser beam at the exit of the EOM, as determined by the EOM *and* the original laser[1] output. All other variable definitions are given in chapter 2. The unit vectors $\hat{p}_{in}$ and $\hat{p}_c$ are real quantities. As in chapter 2, the detected intensity at this point[2] has no components oscillating at the EOM modulation frequency ω_{RF}.

Next, the laser beam, described by equation 3.1, passes through the sample that may be magnetically active. The effect of the axial magnetic field on a

[1]In contrast to FMS, the polarization state of the laser beam in FM-MRS is of crucial importance.

[2]This assumes that the laser's polarization axis is aligned exactly parallel to one of the EOM's crystal axes and that the crystal has no residual birefringence in this configuration. Otherwise, the crystal acts as a sample, and the entrance polarizer becomes the analyzer, producing a background FM-MRS signal.

magnetically active sample is to cause circular birefringence and circular dichroism, creating a *difference* in the effective absorption and dispersion of the two circularly polarized components of the laser field (see Appendix A), and ultimately a rotation of the original linearly polarized laser beam axis. For convenience, "standard normalized"-Jones calculus (Jones 1941,1948; Kliger 1990) is used to describe all quantities throughout this treatment. Hence, the orthonormal vectors describing the linear (as opposed to circular) laboratory axis system are

$$\hat{x} = \begin{pmatrix} 1 \\ 0 \end{pmatrix} \; ; \; \hat{y} = \begin{pmatrix} 0 \\ 1 \end{pmatrix}. \qquad 3.2$$

The linear $\hat{x}$ and $\hat{y}$ axes are defined relative to the right ($\hat{\sigma}_+$) and left ($\hat{\sigma}_-$) handed circular axes or vectors, *via*,.

$$\hat{\sigma}_+ = \frac{1}{2}(\hat{x} + i\hat{y}) \; ; \; \hat{\sigma}_- = \frac{1}{2}(\hat{x} - i\hat{y}). \qquad 3.3$$

Any polarization state can be represented equally well using either the linear or circular axis systems.

In the description of FMS, the polarization state of the laser was unchanged by the sample, so that the sample interaction was effectively modeled by a single effective $S_n = e^{-\delta_n} e^{-i\phi_n}$ parameter . For FM-MRS, a 2×2 Jones matrix is required

to account for the interaction that potentially alters the polarization state of the laser. Formulated in the linear bases set as an effective operator, the needed *matrix* $\mathbf{S}_n$ is,

$$\mathbf{S}_n = \frac{1}{2}\begin{bmatrix} S_n^+ + S_n^- & -i(S_n^+ - S_n^-) \\ i(S_n^+ - S_n^-) & S_n^+ + S_n^- \end{bmatrix} \qquad 3.4$$

where n signifies the optical frequency ω_n, using the usual $\omega_n = \omega_c + n\omega_{RF}$. The elements of the matrix contain combinations of the absorption (*via* $\delta_n^{+/-}$) and phase-shift (*via* $\phi_n^{+/-}$) experienced by the right (indicated by a "+" superscript) and left (indicated by a "-" superscript) handed circularly polarized components of the field defined,

$$S_n^{+/-} = e^{-\delta_n^{+/-}} e^{-i\phi_n^{+/-}}. \qquad 3.5$$

All linearly polarized effects (background absorption and dispersion identical for both the right and left handed circularly polarized fields) have been ignored[3]. The selectivity of FM-MRS is contained in this formulation of $\mathbf{S}_n$; when $S_n^+ = S_n^-$ (for all n), the off-diagonal matrix elements are zero, no rotation of the plane of polarization occurs[4], and $\mathbf{S}_n$ becomes proportional to the (diagonal) identity

[3]Including the effects of linear dichroism or linear birefringence complicates the calculation of the overall sample interaction matrix, since matrices that describe the individual interactions (e.g., linear birefringence and circular birefringence) do not commute (Kliger 1990, 150).

[4]To describe completely the elliptical polarization after the sample, two amplitude and two phase parameters are needed. Hence, two "angles" may rotate or change: the arctangent of the ratio of the two amplitude parameters, or the difference in the two phase parameters (Kliger 1990, 65).

matrix. When any $S_n^+ \neq S_n^-$, the linearly polarized states are "mixed" by the off-diagonal matrix elements in equation 3.4, and the plane of polarization rotates. $S_n^+ \neq S_n^-$ occurs only for magnetically active paramagnetic samples[5].

After the sample, the laser beam is passed through the exit polarizer or analyzer. The analyzer selects the component of the laser's field parallel to the polarizer's axis, $\hat{p}_{out}$. The light emerging from the analyzer, $\vec{E}^S_{FM-MRS}(t)$, also has a polarization axis of $\hat{p}_{out}$,

$$\vec{E}^S_{FM-MRS}(t) = E_{c_n} \sum_{n=-\infty}^{\infty} \{\hat{p}_{out} \cdot [S_n J_n(M) e^{i(\omega_c + n\omega_{RF})t} (\hat{p}_c \cdot \hat{p}_{in}) \hat{p}_{in}]\} \hat{p}_{out} . \qquad 3.6$$

This field then impinges on a suitable photo-detector, developing the intensity, $I_{FM-MRS}(t)$. The RF mixer extracts the components of $I_{FM-MRS}(t)$ oscillating at ω_{RF}. This yields the detected signal, V_{FM-MRS}, whose expression is simplified by noticing that equation 3.6 becomes very similar in form to equation 2.32 of chapter 2, if the substitution $T_n = \{(\hat{p}_c \cdot \hat{p}_{in})\, \hat{p}_{out} \cdot [S_n \hat{p}_{in}]\} \hat{p}_{out}$ is used,

$$V_{FM-MRS} = RQ_{det} \frac{E_c^2}{2} \sum_{a=0}^{\infty} J_a J_{a+1} \left[\left(T_a T^*_{a+1} - T^*_{-a} T_{-a-1} \right) e^{-i\phi_{RF}} + c.c. \right] . \qquad 3.7$$

Equation 3.7 now must be carefully explored. Let us assume that the axis of the entrance polarizer forms an angle θ_{in}, and the analyzer an angle θ_{out} (usually for

[5]Residual birefringence or dichroism (linear or circular) that exists independent of the magnetic field also creates a background rotation. Possible sources include vacuum induced strain of the sample cell windows.

FM-MRS, $\theta_{out} \approx \theta_{in} + \frac{\pi}{2}$) with respect to the linear laboratory axis system so that,

$$\hat{p}_{in} = \begin{pmatrix} cos\,\theta_{in} \\ sin\,\theta_{in} \end{pmatrix} \; ; \; \hat{p}_{out} = \begin{pmatrix} cos\,\theta_{out} \\ sin\,\theta_{out} \end{pmatrix} \qquad 3.8$$

and also that, $P = (\hat{p}_c \cdot \hat{p}_{in})$. The value of P is always less than or equal to unity. Using 3.8 and 3.4, T_n is recast as,

$$T_n = \frac{P}{2}\left[(S_n^+ + S_n^-)cos\,\Delta\theta + i(S_n^+ - S_n^-)sin\,\Delta\theta\right]\hat{p}_{out} \qquad 3.9$$

or even more concisely,

$$T_n = \frac{P}{2}\left(S_n^+ e^{i\Delta\theta} + S_n^- e^{-i\Delta\theta}\right)\hat{p}_{out} \qquad 3.10$$

by employing $\Delta\theta = \theta_{out} - \theta_{in}$.

When $\Delta\theta = \pm\frac{\pi}{2}$, T_n simplifies so that $T_n = \pm\frac{iP}{2}(S_n^+ - S_n^-)\hat{p}_{out}$. Here, the overall effective sample interaction is directly proportional to the difference in the individual right and left handed circular interactions, $S_n^+ - S_n^-$. In this case, the entrance and exit polarizers are both ideal[6] and perfectly crossed.

Evaluation of equation 3.7 continues using the product, $T_a T_b^*$,

$$T_a T_b^* = \frac{P^2}{4}\left(S_a^+ S_b^{+*} + S_a^+ S_b^{-*} e^{i2\Delta\theta} + S_a^- S_b^{-*} + S_a^- S_b^{+*} e^{-i2\Delta\theta}\right). \qquad 3.11$$

The product $T_a T_b^*$ reduces so that $T_a T_b^* = \frac{P^2}{2} S_a S_b^* cos^2\,\Delta\theta$ when $S_n^+ = S_n^- = S_n$. The

[6]Ideal here implies that no light, including shot-noise, comes through the crossed polarizers.

right and left handed circular interactions are identical and the **S** matrix is diagonal when the sample is not magnetically active . How this affects the FM-MRS signal will be discussed later.

Equation 3.11 is substituted into equation 2.7 , yielding a result similar in appearance to, yet more complex than, the earlier result for FMS,

$$V_{FM-MRS} = \frac{P^2}{4} R Q_{det} \frac{E_c^2}{2} \sum_{a=0}^{\infty} V^{I}_{FM-MRS}(a)\, cos\phi_{RF} - V^{Q}_{FM-MRS}(a)\, sin\phi_{RF} \qquad 3.12$$

with

$$V^{I/Q}_{FM-MRS}(a)/J_a J_{a+1} = \begin{Bmatrix} +\left[e^{-\delta^{+}_{a}-\delta^{+}_{a}\cdot 1} c / s(\phi^{+}_{a+1} - \phi^{+}_{a}) \right. & \left. -e^{-\delta^{+}_{-a}-\delta^{+}_{-a}\cdot 1} c / s(-\phi^{+}_{-a-1} + \phi^{+}_{-a})\right] \\ +\left[e^{-\delta^{+}_{a}-\delta^{-}_{a}\cdot 1} c / s(\phi^{-}_{a+1} - \phi^{+}_{a} - 2\Delta\theta) \right. & \left. -e^{-\delta^{+}_{-a}-\delta^{-}_{-a}\cdot 1} c / s(-\phi^{-}_{-a-1} + \phi^{+}_{-a} + 2\Delta\theta)\right] \\ +\left[e^{-\delta^{-}_{a}-\delta^{+}_{a}\cdot 1} c / s(\phi^{+}_{a+1} - \phi^{-}_{a} + 2\Delta\theta) \right. & \left. -e^{-\delta^{-}_{-a}-\delta^{+}_{-a}\cdot 1} c / s(-\phi^{+}_{-a-1} + \phi^{-}_{-a} - 2\Delta\theta)\right] \\ +\left[e^{-\delta^{-}_{a}-\delta^{-}_{a}\cdot 1} c / s(\phi^{-}_{a+1} - \phi^{-}_{a}) \right. & \left. -e^{-\delta^{-}_{-a}-\delta^{-}_{-a}\cdot 1} c / s(-\phi^{-}_{-a-1} + \phi^{-}_{-a})\right] \end{Bmatrix} \qquad 3.13$$

where the symbol c / s is shorthand for either the function *cos* (used for the in-phase component) and the function ***sin*** (used for the quadrature component). The complete general result then contains the infinite sum over a of two sets of terms, as it did for FMS, but now, each set consists of *eight* terms proportional to either a ***sin*** or *cos* function. Although this result is useful for computer simulation of the FM-MRS line shapes[7], done similarly to the previous

[7]In this case, the right and left handed circular components of the absorption and dispersion are obtained from the linear molecular components and the magnetic field using the model for the

description for FMS, it is difficult to understand intuitively the new method when its line shape function is cast in this cumbersome form. The next section will examine the result in certain revealing limits, clarifying how to exploit the unique features of FM-MRS.

3.3 *Understanding the general formulation of FM-MRS*

Equation 3.13, given in the previous section, completely describes the FM-MRS line shape. It is difficult to understand as it stands because of the complex interplay of the sixteen individual terms that occur for each element in the sum that is considered. In the introduction to this chapter, the unique features of FM-MRS were highlighted: shot-noise limited sensitivity *via* substantial optical suppression of the residual non-shot noise FMS background (see chapter 2) and selectivity to samples that are magnetically active *vs* insensitivity to samples that are not. In addition to these unique features, FM-MRS also possesses the internal noise canceling scheme of ordinary FMS and the spectroscopic labeling and "low-J enhancement" ability of MRS (McCarthy 1994; appendix A). In the following sections, most of the unique features of FM-MRS are distilled from the complicated general result. For further details the reader is referred to chapter 2 and appendix A.

MR effect developed in Appendix A.

3.3.1 The suppressed FM-limit of FM-MRS

FM-MRS is potentially a double null technique. One null is provided by FMS's zero background and the other by the polarizers when then are properly aligned. Conversely, generation of an FM-MRS signal *can* require both a differential absorption or dispersion (an FMS signal) *and* magnetic optical activity (an MRS signal). Hence, when a sample is not paramagnetic, regardless of whether it actually possesses a differential absorption or dispersion, no FM-MRS signal *should* be generated.

When the sample is not magnetically active, $S_n^+ = S_n^- = S_n$ (for all n). In this case the product $T_a T_b^*$ reduces so that $T_a T_b^* = \frac{P^2}{2} S_a S_b^* cos^2 \Delta\theta$, and the FM-MRS signal, V'_{FM-MRS}, becomes ,

$$V'_{FM-MRS} = P^2 cos^2 \Delta\theta \, V_{FM} . \qquad 3.14$$

Obviously, the FM-MRS signal, in this limit, is simply the usual FM signal attenuated by $P^2 cos^2 \Delta\theta$-- hence, this section's tittle "the suppressed FM-limit". If our interest lies in the study of a paramagnetic species, the residual FM signal is an "undesirable background". This FM background can be advantageously[8] removed by reducing $cos^2 \Delta\theta$, a unique feature FM-MRS provides. Aligning the

[8]Reducing P^2 reduces the FM background by disadvantageously reducing the intensity of laser light probing the sample.

polarizers so that they are perfectly crossed sets $cos^2 \Delta\theta$ to zero, so that no light (in excess of the shot-noise) impinges on the detector. Hence, equation 3.14 describes only ideal polarizers that provide perfect infinite extinction. In theory all unwanted FMS signals can be removed in this manner. This is the origin of the additional null of FM-MRS . But, unfortunately real polarizers do not provide perfect extinction,thus some light in excess of the shot noise reaches the detector *even when* $cos^2 \Delta\theta = 0$. The consequence of this defect will be discussed later.

Interestingly, performing FM-MRS in this suppressed FMS-limit can be useful in the recording of sought-for FMS-signals. When the entrance and analyzer polarizers are aligned ($\Delta\theta = 0$) and the sample is not paramagnetic, the FM-MRS signal is independent of magnetic field and is precisely the FMS signal modulated by P^2. The term "modulated" is used to suggest that the polarization of the laser beam (perhaps *via* modulation of the DC voltage to the EOM) could be used to create the low-frequency modulation needed to narrow the bandwidth during usual "FM" detection. Additionally, even for magnetically active samples, this modulation may be useful, although other superior methods (described below) exist.

3.3.2 *Weak absorbers*

In the limit that all differences in the molecular parameters are small, the general result, equation 3.13, simplifies significantly *via* the small angle approximation. Retaining only the largest contribution from each molecular parameter, one obtains for use in equation 3.12,

$$V^{I}_{FM-MRS} \approx 2J_aJ_{a+1}\{2cos^2\,\Delta\theta[V'^{\delta}_{FM}(+) + V'^{\delta}_{FM}(-)] + sin2\Delta\theta[V'^{\phi}_{FM}(+) - V'^{\phi}_{FM}(-)]\} \quad 3.15$$

and

$$V^{Q}_{FM-MRS} \approx 2J_aJ_{a+1}\{2cos^2\,\Delta\theta[V''^{\phi}_{FM}(+) + V''^{\phi}_{FM}(-)] + sin2\Delta\theta[V''^{\delta}_{FM}(+) - V''^{\delta}_{FM}(-)]\} \quad 3.16$$

with the "FM-like" signals for each circular component defined,

$$V'^{x}_{FM}(+/-) = x^{+/-}_{-a-1} - x^{+/-}_{a+1} + x^{+/-}_{-a} - x^{+/-}_{a}$$
$$V''^{x}_{FM}(+/-) = x^{+/-}_{a+1} + x^{+/-}_{-a-1} - x^{+/-}_{-a} - x^{+/-}_{a}. \quad 3.17$$

For $a = 0$, $V'^{x}_{FM}(+/-)$ is the first difference of x and, $V''^{x}_{FM}(+/-)$ is the second difference. When the modulation frequency is small compared to the line-width, these differences become (approximately) proportional to derivatives of x with respect to the the optical frequency ω_c. If the Zeeman effect energy splitting is small compared to the line width, as it is for most molecules suitable for study by FM-MRS (McCarthy 1994), the right and left handed circular effects

are nearly identical, so that differences of these quantities in equations 3. 15 and 3. 16 also become approximately proportional to a derivative, while terms involving sums must be individually evaluated.

In the limit of small molecular parameters, small modulation depth (NB-FM approximation where terms with $a > 0$ do not contribute), and small modulation frequency, it is useful to classify FM-MRS line shapes by the "derivative nature" of the signal. Additionally, FM-MRS line shapes may differ for magnetically active or inactive samples, and the differences may be exploited. For magnetically inactive samples, terms above involving the difference of the right and left handed parameters cannot contribute to the FM-MRS signal.

For example, when the polarizers are aligned with $\Delta\theta = 0$, the in-phase term, equation 3.15, becomes proportional to the sum of the FM signal for the right and left handed absorptions. If the molecule (or optical transition) is MRS *inactive*, the line shape appears as the usual FMS line shape-- the first derivative of a Gaussian, because the right and left handed absorptions are identical and sum. Hence, as expected, "non-suppressed" background FMS is recorded. But if the molecule is MRS *active*, the Zeeman splitting causes circular birefringence, creating a difference in the right and left handed absorptions, so that the right and left handed absorptions are no longer identical. In this case, the line shape often

resembles a third-derivative like profile. This is shown pictorially in figure 3.2. Since this line shape arises from the sum of the circularly polarized interactions, the relative sign of the Zeeman splitting cannot be recovered from it, and it contains no additional diagnostically important information. Such additional information, that is always available in MRS experiments (see appendix A), is found only when the FM-MRS signal depends on the difference of the right and left handed interactions.

For nearly crossed polarizer alignment[9], $\Delta\theta \approx \frac{\pi}{2}+\kappa$ and $|\kappa| << 1$, so that $2cos^2\Delta\theta \approx -4\kappa^2$ and $sin2\Delta\theta \approx -2\kappa$. In this case, the terms in the total FM-MRS signal (equations 3.15 and 3.16) involving the sum of the circular interactions are diminished relative to terms involving the differences of the circular interactions by a factor of the uncrossing angle, κ. Hence, to study selectively paramagnetic species in the the presence of non-paramagnetic species and background levels, the crossed polarizer alignment should be employed.

When FM-MRS is performed using nearly crossed polarizers, and both the modulation frequency and Zeeman splitting is small compared to the line width, the dominant contribution to the in-phase term approximates a second derivative of a dispersion profile (similar to a third derivative of a Gaussian absorption) while the quadrature component approximates the third derivative of a Gaussian

[9]The relative "sense" or sign of the uncrossing angle is important as is the direction of the magnetic field vector, parallel or anti-parallel to the laser propagation axis. See note below.

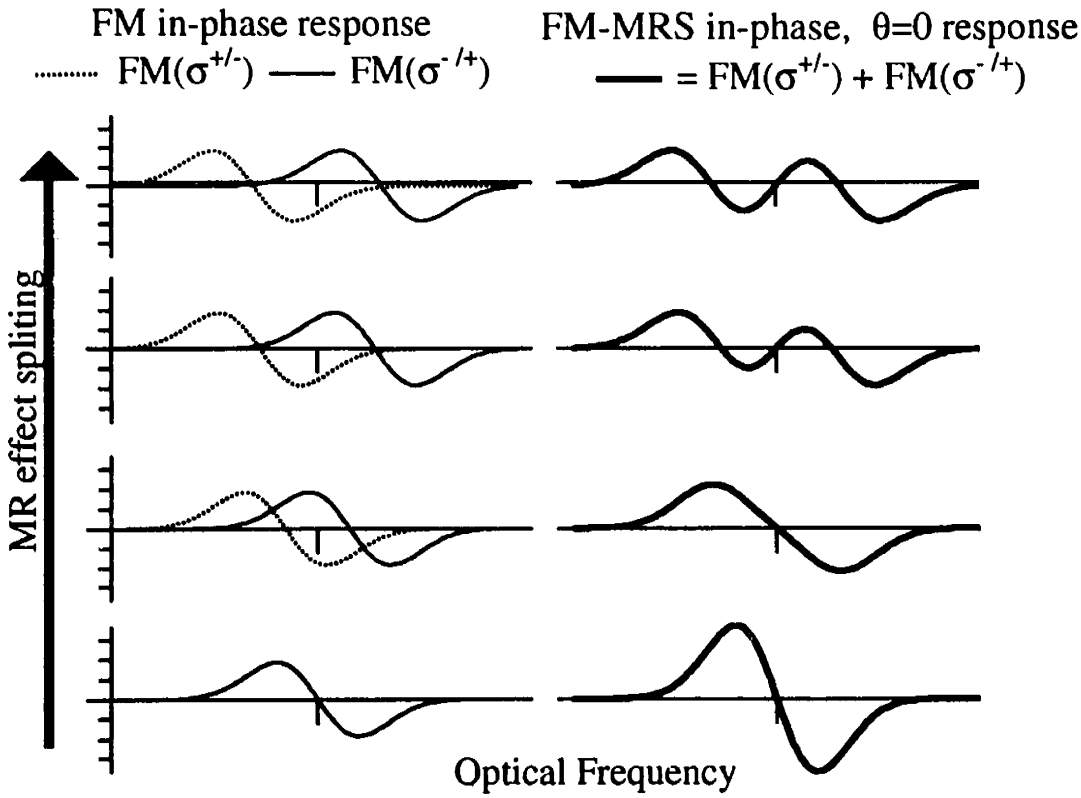

Figure 3.2: Generation of FM-MRS in-phase signals for aligned ($\Delta\theta = 0$) polarizers. The MR energy splitting of the right and left-handed circular interactions increases from bottom to top. The left panels show FMS in-phase signals that would have been recorded using either right or left-handed circularly polarized light. The right panels show the FM-MRS signal, the sum of the FMS signals. The overall sign (phase) of the signals is determined by the magnetic field vector relative and the laser beam propagation axis. The horizontal tick marks indicate zero-field line center

absorption profile. This is shown pictorially in figures 3.3a and 3.3b. For other, intermediate values of the RF detection phase ϕ_{RF}, the detected FM-MRS signal is complicated by the possible interference of contributions from the quadrature and in-phase terms. Furthermore, changing the sense of the uncrossing angle, $\kappa \rightarrow -\kappa$,[10] reverses the sign of the desired MRS-active signals, but leaves the background FMS (or MRS-inactive) terms unaffected.

3 .4 *Signal magnitude, detection sensitivity, and equipment demands*

This section discusses the signal magnitude and the detection sensitivity of FM-MRS, along with the equipment demanded by these issues, when FM-MRS is used to *detect selectively paramagnetic species in the presence of possibly unwanted FM background signals or noise*. In this case, the polarizers are aligned to be crossed or nearly crossed, $\Delta\theta \approx \frac{\pi}{2}+\kappa$ and $\kappa << 1$. The primary concern is the intensity of light reaching the detector under real laboratory conditions.

3 .4 .1 *FM-MRS background intensity, signal ,and implications*

In FM-MRS, some light always reaches the optical detector even through crossed polarizers. The total intensity of the laser light on the detector is the sum

[10]The "sense" is determined by the vector product of the polarizer axis and magnetic field axis.

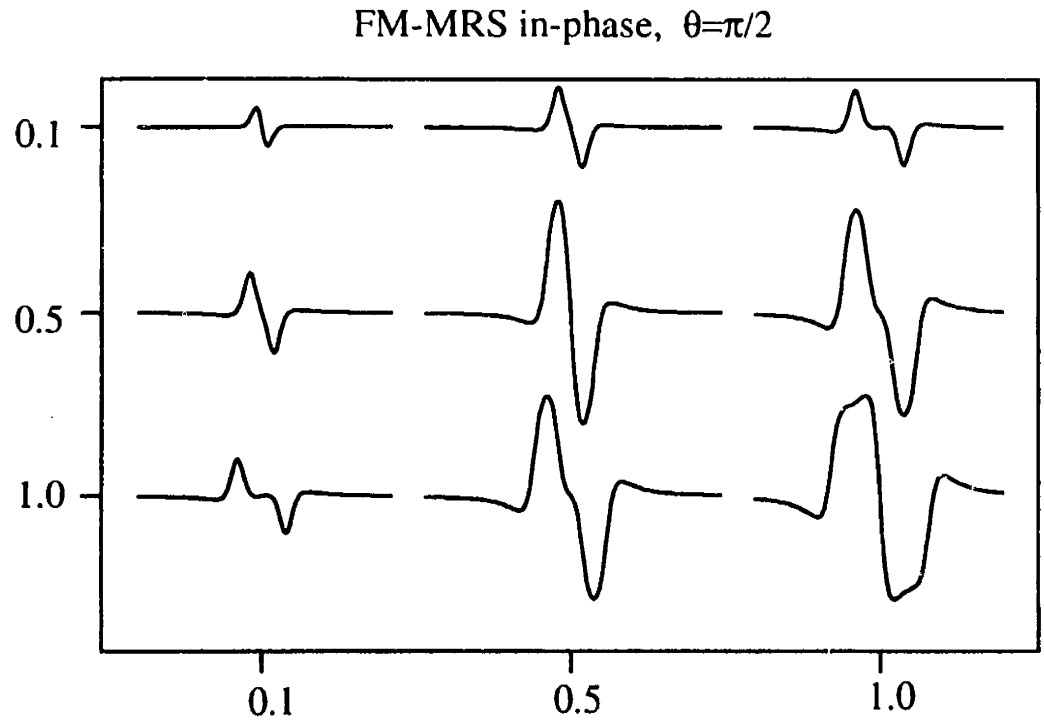

Figure 3.3a: Profiles of FM-MRS in-phase lineshapes for (nearly) crossed polarizers ($\Delta\theta = \frac{\pi}{2}$) assuming that the modulation index is small. The original weak absorption feature was a Gaussian with a full width at half maximum of Γ. The nine subplots have identical horizontal (laser frequency) and vertical (intensity) scales, but the relative MR effect energy splitting $\frac{\Delta E_{Zeeman}}{\Gamma}$ and the relative modulation frequency $\frac{2\omega_{RF}}{\Gamma}$, vary. For quadrature lineshapes see figure 3.3b.

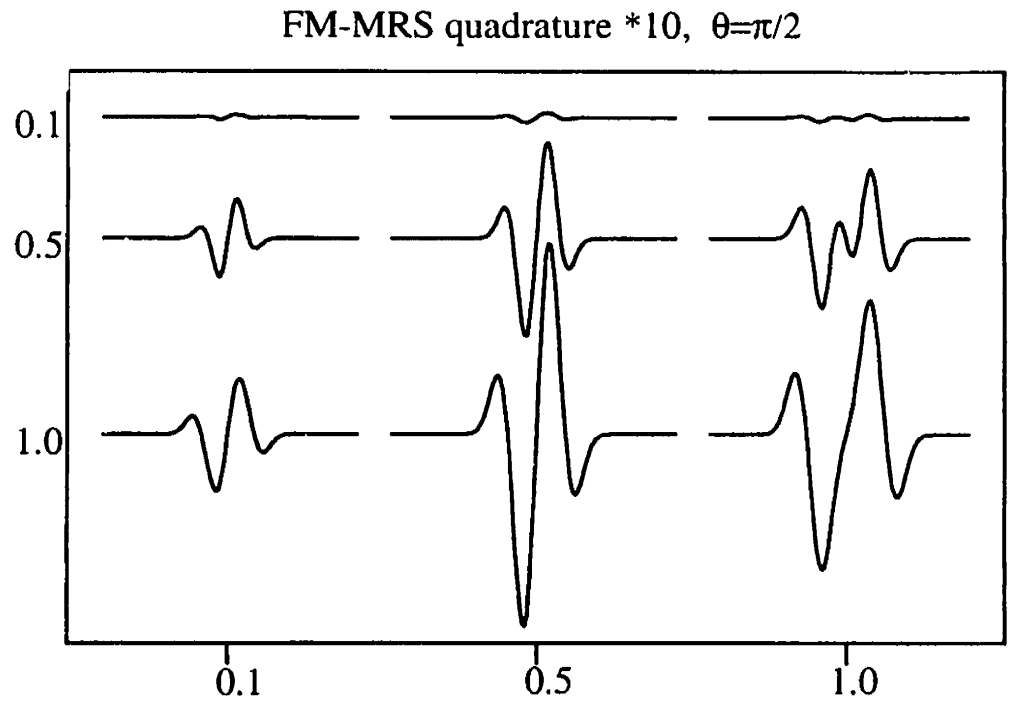

Figure 3.3b: Profiles of FM-MRS quadrature lineshapes for (nearly) crossed polarizers ($\Delta\theta = \frac{\pi}{2}$) assuming that the modulation index is small. For comparison purposes, the nine subplots in this figure have a vertical scale that is ten times smaller than in figure 3.3a, because the quadrature signal is smaller. The original weak absorption feature was a Gaussian with a full width at half maximum of Γ. The nine subplots have identical horizontal (laser frequency) and vertical (intensity) scales, but the relative MR effect energy splitting $\frac{\Delta E_{Zeeman}}{\Gamma}$ and the relative modulation frequency $\frac{2\omega_{RF}}{\Gamma}$, vary.

of the background intensity (that reaches the detector whether or not the laser's frequency is tuned to a molecular transition) and the additional FM-MRS (or MRS) intensity that develops only when the laser is tuned to resonance. Although FM-MRS is an absorption based technique, whenever an FM-MRS signal develops under crossed polarizer conditions, the intensity on the detector increases.

The intensity of the background light depends upon the laser intensity probing the sample, the uncrossing angle κ, and the quality of the polarizers. The contribution to the total background light from ideal polarizers is $4\kappa^2 P^2 I_c$, where I_c is the intensity of the original laser. The contribution due to non-ideal polarizers *and* residual birefringence (and dichroism) is $\zeta P^2 I_c$, where ζ^{-1} is the effective realized extinction of the polarizers. At best, extinction on the order of $10^5 - 10^6$ is possible by matching the polarizer and analyser and by painstakingly minimizing all residual effects[11]. More typically ζ^{-1} approaches only 10^4. Although the background intensity is not an FM-MRS signal, it does have associated shot-noise, and that must be accounted for later when considering the signal to noise ratio.

The background signal (from the detected background optical intensity) under all conditions was given by equation 3.14. Hence, for nearly crossed polarizers,

[11]These figures are obtained from personal experience and supported by others, including M. C. McCarthy, A. Cooksey, and K. Lambrecht, Inc.

it is proportional to $4\kappa^2 P^2 V_{FM}$, assuming that V_{FM} is now the total background FMS signal that would have been measured without the analyzer polarizer and that $4\kappa^2 > \zeta$. The ratio of the FM-MRS signal to this background signal is roughly $2\kappa^{-1}$.

This background signal also creates an undesirable detected noise, even if the signal is infinitely stable, that is proportional to the noise of the original laser. In FMS, the analogous noise was larger than the shot-noise, and it limited the detection sensitivity. In FM-MRS, however, this noise is diminished by $4\kappa^2 P^2$; hence, by adjusting κ (since $|\kappa| << 1$), the effect of this noise can, in principle, be made smaller than the shot-noise. But, since the FM-MRS signal scales linearly with κ, κ should be maintained as large as possible. One expects then, that the total background intensity will be dominated by the contribution from a non-zero uncrossing angle, $4\kappa^2 P^2 I_c$ rather than from the non-ideal nature of the polarizers.

In chapter 2, the residual detected FM noise level was determined to be, for a poor implementation of FMS, a factor of roughly *500* times the shot noise. This noise level is easily suppressed by an uncrossing angle of (somewhat less than) 3^o degrees, a practical value. If much smaller uncrossing angles are needed to suppress more severe levels of FMS background, the extinction of the polarizers becomes a concern.

Even with these moderate uncrossing angles, the total background intensity, $(4\kappa^2 + \zeta)P^2 I_c$, is considerably smaller than the original laser intensity. Hence, measuring it (the background) with a shot-noise limited optical receiver requires specialized equipment. Selection of the equipment needed for FMS was discussed in chapter 2. For FM-MRS, the laser intensity after the analyzer is often less than a milliwatt; hence the use of an avalanche photodiode and very low noise amplifier is necessary.

3.4.2 *Signal*

The magnitude of the FM-MRS signal depends upon the uncrossing angle κ. The FM-MRS signal contains two different sample dependent contributions; the "pure" FM-MRS signal generated by the MR effect and an associated sideband imbalance, and a distorting term from the MR effect converting background FM occurring before and within the sample cell[12] into an FM-MRS signal. Thus, regardless of origin, the FM-MRS signal only occurs when the sample is paramagnetic and when the laser frequency is tuned into resonance with a molecular transition. Hence, the distorting term does not occur off-resonance.

Two factors conspire so that the "pure" signal from a paramagnetic molecule

[12]Background FM generated after the sample cell and analyzer will be considered later.

measured by FM-MRS is always smaller than the signal measured by ordinary FMS. First, the use of crossed polarizers causes a reduction by a factor of $2\kappa P^2$. Secondly, the FM-MRS signal under these conditions is proportional to the difference of the right and left handed interactions. The largest possible difference in the absorption circular interaction parameters can only be half the total interaction[13], since each zero-field absorption feature is actually the sum of one right and one left circularly polarized features of equal intensity[14]. Hence absorption features measured by FM-MRS (in absence of background FM) are smaller by at least another factor of two compared to FMS, due to the MRS differential detection. The exact reduction of signal due to the MR effect is difficult to model, since it depends critically upon the species under study (see appendix A). Generally, at the lowest angular momentum levels, the loss is at its minimum value. This signal reduction is the price paid for the selectivity to paramagnetic species.

The "pure" FM-MRS signal is generated when the sample is magnetically active and when it, *the sample*[15], creates a sideband imbalance. As mentioned already, there is another route to the generation of an FM-MRS signal that should

[13] The largest difference for the bipolar dispersion components are more complicated.

[14]Recall that a linearly polarized laser composed equally of the two circular components does not under go polarization rotation under zero-field.

[15]Actually, the requirement is that the same resonance feature is responsible for both the difference in circular interactions and the sideband imbalance.

be considered. Consider, for example, the case when the laser beam probing the sample already has a substantial sideband misbalence, due perhaps to an accidental etalon. When the sample is paramagnetic, regardless of whether the sample causes a sideband imbalance, an FM-MRS signal is generated. Hence, the generation of an MRS signal alone converts *some* of the residual FM background into an FM-MRS signal. As for the desired FM-MRS signal, this contribution is a signed quantity. This contribution may interfere with the "pure" FM-MRS signal, distorting the recorded FM-MRS line shape from the predicted one (an odd-derivative) to something else unknown, because the FM-background does not have an obvious, predictable relationship to the sample. If the background FMS were known, modeling this on resonance "MRS" distorting contribution could be accomplished by adjusting the amplitude (and phase) of a particular sideband before the cell. A somewhat simpler model, developed in the next section, approximates the absorptive response.

When the FM-background is large, the FM-MRS signal can contain a large distorting contribution. In the limit of very large FM background, the FM-MRS technique becomes equivalent to the MRS technique-- since only an MR effect (and not a *sample* induced sideband imbalance) is needed to produce a sizeable signal. This limit is undesirable. Large FM backgrounds cannot be suppressed by the crossed polarizers and will therefore lead to off-resonance noise, precisely

the problem the use of FM to enhance MRS had intended to solve.

Whenever an FM-MRS signal occurs, the light intensity on the detector is increased, due to the polarization rotation of the MR effect. Hence, shot-noise from the additional light intensity at the detector from the MR effect (even when no FM effect or absorption occurs) must be considered on resonance. The decrease in light-intensity reaching the detector (and its associated shot-noise) due to the absorption is small but easily accounted for (see below).

3.4.3 *Detection sensitivity of FM-MRS*

Using the results of the signal to noise analysis of FMS in chapter 2 and the discussion above, the minimum detectable FM-MRS signal is readily obtained. For comparison purposes, only the absorptive, nearly crossed polarizer response is considered. Additionally, it is assumed that the most favorable MR effect would reduce the FM-MRS signal relative to FMS by a factor of two in addition to the reduction by the polarizers, and that the actual reduction here is $\Re \leq 0.5$. $\Re$ describes the MR effect polarization rotation, while all absorptive (FM) effects are described by other parameters (δ and Δ). Only shot-noise limited optical receivers are considered, so that the remaining significant noise sources are the detected shot-noise of the optical intensity and the cross polarizer-reduced leaked-

FM noise. Assuming $P^2 = 1$, and that the modulation frequency is much larger than the line width, the signal to noise ratio, in electrical power units becomes,

$$\left(\frac{S}{N}\right)_P = \frac{\left[2\Re\kappa(\delta \pm\Delta)M\right]^2}{\frac{8e\,G^x_{det}\,\Delta f}{\left[4\kappa^2+\zeta+2\kappa\Re(1-\delta-\Delta)\right]\rho P_c}+\left[2\Re\kappa(\delta\pm\Delta)N_L\right]^2+\left[(4\kappa^2+\zeta)M\Delta N_L\right]^2} \quad 3.18$$

where δ is the effective absorption parameter, N_L is the laser noise, Δ describes the residual FM background (now including MR on-resonance non-differential absorption), and P_c is optical intensity after the modulator. A more detailed discussion of these variables is given in chapter 2.

The numerator in equation 3.18 is the FM-MRS signal divided by the optical power. The signed contribution $\pm\Delta$ is a distorting term from background FM absorption that occurs only on an MR resonance, $\Re > 0$. The denominator consists of three terms, each with a factor of the optical power removed. The first term is the shot-noise due to the total light on the detector, containing contributions from a non-zero crossing angle, non-ideal polarizers, and FM-MRS signal terms[16]. The second term is the noise contribution from the FM-MRS signal ($\delta > 0$ and $\Re > 0$), and the third term is the noise contribution from a background FMS signal, leaking through the nearly crossed polarizers. If both Δ and M are set to unity, equation 3.18 describes the MRS signal to noise ratio, including on resonance conditions. Hence, the addition of FM detection reduces

[16]The MR part of the FM-MRS signal increases the intensity on resonance. This intensity is decreased by absorption, desired or otherwise.

the amount of detected laser noise, and enhances the MRS technique.

When the FM-MRS signal is large, the noise contribution from an FM-MRS signal dominates all other noise sources, so that $\left(\frac{S}{N}\right)_P$ becomes independent of signal and proportional to the laser noise, and the small distorting contribution to the signal itself from $\pm\Delta$ can be neglected. This behavior is expected, having also occurred for FMS.

For good enough polarizers[17], κ can be made small enough so that the shot noise will dominate. In this shot-noise dominated case, we have,

$$\left(\frac{S}{N}\right)_P^{SNL} = \frac{\left[4\kappa^2 + \zeta + 2\kappa\Re(1-\delta-\Delta)\right]\rho P_c(\kappa\delta M)^2}{8e\,G_{det}^x\,\Delta f}. \qquad 3.19$$

The ratio of shot-noise to other noise sources varies proportionately with κ^{-6} in electrical power units and κ^{-3} in optical power units (when the small shot noise contributions from the FM-MRS signal and non-ideal polarizers have been ignored). This remarkable result underscores the importance of considering both the quality and alignment of the polarizers to obtain the optimal $\left(\frac{S}{N}\right)_P$.

Since it is the uncrossing angle that primarily determines the intensity of light on the detector and the optical shot-noise, it is no wonder that in equation 3.19,

[17]The idea is that the extinction of the polarizers is good enough that the light intensity reaching the detector is dominated by the contribution from the magnitude of the uncrossing angle, at the small uncrossing angle needed. Shot-noise limited behavior is always possible when $\zeta^3 < \frac{8e\,G_{det}^x\,\Delta f}{(M\Delta N_L)^2\rho P_c}$.

$\left(\frac{S}{N}\right)_P^{SNL}$ depends upon the uncrossing angle κ. McCarthy 1994 unfortunately neglects the effect of κ and states that "Equation (11) [of their work, the signal to noise ratio[18],] implies that: in the shot-noise limit, the detection sensitivity of FM-MRS is independent of the uncrossing angle" . This also leads to the erroneous claim that the FM-MRS detection sensitivity "is the same as that of quantum-limited FM spectroscopy". Even if the FM-MRS signal reduction factors are ignored, it is clear that the FM-MRS signal, FM signal, and associated shot-noise levels have different functional dependencies on the uncrossing angle.

When the FM-MRS signal is small, (and the MR effect is small with $\Re < \kappa$,) the minimum detectable absorption due to magnetically active transition δ_{Min}^{FM-MRS}, can be easily calculated. Setting the minimum acceptable $\left(\frac{S}{N}\right)_P$ at unity and neglecting the effect of MR converted background-FM , δ_{Min}^{FM-MRS} is,

$$\delta_{Min}^{FM-MRS} = \frac{\delta_{Min}^{FM}}{\Re} = \left(\sqrt{\frac{\frac{8e\,G_{det}^{x}\,\Delta f}{(4\kappa^2+\zeta)\rho P_c} + \left[(4\kappa^2+\zeta)M\Delta N_L\right]^2}{(1-N_L^2)(\Re\kappa M)^2}} \right). \qquad 3.20$$

Hence, the minimum detectable absorption of "pure" FM-MRS is always somewhat larger than for FMS because of the MR effect. If the distorting

[18]In McCarthy 1994, typographical errors (I assume) have confused the symbols for the minimum detectable signal and the signal to noise ratio.

contribution from the FM-background is considered (by adding it into equation 3.20), FM-MRS may provide improved sensitivity over FMS, at least in the case of well-isolated resonances[19]. When laser noise dominates, and κ decreases, the sensitivity of FM-MRS improves until the shot-noise dominates. Yet, as expected, if is κ decreased further, sensitivity *decreases*. Hence there is an optimum uncrossing angle κ that depends upon the implementation of FM-MRS (the polarizers, the EOM, etc.). At this optimum uncrossing angle, the (shot-noise limited) sensitivity of FM-MRS (still assuming the MR effect reduction by a factor of two) is reduced by a factor of $\sqrt{4 + \frac{\zeta}{\kappa^2}}$ compared to FMS (see equation 2.54).

Only at very small optimum uncrossing angles then, which are employed to suppress only severe FM backgrounds, is the effective relative polarizer signal reduction significantly different than the MR effect reduction alone. Nonetheless, the overall signal to noise ratio remains a very sensitive function of the uncrossing angle. In the laboratory, finding the optimal κ proves difficult in practice[20] due to mechanical and thermal instabilities of the optical components (including unstable residual birefringence, etc.). In the next section of this

[19]If the resonances are not well isolated, the presence of the distortive term makes identifying the occurrence of a signal difficult based on the signal to noise alone.

[20]In practice, the polarizers are first crossed, the residual birefringence is minimized and quantified, and then the uncrossing angle is set so that the total light intensity passed by the polarizers is roughly a factor of two greater than passed due to the *minimized* residual birefringence. The angle is then optimized by repeated measurements of the optical spectrum.

chapter, I briefly detail some improvements to the FM-MRS method that solve these difficulties. Following that, the FM-MRS studies of NO_2 and CeF (in chapter 4) will be presented.

3.4.4 Some FM-MRS improvements

Although FM-MRS can provide shot-noise limited detection of paramagnetic species, such high sensitivity is often difficult to achieve in practice because it involves the optimization of sensitive experimental parameters. In this section, I briefly describe some methods to improve FM-MRS, including both proven enhancements and future possibilities.

Difficulties involved in setting the optimal value of the analyzer uncrossing angle can be circumvented by simple schemes. For example, the uncrossing angle itself can be modulated, so it no longer has to be optimized. Modulation of the uncrossing angle also provides another benefit, the separation of the FM-MRS signal from any remaining (non shot-noise) noise. If simple periodic modulation is employed, such as $k \rightarrow k_0 cos(\omega_k t)$, the resulting modulated FM-MRS signal can be lock-in detected at ω_k. In this scheme, noise terms (FMS background contributions) are not modulated at ω_k while only the desired FM-MRS signal is. In the laboratory, the addition of an electronically variable polarizer/waveplate

such as a Photoelastic modulator (PEM) could be used to facilitate the modulation. Initial attempts with a PEM have been encouraging.

Another possibility that accomplishes the uncrossing angle modulation is the use of an EOM that has been specially designed for amplitude modulation. In this scheme, the entrance polarizer is removed, and the laser beam is input to the EOM with a polarization axis 45° to the crystal axis, while a low frequency modulation is applied, in addition to the RF drive, to the modulator. This effectively modulates the polarization of the field at the output of the EOM. The special EOM design is required to cancel the EOM's residual birefringence[21]. This scheme has not been tried due to the unavailability of an appropriate EOM.

In addition to modulation of the uncrossing angle, the magnetic field can be modulated. This has been the usual scheme for most applications of MR spectroscopy (Liftin 1980). Using magnetic field modulation still requires good polarizer alignment but, as in the case described above, the FMS background terms, which are independent of the magnetic field, are not modulated, while the MRS terms which are dependent upon the field, are. In practice, magnetic field modulation at frequencies $>> 60\ Hz$ requires a current source designed for the *specific* modulation frequency and impedance of the magnet[22]. Furthermore,

[21] An EOM designed for amplitude modulation consists of two equal length crystals, not one. The individual crystals are obtained by cutting one crystal in two. In the EOM, the crystals are mounted with their axes rotated 90° to each other, thereby cancelling any birefringence and dichroism.

stray modulated fields interfere with detection electronics, such as computers, so that careful attention to shielding is required. Field modulation has not been attempted for FM-MRS in order to retain the tunability of the field needed for optimizing the MRS effect (see appendix A).

Another scheme, "*45°*-FM-MRS" (Bloch 1993) not only surmounts the difficulties in obtaining optimal polarizer alignment, but also increases the FM-MRS signal. Based upon the "differential detection scheme" of Adams 1984, proposed to improve *multipass* MRS experiments, FM-MRS could be improved by spatially separating the laser beam after the sample into two linearly polarized components. The components are obtained from the ordinary and extraordinary outputs of a beam splitting polarizer aligned at *45°* to the axis of the entrance polarizer. The FM-MRS signals from each separate component ($k = +\frac{\pi}{4}$ and $k = -\frac{\pi}{4}$) are then subtracted yielding a composite "*45°*-FM-MRS signal". With $|k| = \frac{\pi}{4}$, the FM-MRS signal is at its largest value, but the noise (and FM-background) has also increased. The electronic subtraction cancels the noise, since it is independent of the sign of k, while accumulating the signal. Overall improvement is contingent upon the ability of the two signals to be balanced (*via* the quality of the beamsplitter, etc.) and then subtracted[23]. Initial efforts have

[22]Personal communication, C. Chackerian, Jr., NASA Ames. See also Blake 1996.

[23]In manner similar to that used for the "quantum-limited" FMS technique of Gerhtz 1985, a single photodetector can be employed for both beams.

been limited by the unavailability of suitable detection electronics capable of highly accurate subtractions to remove backgrounds that greatly $(10^3 - 10^6 : 1)$ exceed tiny signals. Nonetheless, 45^o-FM-MRS promises dramatic improvements if the largest contribution of light intensity on the detector in standard FM-MRS is from poor extinction or residual birefringence ($\zeta P^2 I_c$), rather than leaking FM background ($4\kappa^2 P^2 I_c$). Studies of paramagnetic species performed in multipass cells, in which the quality of polarization is degraded and the obtainable extinction limited (Adams 1984), would benefit greatly from the 45^o-FM-MRS scheme.

3.5 *Trace Detection of NO_2 using FM-MRS*

The high sensitivity FM-MRS is demonstrated here on gaseous NO_2 . Detection of trace levels of NO_2 is critical in atmospheric pollution monitoring (Silver 1991, Grant 1992) and also in forensic applications (Khan 1992), since NO_2 is an expected decomposition product of nitroamines (Zhao 1988), nitric esters, and other explosive materials. The 5922Å vibrionic band of NO_2 ($\tilde{A}^2B_2 \leftarrow \tilde{X}^2A_1$) has been well characterized (Stevens 1975, Smalley 1975,Tanaka 1975) and serves as the basis for this investigation. While NO_2 is paramagnetic and therefore detectable by FM-MRS, many other common atmospheric

molecules are not paramagnetic and will not interfere in the laboratory or atmospheric implementation of the FM-MRS technique. Furthermore, since the FM-MRS method probes only for paramagnetic species in a well defined localized volume (between crossed polarizers and contained in an axial magnetic field) and not along the entire beam path, the ambient atmospheric NO_2 concentration produces no significant background signal.

3.5.1 *Experimental*

The FM-MRS experimental arrangement used for the study of NO_2 is illustrated in figure 3.4. Figure 3.4 is very similar to figure 3.1, which shows a simplified arrangement. The output of a single-longitudinal mode cw dye laser (Coherent Inc, 699-29), after first passing through a beam splitter and a linear polarizer, passes through an electro-optic phase modulator (EOM, Quantum Technology TWAP-10) driven with $1-3\ W$ of $\omega_{RF} = 260\ MHz$. At these low modulation depth conditions, the EOM imposes essentially only two sidebands at the laser frequency $\pm\ \omega_{RF}$ with equal amplitudes but complementary (electric field) phases so that the intensity of the frequency modulated laser contains no beat note oscillating at ω_{RF}. Each sideband intensity was approximately *20%* of the carrier[24] corresponding to a modulation index of *0.83*. The input polarizer

[24]At these conditions, the relative intensity of each second order sideband is $< 1\%$.

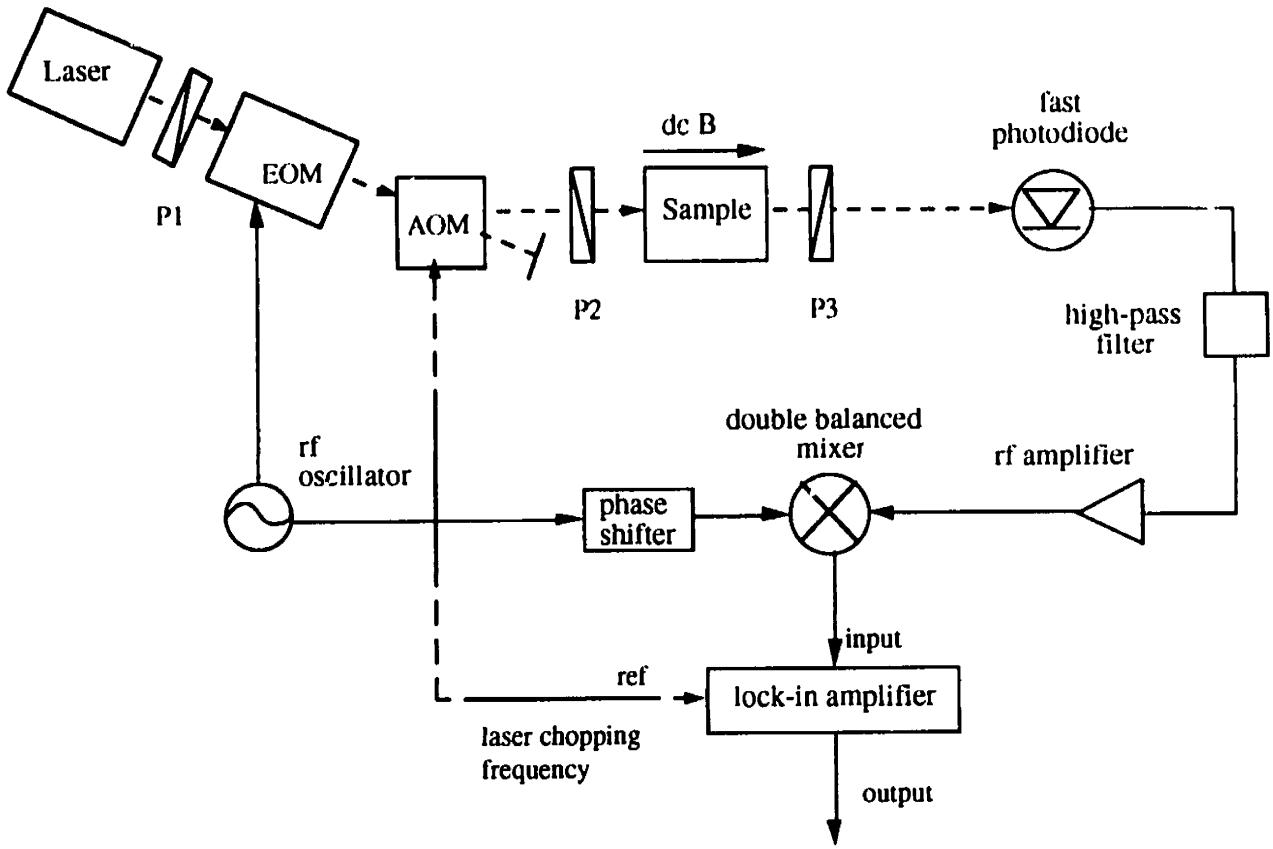

Figure 3.4: Simplified block diagram of the experimental apparatus for FM-MRS trace detection of NO2. P1-P3, polarizers; EOM, electro-optic phase modulator; AOM, acousto-optic amplitude modulator. See text for a description of the experiment

is precisely aligned to the principal axis of the EOM. The output of the EOM passes through a *120 MHz* acousto-optic modulator (AOM), whose drive voltage is *100%* amplitude modulated at *80 KHz*. The AOM (rather than a mechanical chopper at $\approx$ *1KHz*) is used to provide optical isolation of the subsequent beam path from the laser and higher modulation frequencies. The first-order, *100%* amplitude modulated diffracted beam from the AOM passes through another linear polarizer and through a *10 cm* long sample cell located along the axis of an electromagnet (*380 Gauss*) before passing through the analyzer polarizer. The cross sectional area of the laser in the cell is approximately *0.03* cm^2, produced by *1 m* focal length lens (set to a focus after the cell). The analyzer polarizer is first aligned to produce the minimum transmitted light (off resonance). To optimize the signal to noise ratio or *SNR*, the analyzer is then rotated a few degrees (approximately 3^o)(Liftin 1980). The light transmitted by the analyzer impinges on a photo-detector that is carefully shielded from both RF interference and laser scatter. When the laser frequency is tuned to a molecular resonance, absorption and dispersion destroy the amplitude and phase balance (respectively) between the $+\omega_{RF}$ and $-\omega_{RF}$ sidebands and an intensity beat note oscillating at ω_{RF} is produced. If the molecule under study is paramagnetic, the laser beam also undergoes a rotation of its polarization axis and is then partially transmitted

through the polarization analyzer. Depending upon the intensity of the transmitted light on resonance, either a PIN (EG&G FND-100, $> 1\ mW$) or an Avalanche (Hamamatsu S2382, gain=100, $< 1\ mW$) silicon photodiode is used. The signal from the detector, after being amplified and band-pass filtered (centered at ω_{RF}), is phase-sensitively demodulated using a double balanced mixer. A carefully isolated (and appropriately phase-shifted) portion of the original *260 MHz* signal (used also to drive the EOM) serves as the local oscillator input to the mixer. The output of the mixer is low-pass filtered and input into a lock-in amplifier (Ithaco 3990) referenced to the AOM modulation frequency (*80 KHz*). The use of the AOM and lock-in narrows the detection bandwidth to *1Hz* and scales the output ($0 - 10\ V$). The output of the lock-in is then sent to the dye laser's computer and displayed as the laser frequency is scanned. The resulting spectra appear bipolar because of the sensitivity to whether the $+\ \omega_{RF}$ or $-\omega_{RF}$ sideband is preferentially absorbed or phase-shifted. Since the principal modulation and detection is performed at *260 MHz*, a frequency high enough so that the laser's (predominantly $1/f$) amplitude noise is negligible, shot-noise limited detection is feasible.

In addition to the FM-MRS spectra, standard absorption scans were recorded (using the AOM and lock-in only) for calibration purposes on the same

NO_2 samples. Additionally, I_2 fluorescence and the dye laser's internal vernier etalon signals were recorded for wavelength calibration and diagnostics.

Each day, the sample cell was initially filled with 9.5 *Torr* of NO_2 (MKS Baratron 121AA-00001B) and subjected to repeated freeze-thaw cycles that did not noticeably change the pressure. Lower (neat) NO_2 pressures down to *75 mTorr* were obtained by expansion. The number density and hence the concentration relative to *1 atm* was determined at these pressures from the reading on the Baratron. To achieve NO_2 (partial) pressures well below *75 mTorr* and concentrations at the ppb level, the samples were diluted with Ar gas and expanded. At these lowest levels, the equilibrium number density of gas phase NO_2 in the interaction volume could not be accurately determined from the cell pressure; rather, it was calculated from the magnitude of the FM-MRS signal, once the signal's linear dependence on concentration was determined from the higher pressure data.

3.5.2 *Discussion of basic results*

FM-MRS spectra were recorded over five orders of magnitude of NO_2 (partial) pressure. A typical high pressure (*10 Torr* neat NO_2) direct absorption scan and an FM-MRS scan at the same pressure are compared in figure 3.5. Tentative assignments, based on Stevens 1975 and Tanaka 1975, are shown on the

figure. The congestion of the absorption spectrum is so great that it is difficult to accurately determine the absolute baseline transmission from experimental data; hence, we estimate that at *10 Torr* the largest absorption in this region corresponds to $26\% \pm 10\%$. The FM-MRS scan shows regions of obvious signal enhancement . These regions are diagnostic signatures of NO_2 and remain as easily identifiable spectral features at trace levels of NO_2 long after the absorption spectrum features have disappeared into the laser noise.

Figure 3.6 shows a plot of the FM-MRS signal versus pressure of neat NO_2. The relationship between signal and number density was found to be linear as expected at these levels. This relationship was used to determine the concentration at the lower pressures achieved by dilution of the NO_2 in argon more accurately than could be determined by the known dilution and expansion ratios. FM-MRS spectral scans are shown in figure 3.7 covering the range of NO_2 (partial) pressures from *10 Torr* to 2×10^{-5} *Torr*, representing fractional absorbance as small as 6×10^{-7}. At the lowest level, FM-MRS spectra (recorded with a *1Hz* bandwidth) have considerable noise. For an EOM modulation index of *0.83* (and an FM-MRS signal equivalent to approximately *0.1* of the ordinary absorption signal[25]), this sensitivity is found to be within a factor of *3* of the

[25]We allow a reduction factor of 0.1 because neither the modulation frequency nor the magnetic field was optimized.

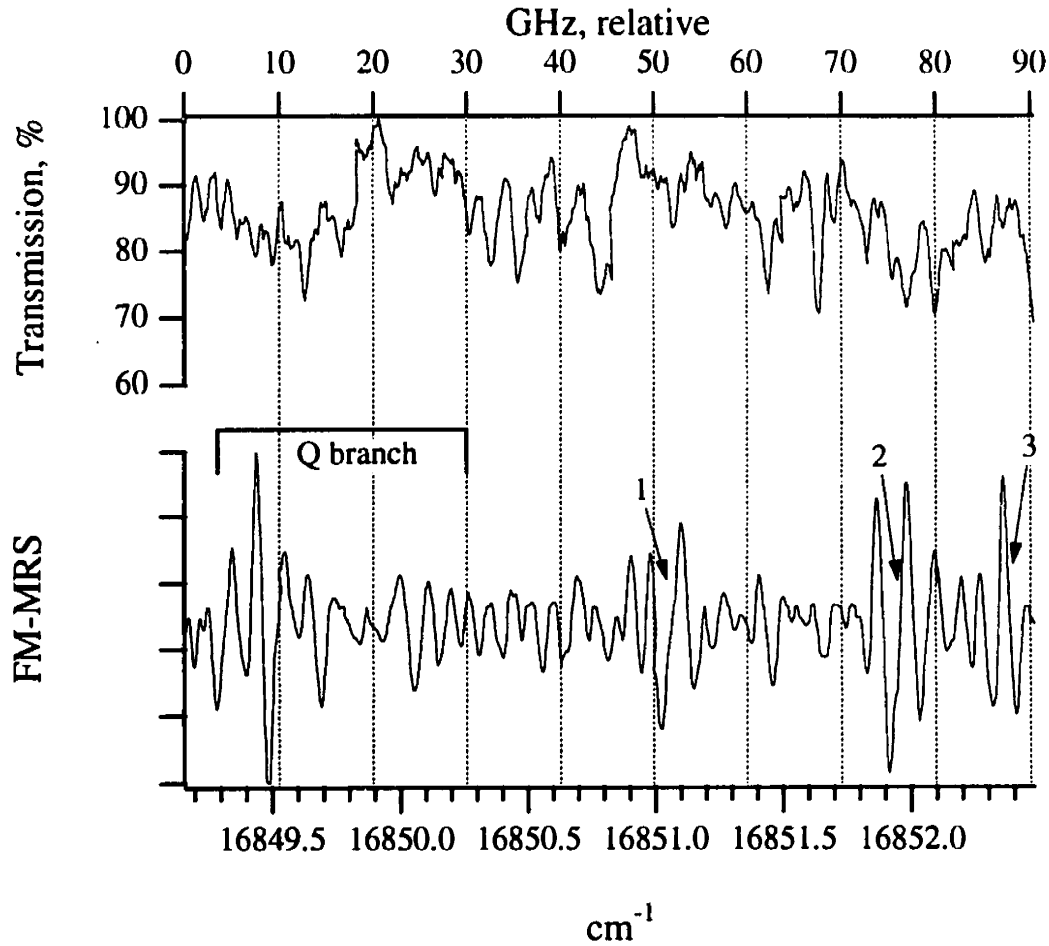

Figure 3.5: Typical direct absorption and FM-MRS spectra recorded under similar conditions (10 Torr). The vertical scale for the absorption scan (Transmission) is only an estimate (±10%) due to the congestion of the spectra. Tentative assignments are shown on the lower, FM-MRS trace. The features labeled 1-3 are assigned as R(1) K_a=2, R(2) K_a=2, and R(2) Ka=0, respectively.

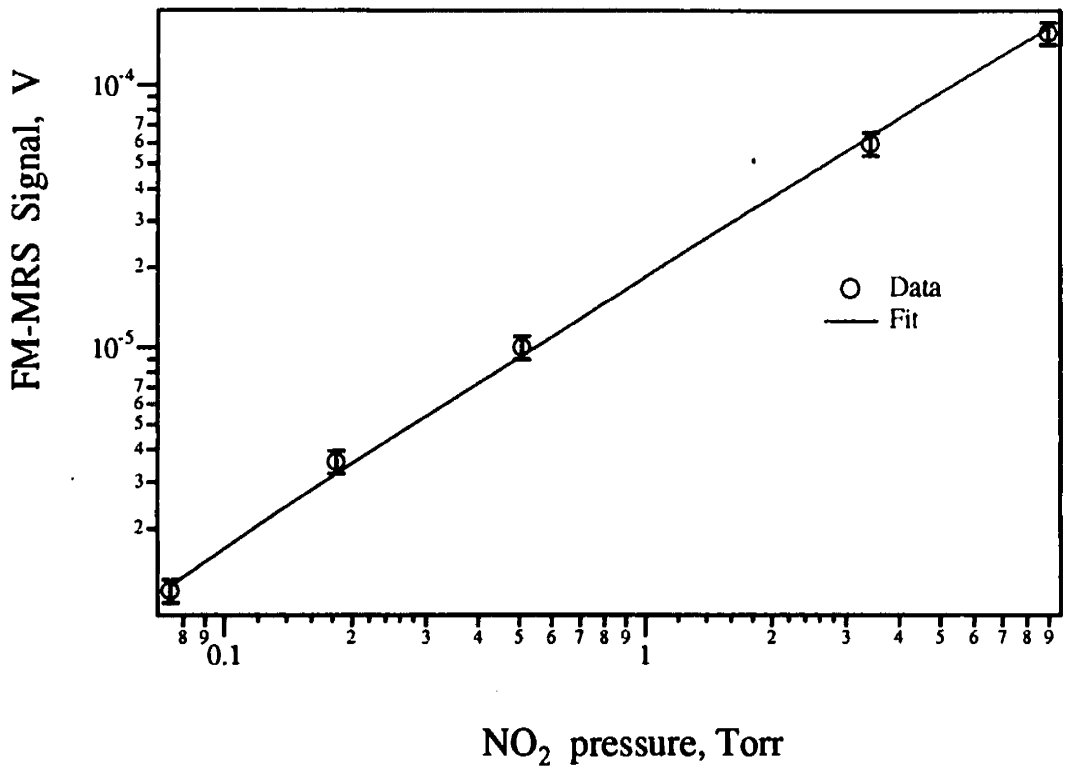

Figure 3.6: FM-MRS signal (peak to peak for strongest Q line in figure 3.5) *vs* NO_2 pressure and fit of data. Error bars are ±10% of signal. Least-squares fit was to a simple line function with weighting equal to the inverse of the datum values.

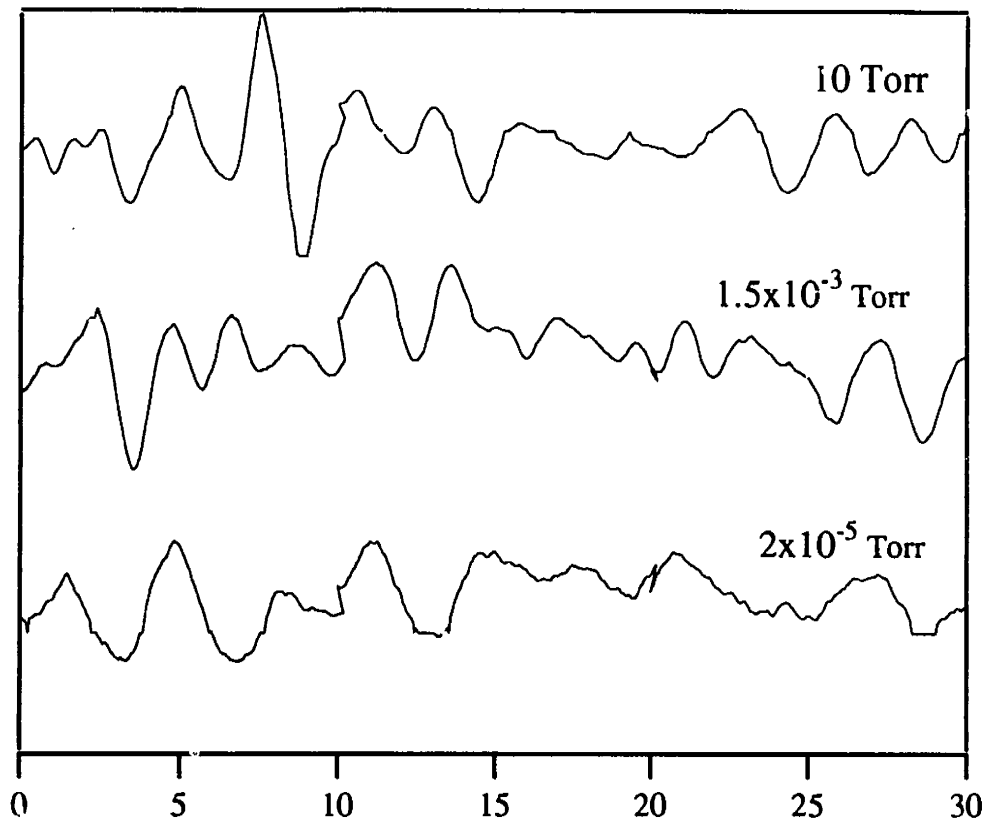

Figure 3.7: FM-MRS spectra as function of NO_2 partial pressure. From top to bottom, the NO_2 pressure was *10 Torr*, 1.5×10^{-3} *Torr* and 2×10^{-5} *Torr* (corresponding to *20 ppb*). The spectra at 2×10^{-5} *Torr* Torr show spectral broadening from background atmospheric NO_2. As discussed in the text, this distorts the spectrum.

($1Hz$) shot noise limit from $50\,\mu W$ of laser light reaching the APD detector (on resonance), $4 \times 10^{-12}\,W$. The bottom trace in figure 3.7 is an FM-MRS spectrum recorded at an NO_2 pressure of $2 \times 10^{-5}\,Torr$ with a $0.3\,Hz$ bandwidth, which corresponds to a $20\,ppb$ level of NO_2 relative to $1\,atm$; even here, the regions of signal enhancement provided by FM-MRS at higher pressures remain identifiable, although there appears to be some spectral broadening from background atmospheric NO_2.

3.5.3 *Sensitivity improvement from Digital Signal Processing*

By measuring the intensity of a particular individual spectral feature from an FM-MRS scan, a detection level of $20\,ppb$ was demonstrated. By measuring the intensity of a family of peaks, or by using the entire intensity-frequency information available in the FM-MRS spectrum, we can, however, increase the effective sensitivity of the present technique. A simple pattern recognition algorithm (Massart 1988, Sharaf 1986) could be employed in the signal processing to identify the characteristic FM-MRS NO_2 signature (shown in figure 3.5) at much lower levels in the presence of background signals and noise.

Figure 3.8 demonstrates the potential of using spectral cross-correlation (Bloch 1992) for pattern recognition to identify the FM-MRS NO_2 signature

distorted by accidental etalons (see trace (c) in figure 3.8) or hidden in broad band noise (see trace (d) in figure 3.8). From the figure it is clear that although a particular FM-MRS peak may be buried in noise an therefore unidentifiable (see trace d), the family of peaks that form the characteristic FM-MRS NO_2 signature can be identified quantitatively by correlation, thereby increasing the sensitivity by several orders of magnitude. Sub-parts-in-10^9 sensitivity levels of NO_2 were thus achieved. Other workers (Riris 1993) have applied similar, but not identical, signal processing techniques to the simple optical spectrum of N_2O obtained by diode laser FMS at $\lambda = 4.554\ \mu m$ and achieved a sensitivity improvement of a factor of ≈ 10.

3.5.4 *FM-MRS Sensitivity and localized selectivity*

By using FM spectroscopy (without MRS), Gehrtz *et al.*(1985), were able to achieve near-shot-noise-limited detection of NO_2 at a noise-equivalent partial pressure of $0.7 \times 10^{-6} Torr / m$. The FM-MRS measurement described here is within a factor of two or three of that limit. Using MRS alone (without FMS), Blake *et al.*, were able to detect *30* parts in 10^9 of *NO* with a tunable diode laser used to probe the molecule's rovibrational transitions near $5.3\ \mu m$. Dillenschnider and Curl in 1983 exploited the high sensitivity of MRS to observe

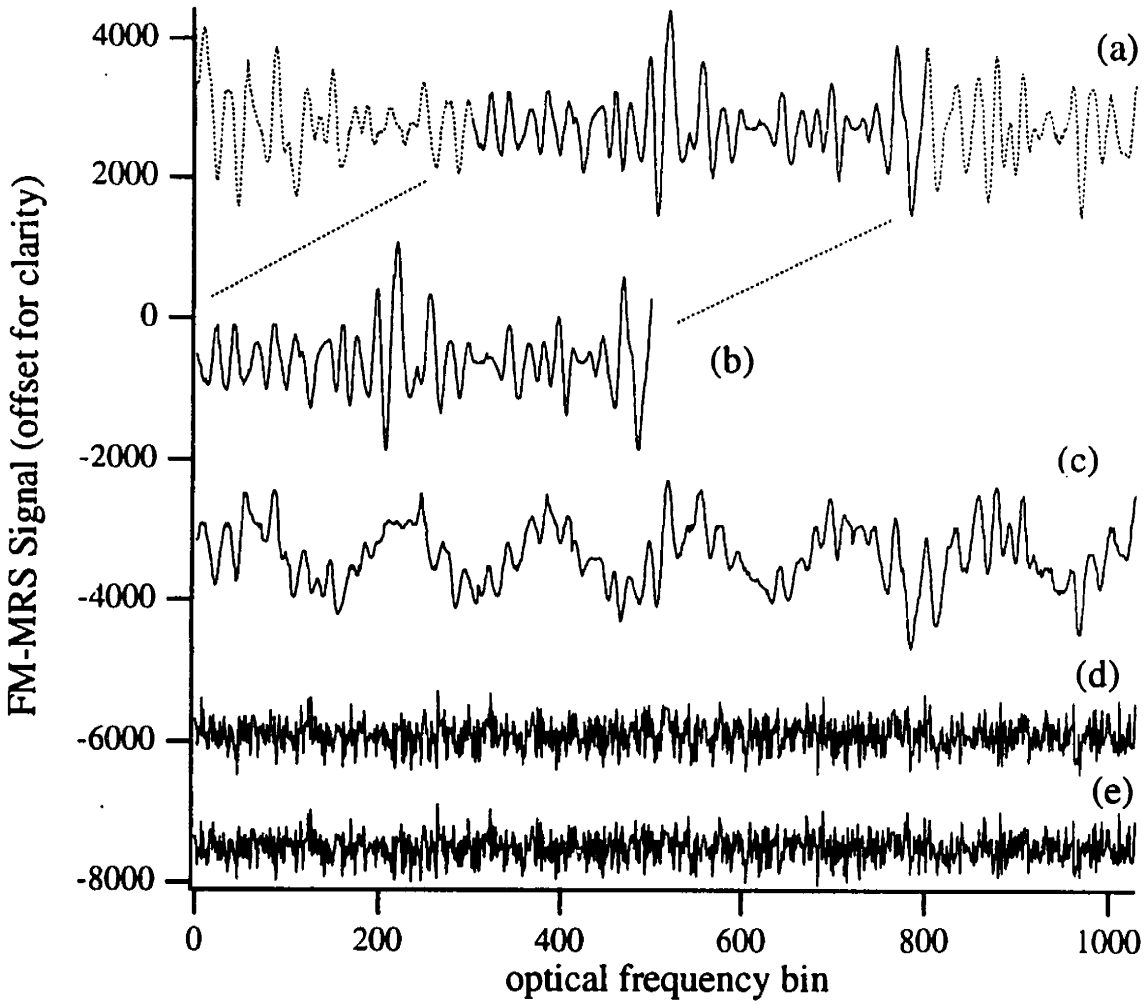

Figure 3.8a: Input spectra for correlation analysis to improve sensitivity. The top trace (a) is a high pressure FM-MRS spectrum. Trace (b) is the highlighted portion of trace (a). Trace (c) is an FM-MRS spectrum contaminated by accidental etalons. Trace (d) is a simulated spectrum, constructed from one tenth of trace (a) and Gaussian noise (amplitude 200), while trace (e) is just the noise. The results are shown in figure 3.3b.

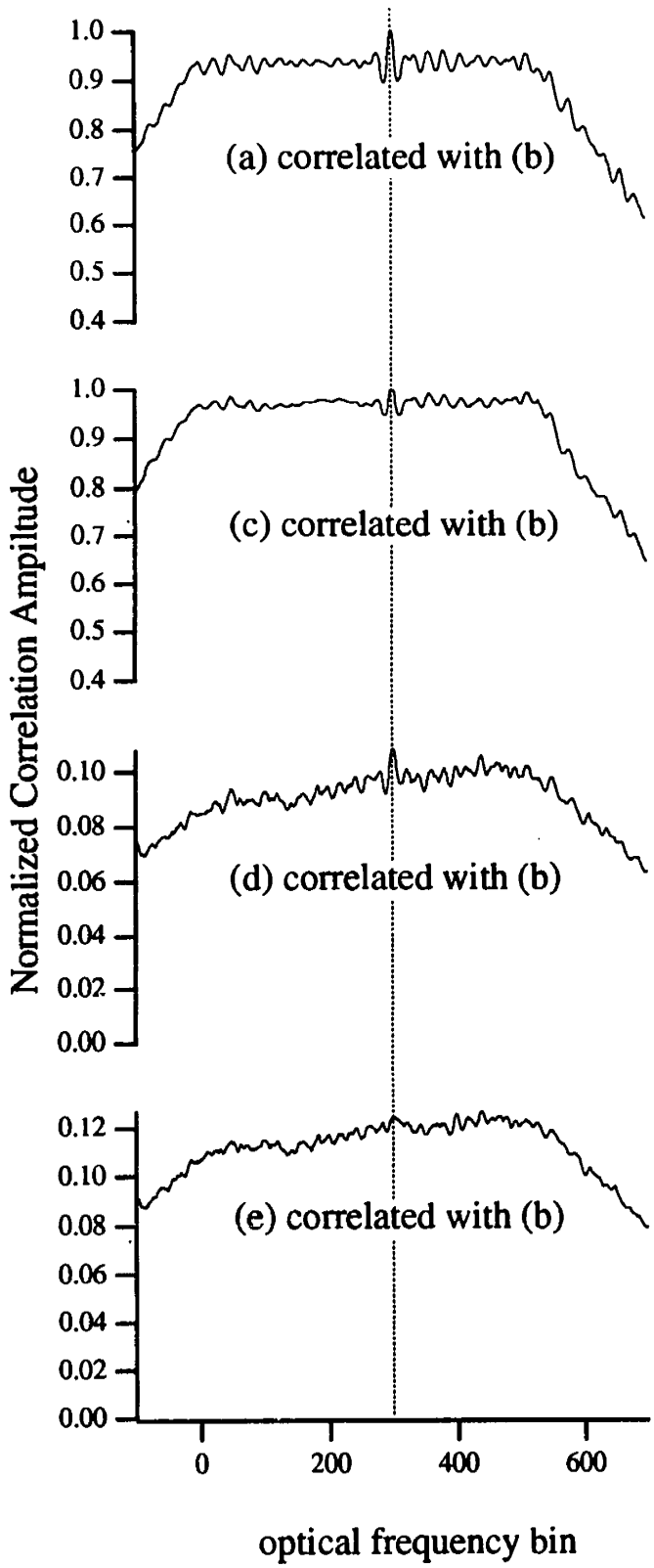

Figure 3.8b: The results of spectral cross-correlations. Input spectra are displayed in figure 3.8a. Each trace is normalized using the auto-correlation of (b). Hence, the location and absolute amplitude of trace (b) is found. Such normalized cross-correlations quantitatively identify the FM-MRS NO_2 signature even in the presence of both strong baseline modulation (etalons) and noise.

a very weak overtone transition in NO_2, using a color-center laser operating near $2.5\ \mu m$. As noted already, FM-MRS possesses several advantages over either the FM or MRS technique alone. Primarily, the complementary combination of the two techniques results in sensitive detection with two types of selectivity--selectivity to paramagnetic species and selectivity to a localized volume. FM-MRS is sensitive to only those molecules contained in the sample cell located within the applied magnetic field; it is much less sensitive to the potentially much larger ambient laboratory concentrations of NO_2 that the laser beam samples along the $> 1\ m$ beam path before and after the sample cell. Before the sample cell, ambient levels of NO_2 can develop a background FM-MRS (or MRS) signal resulting from the Earth's non-zero magnetic field. At a typical ambient NO_2 level of 100 in 10^9 (National 1991) for a $1\ m$ optical path length, this signal is less than a hundredth of the signal from within the cell at 20 parts in 10^9 of NO_2. Additionally, this background FM-MRS signal is further reduced by the polarizer immediately before the cell by a factor approaching 10^5. Hence background FM-MRS (MRS itself) does not cause interference.

Background FM, nonetheless, can pose problems, although the double-null

a background signal (without the MR effect) is the same as that from an accidental etalon, that is, preferential absorption or phase shift of a sideband without polarization rotation. As discussed before (see chapter 3.4.1), the use of FM-MRS reduces *such off-resonance interference* by a factor of the uncrossing angle. For 3^o this factor is 0.05. For the conditions mentioned above, residual background FM from before the sample cell is equivalent (assuming, incorrectly for now, that the *1 atm* line width is the same as the lower pressure line width in the cell) to an FM-MRS signal that would from NO_2 at 100 parts in 10^9 inside the cell. However, because the line width at *1 atm* is 100 times greater than the line width inside the cell (at *0.01 atm*), the background FM is certainly smaller than the FM-MRS signal. Nonetheless, on a magnetically active resonance, some of the background FM is converted into a recordable FM-MRS signal. The FM-MRS line shapes are then distorted by this contribution. When the NO_2 concentration in the cell is at its lowest levels, spectral distortion, as evidenced by pressure broadened line shapes, appears; see figure 3.7. The broadening appears because of MR converted FM background and not background FM-MRS. Since the beam path between the anayzler and detector was kept small, residual FM background generated in this region did not substantially contribute to the spectrum.

3.5.5 *FM-MRS detection of NO_2: Conclusion*

FM-MRS is a promising method for the selective detection of trace quantities of paramagnetic species. A detection level equivalent to *20* parts in 10^9 of NO_2 has been demonstrated in a *10 cm* sample cell in the presence of background NO_2 in the laboratory. The potential of simple signal-processing techniques to increase sensitivity is beginning to be to be explored; using these techniques, detection levels at parts-in-10^{-12} should be achieved. Additionally, several improvements have been suggested (in earlier sections of this chapter) that will overcome the existing experimental difficulties and further increase sensitivity. In the next chapter, FM-MRS will be applied to simplify the spectrum of *CeF* at *2000K*.

3.6 *References*

1984 Adams, H., D. Reinert, P. Kalkert, P., and W. Urban, "A Differential Detection Scheme for Faraday Rotation Spectroscopy with a Color Center Laser," *Appl. Phys. B.*, **34**, 179.

1996 Blake, T. A., C. Chackerian, Jr., and J. R. Podolske, "Prognosis for a mid-infrared magnetic rotation spectrometer for the *in situ* detection of atmospheric free radicals," submitted to *Appl. Opt.*

1993 Bloch, J. C, M. C. McCarthy, and R. W. Field, "45° double-beam frequency modulated magnetic rotation spectroscopy," The 48th Ohio State University International Symposium on Molecular Spectroscopy, Talk RD'01, Columbus Ohio.

1996 Bloch, J. C., L.A. Kaledin, and R.W. Field, R. W., "Laser Spectroscopy of Cerium Monofluoride: Ligand Field Assignments of Some 4f5d6p 4f5d6s Transitions," *J. Mol. Spec.*, **0**, 0.

1992 Bloch, S. C., "SSP: The Spreadsheet Signal Processor", Prentice Hall, New Jersey; references contained therein.

1983 Dillenschnider, W. and R. F. Curl, Jr., "Color center laser spectroscopy of $\nu_1 + \nu_2 + \nu_3$ of NO_2 using magnetic rotation," *J. Mol. Spec.*, **99**, 87.

1985 Gehrtz, M., G. C. Bjorklund, and E. A. Whittaker, "Quantum-limited laser frequency-modulation spectroscopy," *J. Opt. Soc. Am. B*, **2**, 1510.

1992 Grant, W. B. , R. H. Kagmin, and W. A. McClenny, "Optical remote measurement of toxic gases," *J. Air Waste Management Assoc.*, **42**, 18.

1941 Jones, R. C., "A New Calculus for the Treatment of Optical Systems,"

J. Opt. Soc. Am.,**31**, 488.

1948 Jones, R. C., "A New Calculus for the Treatment of Optical Systems. VII. Properties of the N-Matrices," *J. Opt. Soc. Am.*,**38**, 671. See references therein for I-VI.

1992 Khan ,S. M., ed., in *Proceedings First International Symposium on Explosive Detection Technology* (Federal Aviation Administration Technical Center, Atlantic City, NJ).

1990 Kliger, D. S., J. W. Lewis, and C. E. Randall, *Polarized light in optics and spectroscopy*, Boston: Academic Press.

1980 Liftin, G., C. R. Pollock, R. F. Curl, Jr., and F. K Tittel, "Sensitivity enhancement of laser absorption spectroscopy by magnetic rotation effect," *J. Chem. Phys.*, **72**, 6602.

1988 Massart, D. L., B. G. M. Vandeginste, S. N. Deming, Y. Michotte, and L. Kaufman, "Chemometrics: A Textbook", *Data Handling in Science and Technology Vol. 2* (B. G. M. Vandeginste and L. Kaufman, eds.), Elsevier, Amsterdam.

1994 McCarthy, M. C., J. C. Bloch, and R. W. Field, "Frequency-modulation enhanced magnetic rotation spectroscopy: A sensitive and selective absorption scheme for paramagnetic molecules," *J. Chem. Phys.*, **100**, 6331.

1991 National Research Council Commission of Geosciences, Environment, and Resources, Board on Atmospheric Sciences and Climate, Committee on Tropospheric Ozone Formation and Measurement, *Rethinking the Ozone Problem in Urban and Regional Air Pollution*, National Academy of Sciences- National Research Council, Washington D.C., 215.

1993 Riris, H., C. B. Carlisle, R. E. Warren , and D. E. Cooper, " Signal-to-noise ratio enhancement in frequency-modulation spectrometers by digital signal processing," *Opt. Lett.*, **19**, 144.

1986 Sharaf, M. A.,D. L. Illman, B. R. Kowalski, "Chemometrics", *Monographs on Chemical Analysis No. 82* (P. J. Elving and J. D. Winefordner, eds.), J. Wiley & Sons, New York.

1991 Silver, J. A., D.S. Bomse, C. A. and Stanton, in *Optical Methods for Ultrasensitive Detection and Analysis: Techniques and Applications*, Proc. Soc. Photo-Opt. Instrum. Eng. **1435**, 64.

1975 Smalley, R. E., L. Wharton, and D. H. Levy, "The fluorescence excitation spectrum of rotationally cooled NO_2," *J. Chem. Phys.*, **63**, 4977.

1995 Smith, J. M., J. C. Bloch, R. W. Field, and J. I. Steinfeld, "Trace

detection of NO_2 by frequency-modulation-enhanced magnetic rotation spectroscopy," *J. Opt. Soc. Am. B.*, **12**, 964.

1975 Stevens, C. G. and R. N. Zare, "Rotational analysis of the 5933 Å band of NO_2," *J. Mol. Spec.*, **56**,167.

1975 Tanaka, T., R. W. Field, and D. O. Harris, "Microwave optical double resonance and continuous wave dye laser excitation spectra of NO_2: rotational assignment of the K=0-4 subbands of the 593 nm band," *J. Mol. Spec.*, **56**, 188.

1988 Zhao, X., E. J. Hintsa, and Y. T. Lee, "Infrared multiphoton dissociation of RDX in a molecular beam," *J. Chem. Phys.*, **88**, 801.

4.1 *Introduction*

The electronic spectra of the lanthanide monofluoride (*Ln*F) molecules[1] are very complex because of the high density of low-lying electronic states that arise from partially filled atom-like $4f$ and $5d$ orbitals. All of the low-lying states are expected to belong to one of three types of Ln^+F^- superconfigurations: $Ln^+ f^N s$, $f^{N-1}s^2$, and $f^{N-1}ds$. The present chapter describes laser spectroscopic experiments on the CeF molecule. The techniques employed include wavelength selected fluorescence excitation (WSFE), dispersed fluorescence (DF), magnetic rotation spectroscopy (MRS), and frequency modulation enhanced MRS (FM-MRS). The use of the magnetic based methods MRS and FM-MRS is shown to simplify the appearance of the complicated spectra and aid in its spectral assignment.

The experiments discussed here confirm the predictions of both a zero-adjustable parameter model and a semiempirical Ligand Field Theory (LFT) model similar to that previously used to account for the electronic properties of all lanthanide monoxide (*Ln*O) molecules (Field 1982). The LFT predictions confirmed here are: (*i*) the lowest energy superconfiguration for CeF is

[1]see: Azuma 1991; Clements 1984; Effantin 1976; Gurvich 1989; d'Incan 1972; Kaledin 1992,1994,1996; Lee 1977; Lumley 1978; McCarthy 1992, 1996; Gurvich 1989; Lumley 1978; Robbins 1974

$4f5d6s$; (*ii*) the three observed low-lying states have T_0 values (0, 705.15, and 1500 cm^{-1}) and Ω-values (Ω = 3.5, 4.5, and tentatively assigned Ω = 3.5) in good agreement with the three lowest lying LFT- predicted states; (*iii*) the two observed $\Delta G_{1/2}$ values (543.76 and 544 cm^{-1}) are consistent with the characteristic ~550 cm^{-1} vibrational frequency expected for the $4f^{N-1}5d6s$ superconfiguration; and (*iv*) the only known excited state (Ω = 4.5) at 17592.69 cm^{-1} belongs to the $4f5d6p$ superconfiguration. Thus the observed visible wavelength electronic transitions of CeF are all Ce^{+}-centered one-electron $6p \leftarrow 6s$ transitions.

In addition to the complexity associated with a high density of electronic states, the *Ln*F spectra are often further complicated by the large nuclear spins and the numerous significantly abundant stable isotopes typical of most Ln atoms. Laser techniques such as fluorescence excitation, dispersed fluorescence, wavelength-selected fluorescence excitation, and magnetic rotation spectroscopy have enabled us to overcome the difficulties of spectral congestion, perturbations, and hyperfine and isotopic structure for several *Ln*F molecules already: EuF, GdF, TbF, DyF, and HoF[1].

Dispersed fluorescence spectra provide energy linkages among low-lying electronic states by displaying *all* allowed downward transitions from a systematically selected series of single, laser-populated, ~2 eV excited rovibronic states (Linton 1983, Dulick 1985). Each such experiment produces a *partial*

electronic-vibration energy level diagram for the low-lying states. When partial level diagrams obtained from different excited states are cross-compared, states in common between partial diagrams can be recognized by their Ω-values and energy spacings. In this way, all of the low-lying states can eventually be energy linked in a single *global* energy level diagram.

Wavelength selected fluorescence excitation spectroscopy, by eliminating interference from unrelated overlapping transitions, provides high-resolution information, especially in the inevitably congested but diagnostically important regions near the lowest-J lines in each rotational branch (McDonald 1983).

The magnetic-based absorption techniques, MRS and FM-MRS, provide unequivocal identification of the lowest-J lines, thus allowing identification of the possible Ω-values of the states involved. These techniques also produce line shapes that reflect the value of $\Delta J = J' - J''$ for the transition. This information instantly groups the individual transitions into rotational branches with constant ΔJ.

Nevertheless, the enormous number of low-lying *Ln*F electronic states would frustrate the most powerful array of spectroscopic techniques without a zero-order model for the expected patterns of states and their properties. LFT allows us to predict the energy order and diagnostic properties of all low-lying molecular states (Dulick 1982; Hocquet 1988; Schall 1985, 1987). Four kinds of information go into our LFT model: (*i*) the largest, most important, and *never*

adjustable part is an effective Hamiltonian representation of the electronic structure of the free Ln^+ atomic ion as determined from fits of the atomic spectrum (Martin 1978) to orbital energy ε_{nl}, Coulomb $F_k(nl,n'l')$, exchange $G_k(nl,n'l')$, and spin-orbit ζ_{nl} parameters (Goldschmidt 1978, Wyart 1980); (*ii*) empirically adjustable or *ab initio* calculable shifts of orbital energies $B^0_0(nl,nl)$ due to the repulsion of an electron in the n*l* orbital by the -1 charged F^- ion: $B^0_0(4f,4f) > B^0_0(5d,5d) > B^0_0(6s6s) > B^0_0(6p,6p) > 0$; (*iii*) the $B^k_0(nl,nl)$ parameters, the anisotropic part of the ligand field that lifts the $m_l \equiv \lambda$ degeneracy of an n*l* orbital and causes ($\Delta l \neq 0$, $\Delta\lambda = 0$) orbital mixing, the values of which are computed from crude *ab initio* n*l* orbital sizes (McLean 1981, Burns 1964, Herman 1963), or for Ln^+F^- in the $4f^{N-1}$ core configuration, estimated as one half the value of the corresponding parameter in the Ln^2O^{+2-} molecule, in the $4f^{N-1}$ core configuration (Hocquet 1988, Dulick 1986), and (*iv*) some Hund's rule-like ideas about the qualitative structure of supermultiplet patterns (Field 1982). At this stage, there is little doubt about the appropriateness of the LFT model; to make reliable predictions of the energies and properties of all of the low-lying states of all the *Ln*F molecules, one needs only some empirical calibrations of the *ab initio* calculated values and the *n*-dependence of the $B^0_0(nl,nl)$ parameters that control the relative energies of the three relevant lowest energy $f^N s$, $f^{N-1}s^2$, and $f^{N-1}ds$ superconfigurations.

The LFT model works well for *Ln*F and *Ln*O molecules because of the

core-like and non-bonding character of their extremely compact *Ln*-centered 4*f* orbitals. In this paper we exploit another property of the open 4*f* subshell in order to narrow drastically the assignment possibilities for the upper states of strong electronic transitions of *Ln*F or *Ln*O molecules observed in the visible wavelength region. Electronic transitions follow the propensity rule that the initial and final states differ by the *promotion of a single electron* (Kaledin 1994a). For transitions of the type $4f^{N-1}5d(l'\lambda') \leftarrow 4f^{N-1}5d(l''\lambda'')$ (where $(l'\lambda')$ and $(l''\lambda'')$ denote *non*-core valence orbitals), the $4f^{N-1}5d[L_c, S_c, J_c, \Omega_c]$ subshell acts as a *spectator* (the c subscript denotes core); *none* of the L_c, S_c, J_c, or Ω_c quantum numbers is allowed to change simultaneously with the valence orbital $l'\lambda' \leftarrow l''\lambda''$ promotion!

The simplicity of the LFT model will now be illustrated by reviewing its predictions for the majority of the states of *all* configurations of Ce^+ which lie below ~30,000 cm^{-1} in the CeF molecule. Figure 4.1 summarizes the LFT calculations for CeF. Since the electrostatic repulsions between electrons in core-like 4*f* and 5*d* orbitals are much larger than those between these Ln^+-centered core-like electrons and the ~2Å distant -1*e* charged ligand, the ligand field (LF) effects will be a small perturbation on the free Ln^+ energy levels (Field 1982). In this *weak LF limit*, the *Ln*F states will occur in groups that replicate the pattern of the free atomic Ln^+ energy levels and the L_c, S_c, J_c, J_a (c≡core, a≡atom) quantum numbers of these Ln^+ states. In the case of Ce^+,

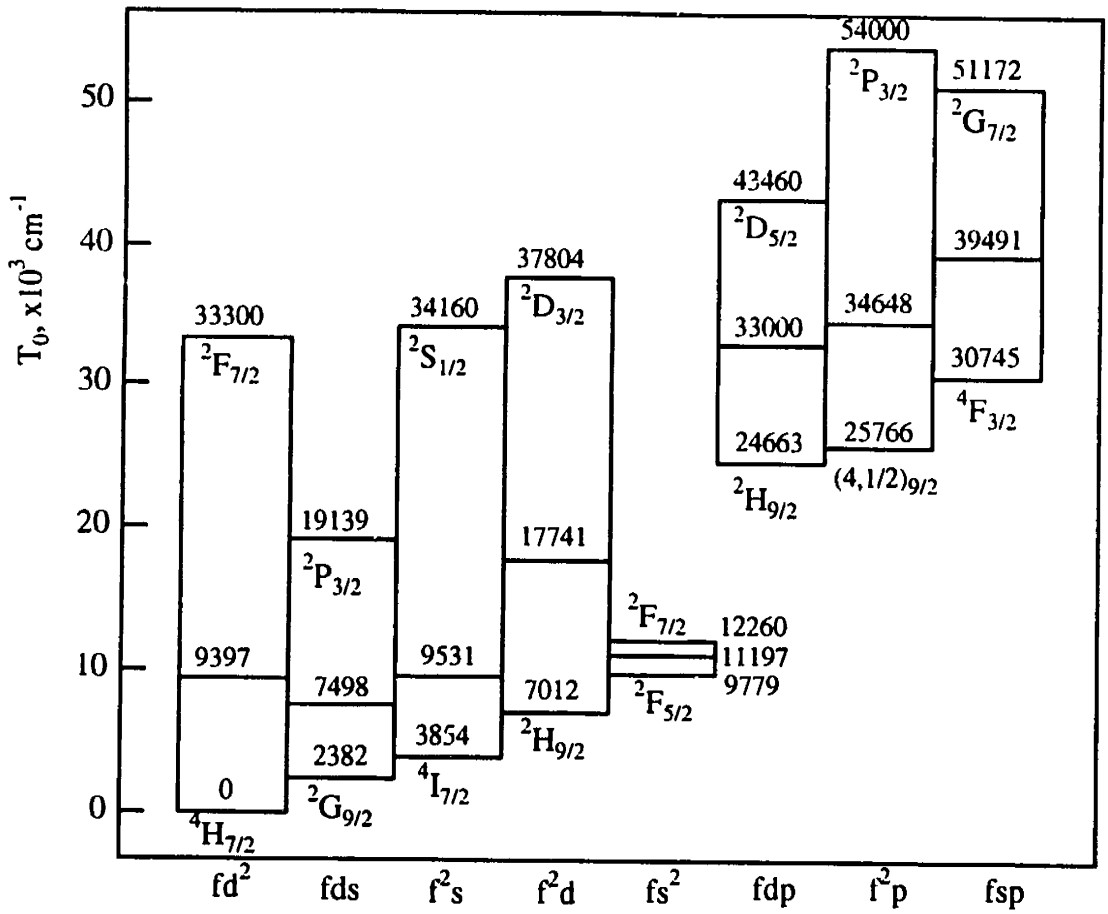

Figure 4.1a: Energy level diagram summarizing the LFT calculations for CeF. This plot shows the lowest and highest energy level (along with most appropriate atomic state designation) and the center of gravity (degeneracy weighted average) value for the lowest-lying parent superconfigurations of Ce^+ with the max-L, max-S $4f^N$ core. These energy levels were effectively the input to the LFT model. Figure 4.1b shows the LFT predictions for CeF arising from the displayed parent superconfigurations of Ce^+.

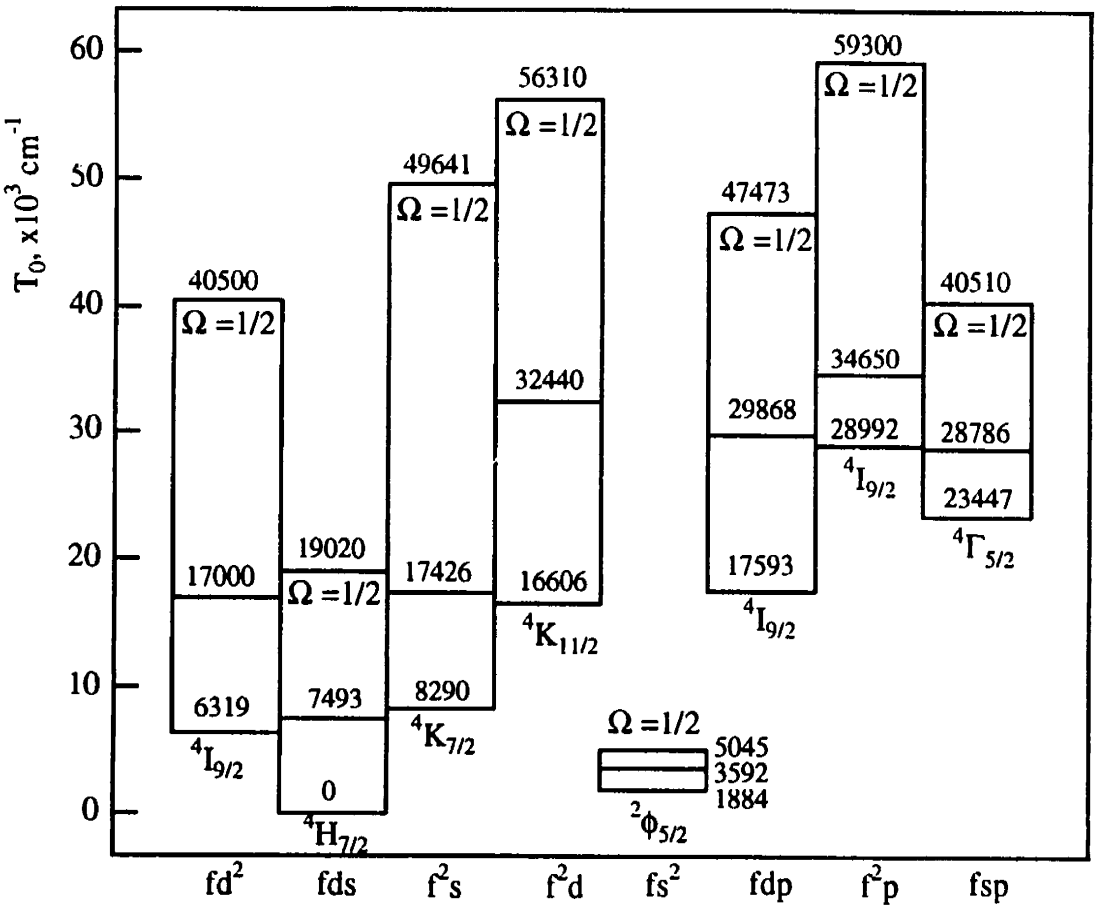

Figure 4.1b: Energy level diagram summarizing the LFT calculations for CeF. This plot shows the LFT predictions for CeF arising from the displayed parent superconfigurations of Ce^+. The predicted lowest energy state and Ω assignments for CeF are shown along with the center of gravity and highest energy level.

both the $4f$ and $5d$ half-subshells are *less than half filled* (*i.e.*, d^N N<3, f^N N<4) , so the lowest energy group of Ce^+ replica states will be those with $\Omega = J_a$. The next lowest energy group [each level in the group shifted up by an amount ~700 cm^{-1}, primarily controlled by $B_0^2(4f,4f)$] will be those with $\Omega = J_a - 1$ (Linton 1983). The electronic states of CeF correspond to the Hund's case (c) limit, and are labeled using the Ω quantum number. Low-lying states, arbitrarily designated as those within 10,000 cm^{-1} of the ground $X(1)3.5$, $v = 0$ state, are denoted by $(i)\Omega$, where i is an index that counts the states of a given Ω value in ascending energy order. States lying above 10,000 cm^{-1} are labeled by $[T_0]\Omega$, where T_0 is the term value (in units of 10^3 cm^{-1}) for the $v'=0$ level relative to $X(1)3.5$, $v''=0$.

The ground state configuration of Ce^+ is $4f5d^2$. This configuration is unique among the Ln^+ ions; hence, we must consider its states in addition to the low-lying states of the three usually lowest lying parent superconfigurations[2] of most Ln^+: $f^N s$, $f^{N-1}s^2$, and $f^{N-1}ds$. The energy splittings and J_a quantum numbers for the lowest energy group of states of the five Ce^+ candidate superconfigurations, $4f5d6s$, $4f^26s$, $4f6s^2$, $4f5d^2$, and $4f^25d$, are sufficiently different as to provide unique diagnostics for the CeF superconfigurational parentage[3].

Superconfigurational assignments, based on the energy and Ω pattern of the

[2]Including the $4f5d^2$ configuration necessitates including the $4f^25d$ configuration.

[3]See Appendix of Bloch 1996.

low-lying electronic states, can be confirmed by the vibrational frequencies, magnetic g-values (Schall 1986), or hyperfine structure (Dulick 1985; Hocquet 1988; Linton 1987,1988). $\Delta G_{1/2}$ intervals of ~610, 550, and 500 cm^{-1} are diagnostic of the $Ln^{+}f^{N-1}s^2$, $f^{N-1}ds$, and $f^{N}s$ parent superconfigurations (Kaledin 1992), respectively, owing to the partial shielding of the bare $Ln^{3+}(f^{N-1})$ core from F^- by two electrons in $4f$, $5d$, and $6s$ orbitals, with the relative shielding effectiveness $f > d >> s$ (Field 1982). The magnetic g-values provide information about the magnitudes and relative orientations of L_c and S_c (Schall 1986). Large *Ln*-centered hyperfine structure is expected for the $f^{N}s$ and $f^{N-1}ds$ superconfigurations as a result of the unpaired electron in the $6s$ orbital.

Prior this work, one CeF band system had been observed in absorption (Clements 1984) and by Doppler-free molecular-beam laser fluorescence excitation spectroscopy (Azuma 1992). We report here analyses of the same [17.6]4.5 upper state and three low-lying states, $X(1)3.5$, (1)4.5, and a state of unknown symmetry, probably (2)3.5, at 1500 cm^{-1}.

LFT calculations for CeF predict that the lowest state of the parent $4f5d6s$ superconfiguration, the $X^4H_{7/2}$ state, will lie 1544 cm^{-1} below the lowest state $^2\Phi_{5/2}$ of the $4f6s^2$ superconfiguration, 6087 cm^{-1} below the lowest state $^4I_{9/2}$ of the $4f5d^2$ superconfiguration, and 8743 cm^{-1} below the lowest state $^4H_{7/2}$ of the $4f^26s$ superconfiguration. The LFT model also predicts $4f5d6s$ states with

(J_a,Ω)=(4.5,4.5) and (4.5,3.5) at 765 and 1706 cm^{-1} above the (J_a,Ω)=(3.5,3.5) $X^4H_{7/2}$ ground state. These $4f5d6s$ states are expected to have $\Delta G_{1/2}$ ~ 550 cm^{-1}. The primary goals of the present work are to confirm the LFT predictions for CeF and to refine the global model for the three lowest energy superconfigurations of all *Ln*F molecules. Encouraged by the recent assignments of the upper states in the optical spectrum of CeO to the $4f6p$ superconfiguration (Kaledin 1993), of GdO to the $4f^7(^8S)6p$ superconfiguration (Kaledin 1994b), and of TbF to the $4f^8(^7F)6s6p$ superconfiguration (Kaledin 1994a), we propose here that the [17.6]4.5 upper state, or the $[17.6]^4I_{9/2}$ state in Hund's case (*a*) notation[4], belongs to the $4f5d6p$ superconfiguration. These assignments are based on computed (Field 1982, Schall 1986) ligand field orbital destabilization energies $B_0^0(nl,nl)$ and $4f5d$-core spectator selection rules.

4.2 *Experiment*

Gaseous CeF was prepared in one of two available high temperature furnaces. The fluorescence based studies, WSFE and DF, were primarily done using the furnace described previously (Kulikov 1984, Kaledin 1994a), referred to as the "Kaledin Oven". The absorption based studies, MRS and FM-MRS (and later

[4]Λ and S are well defined for most of the states of the $4f6s^2$, $4f^25d$, and $4f5d^2$ superconfigurations. For states of the $4f5d6s$, $4f5d6p$, $4f6s6p$, $4f^26s$, and $4f^26p$ superconfigurations, the Λ and S values are well defined only for the few lowest states of each configuration. Here, Hund's case (a) limit notation is used for the predicted lowest energy state of each superconfiguration.

fluorescence studies) were performed in a newly constructed magnetically confined oven that is briefly described below.

4.2.1 *Fluorescence methods: DF and WSFE*

For the fluorescence studies, 0.2 g of Ce metal with 0.2 g of AlF_3 powder were placed in a 9 mm inner-diameter, 60 mm long tantalum tube inside a brass vacuum vessel. The tube was constructed by rolling and spot-welding tantalum foil. By passing an AC current of up to 150 A at 6 V through the tube, temperatures of 2000K, as measured with an optical pyrometer, were achieved. The furnace for these studies was portable and positioned directly in front of an optical monochromator, allowing easy alignment of the laser beam axis to the monochromator's axis and collection of the end-on fluorescence (Kaledin 1994a). The windows of this furnace were fixed at Brewster's angle with respect to the laser beam axis and polarization, to minimize the scattered laser light reaching the monochromator slits.

Wavelength selected-fluorescence excitation (WSFE) and dispersed fluorescence (DF) spectra were recorded using a Coherent 699-29 Autoscan ring dye laser operated with Rhodamine 6G at single longitudinal mode power in the 700-1000 mW range. The WSFE spectra were recorded by scanning the laser excitation frequency while using a 1 meter Spex model 1704X monochromator (1800 groove/mm holographic grating) with 100 μm slits (1 Å or ~2-3 cm^{-1} spectral slit width) to restrict the detected fluorescence to a preselected

wavelength region. The transition frequencies in a CeF fluorescence excitation spectrum are accurate to $\pm 0.02\ cm^{-1}$. DF spectra were recorded, while the Autoscan laser was held fixed on a single rotational transition within one of the previously assigned excitation bands in the visible and near infrared regions, by scanning the monochromator. The measurements of frequency separations within DF spectra are accurate interband to $\pm 5\ cm^{-1}$ and intraband to $\pm 0.5\ cm^{-1}$, limited primarily by a "stick-slip" problem in the monochromator's mechanical sine drive.

4.2.2 *Magnetically confined experiments: MRS and FM-MRS*

For the MRS and FM-MRS experiments, a modified version of the "Kaledin oven" used for the fluorescence experiments was employed. The modifications provided a longer region of gaseous CeF, confinement of this region in an homogeneous magnetic field, and flat (non-brewster angle) windows. Some of these modifications also proved beneficial to fluorescence studies.

A schematic of the new oven is displayed in figure 4.2. The body of the oven was machined from a solid cylinder of brass, thereby reducing the number of vacuum seals. From end to end, along the outer surface of the oven, channels were machined. Exceptional cooling was provided by flowing chilled water through copper refrigeration tubing soldered into these channels. The electrodes, machined from solid brass stock with cooling water conduits drilled directly into

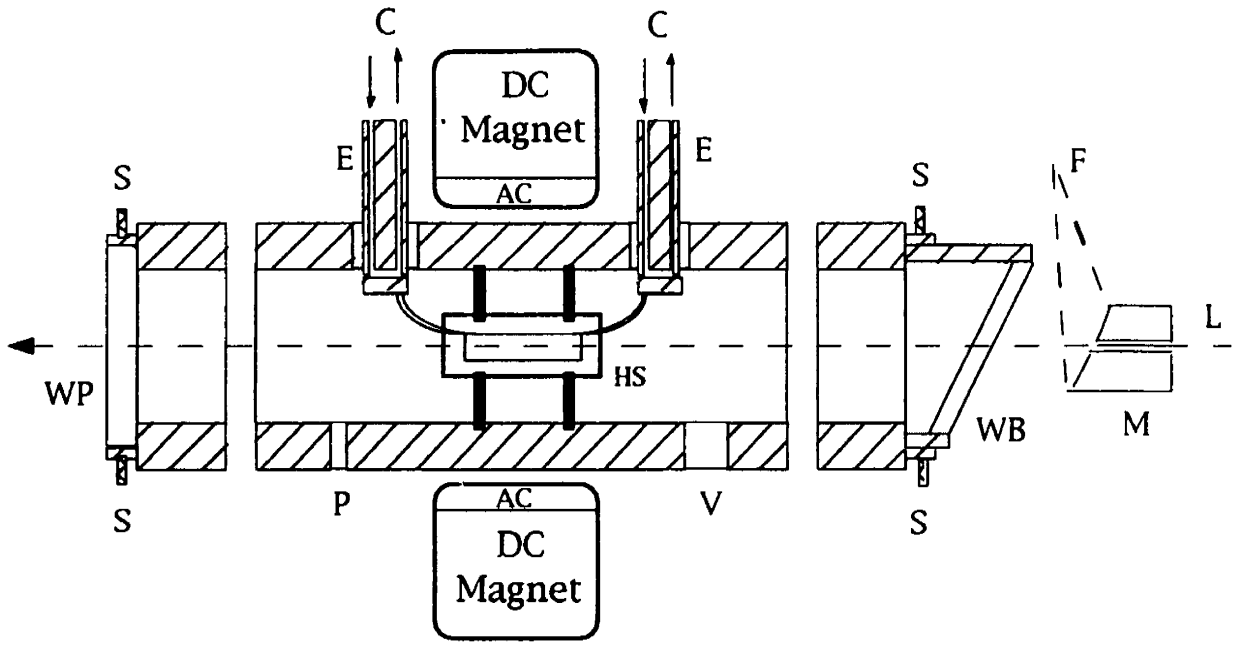

Figure 4.2: Simplified schematic of new high temperature oven. A brief description of the oven and its design advances appears in the text. The central body section is 30 cm long x 12 cm diameter and the small heater, suspended from the electrodes, is 10 cm long x 1 cm diameter. The diagram is not to scale. E = brass electrode; C = cooling channels for E; F = fluorescence collection; HS = heat shielding; L = laser axis; M = mirror with hole; P = metering port; S = screw; V = vacuum port; WP = 2" diameter optical window, perpendicular; WB = optical window, Brewster's angle. Not shown: cooling lines (except for C), flanges between body and window holders, port connectors and feedthroughs.

them, were electrically isolated from the oven body *via* Teflon inserts and corona-dope within the vacuum connectors. The large flanges on the end of the oven were machined to mate with standard 4" sanitized steel flanges such as those available from Alloy Products Corp. (Waukesha, WI). Water cooled window holders, that allowed mechanical cancellation of the vacuum induced birefringence, were constructed to mate with the flange. Once sealed and evacuated[5], the oven leak rate was less than 0.1 Torr/hour. Since the oven was cylindrical in shape, it fit easily in the bore of a large electromagnet[6].

The low-voltage high current power was brought from the power source to the oven *via* 4/40 gauge copper welding wire. The power source was constructed from a 30A variac and a 1:10 (12 Volt) or 1:20 (6 Volt) transformer. Up to three fused AC power lines fed the variac[7], whose output was monitored and sent to the transformer. The output current and voltage of the transformer, limited usually by the resistance of the heater, was monitored, and varied by adjusting the Variac.

This new oven is considerably more versatile than the earlier Kaledin oven.

---

[5]Since the oven operates at high temperature, evacuation should be followed by a bake-out period to reduce outgassing.

[6]The homogeneity of the magnetic field produced by one central coil was determined to be ±10% along the length of the heater (parallel to the laser's propagation axis), sufficient for the studies describe here. For improved homogeneity, additional coils, located at the two ends of the oven could be used. Furthermore Helmholtz coils could reduce the component of the field not along the laser propagation axis.

[7]One 30A line would be sufficient, but alas, was not available. Furthermore, due to power demands from other equipment, the available 20A laboratory circuits often supported only 10-15A before blowing.

Various sizes and types heaters (homemade tantalum tubes up to 11 cm long, or commonly available tungsten coils[8] with ceramic tube inserts[9]) could be used depending upon the molecule and conditions. For CeF, a 10 cm long Ta tube with an inner diameter of 6 mm was employed. This long, thin active region provided a twice longer absorption length and operation times for CeF than the earlier oven.

The new oven also provided significantly improved cooling. This contributed to the longer containment times. The new oven also boasted improved *optical* access[10], allowing the use of strain-released-normal or Brewster windows. For MRS and FM-MRS, both polarization sensitive techniques, normal windows with minimal residual birefringence were crucial in obtaining high sensitivity.

This oven was also suitable for fluorescence studies. Since the windows were closer to the active region, a larger solid-angle of the fluorescence could be collected using this oven than the earlier version. However, due to the weight of the magnet and the additional cooling water lines, this oven was not portable and not usable directly in front of a monochromator. Hence, for collection of the end-on fluorescence, a mirror with a hole in it was used. Specifically, a 1 mm

---

[8]The R. D. Mathis Company (Long Beach, CA) constructs user designed heaters. For this oven, parts numbered RDM-F-29993 and RDM-F-29993-A are appropriate..

[9]Tantalum tube heaters must be constructed (total time 1/2 - 1 hour) and they often are inappropriate for the study of certain aggressive metals, such as Ni or Eu, that destroy them. Ceramic inserts are inexpensive, but produce perhaps undesirable oxygen when heated. At high temperatures, the ceramics melt.

[10]One drawback of the new oven is poor *operator* access to the heater assembly, making loading the oven challenging.

hole was carefully drilled in a metal off-axis parabolic mirror (Janos Technology, #A8037-205), through which the laser beam was passed. The image of the fluorescence collected from the metal mirror was then directed to the monochromator.

For a thorough description of the MRS technique, see McCarthy 1992 and appendix A here; for a description of the FM-MRS technique, see chapter 3. For the CeF MRS and FM-MRS studies, an axial magnetic field of 300 G is used. For both methods, the laser beam is passed through a mechanical chopper and a linear polarizer before entering the oven (propagation direction parallel to the magnetic field axis). After the oven, the laser beam passes through a second polarizer, aligned to be slightly uncrossed from the entrance polarizer, and then impinges on a photodiode. In MRS, the photocurrent was directly demodulated by a lock-in amplifier, the output of which is sent to the dye laser computer for storage. For the FM enhanced MRS studies, optical sidebands are produced using an RF Electro-optical modulator (before the mechanical chopper) and the photocurrent is first demodulated in a double-balanced mixer before being sent to the lock-in amplifier.

In principle, one can record both an absorption technique (MRS or FM-MRS) and an end-on fluorescence technique (WSFE or DF) simultaneously using the new oven. To do so, the entrance polarizer is placed before the mirror with the hole in it, and the entrance window is placed at Brewster's angle. The exit

window is normal to the laser beam propagation axis. Unfortunately, intense laser scatter from the exit window always reaches the monochromator slits, and thus limits the detection of weak fluorescence signals to optical wavelengths far from the laser's. [One solution that creates a modulated fluorescence signal but leaves the scatter un-modulated is to observe only one polarization component of the optical fluorescence[11] while modulating the magnetic field or the polarization of the laser. The polarization of the laser can be conveniently modulated using a photo-elastic modulator (PEM). Initial efforts collecting the "PEM enhanced MR fluorescence" have been encouraging.]

4.3 *Results*

The primary objectives in this analysis of the CeF electronic spectrum are the construction of an energy level diagram and the determination of Ω and vibrational assignments for all observed states. The secondary objectives are the demonstration of the utility of MRS and FM-MRS in the study of high temperature free radicals.

In the Hund's case (*c*) *weak* ligand field limit, which appears to be applicable to all of the low-lying states of all *Ln*F and *Ln*O molecules[12], the rotation-vibration constants of all states that belong to the same superconfiguration are

[11]The throughput of the monochromator is polarization sensitive. Additional polarization sensitivity can be obtained by inserting a high-quality polarizer in front of the entrance slits.

[12] EuF, EuO, GdF, GdO, YbF and YbO are exceptions. Due to the extraordinary stability of the half-filled $4f^7$ (Eu^+, Eu^{2+}, Gd^+, Gd^{2+}) or filled $4f^{14}$ (Yb^+, Yb^{2+}) f-core, these molecules exhibit some Hund's case (*b*) states.

nearly identical (Field 1982). This often makes it difficult, from ΔG intervals and B_v values alone, to recognize whether two electronic transitions have an upper or lower state in common (Linton 1983, Dulick 1985). In the weak-LF limit, the electric dipole transition selection rules, which govern the "hidden quantum numbers" (L_c, S_c, J_c, and J_a), impose more stringent restrictions on observable transitions than the naive $\Delta\Omega=0,\pm1$ Hund's case (c) selection rule. Thus, there are two obstacles to construction of a usefully complete "global" energy level diagram in which all of the observed low-lying states are linked in energy relative to each other: (*i*) recognition of the same state in two transitions; and (*ii*) hidden quantum number selection rule prohibitions on linkages between partial level diagrams. Our primary state-recognition tool is the pattern of Ω values and energy intervals in partial level diagrams obtained by analyzing the dispersed fluorescence spectrum originating from a single Ω', J'-assigned upper state (Dulick 1985). Restrictive selection rules are side-stepped by recording dispersed fluorescence spectra from several different upper states (especially perturbed rotational levels).

The Ω', Ω'' assignments are most definitive when the lowest-J lines in at least two rotational branches can be identified. Spectral congestion in the band origin region frequently obscures the first lines in ordinary absorption and emission spectra and non-selective fluorescence excitation spectra. The wavelength-selective fluorescence excitation technique employed here can often

provide unambiguous identification of first lines.

Sometimes, however, large hyperfine structure intensity dilution, weak Hönl-London factors, and high rotational temperatures conspire to make first lines undetectable. Problems due to high rotational temperatures can often be overcome using MRS and FM-MRS. Figure 4.3 shows the FM-MRS spectrum for the low-J R-branch lines of the [17.6]4.5 $\leftarrow X(1)3.5$ (0,0) band. Although the rotational temperature of the CeF source was ~2000 K, the lowest-J R-lines are easily observable. This is a remarkable achievement considering these lowest levels have only one tenth the rotational population of the most populated higher-J lines, J~53.5. When even these techniques fail due to vanishingly small absorption (or non-magnetically active states) $\Delta\Omega = \Omega' - \Omega''$ can be inferred from the relative branch intensities in the dispersed fluorescence spectrum [$\Delta\Omega$ =+1: $I_Q > I_R > I_P$, $\Delta\Omega$ =0: $I_R \approx I_P > I_Q$ (except at low-J), $\Delta\Omega$ =-1: $I_Q > I_P > I_R$]. The R, Q, P branch intensity ratios are most reliable for $\Delta\Omega$ assignments at the lowest possible J-values, where the strong and ubiquitous $\Delta\Omega$ =±1 heterogeneous perturbations[13] are weakest.

The usefulness of the magnetic rotation based spectroscopies to simplify and presort spectra of CeF has been demonstrated previously (McCarthy 1992, 1994). Figure 4.4 displays the MRS spectrum for the low-J lines of the [17.6]4.5 $\leftarrow X(1)3.5$ (0,0) band. Tie lines in the figure display the rotational assignments

[13]Heterogeneous perturbations are described by the $-BJ \cdot J_a$ term in H^{ROT}. See Lefebvre-Brion 1986.

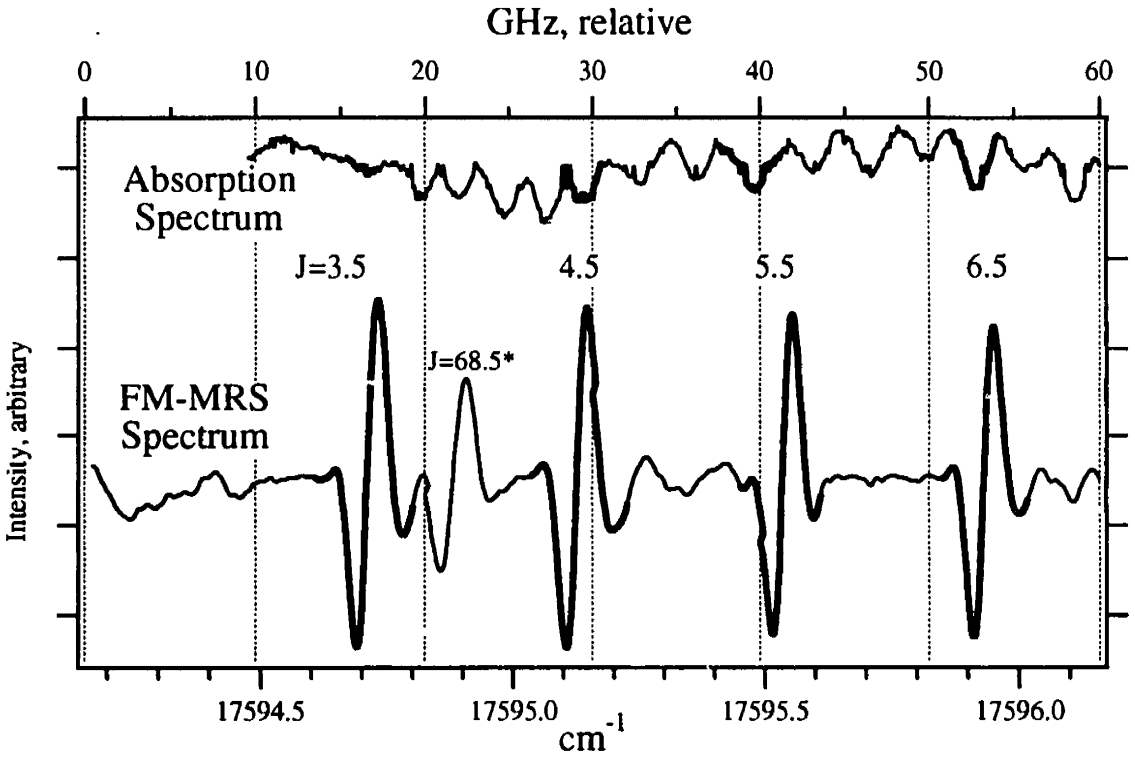

Figure 4.3: CeF absorption and FM-MRS spectra for the low-J lines of the 5684.2 Å band at 1800 K (set to optimize the absorption signal). For FM-MRS, the magnetic field was 300 G and ω_{RF}= 260 MHz. These conditions are not optimal for FM-MRS; yet its spectrum shows regions of enhancement, marked in bold. The low-J lines are enhanced, indicating a reduction of the effective rotational temperature. The J=68.5 line is perturbed (Azuma 1991) and has an anomalous Zeeman splitting and FM-MRS signal. Differences in line positions between traces arise from laser errors and the complicated Zeeman effect from individual and overlapping transitions (see appendix A).

of Azuma 1991. The lowest-J R-lines are easily observable while the phase reversal of the P and Q lines relative to the R-lines, typical of MRS (and FM-MRS), facilitates grouping the transitions into branches and rapid spectral assignment. The strongest feature is interference from an atomic Ce transition.

Table 4.1 lists all CeF bands organized by $\lambda_{excitation}$ and upper state. For two fluorescence bands listed in Table 4.1, only the wavelength near the band origin is listed in Column 3. For these bands (those not investigated by WSFE) no rotational constants are known. Table 4.2 summarizes all assigned lines in the WSFE spectra.

Molecular constants derived from band-by-band fits to rotational term values[14] obtained from the high resolution fluorescence excitation spectra are listed in Table 4.3. The details of the Ω, v-assignments for all observed states of CeF are discussed in the following subsections. This discussion will be clarified by reference to figure 4.5 and Table 4.3, which together summarize the *final* energy level diagram derived from the present work and all previous studies of CeF.

[14]See Herzberg 1989 and Lefebvre-Brion 1984.

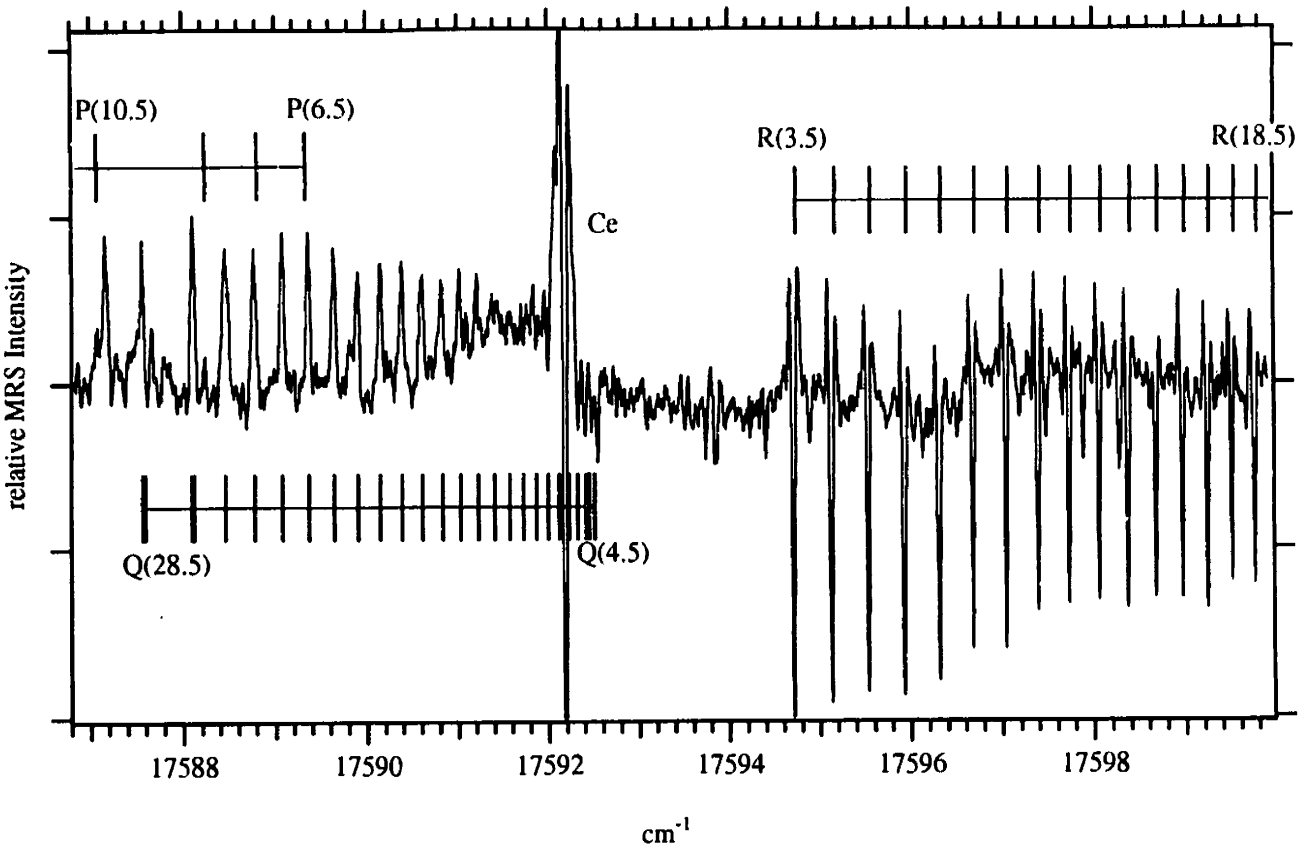

Figure 4.4: The magnetic rotation spectrum (MRS) for the low-J lines of the [17.6]4.5 ←X(1)3.5 (0,0) band. The axial magnetic field was 300G. Tie lines display the rotational assignments of Azuma 1991. Although the rotational temperature of the CeF source was ~2000 K, the lowest-J R-lines are easily observable. The phase reversal of the P and Q lines relative to the R-lines, typical of MRS (McCarthy 1992), facilitates rapid assignment. The strongest feature is interference from an atomic Ce transition.

Table 4.1: Compilation of all CeF Bands

System	Band	λ, Å	ν_0, cm^{-1}	See:
[17.6]4.5-*X*(1)3.5	0-0	5684.2	17592.689	Azuma 1991
	0-1	5865.4	17048.929	Table 4.2
[17.6]4.5-(1)4.5	0-0	5921.5	16887.54	Table 4.2
	0-1	6118	16344	
[17.6]4.5-(2)3.5(?)	0-0	6214	16093	

Table 4.2: Wavenumbers of Assigned CeF Lines (cm^{-1})

Band		5865.4 Å		5921.5 Å	
J''	R	Q	P	R	P
3.5	17 050.973				
4.5	51.397	17 048.805			
5.5	51.817	48.775			16 884.693
6.5	52.227	8.712	17 045.661	16 890.781	84.190
7.5	52.631	48.572	45.123	91.161	83.643
8.5	53.025	48.478	44.572	91.521	83.079
9.5	53.408	48.388	44.018	91.878	82.495
10.5	53.782	48.281	43.465	92.218	81.901
11.5	54.145	48.171	42.891	92.552	81.298
12.5	54.502	48.048	42.307	92.856	80.680
13.5	54.849	47.914	41.717	93.192	80.060
14.5	55.187	47.781	41.120	93.483	79.420
15.5	55.511	47.624	40.506	93.773	78.756
16.5	55.828	47.467	39.886	94.038	78.087
17.5	56.140	47.294	39.260	94.301	77.423
18.5	56.440	47.121	38.628	94.548	76.729
19.5	56.730	46.934	37.973	94.778	76.029
20.5	57.006	46.727	37.324	95.002	75.315
21.5	57.227	46.526	36.657	95.212	74.594
22.5	57.537	46.306	35.981	95.385	73.851
23.5	57.784	46.079	35.298	95.592	73.107
24.5	58.014	45.839	34.601	95.762	72.340
25.5	58.241	45.582	33.897	95.913	71.566
26.5	58.435	45.299	33.179	96.003	70.778
27.5	58.641		32.443		
28.5				96.423	
29.5				96.503	
30.5				96.580	
31.5				96.663	

4.3.1 *Excitation spectroscopy*

High-resolution fluorescence excitation spectra of the three bands[15] at 5684.2 Å, 5865.5 Å, and 5921.5 Å were recorded while selectively detecting fluorescence in the 5865.5 Å, 5684.2 Å, and 5684.2 Å bands, respectively. The perturbations in the upper state reported by Clements 1986 and Azuma 1991 and observed in the present study established a common upper state for these bands which are separated by 543.76 and 705.15 cm^{-1}. The assignment of the 5865.5 Å band as an $\Omega'=4.5$ - $\Omega''=3.5$ transition was established in both excitation and FM-MRS (and MRS) experiments from the observation of first lines. Because of the similarities in the relative branch intensities of the 5684.2 Å and 5865.5 Å bands, Ω', Ω'' assignments, and the 543.76 cm^{-1} separation, we assign here the lower states of these bands as $v''=0$ and $v''=1$ levels of the lowest energy $X^4H_{7/2}$ state of the $4f5d6s$ superconfiguration. The 5921.5 Å band is red degraded, with the $I_R \approx I_P > I_Q$ branch intensity ratios characteristic of a $\Delta\Omega=0$ transition. The first observed line in the P-branch was P(5.5). The intensities of lowest-J'' Q and R lines were weaker than the noise level. Unfortunately, the intensities of all lines of this band were too weak to be observed by the absorption based methods[16]. We assign here the 5921.5 Å band as an $\Omega'= 4.5$ - $\Omega''=4.5$ transition based on one unambiguous first line and branch intensity ratios

[15]Wavelength labels for transitions are the (extrapolated) vacuum wavelengths of the $J''=0$ to $J''=0$ transition. The name for the "5684.2Å band" is slightly different from the notation of Clements 1984, where the wavelength of the R-head at 5679.4Å was used to name the band.

[16]A $\Delta\Lambda\neq0$, $\Delta\Omega=0$ Hund's case (a) limit transition is expected to have weak transition intensity (Herzberg 1989; Lefebvre-Brion 1984).

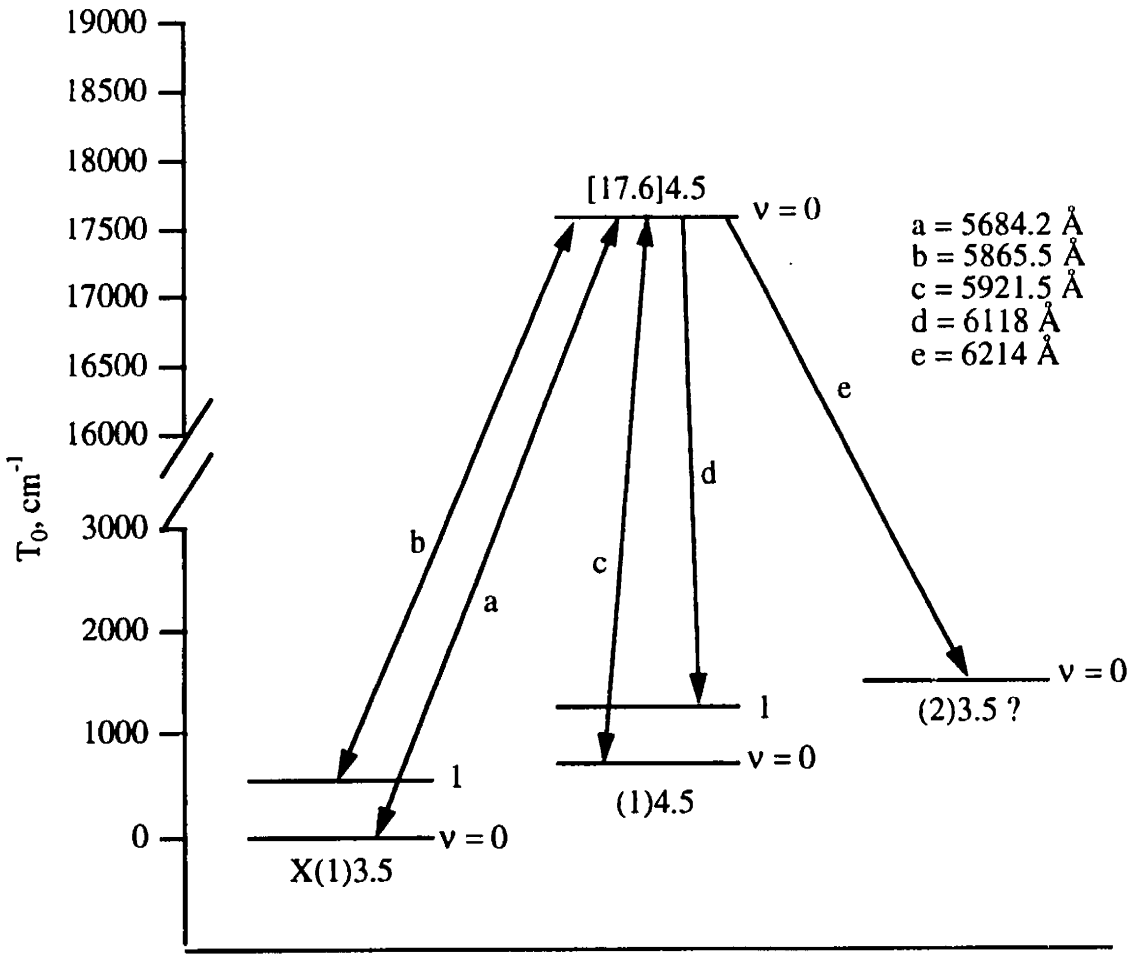

Figure 4.5: CeF energy level diagram including results from this work, Azuma 1991, and Clements 1984. The upper state parent configuration is, *4f5d6p*, while all lower states belong to *4f5d6s*.

Table 4.3: Molecular Constants of CeF (in cm-1)

Ω	v	T_v	B_v	$D_v \times 10^7$	$\alpha \times 10^3$
3.5	0	0	0.240322(17)[a]	1.811(27)[a]	1.2(1)
3.5	1	543.76(1)	0.2391(1)	1.8(1)	
4.5	0	705.15(1)	0.240489(9)	1.8(2)	
4.5	1	1250(20)			
3.5(?)	0	1500(20)			
4.5	0	17592.6894(15)[a]	0.234 64(11)[a]	2.79(55)[a]	

a. Azuma 1991

characteristic of a $\Delta\Omega = 0$ transition[17]. The energy of this state above the X4H7/2 electronic ground state (= 705.15 cm^{-1}) is in good agreement with LFT predictions of the energy of the first excited Ω =4.5 state (at T_0 = 765 cm^{-1}, see Bloch 1996) of the 4*f*5d6*s* superconfiguration.

4.3.2 *Dispersed Fluorescence Bands*

The 5865.5 Å, 5684.2 Å, and 5921.5 Å bands have been observed by dispersed fluorescence (DF) spectroscopy. The DF spectra in the 6000-7000 Å region were very congested. In spite of our use of a single mode cw dye laser, several upper states were simultaneously excited and this gave rise to congestion

[17]Such analysis has a strong historical precedence. The "non-appearance of an intense Q branch can accordingly be used to establish whether or not ΔΩ (and therefore ΔΛ) differs from zero" (Herzberg 1989, 244).

in the 6000-7000 Å region. Overlapping transitions could be separated by comparing the DF spectra recorded from a single upper level excited systematically from different lower levels. The fluorescence features which did not appear in all fluorescence spectra were discarded, thereby avoiding spurious energy linkages. By this technique, two weak bands at 6118 Å and 6214 Å were selected and examined. No Ω'' assignment could be established from the DF spectra. The energy of the lower state of the 6214 Å band (T_0=1500 cm^{-1}) is in good agreement with the LFT prediction for the energy of the (2)3.5 state of the $4f5d6s$ superconfiguration at 1706 cm^{-1} (see Appendix in Bloch 1996). The energy difference between the band origins of the 5921.5 Å and 6118 Å bands (~544 cm^{-1}) is in good agreement with the $\Delta G_{1/2}$ value characteristic of the $4f5d6s$ superconfiguration ($4f^{N-1}5d6s$ type).

4.4 *Summary of Observations*

Three low-lying T_0 < 2,000 cm^{-1} electronic states, $X^4H_{7/2}$[(1)3.5] at T_0 = 0 cm^{-1}, (1)4.5 at T_0 = 705.15 cm^{-1}, an unknown-Ω (probably Ω = 3.5) state at T_0=1500 cm^{-1}, and one excited electronic state [17.6]4.5 at T_0=17 592.69 cm^{-1} are characterized here. The (1)3.5 and [17.6]4.5 states were observed and analyzed by Clements 1984 and Azuma 1991. We propose here the configurational and vibrational assignments for all observed states. All observed electronic-vibration levels of CeF are summarized in figure 4.5.

The $\Delta G_{1/2}$ vibrational intervals of the $X^4H_{7/2}$ and (1)4.5 states are 543.76 and 544 cm^{-1}, respectively, which identify them as components of the $4f5d6s$ superconfiguration. The (1)3.5 and (1)4.5 states have the $\Delta G_{1/2}$ values and energy separation expected for the two lowest energy components of the $4f5d6s$ superconfiguration, thus the dominant (L_c, S_c, J_c, J_a) characters of these two states are:

$X^4H_{7/2} \equiv$(1)3.5 = (5,1,4,3.5) $\quad \Omega = J_a = 3.5,$

(1)4.5 = (5,1,4,4.5) $\quad \Omega = J_a = 4.5.$

The unknown-Ω T_0 = 1500 cm^{-1} state lies very close to the crude LFT prediction for the (2)3.5 state.

The 5684.2 Å band was the only previously reported band in the absorption spectrum of CeF over the entire visible wavelength region (Clements 1984). Since strong electric dipole electronic transitions involve promotion of a single electron, the upper state of the 5684.2 Å band must belong to a superconfiguration with the $4f5d$ core in the atomic $^3H_4$ state. Selection rules based on the atomic-core quantum numbers account for the sparseness of the absorption spectrum (in case of CeF, the reduction to only *one intense band* in the entire visible wavelength region is extraordinary) and provide clues to the complete superconfigurational assignments and to the validity of the weak LFT picture.

4.5 *Ligand Field Theory*

A Ligand Field (LF) model explained the electronic structure of the low-lying states of all *Ln*O molecules (Field 1982, Dulick 1982, Hocquet 1988) in terms of a zero-order $Ln^{2+}O^{2-}$ structure. Considering only the lowest energy (maximum S_c, maximum L_c) 4*f*-core Ln^+ atomic multiplet state and using no adjustable parameters, preliminary Ln^+F^- LF calculations were carried out for the low-lying states of the $f^N s$, $f^{N-1}s^2$, and $f^{N-1}ds$ superconfigurations of all *Ln*F molecules (Kaledin 1992).

LF Hamiltonians for the $4f5d6s$, $4f6s^2$, $4f^2(^3H)6s$, $4f5d^2(^3F)$, $4f^2(^3H)5d$, $4f5d6p$, $4f6s6p$, and $4f^2(^3H)6p$ superconfigurations of Ce^+F^- were constructed using the $F_k(nl,n'l')$, $G_k(nl,n'l')$, and ζ_{nl} parameters as derived from multiconfigurational fits to Ce^+ data (Goldschmidt 1978). The $B_0^k(nl,nl)$ parameters were computed using Herman- Skillman wavefunctions[18] (Herman 1963) for 4*f* core electrons or taken to be equal to those derived from the spectrum of the LaF molecule (Kaledin 1994c). Center of gravity values for the above mentioned Ce^+ parent configurations were calculated using $F_k(nl,n'l')$, $G_k(nl,n'l')$, and ζ_{nl} parameters as derived from multiconfigurational fits to Ce^+ data. All parameters which have been used in the calculations are listed in Table 4.4 and a summary of the calculations is listed in Table 4.5.

The LF model is also capable of predicting the relative energies of the lowest energy component of each of the three low-lying *Ln*F superconfigurations.

[18]Simple FORTRAN programs that accomplish this are listed in appendix C.

These interconfigurational energy differences are primarily determined by the free Ln^+ atomic-ion configurational energies shifted by the LF monopole terms: $B_0^0(4f,4f) > B_0^0(5d,5d) > B_0^0(6s,6s) > B_0^0(6p,6p) > 0$. These computed $B_0^0(nl,nl)$ parameters are very sensitive to the choice of radial wavefunction and internuclear distance, r_e (Dolg 1989, 1992). A sufficient number of low-lying states of other *Ln*F molecules are known that reliable empirical estimates of $\Delta B_0^0(4f^N6s,4f^{N-1}6s^2) = B_0^0(4f^N6s,4f^N6s) - B_0^0(4f^{N-1}6s^2,4f^{N-1}6s^2)$ may be made (Kaledin 1994a). It has been shown, from the behavior of the ionization potentials for the GdF through YbF molecules (Gotkis 1991), that the $\Delta B_0^0(4f^N6s,4f^{N-1}6s^2)$ value is independent of the number of *f*-electrons in the *f*-core. For CeF calculations, we used $\Delta B_0^0(4f^N6s,4f^{N-1}6s^2)$ = 14200 cm^{-1} as derived from the analysis of the optical spectra of DyF (McCarthy 1996).

The results of the LFT calculations are compared to the observed levels in Table 4.5. Table 4.6 lists the ΔB_0^0 parameters used in the LFT model to calculate the center of gravity values for all superconfigurations of CeF which have electronic states at $T_0 \leq$ 30,000 cm^{-1}. The complete results of the intraconfigurational LF calculations[19] are collected in the appendix of Bloch 1996.

[19]It should be noted that although these predictions in Bloch 1996 are be reliable for electronic partition function calculations, they are likely to become increasingly poor as the energy increases.

Table 4.4: Parameters (cm^{-1}) which have been used in the CeF LFT Calculation

Para-meters	Superconfigurations $4f5d6s$	$4f6s^2$	$4f5d^2(^3F)$	$4f^2(^3H)6s$	$4f^2(^3H)5d$	$4f5d6p$	$4f6s6p$	$4f^2(^3H)6p$
$F_2(fd)$	169		154			148.9	177	
$F_4(fd)$	20.7		18.6			17	21.4	
$G_1(fd)$	278		257			274.9	284	
$G_3(fd)$	32.5		29.3			29	33.5	
$G_5(fd)$	4.48		3.54			3.5	4.5	
$F_2(fp)$						68	68	64
$G_2(fp)$						7	7	12
$G_4(fp)$						5	5	6
$G_3(fs)$	220			190			298	
$F_2(dp)$						306		
$G_1(dp)$						383		
$G_3(dp)$						7		
$G_2(ds)$	1854							
$G_1(sp)$							5865	
ζ_f	630	630	630	526	526	650	650	529
ζ_d	600				399	688		
ζ_p						1486	1853	1234
$B^2_0(4f,4f)$	1678[a]	1678[a]	1678[a]	4663[b]	4594[b]	1678[a]	1678[a]	4806[b]
$B^4_0(4f,4f)$	771[a]	771[a]	771[a]	972[b]	995[b]	771[a]	771[a]	1006[b]
$B^6_0(4f,4f)$	64[a]	64[a]	64[a]	379[b]	409[b]	64[a]	64[a]	391[b]
$B^2_0(5d,5d)$[c]	7600		7600		7600	7600		
$B^4_0(5d,5d)$[c]	2660		2660		2660	2660		
$B^2_0(6p,6p)$[d]						3400	3400	3400

a. One half of fitted values for CeO (Kaledin 1995); *b*. Parameters were computed using Herman-Skillman wavefunctions (1963); *c*. Parameters are taken as those for the $5d6s$ configuration of LaF (Kaledin 1994c); *d*. Parameter is taken as one half of fitted values for *Ln*O (Kaledin 1994b).

The observed $\Delta G_{1/2}$ values and the pattern of Ω-values in the (1)3.5, (1)4,5, and tentatively assigned (2)3.5 low-lying states confirm LF predictions of intra- and inter- configurational energy level patterns. We have demonstrated here that the LF model that successfully accounts for all properties of all low-lying states of all *Ln*O molecules can be extended with equal success to the *Ln*F molecules.

Table 4.5: Comparison of CeF LFT Level Predictions (v=0) to Experimentally Observed CeF Levels (in cm^{-1})

Configuration	State	Predicted	Observed
$4f5d(^3H)6s$	$X(1)^4H_{3.5}$	0	0
	(1)4.5	765	705.15
	(2)3.5	1706	1500

Table 4.6:Low Lying States of *Ln*F (cm^{-1})

	Ln+		*Ln*F				
Ln+	Configur-ation	Center of gravity	Center of gravity	Destabilization energies $nl,n'l'$	ΔB	Ω	T()
Ba^+	$6s$	0[a]	0[b]			$X^2\Sigma^+$	0
	$5d$	5354[a]	11 956	$5d,6s$	6600	$A'^2\Delta_{3/2}$	10718
La^+	$6s^2$	7394[c]	0[d]			$X^1\Sigma^+$	0
	$5d6s$	4594[c]	4 795	$5d,6s$	7600[d]	$a^3\Delta_1$	1432
Ce^+	$4f5d6s$	7773	7586			$X^4H_{7/2}$	0
	$4f6s^2$	11039	3252	$5d,6s$	7600[e]	$^2\Phi_{5/2}$	1544
	$4f5d^2(^3F)$	5 560	12973	$5d,6s$	7600[e]	$^4I_{9/2}$	6087
	$4f^4(^3H)6s$	5622	12035	$4f,6s$	14200[f]	$^4H_{7/2}$	8743
	$4f^2(^3H)5d$	12654	26667	$5d,6s$	7600[e]	$^4K_{11/2}$	17575
	$4f5d6p$	32827	27610	$6p,6s$	-5030[g]	$^4I_{9/2}$	17600
	$4f6s6p$	38450	25633	$5d,6s$	7600[e]	$^4\Gamma_{5/2}$	18808
	$4f^2(^3H)6p$	28989	30402	$6p,6s$	-5000	$^4I_{9/2}$	25312
Dy^+	$4f^9(^6H)6s^2$	17450	6160			$X^6H_{15/2}$	0[h]
	$4f^{10}(^4I)6s$	5740	8600	$4f,6s$	14200[h]	$^6I_{17/2}$	2431[h]

a.Calculated using Moore 1971; *b*.Calculated using Effantin 1990; *c*.Calculated using Goldschmidt 1980; *d*.See Kaledin 1993; *e*.Taken to be equal to the $\Delta B^o_\alpha(nl,n'l')$ value of LaF (*29*); *f*. Taken to be equal to the $\Delta B^o_\alpha(nl,n'l')$ value of DyF (McCarthy 1996); *g*.Present work; *h*.See McCarthy 1996.

4.6 *References*

1991 Azuma,Y., W. J. Childs, K. L. and Menningen, K. L.,*Mol. Spec.*, **145**, 413.

1975 Barrow, R. F. and A. H. Chojnicki, *J. Chem. Soc. Faraday Trans. 2*, **71**, 728.

1996 Bloch, J. C., L.A. Kaledin, and R.W. Field, R. W., *J. Mol. Spec.*, **000**, 000.

1964 Burns, G., *J. Chem. Phys.*, **41**, 1521.

1984 Clements, R. M. and R. F. Barrow , *J. Mol. Spec.*, **107**, 119.

1989 Dolg, M. and H. Stoll, *Theor. Chim. Acta.*, **75**, 369.

1992 Dolg, M., H. Stoll, H. J. Flad, and H. Preuss, *J. Chem. Phys.*, **97**, 1162.

1982 Dulick, M., Ph.D. thesis, MIT, (1982).

1985 Dulick, M., and R. W. Field, *J. Mol. Spect.*, **113**, 105.

1986 Dulick, M., E. Murad, and R. F. Barrow, R. F, *J. Chem. Phys.*, **85**, 385.

1976 Effantin, C., G. Wannous, J. d'Incan, and C. Athenour, *Canad. J. Phys.*. **54**, 279.

1990 Effantin, C., A. Bernard, J. d'Incan, G. Wannous, J. Verges, and R. F. Barrow, R.F., *Mol. Phys.*, **70**, 735.

1982 Field, R.W., *Ber. Bunsenges. Phys. Chem.*, **86**, 771.

1978 Goldschmidt, Z. B., "Atomic Properties (Free Atom)", in *Handbook on the Chemistry of Rare Earths*, **1**,Gschneidner, K. A. Jr. and Eyring, L., eds.(North Holland).

1991 Gotkis, I. S., *J. Phys. Chem.*, **95**, 6086.

1989 Gurvich, L. V., Yu N. Dmitriev, L. A. Kaledin, A. I. Kobyliansky, A. A. N. Kulikov, and E. A. Shenyavskaya, *Bul. Acad. Sci. USSR* (Phys.Ser.), **53**, 75.

1963 Herman, F. and S. Skillman, *Atomic Structure Calculations*, Prentice-Hall, Englewood Cliffs, NJ.

1988 Hocquet, A., Ph.D. thesis, Université des Sciences et Techniques de Lille; P. Carette and A. Hocquet, *J. Mol. Spect.*, **131**, 301.

1972 d'Incan, J., C. Effantin, and R. Bacis, *J. Phys. B.*, **5**, L189.

1992 Kaledin, L. A., C. Linton, T. E. Clarke, and R. W. Field, , *J. Mol. Spect.*, **154**, 427.

1993 Kaledin, L. A., J E. McCord, and M. C. Heaven, *J. Mol. Spect.*, **158**, 40.

1994a Kaledin, L. A., J. C. Bloch, M. C. McCarthy, L. V. Gurvich, and R. W. Field, *Mol. Phys.*, **83**, 881.

1994b Kaledin, L. A., M. G. Erickson, and M. C. Heaven, *J. Mol. Spect.*, **165**, 323.

1994c Kaledin, L. A., J. E. McCord, J. E., and M. C. Heaven, *J. Opt. Soc.*

Am. B., **11**, 219.

1995 Kaledin, L. A., J. E. McCord, and M. C. Heaven, *J. Mol. Spec.*, **170**, 166.

1996 Kaledin, L. A., J. C. Bloch, M. C. McCarthy, E. A. Shenyavskaya,and R. W. Field, *J. Mol. Spect.*, **000**, 000.

1984 Kulikov, A. N., L. A. Kaledin, A. I. Kobyliansky, A. I., and L. V. Gurvich, *Can. J. Phys.*, **62**, 1855.

1977 Lee, H. U. and R. N. Zare, *J. Mol. Spect.*, **64**, 233.

1987 Linton, C., G. Bujin, R. S. Rana, and J. A. Gray, *J. Mol. Spect.*, **126**, 370.

1988 Linton, C. and Y. C. Liu, *J. Mol. Spect.*, **131**, 367.

1983 Linton, C., M. Dulick, R. W. Field, P. Carette, P. C. Leyland, and R. F. Barrow, R. F., *J. Mol. Spect.*, **102**, 441.

1978 Lumley, D. J. W., and. R. F. Barrow, *J. Mol. Spect.*, **69**, 494.

1978 Martin, W. C., R. Zalubas, and L. Hagan, "Atomic Energy Levels - The Rare Earth Elements", NSRDS-NBS-60.

1992 McCarthy, M. C., and R. W. Field, *J. Chem. Phys.* 96, 7237.

1996 McCarthy, M. C., J. C. Bloch, R. W. Field, R. W., and L. A. Kaledin, *J. Mol. Spect.*, **000**, 000.

1990 McDonald, S. A., S. F. Rice, R. W. Field, R. W. and C. Linton, *J. Chem. Phys.*, **93**, 7676.

1981 McLean, A. D., and R. S. McLean, *At. Data Nucl. Data Tables*, **26**, 197.

1971 Moore, C. E., *"Atomic Energy Levels as Derived from the Analysis of the Optical Spectra"*, NSRDS-NBS 35, v.3.

1974 Robbins,D. J. W. and R. F. Barrow, *J. Phys. B.*, 12, L234.

1985 Schall, H., Ph.D. thesis, MIT.

1986 Schall, H., J. A. Gray, M. Dulick, and R. W. Field, *J. Chem. Phys.*, **85**, 751.

1987 Schall, H., M. Dulick, and R. W. Field, *J. Chem. Phys.*, **87**, 2898.

1980 Wyart, J. F., and C. Bauche-Arnoult, *Physica Scripta*, **22**, 583.

5.1 *Introduction*

This chapter describes a new method of generating high power, near-transform-limited nanosecond pulses of phase-modulated laser radiation and the application of this light in FM spectroscopy[1] in the visible and ultraviolet spectral regions. In this chapter, the phase-modulated pulsed radiation will be called pulsed-FM, and the FM spectroscopy performed with it, pulsed-FMS.

In the new scheme, pulsed-FM laser radiation is generated by optical amplification of a *cw* phase-modulated laser field. The amplification occurs for short time periods, typically 5-20 nanoseconds, in one or more capillary-type dye cells[2], and produces a relatively high intensity *pulse* of phase-modulated radiation. The original characteristics of the *cw* phase-modulated radiation that made FM spectroscopy possible, the unique phase and amplitude balance of the sidebands, are preserved in the amplification process. This allows pulsed-FM radiation to be used instead of ordinary *cw*-FM light in performing FM spectroscopy; hence, pulsed-FM spectroscopy.

[1]The reader should understand the fundamentals of *cw*-FMS as presented in chapter 2.

[2]Also known as Bethune Cells; see Bethune 1981.

Pulsed-FM spectroscopy possesses advantages over ordinary *cw*-FM spectroscopy. These advantages stem from the much higher peak power levels of pulsed-FM radiation (Tran 1984). Both *cw* (1 fJ in 10 ns) and pulsed-FM (1 mJ in 10 ns) spectroscopies provide a means to measure the absorption and dispersion of a sample with very high sensitivity in the visible and near-IR. But, through non-linear conversion (harmonic, sum or difference frequency generation) made efficient by the higher peak powers, pulsed-FM also provides access to the ultraviolet and IR spectral regions, where suitable *cw* sources are practically unavailable.

In shot-noise limited FM-based experiments (including FM-MRS discussed in chapter 3), in FM studies of samples with very high optical density (which fully extinguish a weak *cw* laser beam), in FM-remote sensing applications[3], and in FM intra-cavity measurements (Ma 1995), detection sensitivity improves with increased optical power. In such cases, the high peak power of pulsed-FM provides a superior signal to background ratio than *cw*-FM spectroscopy.

5.1.1 *Previous work*

Prior to this work, a fundamentally different scheme of producing pulsed frequency modulated radiation had been thoroughly investigated. In 1981,

[3]Personal Communication with Clint Carlilse, Stanford Research International.

Gallagher and coworkers directly phase-modulated the output of an etalon-narrowed pulsed laser to produce pulsed-FM radiation. The modulation frequencies employed were 1-2 GHz. They obtained a useful detection sensitivity of 2% absorption by averaging the pulsed-FM signal from 10 laser-pulses. Subsequently, Tran *et al* (1983), using higher modulation frequencies (4 GHz), observed a sodium atom transition at 3302 Å using frequency-doubled pulsed-FM radiation. Nonetheless, their UV-FM signals were quite noisy, limiting applicability to strong absorptions of about 5% or more.

Finally, in 1984 Tran *et al* obtained useful pulsed-FMS sensitivity levels (0.1% absorption, 10 pulsed-average, signal to noise ratio of unity). They found it was necessary both to increase the modulation frequency (to 12 GHz) and to narrow the laser line width as much as practically possible. Through a careful analysis of the sensitivity and useful features of their method, Tran and coworkers concluded: (1) that the practical pulsed-FM detection sensitivity was determined primarily by the ratio of the modulation frequency to laser linewidth and (2), that when a high modulation frequency was employed to obtain a large ratio, the method was best suited for observation of very broad spectral features.

5.1.2 *Primary obstacle for high sensitivity pulsed-FMS*

A high ratio of modulation frequency to laser linewidth is needed so that the

spectral wings of the sidebands will not overlap-- and therefore interfere with-- the carrier. Such interference, if it occurs, would make the *perfect* phase and amplitude balance needed for high sensitivity FMS impossible. Hence, limiting this interference is the key to obtaining high detection sensitivity for pulsed-FMS.

The largest ratio of modulation frequency to laser linewidth Tran 1984 achieved approached only 12. The ratio was primarily limited by the large linewidth of the noisy, multi-mode, pulsed laser, 1 GHz. Contrast that to *cw*-laser FM spectroscopy, where the <1 MHz narrow linewidth of the *cw*-laser and <1 GHz modulation frequencies provide a considerably higher ratio so that interference between the sidebands and carrier is eliminated. It should be clear that the relationship between the ratio of the modulation frequency to laser linewidth and the resulting interference is not linear. When the ratio is large enough that the interference is zero (or below the shot-noise limit) any further increase of the ratio *will not* further decrease the interference.

In theory, the earlier pulsed-FM scheme could be improved by further increasing the modulation frequency and further narrowing of the laser bandwidth. In practice, though, both of these quality factors have reached their practical limits. Using a larger modulation frequency (>15 GHz) is a disadvantage when the optical spectrum is complex and the features are narrow

(<3 GHz), and requires the design and construction of a narrow RF bandwidth modulator. Likewise, optical filtering of the the laser pulse in an external Fabry-Pérot resonator would undesirably reduce the intensity of the pulse and usually would not produce *transform limited pulses* (Fee 1992). This in turn would reduce the efficiency of any subsequent non-linear conversion and, in turn, the shot-noise-limited sensitivity. Transform limited pulses, classified as such because they possess the minimum possible duration bandwidth product, $\Delta\upsilon\ \Delta t$, allowed by the uncertainty principle (Seigman 1986, 335), are certainly desirable. If the primary obstacle to achieving high sensitivity pulsed-FMS, carrier/sideband interference, is to be overcome, some new method that does not require large modulation frequencies or optical filtering is needed.

5.1.3 *High sensitivity pulsed-FMS*

The new method described here produces transform-limited pulsed-FM radiation by a fundamentally different process than the method originally presented by Gallagher *et al* in 1981. In the new scheme, high detection sensitivity can be achieved using a modulation frequency of less than 1 GHz because the spectral linewidth of *each* component of the *pulsed-amplified cw-FM laser* is less than 100 MHz (Eyler 1996). The modulation frequency to

linewidth ratio is typically more than 20, implying that the interference of the sidebands with the carrier, which had severely limited the detection sensitivity of the earlier schemes (Gallagher 1981), is now minimized[4]. The combination of low modulation frequency and transform-limited laser linewidth also facilitates high-resolution studies of complicated optical spectra. However, the new scheme is not without its own limitations. Noise can be generated in the amplification process that would limit sensitivity.

The origen of additional noise in a *single* optical amplifier is amplified spontaneous emission or ASE (Shimada 1994, 56). The ASE interferes with the pulsed-FM field, creating ASE-stimulated beat noise[5]. When multiple amplification cells are used, optical feedback (of both the ASE and pulsed-FM radiation) between stages introduces more noise. Interestingly, amplifier saturation, a method which suppresses the larger of these noise sources, optical feedback, also reduces any background sideband imbalance that may have been present on the *cw*-FM laser. These issues will be discussed in later sections of this chapter. In short, by using the new method, pulsed-FMS detection sensitivity of better than 0.1% absorption *in a single laser pulse* has already been demonstrated both in the visible and ultraviolet spectral regions using a laser with

[4]It is difficult to exactly quantify these quantities for arbitrary non-Gaussian (real) pulses.

[5]In an ideal quantum limited amplifier, the ASE-beat noise reduces the detection sensitivity of pulsed-FMS by at least a factor of two (Yariv 1991, 449).

some residual carrier/sideband interference. Current efforts using a new laser with essentially no carrier/sideband interference, promise substantially increased detection sensitivity.

5.2 *Generation of pulsed-FM radiation*

Pulsed-FM laser radiation is produced by pulsed-dye laser amplification of a phase-modulated *cw*-laser field. A simplified diagram of the experiment is shown in figure 5.1. The *cw*-input field *drives* the amplifier, while the output of a suitable *pulsed* laser *pumps* the cell. The amplifier is a capillary-type dye cell. As shown in figure 5.2, the design of the capillary-type dye cell provides optical pumping from all sides and therefore spatially uniform gain. In practice the capillary-type dye cell has been shown to be relatively insensitive to optical mis-alignment (Gangopadhyay 1994). The most crucial feature of the amplifier is not its ease of use, but rather, its ability to provide amplification without causing spectral broadening of the output field beyond its transform limit[6]. Other transverse non-capillary-type and longitudinal amplification cells do not provide spatially uniform or stable gain and therefore usually spectrally broaden

[6]For a Gaussian pulse with a full width at half maximum of $\Gamma = 10 \times 10^{-9}$ sec, the Fourier power spectrum is a Gaussian with a width of $\frac{\sqrt{2}\pi}{\Gamma} = 44\ MHz$. For an amplifier pumped by this pulse, a spectral width of the output pulse greater than *44 MHz* would indicate non transform limited-behavior.

since they determine the practical detection sensitivity limit of pulsed-FM. The presence of all three of these single amplification stage noise sources was demonstrated by careful recording of pulses using a fast-digitizing oscilloscope (Tektronics DSA 602 with 1 GHz bandwidth) and processing the recorded waveforms in the frequency domain. An example of recorded pulses and their Fourier spectra is shown in Figure 5.4.

5.3.1.1 *Background noise sources in one cell*

In figure 5.4a and b, the high frequency tail of the laser pulse envelope overlaps and interferes with the FM beat signal on-resonance. This indicates the presence of carrier/sideband spectral overlap even off-resonance. This carrier-sideband interference is the *largest* source of noise in these excimer pumped experiments.

Even though the full width of the frequency spectrum is 85 MHz or less, its tail, visible in the figure, extends to 1 GHz and beyond. Therefore, even a large increase in the modulation frequency would not significantly reduce the overlap of the sidebands with this high frequency noise. This noise comes from fluctuating fast substructure in the pulsed-FM laser pulse shape. The pulsed-FM laser pulse shape is determined by the excimer pump laser (which appears quite similar to the off-resonance pulse in figure 5.4) that provides the gain. The

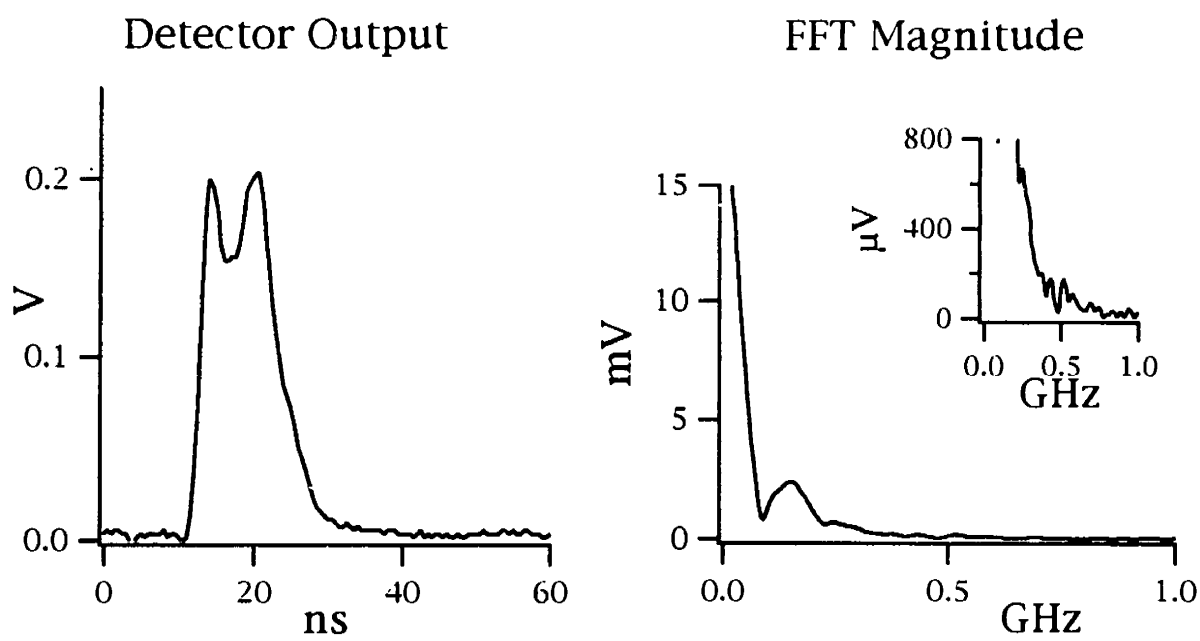

Figure 5.4a: Detector output and Fourier spectrum for excimer pumped pulsed-FMS off-resonance. The output of the fast detector was recorded on a fast digitizing oscilloscope (1 GHz Nyquist limit) and the Fourier spectrum was calculated (on the entire data set) on a personal computer. Since the pulsed-FM laser is not tuned into resonance, this figure shows the pulsed-FMS background. There is a substantial high frequency tail from fast substructure of the pulse. This high frequency tail limits the detection sensitivity of excimer laser pumped pulsed-FMS. In figure 5.4b, the pulsed-FM laser is tuned into resonance.

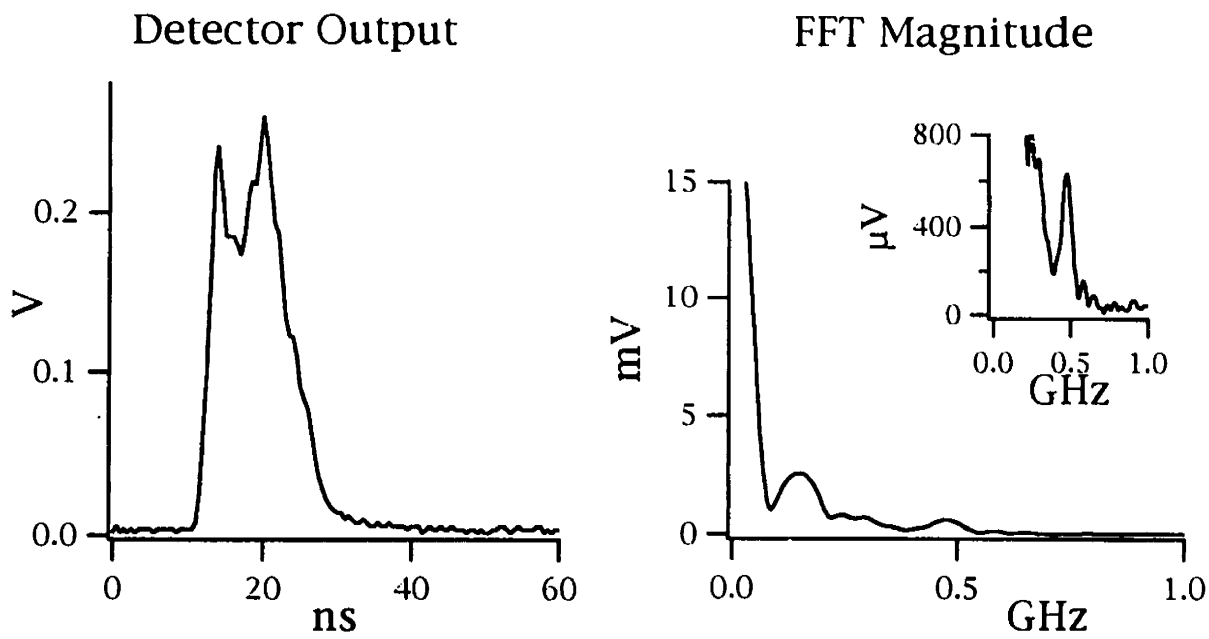

Figure 5.4b: Detector output and Fourier spectrum for excimer pumped pulsed-FMS on-resonance. The output of the fast detector was recorded on a fast digitizing oscilloscope (1 GHz Nyquist limit) and the Fourier spectrum was calculated (on the entire data set) on a personal computer. Since the pulsed-FM laser is tuned into resonance, this figure shows a beat note at the modulation frequency. There is a substantial high frequency tail from fast substructure of the pulse that interferes with the beat note.

excimer pulse has fast temporal noise, a sharp rise time, and a non-Gaussian, double-peaked structure. The high frequency tail would be reduced by using a smoother pump pulse with less substructure, such as the frequency doubled output of an injection seeded Nd:YAG laser.

Accidental etalons also contribute to the noise level for these one cell experiments, but, overall (at sensitivity levels of 8×10^{-4}), their effect is considerably smaller than that from the carrier/sideband interference. Once the interference problem is overcome, etalon effects would then become the limiting off-resonance noise source, since no ASE-stimulated beat noise was detected.

ASE-beat noise certainly does contribute to the total-noise on and off-resonance, but it is smaller than the etalon effect[13]. Specific, random-phased frequency components of the spectrally broad ASE always beat with the components of the pulsed-FM field (Yariv 1991, 449). The problematic ASE components have frequencies equal to the sideband frequencies plus the modulation frequency. The further influence of ASE will be discussed in later sections of this chapter.

Methods that deal effectively with the etalon problem were discussed in

[13]The ASE also beats with itself, and the ASE has shot-noise. Partial internal reflections (from the input and output windows) within the amplifier cell can cause an ASE (or signal) resonance effect (similar to the effect found in semiconductor laser amplifiers; Shimada 1994). Here, the frequencies of these resonance effects are much higher than the overall laser bandwidth (or modulation frequency) because the amplifier cell is short compared to the pulse lengths.

chapter 2. FM-MRS, a shot-noise limited double null scheme that was presented in chapter 3, optically suppresses the background signal from an accidental etalon. The combination of pulsed-FM and FM-MRS (to make pulsed-FM-MRS) would be a particularly attractive technique because the use of crossed polarizers significantly reduces the detected laser intensity off-resonance. This would eliminate the reduction of the shot-noise limited signal to noise ratio that occurs when ordinary attenuation is used to avoid damaging the photodetector.

5.3.1.2 *On-resonance noise sources in one cell*

Although the on-resonance noise sources do not significantly affect the overall detection sensitivity, when they are large, they are nonetheless problematic, causing large fluctuations of the FMS signal. In chapter 2, it was shown that the on-resonance signal to noise ratio for *cw*-FM spectroscopy is the same as carrier to noise ratio of the original laser[14]. The same is true for pulsed-FMS. But because the pulsed laser's intensity fluctuations are so large, the effect seems worse: the pulsed-FM signal appears to fluctuate 30% or more on-resonance, making optimization of experimental parameters, which is done on-resonance, difficult.

[14]In other words, if the original *cw*-laser had 10% peak-to peak intensity fluctuations, the *cw*-FM signal on-resonance would also have 10% fluctuations.

This problem can be overcome at least partially by normalization techniques. For pulsed-FMS, the FM signal can be normalized by (divided by) the DC (or lowest frequency) component of the original pulse. This is a particularly elegant normalization method for pulsed-FMS, because both the signal and the reference are obtained from the same pulse.

For pulsed-FM, on-resonance, the most significant noise source was pulse-to pulse-intensity fluctuations. Normalization or perhaps amplifier saturation (Seigman 1986, 305) would reduce the effect of the pulse-to pulse-intensity fluctuations. Small and apparently random phase-shifts of the pulsed-FM beat-note were the next largest significant source.

The phase-shifts were discovered by carefully recording a large number of on-resonance pulses along with a portion of the local-oscillator and comparing the phase of the beat to the phase of the local oscillator *while the cw-laser frequency was held fixed.* To eliminate the possibility of timing errors between channels, a fast switch (MCL ZYSWA-50-DR) was used to allow both the pulse and reference signals to be recorded on the same oscilloscope trace[15]. A typical trace is shown in figure 5.5. The usual phase-sensitive mixer arrangement for recording FM signals is not, however, suitable for detecting phase-noise. This is

[15]By recording the entire beat-note waveform in this way, phase errors can be discerned from amplitude fluctuations.

because the mixer converts phase-noise (a random *difference* in the phase of the beat-note and RF signals at the mixer) into amplitude-noise at its output. Using an ordinary mixer, this phase-noise induced amplitude-noise cannot be separated from the amplitude-noise caused by pulse-to-pulse intensity fluctuations. Furthermore, the large intensity fluctuations in these one-cell experiments swamp the the effects of the phase-jumps problem.

The phase-shift problem arises from a number of possible sources, the smallest of which include phase jumps of the original *cw*-laser and of the reference RF drive (which travels a different path-length than the optical pulse). Likely, the largest source is the gain of the dye amplifier which fluctuates from pulsed-to pulse. This gain fluctuation causes the overall phase-shift of the amplifier to differ from pulsed-to pulse[16]. If present, the contribution from an unstable RF drive could be removed by using a phase-locked RF source or by ensuring that the total propagation times of the two signals into the mixer are identical. The contribution from gain fluctuation could be lessened by using a more stable pump laser and by tuning the frequency of the cw-laser to a point of the dye curve where the dye's real polarizability is zero. Not much can be done about the *cw*-laser's random phase jumps (Yariv 1991, 386). Since the phase problem at this point was considerably smaller than the intensity

[16]A similar gain dependant phase-shift effect in semiconductor laser amplifiers has been exploited to make a usable phase-modulator device (like an EOM). See Mellis 1989ab.

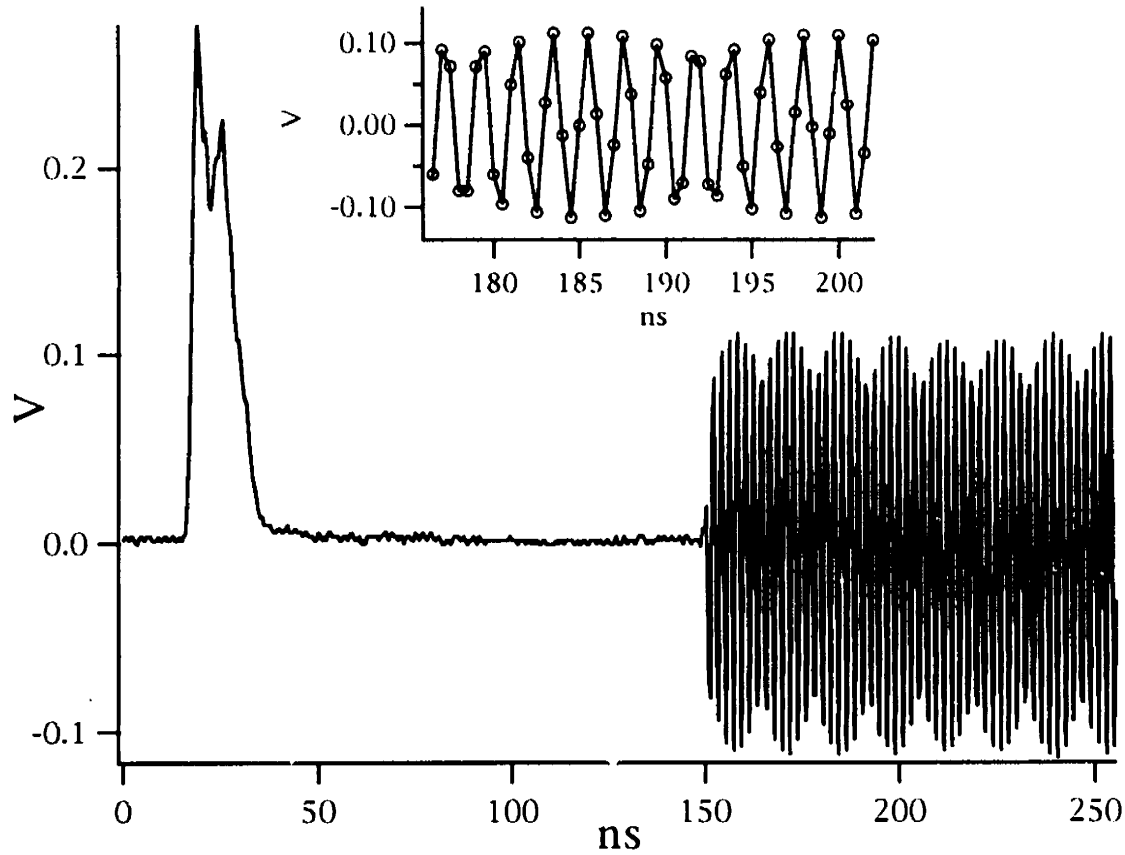

Figure 5.5: Fast digitizing oscilloscope trace showing the detected laser pulse and a portion of the local oscillator as a frequency reference. The two signals were recorded on one channel by using a fast switch. The inset is an expanded plot of the local oscillator, where the circles indicate sampling points. The low frequency modulation arises from a beat between the sampling frequency (1 GHz) and the modulation frequency (480 MHz). Since many cycles of the reference frequency are recorded, its phase can be accurately determined.

fluctuations[17], none of these fixes need be employed, if the standard mixer signal recovery scheme is used.

5.4 *Tests of pulsed-FMS in the UV region*

As a more substantial test of the new pulsed-FM scheme, the pulsed-FMS spectrum of NO at 214.5 nm was recorded. The 214.5 nm pulsed-FM radiation was obtained by non-linear conversion of intense 644 nm pulsed-FM radiation. A simplified experimental diagram is presented in figure 5.6

A three cell amplifier chain driven by 100 mW of phase-modulated *cw*-laser radiation was used to produce 644 nm pulsed-FM radiation with 2 mJ of energy per pulse. The 532 nm output of an injection seeded Nd:YAG laser pumped each of the three capillary cells. Respectively, 10, 12, and 21 mJ was used to pump the three cells, the bore diameters of which were 1, 1, and 2 mm. The rise-time of the pump pulse was somewhat shorter than the fall-time. However, the pump pulse was smooth, with no observable fast substructure, and had a full-width at half maximum of approximately 7 ns. The modulation frequency was set at 720 MHz. The modulator for these experiments was a custom designed product from Con-Optics (model 360-40P).

[17]When the amplitude fluctuations of the laser are kept negligibly small by gain saturation, the main contribution to laser noise is due to fluctuations of the phase (Yariv 1991, 381).

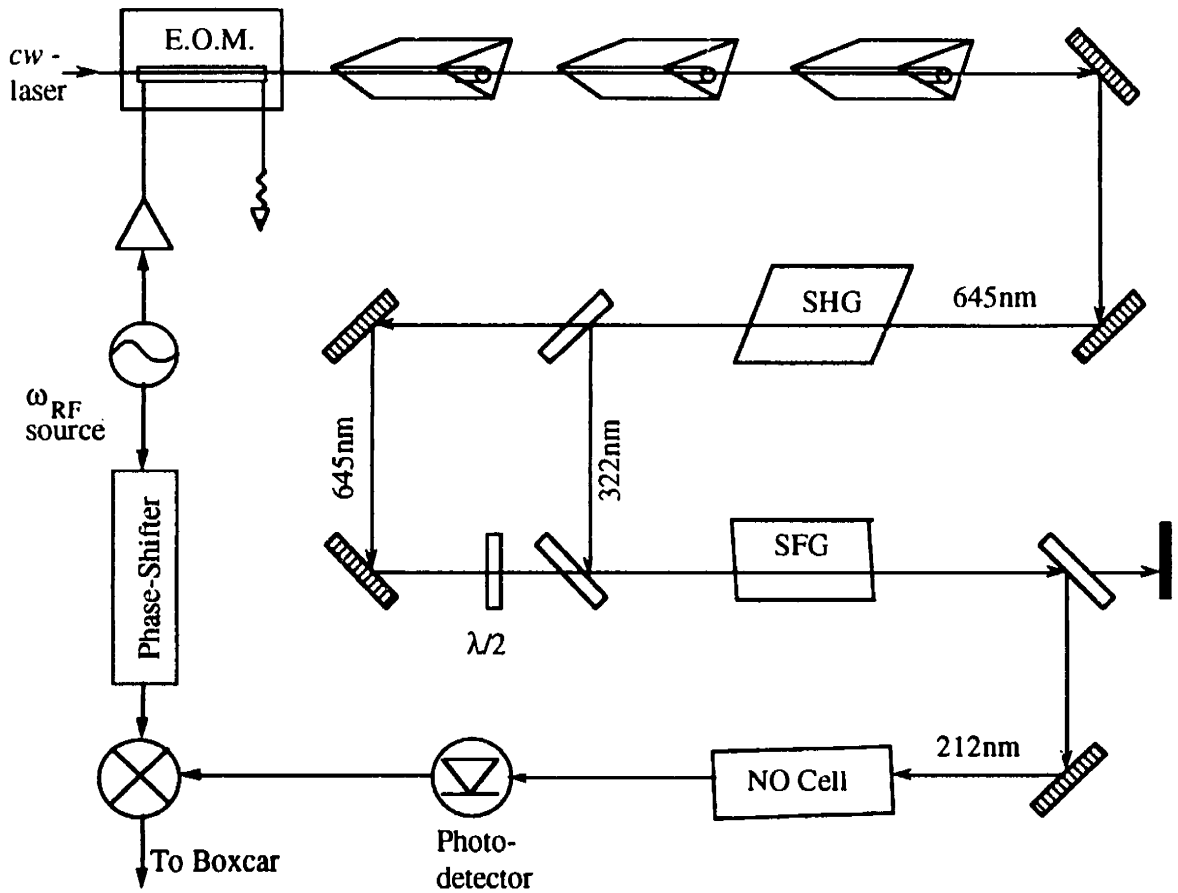

Figure 5.6: Simplified diagram of the UV-pulsed-FMS experiment. The pump beam and many optics have been omitted for clarity. A description of the experiment is given in the text. SHG = Second Harmonic Generator. SFG = Sum Frequency Generator.

The 644 nm pulsed-FM laser was frequency tripled by generating the second harmonic in a KDP crystal, then mixing the second harmonic with the fundamental in a BBO crystal. The beams were collimated and the crystals were carefully phase-matched to minimize phase distortions in the non-linear mixing (Gangopadhyay 1994a,b). To avoid etalons, the crystals used were cut so that the incidence and exit angles were far from normal. The resulting far-UV pulse energy was typically 50 mJ and 4-5 ns in duration.

The UV-pulsed-FM beam was passed through a fused silica cell about 3 cm long, filled with about 1 Torr of a gas mix containing 8% NO in argon. To avoid damaging the detector the UV-pulsed-FM beam was attenuated by 10^3.

The output of the photodetector was processed in an arrangement similar to that previously described for the visible pulsed-FM work on iodine. The UV-pulsed-FM signal is detected at the original modulation frequency because the sideband spacing does not change during the harmonic generation (Tran 1993).

Figure 5.7 shows the pulsed-FMS spectrum of NO, obtained by averaging three scans recorded in a total acquisition time of 162 seconds. Generally, slow scan, because it provides partial statistical cancellation of laser amplitude drifts and other low frequency noise sources. Although the NO absorption is strong (about 58%) at these conditions, the signal-to-noise ratio for this far-UV

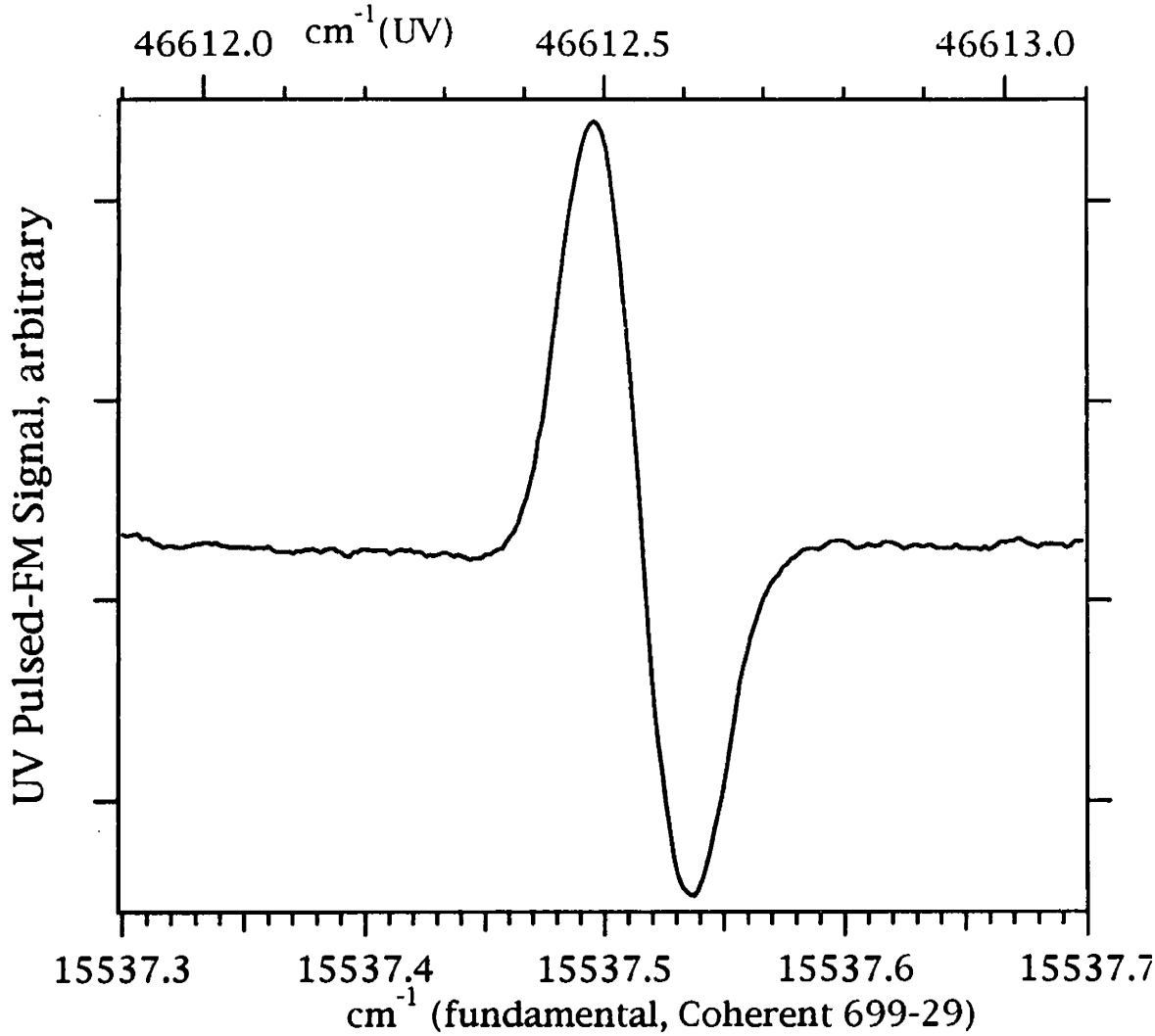

Figure 5.7: Far UV-pulsed-FMS spectra of NO. The trace shown is the average of three separate scans, with a detection limit of approximately 0.1% absorption. The experimental setup is discussed in the text.

averaging several rapid scans was found to be preferable to acquiring a single spectrum is as least as good as for the visible pulsed-FM iodine spectrum in figure 5.3[18].

An estimate of how well the sidebands are preserved in the three cell amplification and harmonic generation process was made. The modulation depth of the *cw*-laser was directly measured with an optical spectrum analyzer, but only a rough, indirect measurement of the pulsed-FM modulation depth was possible because a suitable far-UV optical analyzer and isolator were unavailable. Instead, for the far-UV beam, an estimation of the effective modulation depth was derived from the amplitude of the FM beat and knowledge of the absorption strength (58%) and linewidth (Doppler broadened, somewhat too large for optimal FM detection[19]). The modulation index of the UV-pulsed-FM laser was found to be 50% or more, about the same as the modulation of the fundamental.

Though it may appear surprising that the modulation is preserved so well, this is to be expected so long as the phase perturbations in amplification and nonlinear mixing are small. In fact, so long as the carrier is more intense than the

[18]When the absorption is as large as this, attenuation of the carrier reduces the signal strength, as described in chapter 2.

[19]With the laser tuned to obtain the largest FMS signal, the pulse amplitude (the carrier) was obviously attenuated. Hence, the Doppler width is too large, or the sideband spacing too small for optimal (no carrier absorption) FM detection. See chapter 2.

sidebands of the fundamental, the modulation index is expected to *increase* during harmonic generation, consistent with a detection frequency that is independent of the non-linear conversion. This is quite evident if the non-linear process is considered to be independent of the optical frequency so that the n^{th} harmonic the pulsed-FM light is (approximated for $M < 1$ as),

$$\begin{aligned}\left[\vec{E}_{p-FM}(t)\right]^n &\approx Re\left[E_c^n \hat{p}_c G(\omega_c;t)^{n/2} e^{in\beta(\omega_c;t)} e^{in(\omega_c t + M\sin\omega_{RF} t)}\right] \\ &\approx Re\left[E_c^n \hat{p}_c G(\omega_c;t)^{n/2} e^{in\beta(\omega_c;t)} \sum_{x=-\infty}^{\infty} J_x(nM) e^{i(n\omega_c + x\omega_{RF})t}\right].\end{aligned} \tag{5.6}$$

Although the effective modulation index has now increased to nM, where n is the harmonic order, the apparent modulation frequency remains unchanged.

Obviously, the detected UV-pulse at 50 nJ has fewer photons than a similar energy pulse in the visible. But the difference, a factor of three, still would provide for a shot-noise limited detection sensitivity on the order of 10^{-6}. The 0.1% sensitivity for these initial far-UV pulsed-FM experiments is still far from optimal. Hence, an analysis of the noise sources for this three-amplifier cell experiment is warranted.

5.4.1. *Noise sources in multiple ,Nd:YAG pumped cells*

In these multi-amplifier experiments, it appeared that there were sources of noise that were not present in the earlier single-amplifier experiments and that the relative magnitudes of the previous noise-sources had now changed. The

largest noise sources after three amplification stages were inter-stage optical feedback (both on and off-resonance) and beat-note RF phase jumps (on resonance only), while after only two amplification stages, the inter-stage feedback noise was considerably larger and swamped the phase jumps. Directly after the third amplification stage, no evidence for accidental etalons (or any constant off-resonance background signal) was found. This is consistent with full-saturation conditions developing within the third stage of amplification and the independent observation that pulse-to-pulse intensity fluctuations were reduced considerably after the third stage of amplification. A crude model that accounts for some of the saturation behavior will be presented below. Since the inter-stage optical feedback noise was so large, single stage beat noise (spontaneous emission beating directly with the laser emission from one cell) could not be discerned. As before, the presence of these various noise sources was demonstrated by careful recording of pulses using a fast-digitizing oscilloscope.

The inter-stage optical feedback noise that arises after two and three stages of amplification is shown in figure 5.8. The Fourier spectrum of the output of the shows periodic structure from inter-stage beat noise. The frequency spacing of these noise features is approximately 100 MHz (the corresponding cell

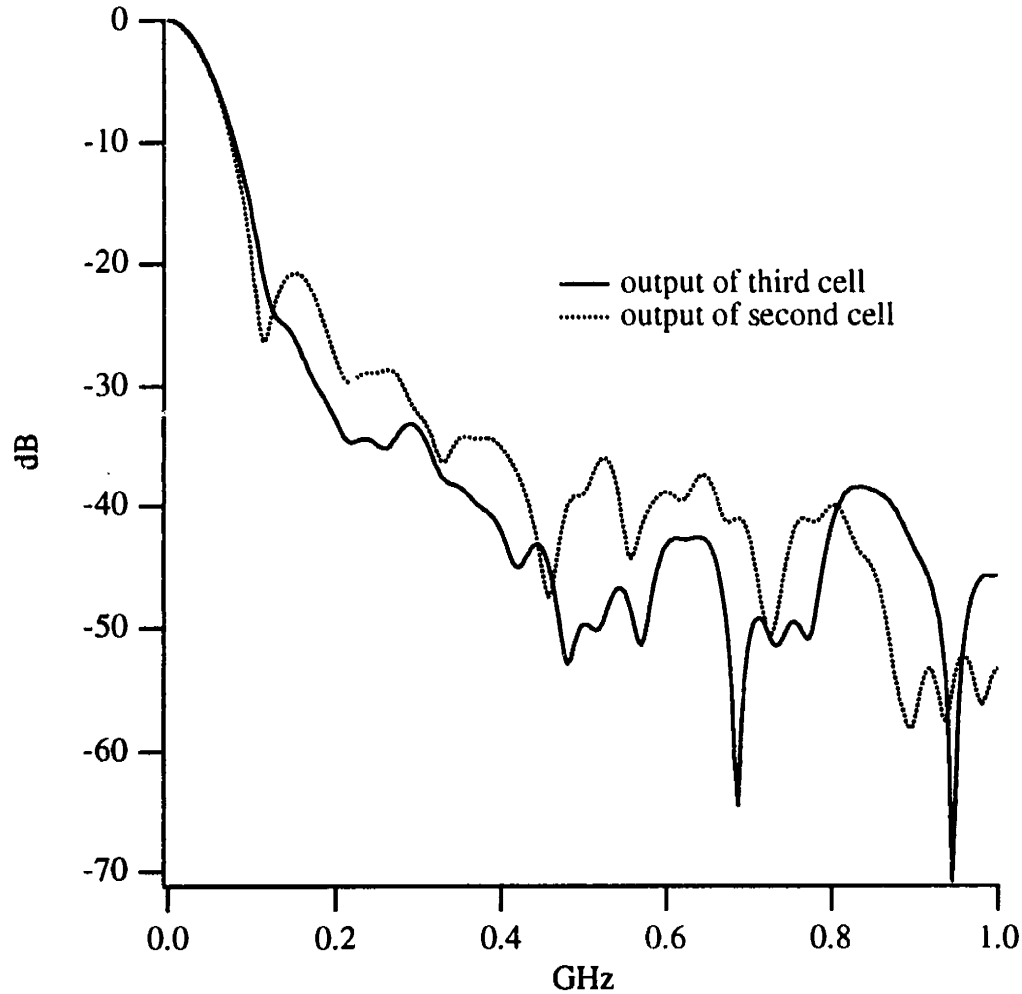

Figure 5.8: Fourier spectra of pulsed-FM laser pulses calculated from recorded off-resonance pulses. The black trace is for the output of a three cell amplifier chain. The doted trace is for the output of a two cell chain. For both, the recorded pulse was gated with a simple rectangular function centered around the pulse to remove baseline noise before Fourier processing. The output of the second cell shows periodic structure from inter-stage beat noise that is reduced by saturation in the third cell.

separation was about *1* m) . The periodic structure is smaller in the Fourier spectrum of the output of the third cell, indicating a reduction of the inter-stage beat noise. This is a beneficial effect of gain saturation. The inter-stage noise could be reduced further by optical isolators, by changing the optical propagation time between cells (by changing the cell separation ΔL), or by using anti-reflection coated dye-cell windows. The cells separation should be made either very small so that $\frac{C}{\Delta L} >> \omega_{RF}$ or very large so that $\frac{C}{\Delta L} << \omega_{RF}$. For $\omega_{RF} \approx 1\ GHz$, $\lambda_{RF} = \frac{C}{\omega_{RF}} \approx 0.3$ m, so it might be more convenient to shorten the separation to shift the beat-noise to higher frequency. When more than two cells are used, the total amplifier path length should be kept small also. No other significant off-resonance noise sources could be discerned.

An important on-resonance noise source after three cells is random phase jumps. These were first discussed for the visible pulsed-FM experiments. For the UV work, with three cells, the shifts were often considerably larger, and even sometimes (approximately 1 out of 800 pulses) as large as π radians. A phase shift as large as π, reverses the sign of the pulsed-FMS signal and is certainly problematic!

The increase in the size of the phase-jumps is explained by considering the

fact verified by systematically reducing the *cw*-FM drive intensity to the first stage. Reducing the drive intensity by one third resulted in only a 5-10% drop in third stage output intensity, while it took a ten-fold input intensity reduction to force a 50% output reduction. Saturation conditions were also observed in earlier work on the same amplifier chain driven by 80 mW of a un-modulated *cw*-laser (Gangopadhyay 1996). Saturation beneficially reduces the effect of drive intensity fluctuations. The mechanism for this effect is gain reduction. If the amplifier output remains constant when the input intensity changes, the gain of the amplifier must have changed. This is evident in the definition of amplifier gain, given in equation 5.2. However, drive-intensity induced change in gain must be accompanied by a change in phase (so long as the dye's real polarizability is non-zero at the drive wavelength). Therefore we expect that saturation transfers changes of the input field intensity to changes of the output field's phase. When a mixer is used to record (an on-resonance) pulsed-FM signal, these phase-changes are then converted (back) into signal-amplitude changes.

One obvious solution to the phase-shift problem is tune the frequency of the drive laser to a wavelength with a real dye polarizability of zero. When this is not possible, a dual-phase detection scheme should be employed. By using a commercially available dual-phase mixer known as an I & Q demodulator, both

the in-phase and quadrature components of the pulsed-FMS signal can be recorded simultaneously. The square root of the sum of the two values is then a phase-independent hybrid FM-signal[20] (North 1996).

The amplifier saturation occurring in the generation of intense pulses is a non-linear effect. As for other non-linear effects such as harmonic generation, saturation may alter the effective modulation depth on the pulsed-FM field. Furthermore, pulsed-dye amplifier saturation is known to generate sidebands when two-single-frequency *cw* fields are simultaneously injected into one amplifier (Comaskey 1988). In pulsed-FM, a comb of single-frequency *cw* fields is injected. Hence, saturation, which may be altering the optical spectrum is profound ways, must be analyzed carefully.

5.4.2 *Saturation behavior*

In the generation of intense mJ pulses of pulsed-FM radiation, saturation conditions surely develop within the multi-cell amplification system. A typical visible wavelength liquid-dye medium might have a cross section of $\sigma \approx 10^{-16} cm^2$ and an effective response time of $\tau \approx 10^{-9} sec$ (or less)[21]. This leads to a saturation intensity =, defined as the intensity at which the observed gain has been

[20]Line shape simulations for FM signal recorded using this phase-independent scheme are presented in Bjorklund 1983.

[21]This data from Seigman 1986, 295. Also available in Comaskey 1988 and others.

reduced to one half of the small-signal gain, of $I_{sat} = 1\ MW / cm^2$ (Seigman 1986, 295). For a 10 ns pulse, the saturation intensity in our 1 *mm* bore capillary amplifier with area=πmm^2 is only $10\ \mu J / mm^2$.

In a typical three cell capillary type amplifier, the observed gain of the first cell is on the order of 10,000, the second cell, 100, and the third cell 10. The primary cause of this gain reduction is gain saturation. If multiple optical frequencies are injected into the first amplifier, the overall gain experienced by any one component is also indirectly reduced and affected, to some degree, by the gain experienced by all other components. In fact, the gain of certain optical amplifiers is determined solely by the *total* input light intensity (Shimada 1994, 62). Since the gain is governed by the total input intensity, saturation therefore couples multi-frequency component input fields[22]. This coupling, a form of non-linear mixing, is extremely complicated and important (Seigman 1986, 318). The pulsed nature of the gain further complicates the situation.

5.4.2.1 *Uncoupled Saturation*

If the individual components of the *cw*-FM drive field experience saturated gain but are not coupled[23], the effect on the output spectrum is straightforward

[22]In optical communication, this effect is known as inter-channel cross-talk (Shimada 1994).

[23]The fields are completely uncoupled when the frequency separation of the input components is far greater than the inverse of the response time of the dye. This will be explored further later.

to understand (if the possibility of chirp is ignored). Essentially, the weaker drive components (the sidebands) experience more gain than the single, more intense component, the carrier. This translates into an increase of the modulation depth[24]. A similar effect was observed for non-linear harmonic generation. Figure 5.9 displays the optical spectrum of a pulsed-FM laser generated in a two-cell dye chain at a series of different drive power input levels. The modulation index of the drive field is the same in each spectrum. As the drive power increases in the figure, there is an increase in the modulation depth of the pulsed-FM output due to saturation. An increase of modulation depth is also observed as the pump power is increased even when the drive power is held constant[25] .

Not only do the sidebands experience a different saturated gain than the carrier, but also they experience a different phase shift than the carrier unless the real part of the dye's polarizability is zero. Since both first sidebands have the same intensity when input to the amplifier, each experiences the same saturated gain and phase-shift. So the FM null is preserved. Nonetheless, saturation, in this (unrealistic[26]) limit of no absolutely no coupling and no

---

[24]The term modulation depth rather modulation index is used to stress that the modulation was not created by the EOM, and is not therefore simply related to the original modulation *index*.

[25]Increasing the pump intensity increases the small-signal gain and does not affect the saturation intensity (large-signal gain) (Seigman 1986, 255, 295). However, severe over-pumping likely results in a non-linear effect that would therefore increase the modulation depth.

[26]For modulation frequencies less than <10 Ghz or so, the sidebands and carrier will be at least partially coupled. The fully coupled limit will be explored in the next section.

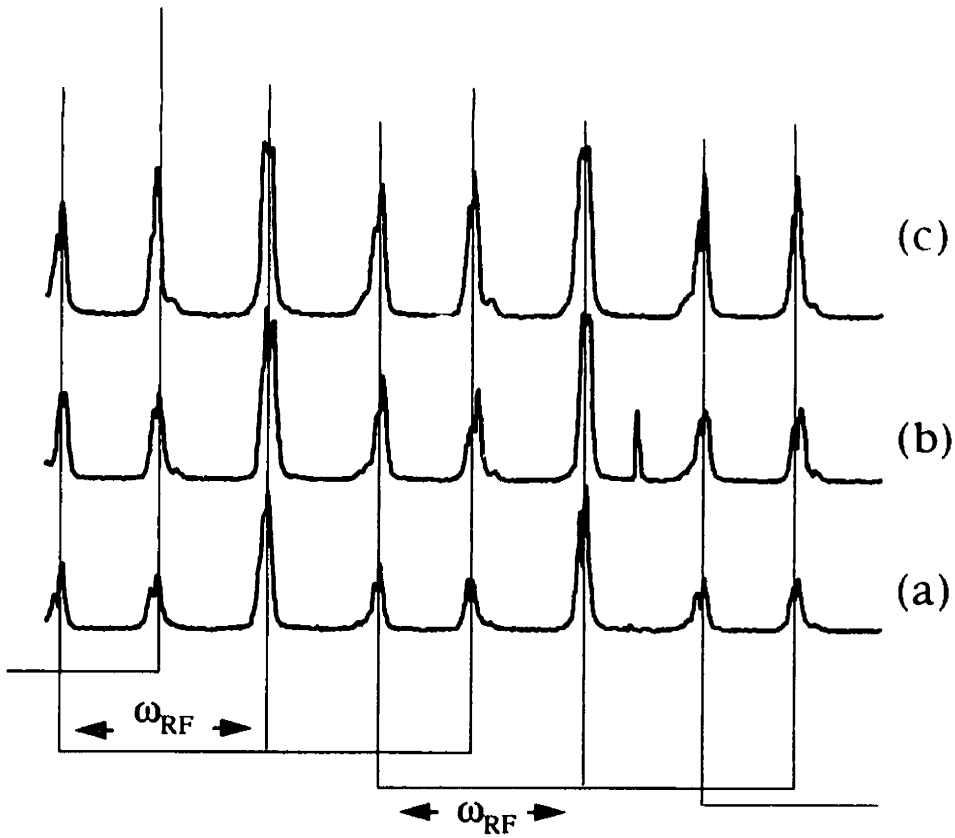

Figure 5.9: Optical spectra of the pulsed-FM laser from two amplification stages recorded using a 1.5 GHz FSR etalon. The RF frequency was 900 MHz. Thin lines tie together the components for each order of etalon transmission. The spectra are of poor quality because the etalon could not aligned exactly perpendicular to the entering laser beam due to feedback to the *cw*-laser. The intensity of the *cw*-drive laser was increased from (a) to (c). Due to saturation, the modulation depth increases from (a) to (c).

frequency chirp, is a source of on-resonance phase-shifts.

In this no coupling limit, the phase-shift added during amplification to each sideband (relative to the carrier) can be estimated by assuming that the phase-shift varies linearly with distance. Integrating over the amplifier's active length yields[27],

$$\Delta\phi = \phi_{dye} ln\left(\frac{G_0}{G_{\pm 1}}\right) = \phi_{dye} ln\left(\frac{2}{M}\right), \qquad 5.6$$

where is ϕ_{dye} the unsaturated phase-shift of the dye, G_0 and $G_{\pm 1}$ are the saturated gain of the carrier and either first sideband respectively, M is the modulation index (for weak modulation). Clearly, the gain ratio in equation 5.6 is determined by the relative intensities of the individual components (which is fixed by the modulation depth) so that the phase-shift should *not* vary from laser pulse to laser pulse.

Physically, this uncoupled saturation behavior corresponds to each component of the driving field burning an optical hole in the gain medium. The depth of any one hole does not, in this limit, effect the depth of any other hole. For liquid dyes, saturation surely has a broader than laser bandwidth homogeneous component. Therefore, each injected optical frequency will affect all others.

[27]The phase-shift associated with free-space propagation is ignored and only that due to the dye is calculated. Also time-dependance (such as optical Rabi-flopping) imposed by the non-linear dye-field interaction is ignored. See Seigman 1986, 303.

Comaskey et al 1988 estimate that a the -3 db bandwidth of the (homogeneous) interaction is about 10 GHz, governed by the response time of the dye solution (which varies with wavelength, dye, concentration, and both pump and drive intensities).

5.4.2.2 *Coupled Saturation and FMS background reduction*

For most liquid dyes, intense enough driving forces cause homogeneous gain saturation (along with some of the hole-burning or heterogeneous saturation that was previously discussed). The homogeneous gain saturation nonlinearly couples the input fields. This coupling has been exploited to design arbitrary optoopto modulators (Gray 1978). Comaskey and coworkers (1988) also found that saturation could generate new optical sidebands during pulsed-amplification.

Homogeneous saturation affects the frequency spectrum of the pulsed-FM laser in complicated ways. In a *fully* saturated amplifier, the output intensity *is* completely insensitive to small changes of the input intensity. A small residual intensity beat at the modulation frequency (caused perhaps by an accidental etalon before amplification) cannot then appear on the output spectrum of the amplifier. As mentioned already, intensity fluctuations on the input field are converted into phase-modulation on the output field of a saturated amplifier. If the input intensity varies sinusoidally, the saturation induced phase modulation creates

new sidebands. If the input intensity varies in other, more complicated ways, the induced phase modulation may spectrally broaden the input field.

The starting point for understanding these effects for pulsed-FM[28] is the simple model developed by Comaskey *et al* (1988) to explain their observations that simultaneously injecting two *cw* single mode drives into a saturated pulsed amplifier system generated several new sidebands spaced by the difference in input frequencies[29]. Their model considered only a *fully* saturated homogeneous *cw*-dye amplifier and ignored frequency chirp, even though they tested their model on a *cw*-driven pulsed-dye multi-cell amplification system.

Since the amplifier is assumed to be fully saturated, the output intensity, I_{out}, in their model is set to a constant. To accommodate pulsed gain, I_{out} is set here to an arbitrary, but still input intensity *independent*, pulse shape of constant peak intensity. By making I_{out} input intensity independent, the gain, $G(t)$, is forced *via* equation 5.2, to be inversely related to the *total* input intensity $I_{in}(t)$. The total intensity is used because the saturation is assumed to be homogeneous, fully coupling all frequency components. It is this non-linear relationship, shown in figure 5.10, that causes distortion of the input field.

---

[28]There has been some detailed studies on both the absorption and fluorescence of isolated molecules subjected to intense, saturating *cw*-FM fields (Nayak 1985;Xia 1994) that could be extended to the present case.

[29]The generation of new optical frequencies is actually a four-wave mixing process (Inoue 1987, Mukai 1990).

The amplifier's time-dependant phase-shift $\beta(t)$ is related to the amplifier's time dependent gain $G(t)$,

$$\beta(t) = \beta_0 \, lnG(t) + k \qquad 5.7$$

where β_0 and k are constants that depend on the particular dye solution and wavelength[30]. If the real-part of the dye's polarizability is zero, β_0 is zero. The output electric field is found using equation 5.3 and 5.7,

$$E_{out}(t) = Re\left\{e^{i\beta_0 G(t)}\sqrt{G(t)}E_{in}(t)\right\}, \qquad 5.8$$

where the constant phase shift e^{ik} has been dropped. Since the intensity of $E_{out}(t)$, I_{out}, is a constant, any modulation of $E_{in}(t)$ in equation 5.8 must be purely phase-modulation.

To gain an intuitive sense of how sidebands are generated, consider the case studied by Comaskey *et al* (1988): the injection of two copropagating (single mode, coherent) *cw* fields with intensities I_a, angular frequencies ω_a, and phases ϕ_a , using $a = 1,2$. The total input intensity $I_{in}(t)$ has an oscillatory component at the beat frequency, $\Delta\omega_{12}$,

---

[30]The derivation of equation 5.7 in given in Comaskey 1988, and by a somewhat different route in Seigman 1986. The values of the constants are found using the using the Kramers-Kronig integration of a known absorption cross section for the optical dye.

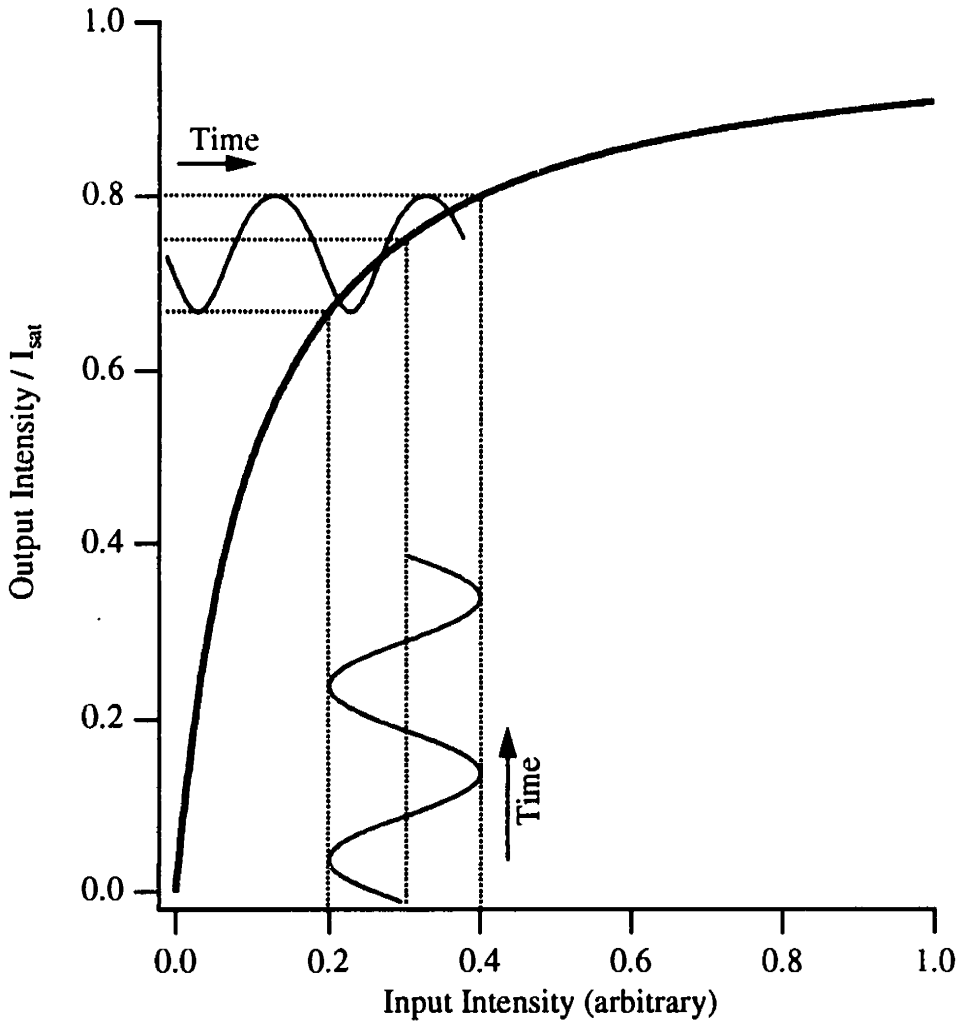

Figure 5.10: Non-linear transfer function for a saturated amplifier, showing a sinusoidal input field and a distorted output field. The output field is no longer a sinusoid because the more intense part of the input field receives less gain than the less intense part. A Fourier spectrum of the distorted output field would show many harmonics of the input frequency.

$$I_{in}(t) = I_1 + I_2 + 2\sqrt{I_1 I_2}\cos(\Delta\omega_{12}t + \Delta\phi_{12}). \qquad 5.9$$

Recall equation 5.2, $G \equiv \frac{I_{out}}{I_{in}}$. Clearly then, this low frequency intensity oscillation creates a low-frequency amplitude-modulated gain since the output intensity is constant. As described by equation 5.8, the time-dependent gain modulates the input field. This generates new sidebands. The new sidebands appear spaced by the beat frequency, $\Delta\omega_{12}$, or its harmonics. The number and intensity of the new sidebands depends upon the specific dye. Using this model, some spectral broadening (had the authors considered pulsed gain) would occur since the phase-modulation, inversely proportional to the square root of the gain, is not a simple sinusoid.

In the generation of pulsed-FM radiation, many optical frequencies are injected into one dye amplifier. Therefore, the intensity of the drive field may contain *many* low frequency components.

The intensity of *real* phase-modulated *cw*-FM light contains strong beat notes at the *even* harmonics of the modulation frequency ($2\omega_{RF}$, $4\omega_{RF}$,...) and weaker beats at the *odd* harmonics (ω_{RF}, $3\omega_{RF}$, $5\omega_{RF}$,...) due to imperfections in the EOM[31]. In fact, it is the weak beat notes at the original modulation frequency that limits the sensitivity of *cw*-FMS (see chapter 2).

[31] Accidental etalons and other factors also cause a beat note to be generated. See chapter 2

When this imperfect *cw*-FM drives the amplifier, saturation creates new optical sidebands of each input component spaced by both the *even* and *odd* harmonics of the modulation frequency. Because every newly generated sideband occurs at one of the possible original sideband frequencies, complicated interference develops. Nonetheless, we expect that saturation will decrease or eliminate the amplitude modulation present on the input field including any unwanted background signal. The price for this reduction of background is unwanted phase-modulation, which may broaden the optical spectrum of the pulse beyond its transform limit, distort the output spectrum, and create or reintroduce problems from carrier/sideband interference.

When the small-signal gain is pulsed, the timing of the pulse relative to the modulation phase could be a concern (Lotem 1986) especially when only a few cycles of the frequency modulation occurs during the pulse. In the amplification scheme described here for FMS, the period of the phase-modulation (and its harmonics) is considerably shorter than the pulse duration, so that the relative timing can be ignored.

Figure 5.11 shows how saturation alters the spectrum of a *perfectly cw*-FM driven amplifier[32]. Effects from saturation broaden each frequency component

[32]Self-phase modulation of the input field in saturation semiconductor laser amplifiers has been used to pre-chirp the light to compensate for chromatic dispersion that may occur in the fiber following the amplifier. (Agrawal 1989)

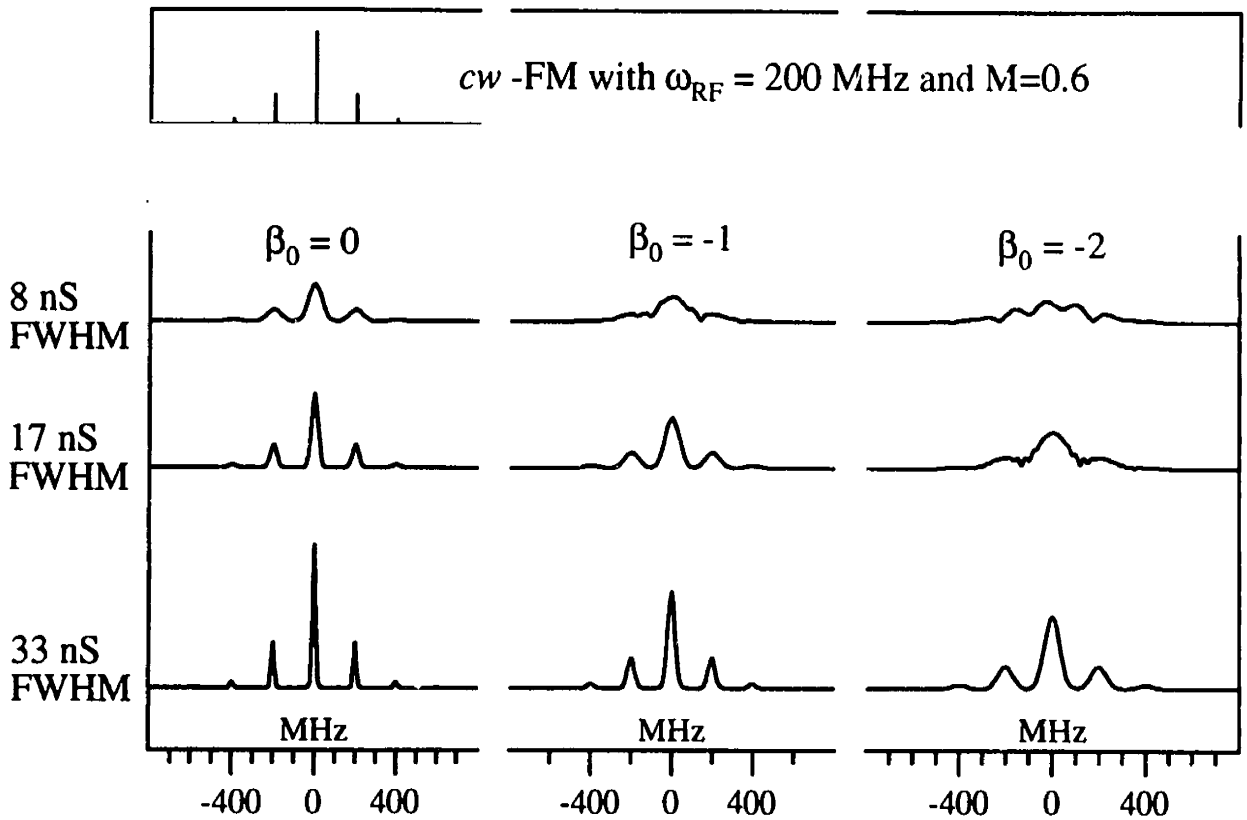

Figure 5.11: Spectra showing how short-pulse optical amplification distorts the input *cw*-FM field. The pulsed output spectra are calculated assuming that the input field has been perfectly phase-modulated using the model for homogeneous saturation developed in the text. For typical rhodamine 6G dye solutions, the phase-shift parameter β_o is approximately -0.9 (Comaskey 1988). β_o =0 can be achieved by proper choice of wavelength and/or dye concentration. As deviates β_o from zero and the pulse becomes shorter, the sidebands and carrier broaden and interfere.

somewhat beyond its transform limit. The broadening is governed by the phase-shift parameter β_0. Yet, the spectral linewidth of each spectral component is still primarily determined by the pulse duration. When the ratio of modulation frequency to spectral linewidth is reduced enough by increasing the magnitude β_0 or by shortening the pulse duration, interference occurs. Although interference surely destroys the FMS-null, it cannot be quantified by this model because the relative timing between the gain pulses and modulation wavetrain that had been ignored becomes important. Nonetheless, these simulations show that increasing the modulation frequency compensates for any saturation (phase) broadening, and emphasize the value of choosing the wavelength so that the real part of the dye's polarizability is zero, $\beta_0=0$.

Figure 5.12a and b demonstrate how saturation removes a large residual beat note from a real *cw*-FM drive field. To help quantify the effect of saturation, the intensity beat note at the modulation frequency is calculated and normalized by the carrier intensity. The normalized quantities are proportional to the FMS signal and are calculated before and after amplification. For perfectly phase-modulated light, the normalized beat note is zero. If the normalized beat note increases during amplification, saturation has degraded the detection sensitivity of FMS spectroscopy. If imperfectly modulated light is injected into the amplifier, the input beat note is non-zero.

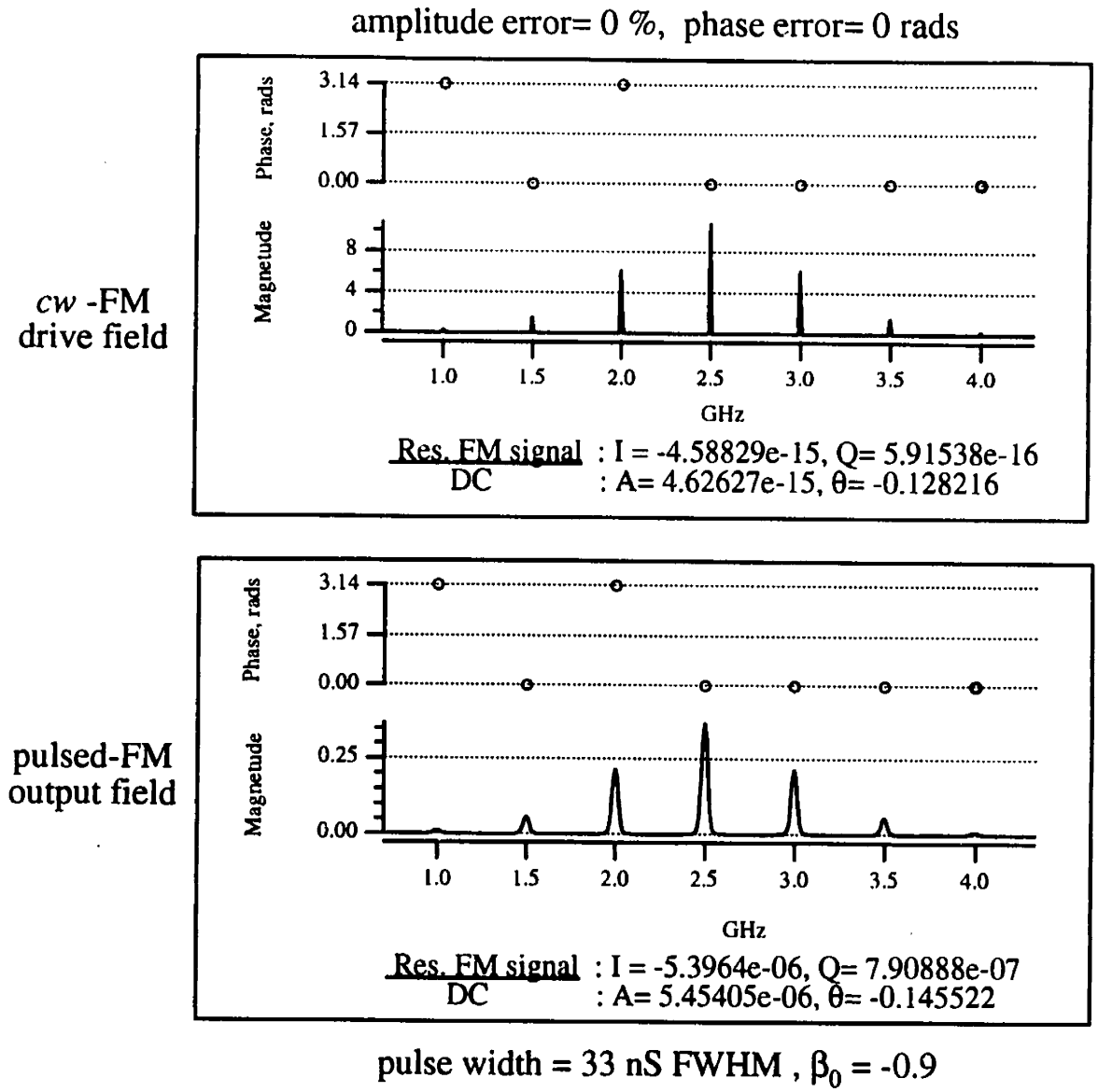

Figure 5.12a: Calculated pulsed-FM spectra for a fully coupled saturated amplifier driven by a *cw*-FM field with no amplitude modulation. A normalized FMS signal is calculated for the input and output fields. The increase in the pulsed signal is a numerical artifact. See figure 5.12b.

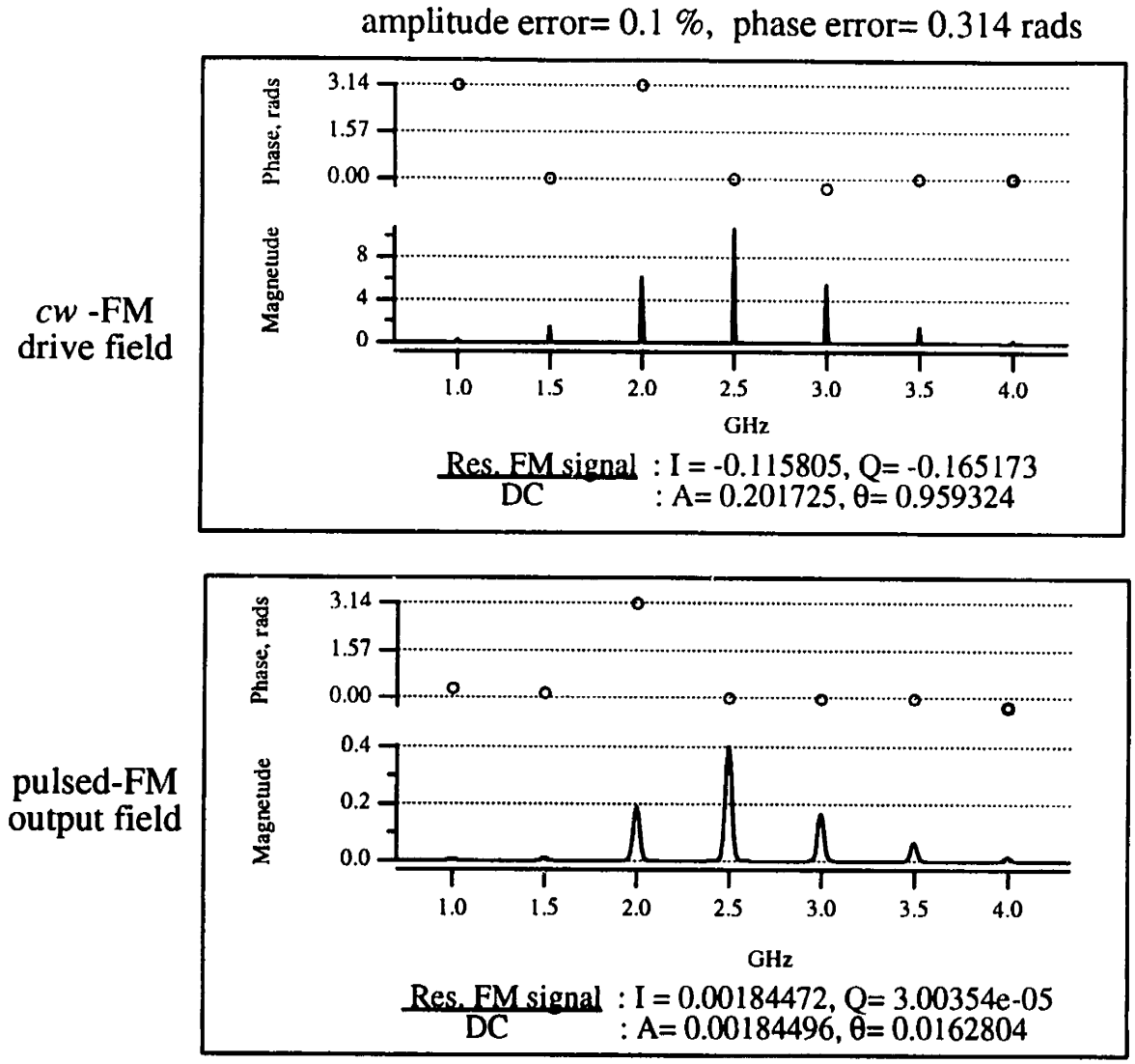

Figure 5.12b: Calculated pulsed-FM spectra for a fully coupled saturated amplifier driven by a *cw*-FM field with first sideband amplitude and phase errors. A normalized FMS signal is calculated for the input and output fields. Saturation decreases the pulsed signal but distorts the spectrum.

Figure 5.12 shows that saturation significantly reduces the normalized beat note, regardless of whether the beat note initially arises because of an amplitude or phase imbalance in the original sidebands. We know this reduction must occur in order for the output intensity to be constant. If full saturation conditions exist in the laboratory, the non-zero beat note that limits the detection sensitivity of *cw*-FMS will not limit the sensitivity of pulsed-FMS. But, saturation improves the sensitivity at a cost. The new sidebands distort the frequency spectrum. This distortion is obvious by the change in amplitudes of the second order sidebands in figure 12b and in the pulse-broadening in figure 5.11. Now that the amplitude of the sidebands cannot be known accurately, the pulsed-FM signal cannot be accurately related to the samples absorption.

Another potential drawback to homogeneous saturation, is the generation of intensity dependent beat-note phase-shifts[33]. An overall change in input intensity causes a change in the gain, and a change in the amplifier phase-shift. This problem was discussed already for an uncoupled amplifier. For the homogeneous (fully coupled) amplifier, the phase-shifts are the same for each component of the input field, but now vary with observed gains, something like,

$$\phi = \phi_{dye} ln\left(\frac{G'}{G''}\right), \qquad 5.10$$

[33]Intensity dependant phase-shifts in *cw*-FMS have been observed before for Rb atoms and modeled using the optical Bloch equations (Xia 1994).

where G' and G'' are observed peak gains for two different pulses and ϕ_{dye} is the mean phase-shift measured under non-saturation conditions. An accurate estimation of the gain (or intensity) dependent phase-shift is, of course, impossible without a detailed understanding of the behavior *within* the amplifier system. For example, the first unsaturated amplifier cell adds random intensity fluctuations that are then removed, and therefore hidden, by the gain of the third, fully saturated cell. The phase-shifts depend on this hidden gain. In this case, when the model is based on the overall gain (calculated from the input and output intensity levels[34]), equation 5.10 is surely insufficient. Clearly, a more sophisticated model is warranted. But once again, if $\phi_{dye} = 0$, no phase-shifts will occur.

5.5. *Current developments: custom Nd:YAG pumped pulsed-FMS*

The detection sensitivity obtained thus far, in the visible with an excimer laser pump, and in the UV with a Nd:YAG laser pump, has been considerably short of the shot-noise limited level. To improve the sensitivity, the background off-resonance noise sources must be made smaller. Both carrier/sideband interference and the inter-stage beat noise must be eliminated.

[34]This is actually a restatement of the fact that the optical phase cannot be determined by measuring the intensity only.

Figure 5.13 shows recorded pulsed-FM laser shots with $\omega_{RF} = 980\ MHz$ generated in one capillary cell pumped by the doubled output of a custom, long-pulse, injected seeded, Nd:YAG laser (Continuum, Inc.). The pump pulse was very smooth, and quite Gaussian-like with a fullwidth of 17 ns.

Using such a smooth pump pulse with no observable fast substructure results in an output pulse that has almost no observable high-frequency noise at the modulation frequency. The high frequency noise in the Fourier spectrum in figure 5.13 is a combination of baseline (detector noise, oscilloscope noise, and low-level pickup), digitization noise (oscilloscope), and numerical noise (FFT algorithm). With the pulse blocked before the photodetector, the high-frequency noise around the modulation frequency was of the same magnitude. The combination of the smooth, long-pulse, pump laser and somewhat increased modulation frequency has effectively eliminated the carrier-sideband interference problem.

Elimination of the next largest noise sources, inter-stage feedback and residual FM signals generated by accidental etalons and imperfect modulation, requires multiple steps. The prescription is as follows. First, use enough amplification cells so that the last cell is fully saturated (usually 3 or 4)[35]. Separate the first

[35]Only perfectly full saturation removes *all* residual signals. Partial (real) saturation does not. If the residual signals are not suppressed enough, other methods (discussed in chapter 2) are necessary.

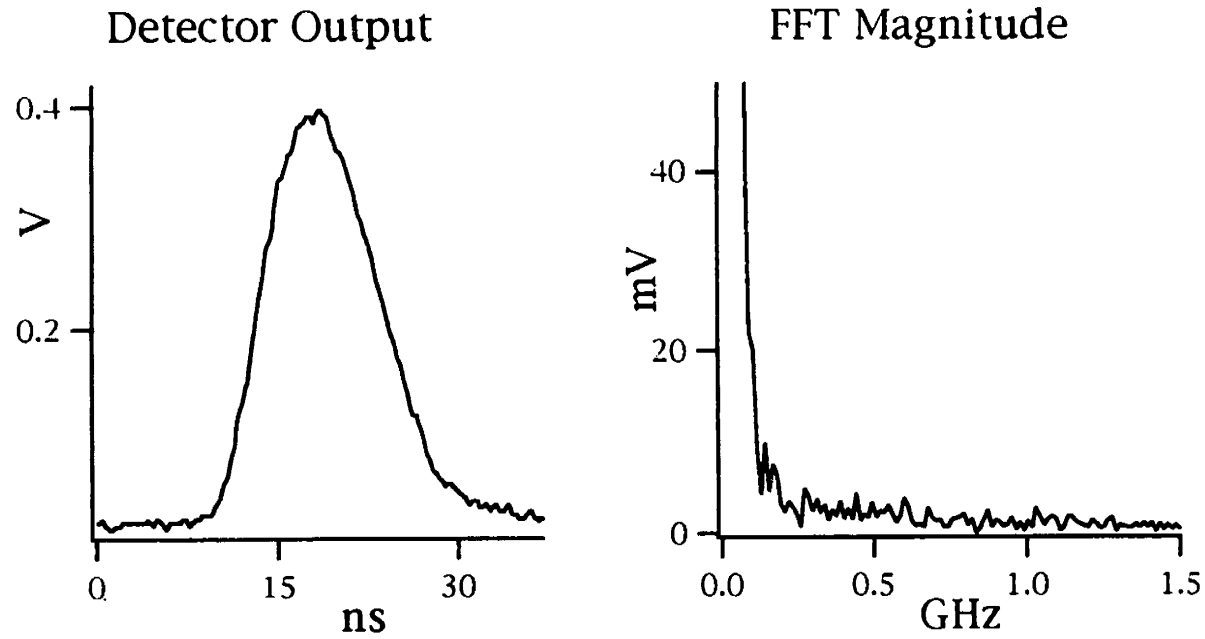

Figure 5.13a: Off-resonance pulses of phase-modulated radiation generated in a single amplifier cell pumped by a smooth 17 FWHM ns doubled Nd:YAG laser. The modulation frequency was 970 MHz. This figure shows a zero pulse-FMS background. The baseline noise at the modulation frequency does not change when the pulse is blocked from reaching the detector. See figure 5.13b.

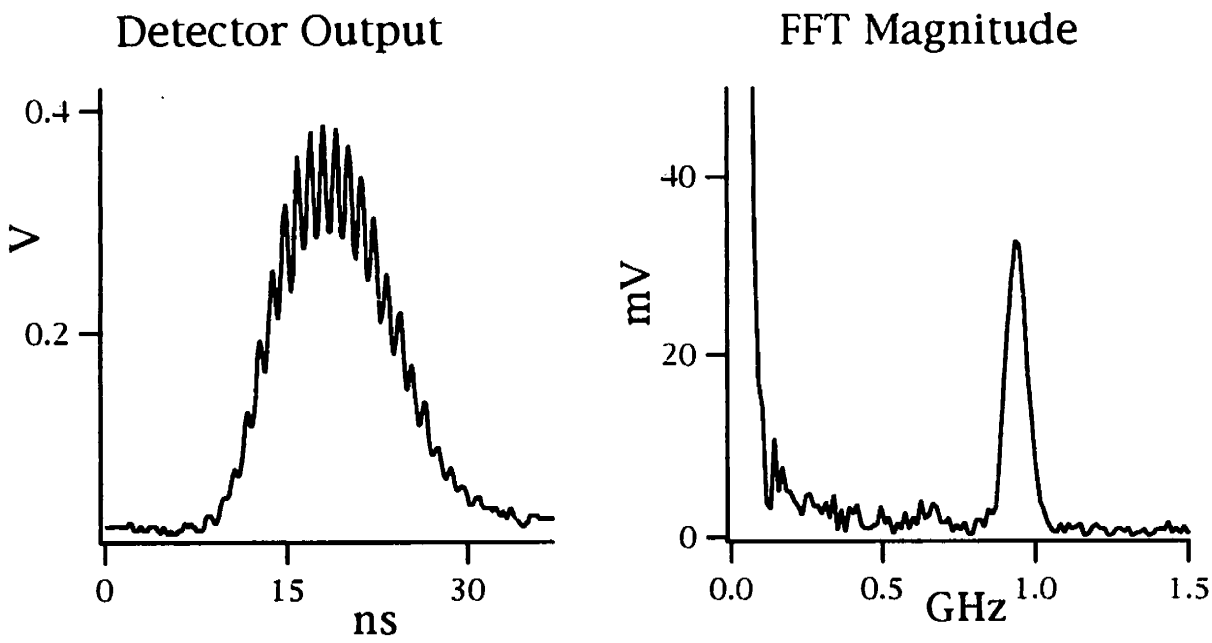

Figure 5.13b: On-resonance pulses of phase-modulated radiation generated in a single amplifier cell pumped by a smooth 17 FWHM ns doubled Nd:YAG laser. The modulation frequency was 970 MHz. This figure clearly shows the pulse-FM beat note at the modulation frequency. By using the smooth, long-pulse pump laser, the sideband/carrier interference problem that had limited the sensitivity of pulsed-FMS has been eliminated.

cell from the last cell by a distance less than $\frac{C}{\omega_{RF}}$. Isolate each cell from the others with Faraday isolators. Use anti-reflection coatings on amplifier cell windows. Minimize amplified spontaneous emission (ASE) using spatial filters and by avoiding over-pumping of the cells. Adjust the dye mixture so that its real polarizability is zero at the desired wavelength. Remove more ASE, inter-stage beat noise, and other relatively *weak* (optical intensity) noise sources by non-linear conversion[36] of the pulsed-FM output.

Following this prescription will remove most of the excess noise, but will not, however, produce truly shot-noise limited pulsed-FMS. This is because, as discussed in chapter 2, all real amplifiers must add some noise.

In optical amplifiers, the noise source is the ASE. The ASE beats with each component of the pulsed-FM field, subtly destroying the perfect null[37]. It is difficult to estimate the fundamental lowest noise figure (see chapter 2) for the optical amplifier in a pulsed-FM experiment, since it depends on subtle details of the dynamics of the amplification process, including hidden saturation effects. For a single, *ideal* high-gain optical amplifier (using four energy levels), the

[36]Non-linear conversion such as frequency doubling should be used. If the study is to be done at the fundamental wavelength, a saturable absorber before the cell, or doubling after the sample cell, could also be used.

[37]Other, smaller ASE related noise sources include ASE-ASE beat noise, and the shot noise of the ASE itself (Yariv 1991, 453).

noise figure could be as small as 3 db (Yariv 1991, 452). Noise levels close to this have been already achieved in semiconductor and fiber optical amplifiers (Mukai 1987, Saitoh 1990, Mears 1987, Olshansky 1988).

Once the ASE is made as small as possible (by spatial and polarization filtering, pump power and dye concentration adjustment, etc.) one must strive to *detect* as little of the ASE-signal beat noise as possible. One way to limit the detection of the beat noise is to optically filter the pulse in a Fabry-perot cavity (to remove ASE before the beat is generated during detection). This will be discussed below. Electronic filtering of the pulsed- FM signal would also help remove the beat-noise. The pulsed-FM signal out of the mixer will have a pulse shape that reflects the pulse-shape of the pulsed-FM laser that probes the sample. The beat-noise will not have the same pulse shape. Hence, a matched filter or simple correlation algorithm (see chapter 3) could provide an electronic or digital means to discriminate the signal-pulse from the noise-pulse[38].

5.6 *The limit, future developments.*

This chapter has proposed a new method of generating high power, near-transform-limited nanosecond pulses of phase-modulated laser radiation and

[38]The idea is that the actual pulsed-FM signal out of the mixer will be a pulse in time that reflects the shape of the pulsed-laser, while (at least some part of) the noise will have a different signal "shape".

presented the results of initial pulsed-FMS demonstration experiments in the visible and far-UV spectral regions. Even though the sensitivity achieved to date has been far from the shot-noise limit, this new method holds considerable promise since substantial improvements are expected. At least partial solutions to all of the significant remaining noise sources are known and are currently being implemented.

Once the sensitivity of pulsed-FM is improved, another significant problem develops. Presently no fast, high efficiency detector is available that can handle 1 mJ of visible or 1 μJ of far UV radiation with sufficient dynamic range. One general solution to this problem is to place the sample in an optical cavity, and, sending the pulsed-FM beam through the cavity, detect the FM signal on the much less intense field exiting the cavity[39]. Any disruption of the perfect FM null can be avoided if the spacing of the cavity modes corresponds exactly to the components of the pulsed-FM field. The cavity also provides two substantial benefits: first, it filters out some ASE; second, the FM signal increases due to the multi-passing within the resonator. However, if the laser frequency and cavity modes do not correspond, or if the bandwidth of the cavity modes is too small, residual FM signal and frequency chirps will be generated[40].

[39] A similar scheme for cw-FM has been developed by J. Hall at the JILA.

[40]Unavoidable frequency chirping occurs during the rising and falling edges of the pulse (exiting the cavity). If the output pulse is long enough, the portion of the pulse that is chirped need not be detected.

Figure 5.13, which presented current developments using a long-pulse pump laser, also demonstrates the possibility of two more advances. First, less-than-pulse-duration time resolution may be obtained using the long-pulse pulsed-FM radiation. That is, one or less of the wiggles on the pulse in figure 13b could be selectively detected. Through an elegant normalization technique (described earlier), a pulsed-FM signal that is independent of the pulse intensity can be obtained, so that any wiggle, even those in the rising or falling parts of the pulse, can be quantitatively related to the absorption. This signal would have time resolution limited approximately by the transform-limit of the modulation frequency, approximately 1 ns or so for typical experiments.

A second possible advance arises from the increased duration of the long-pulse pulsed-FM radiation. The many cycles of the modulation frequency that occur during the pulse allow the possibility of further modulation, perhaps a slow (1< GHz) amplitude modulation. Rather than using a boxcar to time average the mixer's output, the entire pulse waveform may be recorded using a fast oscilloscope. Then an improved pulsed-FM signal can be obtained by fitting the entire waveform to the function that describes the FM signal recorded with the additional modulation, or by using a correlation algorithm (see chapter 3). By processing the entire waveform at once rather than by averaging it bit by bit,

wiggles that appeared buried in noise should be detectable.

Another possibility to improve detection sensitivity is to use a phase diversity receiver[41], which simultaneously measures at least three different phases of the pulsed-FM beat note using an optical hybrid splitter[42]. For example, measurements of the beat note at the (relative) phases of $\frac{2\pi}{3}, \frac{4\pi}{3}, 2\pi$, produce three pulsed-FM signals which have partially correlated intensity noise components. When the signals are summed, some of the noise will cancel. This technique works best for intense optical fields (Elrefaie 1987).

5.7 *References*

1989 Agrawal, G. P. and N. A. Olsson, "Self-phase modulation and spectral broadening of optical pulses in semiconductor laser amplifiers," *IEEE J. Quantum Electron.*, **25**, 2297.

1981 Bethune, D. S., "Dye cell design for high-power low-divergence excimer-pumped dye lasers," *Appl. Opt.*, **20**, 1897.

1988 Comaskey, B., T. Daly, C. Haynam, J. Morris, J. Paisner, and R. Young, "Sideband generation in saturated pulsed dye amplifiers with multiple cw single mode injection," SPIE Vol. 912, "Pulsed Single-

[41]See, for example, Patzak 1988 and references therein.

[42]An optical hybrid splitter is some device whose optical outputs are phase-shifted relative to each other.

Frequency Lasers: Technology and Applications", 73

1987 Elrefaie, E. F., D. A. Atlas, L. G. Kazovsky, R. E. Wagner, "Intensity noise in ASK coherent lightwave receivers," *Elec. Lett.*, **24**, 158.

1996 Eyler, E. E., S. Gangopadhyay, N. Melikechi, J. C. Bloch, and R. W. Field, "FM spectroscopy with transform-limited nanosecond laser pulses", *Opt. Lett.*, **21**, 225.

1981 Gallagher, T. F., R. Kachru, F. Gounand, G. C. Bjorklund, and W. Lenth, "Frequency-modulation spectroscopy with a pulsed dye laser," *J. Opt. Soc. Am.*, **7**, 28.

1996 Gangopadhyay, S., Ph.D. Thesis, University of Delaware; Gangopadhyay, S., N. Nelikechi, and E. E. Eyler, " Optical phase perturbations in nanosecond pulsed amplification and second-harmonic generation," *J. Opt. Soc. B*, **11**, 231 (1994).

1995 Ma, L-S., J. Ye,P. Dubé, and J. L. Hall, "A new modulation method for sensitive nonlinear spectroscopy-- application to molecular overtones as visible frequency references," Laser Spectroscopy XIII, Capri, June.

1987 Inoue, K., T. Mukai and T. Aitoh, "Nearly degenerate four-wave mixing in a traveling-wave semiconductor laser amplifier," *Appl. Phys. Lett.*, **51**, 1051.

1978 Lonheim, T. S., and L. G. DeShazer, "Determination of optical cross

sections by the measurement of saturation flux using laser-pumped oscillators," *J. Opt. Soc. Am.*, **68**, 1575.

1986 Lotem, H., M. Amit., S. Lavi, Y. Liran, and G. Erez., "Interference between broadened sidebands of a pulse-amplified phase-modulated continuous-wave dye laser," *J. Opt. Soc. Am. B*, **3**, 827.

1987 Mears, R., J. L. Reekie, I. M. Jauncey, and D. N. Payne, "Low noise erbium-doped fiber amplifier operating at 1.54 μm," *Elec. Lett.*, **23**, 1026.

1994 Melikechi, N., S. Gangopadhyay, and E. E. Eyler, E. E., "Phase dynamics in nanosecond pulsed dye laser amplification" , *J. Opt. Soc. B*, **11**, 2402.

1989a Mellis J., "Direct optical phase modulation in semiconductor laser amplifier,"*Electron. Lett.*, **25**, 679.

1989b Mellis J., M. J. Creaner, "Coherent detection of 565 Mbit/s DPSK data using semiconductor laser amplifier as phase modulator," *Electron. Lett.*, **25**, 680.

1987 Mukai, T. and T. Saitoh, "5.2 db noise figure in a 1.5 mm InGaAsP travelling-wave laser amplifier," *Electron. Lett.*, **23**, 216.

1990 Mukai, T. and T. Saitoh, "Detuning characteristics and conversion

efficiency of nearly degenerate four-wave mixing in a 1.5 μm traveling-wave semiconductor laser amplifier," *IEEE J. Quantum ELectron.*, **26**, 865.

1985 Nayak, N. and G. S. Agarwal, "Absorption and fluorescence in frequency-modulated fields under conditions of strong modulation and saturation," *Phys. Rev. A*, **31**, 3175.

1996 North, S. W., X S. Zheng, R. Fei, and G. E. Hall, "Line shape analysis of Doppler broadened frequency-modulated line spectra," *J. Chem. Phys.*, **104**, 2129.

1987 Olshansky, R., "Noise figure for Er-doped optical fibre amplifiers," *Elec. Letts.*, **24**, 1363.

1989 Patzak, E., R. Langenhorst, "Sensitivity degradation of conventional and balanced 3x3 port phase diversity DPSK receivers due to thermal and local oscillator intensity noise," *Elec. Letts.*, **25**, 545.

1990 Saitoh, T., Y. Suziki, and H. Tanaka, "Low noise characteristics of a GaAs-AlGaAs multiple-quantum-well semiconductor laser amplifier," *IEEE Photonics Technol. Lett.*, **2**, 794.

1986 Seigman, A. E., *Lasers*, 2 Ed., Mill Valey: University Science Books.

1994 Shimada S., and H. Ishio, *Optical Amplifiers and their Applications*,

John Wiley & Sons:New York.

1983 Tran, N. H., R. Kacharu, T. F. Gallagher, J. P. Watjen, and G. C. Bjorklund, "Pulsed frequency-modulation spectroscopy at 3302Å,"*J. Opt. Soc. Am.*, **8**, 157.

1984 Tran, N. H., R. Kacharu, P. Pillet, H. B. van Linden van den Heuvell, T. F. Gallagher, and J. P. Watjen, "Frequency-modulation spectroscopy with a pulsed dye laser: experimental investigations of sensitivity and useful features," *Appl. Opt.*, **23**, 1354.

1994 Xia, H.-R., J. I. Cirac, S. Swartz, B. Kohler, D. S. Elliot, J. L. Hall. and P. Zoller, "Phase shifts and intensity dependance in frequency-modulation spectroscopy," *J. Opt. Soc. Am. B.*, **11**, 721.

1991 Yariv, A. , *Optical Electronics*, 4e, Philadelphia: Saunders College Publishing.

FM-MRS and pulsed-FMS substantially extend the limits of high resolution, high sensitivity, linear, laser absorption spectroscopy. FM-MRS provides both shot-noise limited sensitivity and selectivity to paramagnetic species. Pulsed-FMS is a relatively high sensitivity form of wavelength-versatile absorption spectroscopy which is not degraded by noisy pulsed-lasers.

In this thesis, expressions that describe the complicated FM-MRS lineshape are derived, and the FM-MRS investigations of NO_2 and CeF are reported. Trace amounts of NO_2 were detected using FM-MRS, even though the ambient laboratory NO_2 pressure-pathlength was considerably greater than that of the sample cell. The achieved detection sensitivity approached the quantum limit and the potential for further sensitivity enhancement using digital processing was proposed. The study of CeF at 2000 K demonstrates how FM-MRS reduces the effective rotational temperature of the sample and aids in the rotational assignment of its electronic spectrum. Because of its high sensitivity and selectivity, FM-MRS is beginning to find application in other laboratories. For example, FM-MRS is now being used at the University of Mississippi to study carbon chain free radicals produced in a supersonic jet by pyrolysis[1]. In these

[1]Personal communication with Andy Cooksy, University of Mississippi

studies, the advantages of FM-MRS over ordinary absorption are crucial to the project's success.

Pulsed-FM, a new scheme for generating intense pulses of phase-modulated laser radiation is described in chapter 5 and the results of initial FM experiments using the pulsed-FM radiation in the visible and far UV spectral regions, are presented. These initial experiments demonstrate the wide-ranging potential of the new technique. With pulsed-FMS, high resolution, high sensitivity absorption measurements should be possible at any optical wavelength accessible by non-linear wave-mixing techniques. These initial experiments, which were performed at the University of Delaware, have led to the construction of a pulsed-FM facility at MIT, using a custom-long pulse Nd:YAG laser[2] and similar pulsed-FM installation at University of Connecticut. At MIT, pulsed-FM will be used to enhance the technique of Stimulated Emission Pumping, the best method for studying vibrationally excited states of polyatomic molecules. At University of Connecticut, pulsed-FM will be used for VUV precision spectroscopy of small molecules that do not appreciably fluoresce, but for which detailed calculations exist, such as CH and OH (Kirby 1988) or heliumlike neon (Hallett 1993). In the future, multi-component, transform limited, pulsed-FM radiation may be used in reaching one of the central goals of chemical physics: the possibility of radiative control of molecular reactions. Although the pulsed-FM laser has a pulse

[2]The usefulness of the MIT custom long-pulse Nd:YAG laser has led to the sale of at least three similar system by Continuum.

duration of nanoseconds and a transform limited bandwidth <100 MHz, it can nonetheless be used for coherent control of photodissociation. The key is to take advantage of the well-defined phase-relationship between the carrier and sidebands, and tune each individual frequency component into resonance with different transitions that involve lower state energy levels separated by a multiple of the modulation frequency, up to a few GHz.

So far, the FM-MRS and pulsed-FMS experiments have all used a single-longitudinal mode *cw*-dye laser pumped by an ion laser. This laser system has a number of serious drawbacks. Today, such a system costs over $150,000 and requires more than 20 square feet of laboratory space. The dye solution and other consumables need regular replacement and disposal. Disposing of the dye waste, which may contain mutagens and dangerous solvents, will incur further expense. Daily operation of the ion-pumped *cw*-dye-laser system also demands the full attention of a technically adept person. Every six years or so the ion laser will need major refurbishing at a cost of $30,000. If FM-MRS and pulsed-FMS are to ever find application outside the elite group of well funded researchers, the techniques must be adapted to take advantage of less costly, more rugged, and easier to use technology.

The best solution will be to use the equipment (lasers, modulators, fiber links, optical amplifiers and detectors) developed for optical communication. This

equipment is rugged and commercialized. Hence, its performance is more reliable even without a dedicated technician. However, the optical communication equipment has all been designed for use at non-visible wavelengths, usually at 1.0 and 1.5 μm. Only now that a high peak-power FM pulsed method has been developed, can this equipment can be well utilized. Using the optical communication equipment, small, self contained, all solid-state pulsed-FM based-*devices* for optical sensing should soon be feasible.

6.1 *References*

1988 Kirby, K. P., E. F. vanDishoeck, "Photodissociation processes in diatomic molecules of astrophysical interest," Ad. At. Mol. Phys., Vol. 25, Academic Press, 437.

1993 Hallett, W. A., D. D Dietrich, J. D. Silver, "Measurement of wavelengths on heliumlike neon," *Phys. Rev. A*, **47**, 1130.

A.1 *Introduction*

This appendix presents simulations of Magnetic Rotation (MR) Spectra for two classes of electronic states of linear paramagnetic molecules. The MR spectra are calculated from the energy level structure of molecules placed in a magnetic field. The magnetic field causes the energy levels to change from the field-free case. These "Zeeman effect" changes may be subtle (<<1 GHz), yet they are detectable in molecule's optical spectrum recorded with laser MR or FM-MR (see chapter 3) spectroscopy, even at Doppler limited frequency resolution of 1 GHz or so. The understanding of these relatively gross *spectral* effects created by the much finer-scale energy level changes is the focus of this appendix. It will be shown that in some cases the gross spectral effects can be exploited to aid in spectral assignment, while in others, the effects obscure the extraction of useful information from a spectrum.

Electronic states belonging to the first class have rotational wavefunctions that are described by Hund's case (a) eigenfunctions (Lefebrve-Brion 1986, 41). These electronic states posses well separated rotational energy levels often due to

large spin-orbit coupling. For many open-shell metal-atom containing molecules, all of their electronic states belong to this class.

Electronic states belonging to the second class have rotational wavefunctions that are usually described by Hund's case (b) eigenfunctions. These states posses dense multiplets of interacting rotational levels. Most ground state Σ states belong to this class as do many of the higher orbital angular momentum electronic states of polyatomic species (Hirota 1985, 25). Many molecules have isolated Hund's case (b) ground states and a manifold of Hund's case (a) excited states.

At this point it must be stressed that this appendix does not aim to present a comprehensive review of the MR effect, whose description first appeared in 1898 (Righi 1898). Rather, the goal here is to extend and generalize McCarthy and Field's 1992 Hund's case (a) MR effect analysis to more complicated cases that may require computer spectral simulation (Yan 1985).

A.2 *Molecules in a magnetic field: The Linear Zeeman Effect*[1]

The effect of an external magnetic field on the energy levels of a molecule is found by adding an effective Hamiltonian for the total electronic linear Zeeman

[1]Linear Zeeman effect refers to the interaction linear with the applied magnetic field (Judd 1977, 170). For discussion of small non-linear terms (often called the diamagnetic contribution) see Cohen-Tannoudji 1977, 835, 1233.

effect $\mathbf{H}_{Zeeman}$ to the hamiltonian describing the molecule in field-free space $\mathbf{H}^0$,

$$\mathbf{H} = \mathbf{H}^0 + \mathbf{H}_{Zeeman}. \qquad \text{A.1}$$

The Zeeman Hamiltonian is

$$\mathbf{H}_{Zeeman} = -\mu_{Zeeman} \cdot \mathbf{B}, \qquad \text{A.2}$$

where μ_{Zeeman} is the total Zeeman magnetic moment, a first rank tensor operator, and $\mathbf{B}$ is the laboratory fixed magnetic field vector. Because of the inclusion of $\mathbf{H}_{Zeeman}$, the symmetry of the total molecular Hamiltonian $\mathbf{H}$ is reduced from the high-symmetry of $\mathbf{H}^0$ (Bunker 1979, 326). The operator $\mathbf{J}^2$ no longer commutes with the symmetry-reduced Hamiltonian $\mathbf{H}$, so that J, the total angular momentum, is no longer a rigorously good quantum number. We expect this "breakdown" of J to have profound effects on the appearance of the simulated MR spectra.

There are a number contributions to the total magnetic moment μ_{Zeeman}, the largest of which are the electron spin-magnetic moment, μ_S, and orbital angular momentum μ_L,

$$\mu_S = -\mathbf{g}_S \beta \mathbf{S} \qquad \text{A.3}$$

$$\mu_L = -\mathbf{g}_L \beta \mathbf{L}, \qquad \text{A.4}$$

where $\mathbf{L}$ is the total orbital-angular momentum operator, $\mathbf{S}$ is total spin-angular momentum operator[2], and under field-free conditions, $\mathbf{J} = \mathbf{L} + \mathbf{S}$. The electronic Bohr magneton β is defined,

$$\beta = \frac{e\hbar}{2mc} = 1.3996 \text{ Mhz/G} = 0.046686 \text{ cm}^{-1}\text{/kG}, \qquad \text{A.5}$$

where $-e$ is the charge and m the mass of an electron[3]. Two dimensionless "g-factors" appear above, $\mathbf{g}_s$, the electron-spin g-factor[4], with approximate value of 2.002, and $\mathbf{g}_L = 1$, the electron orbital g-factor. Hence typical magnetic moments obtainable for reasonable laboratory fields are on the order of hundreds of MHz. Hence, we expect the effects on the energy levels to be usually less than the typical visible wavelength Doppler limited linewidths, 1-2 Ghz. The contributions to the total magnetic moment neglected here are all much smaller than the electronic moments, μ_S and μ_L, by a factor of the particle's mass[5].

For simplicity, we assume that the magnetic field is along the laboratory Z-

---

[2]The spin-angular momentum are expressed in units of $\hbar$.

[3]All the possible relativistic corrections have been neglected. See Judd 1977, 172.

[4]Rigorously, the g-factor is a tensor because it depends on the electron's molecular environment. Even in spatially symmetric molecules, the electronic spin- g factor often deviates somewhat from the free-electron value of 2.00232 because of spin-orbit coupling (Carrington 1967, 25).

[5]The nuclear Bohr magneton (and hence the nuclear magnetic moment) is nearly two thousand times smaller than the electronic magneton.

axis[6]. This leads to[7]

$$\mathbf{H}_{\text{Zeeman}} = \beta \mathbf{B}_Z (\mathbf{g}_L \mathbf{L}_Z + \mathbf{g}_S \mathbf{S}_Z), \qquad \text{A.6}$$

where $\mathbf{B}_Z$, $\mathbf{L}_Z$, and $\mathbf{S}_Z$ are operators, not quantum numbers.

The $\mathbf{H}_Z$ operator connects[8] states that have the same value of the quantum number L and the quantum number S. This is easily seen from the matrix elements of $\mathbf{H}_{\text{Zeeman}}$,

$$\langle L'M'_L S'M'_S | \mathbf{H}_Z | L''M''_L S''M''_S \rangle = \beta \mathbf{B}_Z (M'_L + \mathbf{g}_e M'_S) \delta_{L'L''} \delta_{S'S''} \delta_{M'_L M''_L} \delta_{M'_S M''_S} \qquad \text{A.7}$$

where the laboratory Z-axis projections of $\mathbf{L}$ and $\mathbf{S}$, M_L and M_S respectively, are known. Clearly no new restriction is placed on the value of J even though, under field-free conditions, $\mathbf{J} = \mathbf{L} + \mathbf{S}$. Zeeman matrix elements between states with different values of the quantum number J are, in theory, allowed. When these elements are comparable in magnitude to the spacing of the field-free molecular energy levels, they can not be neglected in the simulation of MR spectrum. This is an important (and complicating) consequence of the field

[6]For describing coordinate systems, upper-case letters to refer to the laboratory or space-fixed system while lower case letters refer to the molecule fixed system (Lefebvre-Brion 1986; Zare 1988; Hougen 1970).

[7]When the field lies along the laboratory Z-axis, the g-factor tensor often reduces to single component scalar if the remaining anisotropic parts due to spin-orbit, lambda doubling, etc., are accounted for separately (Carrington 1969; Carrington 1970).

[8]That is to say, that there are non-zero matrix elements between the different states (sufficiently specified by the given labels).

destroying the spatial isotropy and high symmetry of field-free space.

A.3 *Individual Hund's case (a) states*

The Hund's case (a) rotational wavefunctions of diatomic (or linear polyatomic) molecules are,

$$|L\,\Lambda;S\,\Sigma;\Omega\,J\,M_J\rangle, \tag{A.8}$$

where Λ, Σ, *and* Ω are the molecule fixed projections of **L**, **S**, *and* **J** (*L*, *S*, *and J* are the quantum number wavefunction labels) respectively and all other labels (vibrational, or electronic, for example) have been suppressed for clarity. Note that the laboratory projections M_L and M_S are unknown even though $M_J = M_S + M_L$. Nonetheless, we can crudely estimate the largest possible energy shift due to the Zeeman effect using perturbation theory,

$$\Delta E_{Zeeman}(J',M_J) \approx \frac{\langle J'\,M_J;S|\mathbf{H}_Z|J'\,M_J;S\rangle^2}{E_{J',M_J}-E_{J'',M_J}} = \frac{[(J'+S)\beta\mathbf{B}_Z]^2}{E_{J',M_J}-E_{J'',M_J}} \tag{A.9}$$

because the maximum of $M_L + \mathbf{g}_s M_S = M_J - (\mathbf{g}_s - 1)M_S$ is approximately $J+S$. Clearly, the above approach fails when the energy denominator, the difference in the field-free energies of the two rotational levels J' and J'', becomes small. For Hund's case (a) states, the difference $E_{J',M_J} - E_{J'',M_J}$ is large compared to the

numerator in equation A.9 because the energy levels are well separated[9]. Therefore, the Zeeman matrix elements between levels with different values of J, which are vanishingly small, can be neglected entirely. Neglecting these "off-diagonal" matrix elements is equivalent to assuming that $\mathbf{J} = \mathbf{L} + \mathbf{S}$ holds in the presence of the magnetic field. Another way to express this idea is that the field is *so weak* that $\mathbf{L}$ and $\mathbf{S}$ are still coupled (to the molecular frame) to form $\mathbf{J}$.

In this weak field (spin-coupled limit), we use the expressions developed in appendix B with the restriction $\Delta J = 0$ to find the *energy shifts* due to the Zeeman effect for the Hund's case (a) molecule[10],

$$E'^{a}_{Z} = \frac{g_a \beta B_Z \Omega M_J}{J(J+1)}, \qquad \text{A.10}$$

with the new molecular Hund's case (a) g-factor[11] defined,

$$g_a = \Lambda + g_S \Sigma. \qquad \text{A.11}$$

The overall energy spread of the molecular $2J + 1$ components scales approximately as $\frac{1}{J}$. This is shown in figure A.1. As J increases, the number

---

[9]See Lefebvre-Brion 1986. The energy denominator is certainly large for states with large spin orbit interaction. As the denominator becomes small (perhaps at high J), the MR effect for this state is better described using the Hund's case (b) treatment given latter.

[10]Another route to the same result uses the "classical" vector model. See Herzberg 1989, 301.

[11]For simplicity, the new g-factor is a scaler. Therefore the field is now a scaler.

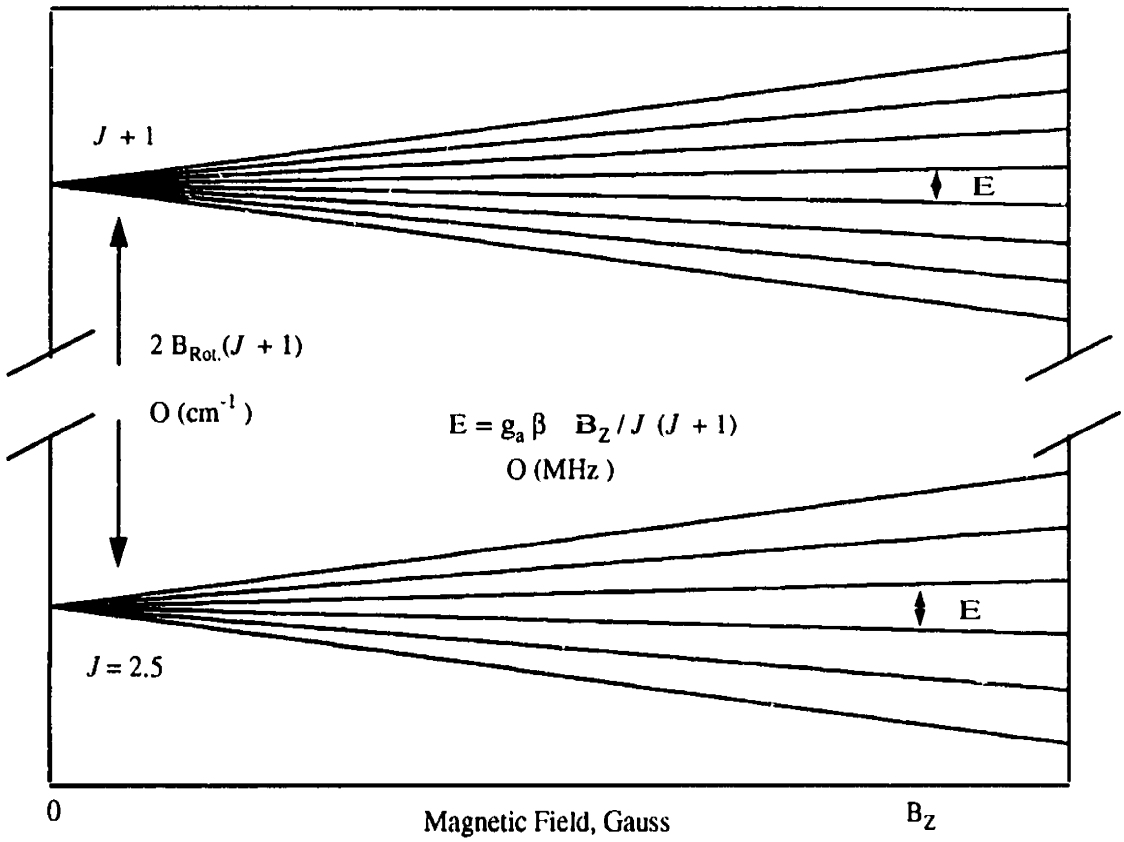

Figure A.1: Energy Levels of a Hund's case (a) molecule in a weak magnetic field, $\mathbf{B_Z}$. The lower "fan" pattern is for the 6 M_J components of a $J = 2.5$ level, while the upper pattern with 8 components is for a $J = 3.5$ level. The splitting between the two fan patterns is primarily due to molecular rotation, characterized by the constant $B_{Rot.}$, and is on the order of cm^{-1}. However, the splitting between the $2J + 1$ components within each fan are considerably smaller, on the order of the electron bohr magneton.

of components increases as $2J + 1$, only to be "squashed" (Steinfeld 1974, 182) into less and less (energy) space!

A.4 *MR transitions between Hund's case (a) states*

This section develops expressions for laser induced MR transitions between two Hund's case (a) states. In an MRS (or FM-MRS, see chapter 3) experiment a linearly polarized laser beam traverses a sample that has been placed in a magnetic field. The magnetic field axis always lies along the laser propagation axis. An analyzer polarizer is placed in the beam path after the sample cell and rotated to extinguish the laser beam. In this crossed polarizer configuration, the MR spectrum measures circular birefringence (Liftin 190; McCarthy 1992a). The linearly polarized laser is composed of both right-handed, σ^+, and left-handed, σ^-, circularly polarized light[12]. Hence, the MR spectrum measures the *difference* in the dispersion experienced by these two circular components of the probe field. Therefore our interest lies only in the transitions circularly polarized light induces between arbitrary Hund's case (a) electronic states.

All of the allowed transitions are found using the formulas presented in appendix B[13]. The relevant laboratory-fixed electric dipole moment operators

[12]For relationships between the coordinates systems see chapter 3.

[13]An alternate, but less sophisticated approach is offered in the excellent monograph by J. Hougen (Hougen 1970).

are μ_1 for σ^+ light and μ_{-1} for σ^+ light (Zare 1988, 283). The results are, where the primes indicate final states, and the double-primes designate initial states: for σ^+, $M'_J = M''_J + 1$ and $\Omega' - \Omega'' = 0 \text{ or } \pm 1$; for σ^-, $M'_J = M''_J - 1$, and $\Omega' - \Omega'' = 0 \text{ or } \pm 1$.

The energies of the various allowed transitions are found using equation A.10. The transition energies are, where the electronic, vibrational, and rotational transition *energies* and quantum numbers have been suppressed for clarity,

$$\Delta E_Z^a(\Lambda'\ \Sigma'\ \Omega'\ J'\ M'_J, \Lambda''\ \Sigma''\ \Omega''\ J''\ M''_J) = \beta B_Z \left[\frac{g'_a \Omega' M'_J}{J'(J'+1)} - \frac{g''_a \Omega'' M''_J}{J''(J''+1)} \right] \qquad \text{A.12}$$

Using the M_J-selection rules given above, we simplify equation A.12,

$$\frac{\Delta E_Z^a(J'\ M_J \pm 1, J''\ M_J)}{\beta B_Z} = \mp \left[\frac{g'_a \Omega'}{J'(J'+1)} \right] + M_J \left[\frac{g'_a \Omega'}{J'(J'+1)} - \frac{g''_a \Omega''}{J''(J''+1)} \right] \qquad \text{A.13}$$

Equation A.13 is equivalent to the result given without derivation in McCarthy 1992a/b.

The first term in equation A.13 is independent of M_J. It represents the energy *splitting* between the two groups of σ^+ and σ^- transitions, known as the centroid splitting (McCarthy, 1992a/b). The second term is M_J-dependent. It describes the energy *spread* of the M_J transitions caused by different g-factors or quantum numbers in the two Zeeman-split states involved.

A.5 *Simulation of Hund's Case (a) MR spectra*

The process of simulating MR spectra is illustrated by figure A.2. MR spectra for various transitions of the NiH $B^2\Delta_{5/2}-X^2\Delta_{5/2}(1,0)$ band discussed by McCarthy 1992 are presented as examples.

In the first step of the simulation, the transition energies of all allowed MR transitions are calculated using equation A.13 while the corresponding relative transition intensities are calculated using the formulas given in appendix B[14]. Table A.1 lists this information for the Q(2.5) transition with identical upper and lower state constants (including g-factors) for 300 Gauss. In this case the second term in equation A.13, the spreading term, is zero. Also note that the sum of the intensities of the 5 ΔM_J transitions is equal to the zero-field Hönl-London intensity. This information is also displayed in a "stick" spectrum in the top panel of figure A.2

In a stick spectra, the sign of $\Delta M_J = M'_J - M''_J$ is indicated by plotting the intensity times ΔM_J. Therefore σ^+ induced transitions with $\Delta M_J = 1$ are plotted upward going while σ^- transitions with $\Delta M_J = -1$ are plotted negative going. Furthermore, degenerate sticks with the same value of ΔM_J are simply drawn on top of each other in the stick spectrum, rather than piled up, so that the intensity

[14]Only the relative intensities are calculated because $\langle L'\Lambda';S'\Sigma'|\mu_z|L''\Lambda'';S''\Sigma''\rangle$ is an unknown factor. See Hougen 1970 and Zare 1988, 285.

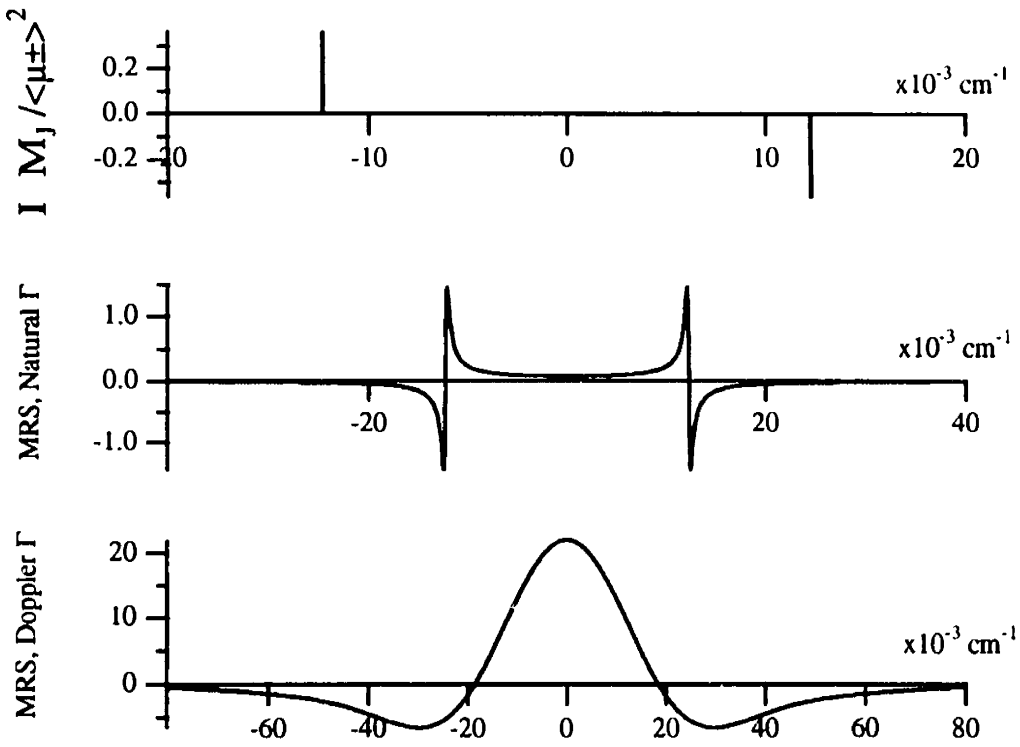

Figure A.2: Graphical illustration MR spectral simulation for the Q(2.5) line of the NiH $B^2\Delta_{5/2}-X^2\Delta_{5/2}(1,0)$ band (McCarthy 1992). The electronic, vibrational, and rotational energies have been removed. The magnetic field was 300 Gauss. The upper and lower g-factors for this transition are identical. The top panel is the stick spectrum. The middle panel shows the stick spectrum broadened by convolution with a dispersion profile, $\Gamma_{Nat.}$ =10 MHz. The bottom spectrum is the convolution of the middle spectrum with a Doppler profile with Γ_{Dop}=0.85. See text for details.

Table A.1 Relative Zeeman transition energies and transition Intensities[a] and zero-field parameters[b] for a Hund's case (a) Q(2.5) $\Delta\Omega = 0$, $\Omega = 2.5$ transition with electronic, vibrational and rotational energies removed.

	$\Delta M_J = M'_J - M''_J = 1$		$\Delta M_J = M'_J - M''_J = -1$	
M'_J	ΔE_Z^a	$\frac{I}{\langle \mu_\pm \rangle^2}$	ΔE_Z^a	$\frac{I}{\langle \mu_\pm \rangle^2}$
-2.5	-0.0122851	0.204082		
-1.5	-0.0122851	0.326531	0.0122851	0.204082
-.5	-0.0122851	0.367347	0.0122851	0.326531
+.5	-0.0122851	0.326531	0.0122851	0.367347
+1.5	-0.0122851	0.204082	0.0122851	0.326531
+2.5			0.0122851	0.204082
$\sum_{M'_J} \frac{I}{\langle \mu_\pm \rangle^2}$		1.42857		1.42857
Zero-Field	0.0000000	1.42857	0.0000000	1.42857

(a) $\langle \mu_\pm \rangle = \langle \Lambda' \Sigma' \Omega' | \mu_\pm | \Lambda'' \Sigma'' \Omega'' \rangle$, see appendix B; (b) calculated using standard Hönl-London formulas. See Hougan 1970 and Zare 1988, 287.

shown is that of the strongest single stick at a specific energy.

Next, each signed stick is converted into a dispersion profile with an appropriate width (determined for *cw*-laser MRS usually by the natural and

Doppler widths) and the dispersion profiles are summed. For simplicity this is done in two steps. First, the stick spectrum is convolved with a unit-peak height dispersion line shape profile with a width determined by the transitions natural-line width (estimated as $\Gamma_{Nat.}$ =10 MHz full width at half maximum[15]). Performing this operation on the stick spectra in the top panel of figure A.2 yields the middle panel of the figure.

In the second step of the stick-broadening process, the natural-line width dispersion spectrum (the middle panel of figure A.2) is convolved with a unit-peak height Doppler profile (to account for the laboratory distribution of molecular velocities)[16]. For NiH at 300 K, a Doppler profile with Γ_{Dop}=0.85 GHz FWHM was used. Performing the convolution on the spectrum in the middle panel of figure A.2 yields the bottom panel of the figure. This spectrum is the *relative* MRS spectrum (because only the relative intensity has been used), and appears in this particular case similar to the second derivative of a Gaussian.

Figures A.3 illustrates the calculation of MR spectra for the Q(3.5) of the same branch illustrated in figure A.2. Table A.2 lists the relevant transition data. This Q(3.5) transition involves lower and upper levels with slightly different g-

---

[15]Personal Communication with M. C. McCarthy

[16] The Plasma Dispersion Function, Z, is a closed form function for the convolution of a dispersion profile with a Gaussian distribution. Although approximate numerical tables are available (Fried 1961), analytic calculation of Z is difficult (Seigman 1986, 162,173). Hence, discrete convolution on a computer (in two steps) is the preferred method.

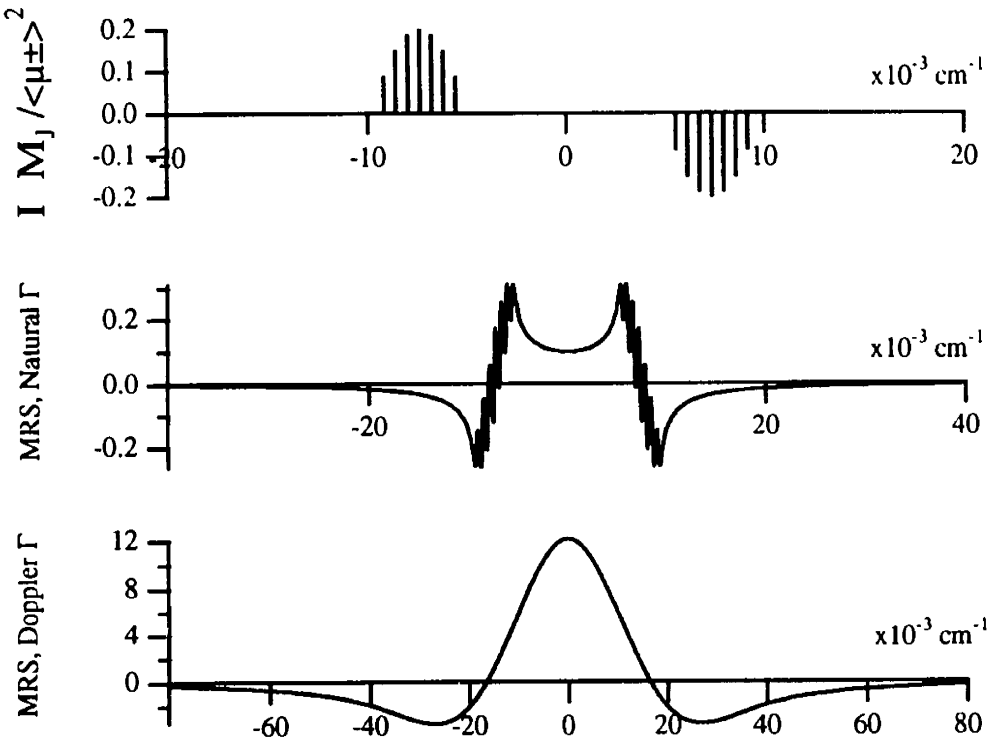

Figure A.3: Graphical illustration MR spectral simulation for the Q(3.5) line of the NiH $B^2\Delta_{5/2}-X^2\Delta_{5/2}(1,0)$ band (McCarthy 1992). All of the parameters are exactly the same as for figure A.2, except that now the Q(3.5) transition involves lower and upper levels with slightly different g-factors, 3.18 and 3.45 respectively. Hence, all transitions occur at slightly different energies and are resolved completely in the plot in the middle panel here.

-factors, 3.18 and 3.45 respectively. Therefore the spreading term in equation A.14 is non-zero, and there are no degenerate sticks in the top panel of the figure. The resulting Doppler broadened MR spectrum is less intense than the spectrum from the Q(2.5) line. In a zero-field absorption experiment, the Q(2.5) to Q(3.5) intensity ratio would be 1.4, while in the Doppler limited MR experiment, the corresponding ratio is about 1.8.

Figure A.4 illustrates the calculation of MR spectra for the P(5.5) line of the same branch illustrated in figure A.2. Although none of the experimental parameters are different from those used in calculating figure A.2-3, the P(5.5) transition involves levels with both different J-values and different g-factors. Hence, the spread of the two groups of transitions is larger that the centroid splitting. This ultimately leads to a considerable less intense peak MR signal than found for the Q transitions and an overall lineshape with opposite phase.

A.6 *Hund's case (a) analysis*

The results of the MR spectral simulations are summarized in table A.3. When the second term in equation A.13 is zero there is no spreading of the transition energies within the two sets of ΔM_J transitions so that the individual dispersion curves of one set always perfectly overlap. These dispersion curves (that occur

Table A.2 Relative Zeeman transition energies and transition Intensities[a] and zero-field parameters[b] for a Hund's case (a) Q(3.5) $\Delta\Omega = 0$, $\Omega = 2.5$ transition with electronic, vibrational and rotational energies removed.

		$\Delta M_J = M'_J - M''$		$\Delta M_J = M'_J - M''$	
	M	ΔE	$\frac{I}{\langle \mu_\pm \rangle^2}$	ΔE_Z^a	$\frac{I}{\langle \mu_\pm \rangle^2}$
	-3.5	-0.00556897	0.0881834		
	-2.5	-0.00616922	0.151172	0.00917046	0.0881834
	-1.5	-0.00676947	0.188964	0.00857022	0.151172
	-.5	-0.00736972	0.201562	0.00796997	0.188964
	+.5	-0.00796997	0.188964	0.00736972	0.201562
	+1.5	-0.00857022	0.151172	0.00676947	0.188964
	+2.5	-0.00917046	0.0881834	0.00616922	0.151172
	+3.5			0.00556897	0.0881834
$\sum_{M'_J} \frac{I}{\langle \mu_\pm \rangle^2}$			1.0582		1.0582
Zero-Field		0.0000000	1.0582[b]	0.0000000	1.0582[b]

(a) $\langle \mu_\pm \rangle = \langle \Lambda' \Sigma' \Omega' | \mu_\pm | \Lambda'' \Sigma'' \Omega'' \rangle$, see appendix B; (b) calculated using standard Hönl-London formulas. See Hougan 1970 and Zare 1988, 287.

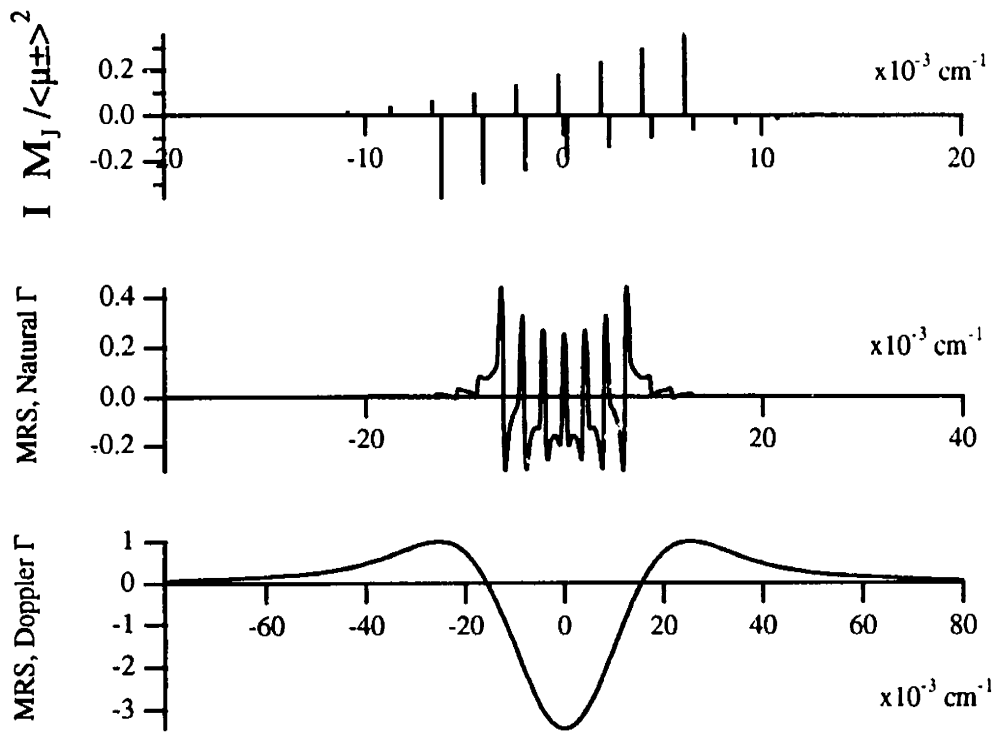

Figure A.4: Graphical illustration MR spectral simulation for the P(5.5) line of the NiH $B^2\Delta_{5/2}-X^2\Delta_{5/2}(1,0)$ band (McCarthy 1992). All of the parameters are exactly the same as for figure A.2, except that now the the P(5.5) transition involves levels with both different J-values and different g-factors. Hence, the spread of the transitions is larger that the centroid splitting in the top panel. This results in the complicated spectrum in the middle panel, and the weak and opposite phase (relative to the Q(2.5) line) MR signal.

Table A.3: Results of Hund's case(a) MR simulations for some NiH $B^2\Delta_{5/2}-X^2\Delta_{5/2}(1,0)$ transitions.

	Intensity relative to Q(2.5)			
	Absorption	MRS	ΔJ	$g'_a-g''_a$
Q(2.5)	1	1	0	0
Q(3.5)	.74	.55	0	0.27
P(5.5)	1.02	-.16	-1	0.43

for a value of ΔM_J) have the same relative phase. When they overlap without any frequency displacement there is no interference. This leads to the fact that the largest MR signal occurs when the spreading term is zero, as it was for the Q(2.5) transition. As the spreading term deviates from zero, the individual dispersion curves no longer perfectly overlap. Due to the fact that the dispersion curves are bipolar functions, the overlap of displace curves results in interference and ultimately a reduction of MR signal, as it was for the Q(2.5) transition. When the spreading term becomes comparable to the centroid splitting, the dispersion curves from the two different sets of ΔM_J transitions now interfere in a complicated manner. In general the MR signal is then small, as it was for the P(5.5) transition. The MR signal also reflects the overall sign of the second term

in equation A.13. The sign of the MR signal can be used to separate a transition from one branch with one value of ΔJ from another branch with a different value of ΔJ. One branch out of the three possible ΔJ branches can always be uniquely separated in this manner. However, the ΔJ value of the unique branch is not determinable *a priori* unless the g-factors are already known.

When the second term in equation A.13 is zero, a useful expression for the optimal magnetic field can be derived. Consider the MR spectrum that arises in such a case, shown in figure A.2. Ultimately, the MR signal is generated by the interference of only two opposite-phase dispersion profiles (one for each value of ΔM_J). If these opposite-phase curves were displaced from each other by one-half of their full-width at half-maximum (FWHM) maximally *constructive* overlap would occur. Hence, for this case when equation A.13 is M_J-independent, the most intense MR signal[17] occurs when the centroid splitting is precisely half the Doppler width. Therefore the optimal magnetic field is (for Q branches),

$$B_{opt} = \frac{\Gamma_{Dop} J(J+1)}{4 g_a \beta \Omega} \qquad \text{A.14}$$

[17]The phrase "most intense signal" is meant to imply largest signal deviation from zero, positive or negative. Alternative measures of intensity could be used, such as the integral of the absolute value of the signal. However, methods relying on such an integral overemphasize broad flat lines (that are often harder to detect experimentally) over narrow, sharper ones (that are easier to detect).

where Γ_{Dop} is the (effective)[18] full width at half maximum of the Doppler distribution.

Because B_{opt} increases quadratically with J it can be used to immediately deduce the relative J-numbering of the lines in one branch. If B_{opt} is measured with sufficient accuracy over enough lines, the actual J- value could be found from a single branch. To do so, one needs to know what type of branch (P, Q, or R) is being observed *and* that the upper and lower state effective g-factors are identical. Unfortunately, however, as J increases, the $\mathbf{g}_a\Omega$ factors tend to increase and differ from each other. So that this method of determining the value of J is rarely applicable.

When the second term in equation A.13 is not zero, a simple expression for optimal field can no longer be found. If the displacements of the same-phase dispersions within each ΔM_J group of transitions become comparable to the centroid splittings, the MRS signal tends not only to be small, but also it cannot be substantially increased by changing the value of the magnetic field[19], because both terms in equation A.13 scale identically with B. For moderate spreading

[18]The actual effective FWHM of the Doppler broadened dispersion profile is not the FWHM of the Doppler distribution owing to the small contribution from the (homogeneous) dispersion FWHM. If the plasma-dispersion function (mentioning in the preceding note) was used to describe the final line shape, its argument Z would have been a complex number.

[19]The MRS signal for higher J lines can always be increased from the value obtained at the optimal field value from a lower J line. For the P(5.5) line featured in figure A.5, the signal increases to a maximum at about 1200 Gauss, but at this field the signal is still only 1/3 of the Q(2.5) line's intensity (at 300G).

less than the centroid splitting, some signal improvement can be gained by optimization of the magnetic field using (the now approximate) equation A.14.

In conclusion, Hund's case (a) MR spectra are expected to have some predicable J, ΔJ and magnetic field dependances that can be exploited to help identify a specific transition. Transitions can be grouped by ΔJ by the relative sign or phase[20] of the MR signal and the relative J numbering can be established by a combination of measuring the field dependance of the signal, and the fact that the MR signal decreases as J-increases. In fact, the MRS signal decreases at a somewhat faster rate than the signal from absorption spectroscopy does, because as J increases $g'_a - g''_a$ tends to grow, the magnitude of the spreading term increases (equation A.13) and the same-phase dispersion curves within one ΔM_J group destructively interfere. This effect, termed MR low-J intensity enhancement (McCarthy 1992), can in fact be quite substantial and useful in specific cases (see chapter 4).

Using MRS, one can also identify specific transitions in complicated spectra because only those Q branch transitions with identical $\mathbf{g}_a\Omega$ products or $J' \neq J''$ transitions with the differing J-values perfectly offset by different $\mathbf{g}_a\Omega$ values

[20]Although not demonstrated yet (see discussion of Hund's case (b)), the MR line shape need not have second-derivative of a Gaussian profile and then, the idea of "phase" and its usefulness must be examined on a case by case basis with the aid of line shape predictions. For example, although incredibly weak, the predicted line shape of the P(3.5) line is quite different from that of the P(5.5) line.

are expected to have the strongest signals. For $J' \neq J''$, the MR signal is at its maximum usually when $\Delta\Omega = \Delta J$.

A.7 *Introduction to Hund's case (b) MR spectra*

Both the Zeeman effect and the calculation of MR spectra fo. Hund's case (b) molecules are, in general, more complicated than for Hund's case (a) molecules. This occurs because Hund's case (b) molecules have many eigenstates at nearly the same energy. We cannot, therefore, expect to find a simple expression analogous to the case (a) results for the Zeeman energies or even use perturbation theory. Since many, if not most, Hund's case (b) molecules have states with zero total electron orbital angular momentum (Σ states, Hirota 1985, 64), we will consider only such states here, noting that straightforward extension to all other Hund's case (b) states is possible, albeit at the cost of additional computational complexity. Furthermore, we restrict this discussion to linear molecules, recognizing that Hund's case (b) non-linear polyatomic Σ states are treated very similarly.

A.8 *Individual Hund's case (b) states*

Hund's case (b) diatomic (or linear) molecules are sufficiently described by

the following wavefunctions (Hougen 1962)

$$|L\,\Lambda;\,N\,S\,J\,M_J\rangle, \qquad \text{A.15}$$

where $\mathbf{J}$ is the sum of $\mathbf{N}$ and $\mathbf{S}$, and all other *labels* have been suppressed for clarity. Since we are considering only states with no total orbital angular momentum, $\Lambda = 0$, we can specify the wavefunctions more simply as

$$|N\,S\,J\,M_J\rangle, \qquad \text{A.16}$$

still with $\mathbf{N}$ and $\mathbf{S}$ coupled. As before, we will be interested in calculating all the matrix elements of laboratory-fixed operator $\mathbf{S}_z$ only. However, for the Hund's (b) wavefunctions given in equation A.16, the molecule-fixed projection of $\mathbf{S}$ is not specified. Hence, the calculation of the Hund's case (b) matrix elements will be performed differently than it was for Hund's case (a).

Two different approaches can be used find the needed matrix elements. Initially, a somewhat clumsy, yet intuitive approach to find the laboratory projections will be presented in which $\mathbf{N}$ and $\mathbf{S}$ are uncoupled using the Clebsh-gordan coefficients[21] or 3-J symbols. Later, a more powerful (Zare 1988, 180) yet somewhat mysterious spherical tensor algebraic method will be employed.

The effective Hamiltonian model for a Hund's case (b) state in a magnetic

[21]See, for example, Edmonds 1960, 38.

field includes a number of interactions even when the electronic and vibrational energies are ignored,

$$\mathbf{H}_b = \mathbf{H}_{Rot} + \mathbf{H}_{Spin-Rot} + \mathbf{H}_{Spin-Spin} + \mathbf{H}_{Zeeman} \qquad \text{A.17}$$

$\mathbf{H}_{Rot}$ is the rotational contribution, whose matrix elements,

$$\langle | \mathbf{H}_{Rot} | \rangle = BN(N+1) - D[N(N+1)]^2 \qquad \text{A.18}$$

are purely diagonal in a Hund's case (b) basis set (Lefebvre-Brion 1986, 41). $\mathbf{H}_{Spin-Rot}$, the most important of the Hund's case (b) fine structure interactions (Hirota 1985, 24), accounts for the (linear molecule) spin-rotation interaction,

$$\mathbf{H}_{Spin-Rot} = \gamma N \cdot S, \qquad \text{A.19}$$

with the purely diagonal and simple matrix elements (Lefebvre-Brion 1986, 94),

$$\langle | \mathbf{H}_{Spin-Rot} | \rangle = \gamma/2[J(J+1) - N(N+1) - S(S+1)]. \qquad \text{A.20}$$

While $\mathbf{H}_{Spin-Spin}$, which models the spin-spin interaction,

$$\mathbf{H}_{Spin-Spin} = 2/3\lambda(3\mathbf{S}_Z^2 - \mathbf{S}^2) \qquad \text{A.21}$$

is needed only for $S \geq 1$ states. The matrix elements of $\mathbf{H}_{Spin-Spin}$ are

unfortunately not only complex, but they also connect states with $\Delta N = 0$, *and* $\Delta N = \pm 2$ (McDonald 1985, 93),

$$\langle N' S J | \mathbf{H}_{Spin-Spin} | N'' S J \rangle = \lambda (-1)^{N'+N''+S+J} \sqrt{(2N'+1)(2N''+1)} \times \begin{Bmatrix} N' & S & J \\ S & N'' & 2 \end{Bmatrix} \begin{pmatrix} N'' & 2 & N' \\ 0 & 0 & 0 \end{pmatrix} \quad \text{A.22}$$

The Zeeman Hamiltonian, $\mathbf{H}_{Zeeman}$, is the same as described earlier by equation A.6. For Hund's case (b) electronic states there are $2S + 1$ (or $2J + 1$ for $N < S$) different J-levels with the same N-value[22]. These different J-levels all have identical rotational energy, yet they are not *exactly* degenerate because of small energy shifts due to the J dependant spin-rotation and spin-spin matrix elements. The energy spread of the same-N different J-levels is primarily determined by the two (largest) fine-structure constants, γ and λ. Even when the magnetic field is weak, these fine-structure splittings may be comparable to the Zeeman interaction! Hence, the entire Hamiltonian must be considered at one time; the Zeeman effect is not a small perturbation to Hund's case (b) states.

A.8.1 *Intuitive approach to the Hund's case (b) Zeeman effect*

To calculate the matrix elements of the entire Hamiltonian which contains $\mathbf{S}_Z$, we need to find the laboratory fixed projections of $\mathbf{S}$ and $\mathbf{N}$ that are not specified in the wavefunctions of equation A.16, written $|N S J M_J\rangle$. The $\mathbf{J} = \mathbf{N} + \mathbf{S}$

[22]Recall that the possible maximum degeneracy of any level is limited to the *maximum* of either $2N+1$ or $2S+1$.

coupled basis set must be expressed as a sum over the **S**, **N** *uncoupled* basis set $|N M_N\rangle|S M_S\rangle$ (Brown 1976), *via*,

$$|N S J M_J\rangle = \sum_{M_S, M_N} (-1)^{N-S+M_J}\sqrt{2J+1}\begin{pmatrix} N & S & J \\ M_N & M_S & -M_J \end{pmatrix}|N M_N\rangle|S M_S\rangle \quad \text{A.23}$$

The sum is actually over the single index M_N *or* M_S since M_J,

$$M_J = M_N + M_S \quad \text{A.24}$$

is *still* a rigorously good quantum number. The *only* non-zero Zeeman matrix elements are then,

$$\langle N S J' M_J|\mathbf{S}_z|N S J'' M_J\rangle = \sum_{M_S=-S}^{S}(-1)^{2S}\sqrt{(2J'+1)(2J''+1)}\times \begin{pmatrix} N & S & J' \\ M_J-M_S & M_S & -M_J \end{pmatrix}\begin{pmatrix} N & S & J'' \\ M_J-M_S & M_S & -M_J \end{pmatrix} \quad \text{A.25}$$

Since equation A.25 provides for non-zero matrix elements with $\Delta J \neq 0$, our Hamiltonian matrices are best organized by the good quantum number M_J. A typical matrix is shown in table A.4. Sub-blocks with a constant value of N appear with dimensions of $2S + 1$ x $2S + 1$ (for $N \geq S$). Each different J-level within each sub-block is coupled to neighboring J-levels within the same sub-block by the Zeeman interaction. But, the spin-spin interaction couples the N-

Table A.4: Hamiltonian Matrix for a Hund's case (b) state in a magnetic field organized by M_J

M_J		N			N+1			N+2		
		J=N-S... ...J=N+S			J=N-S+1... ...J=N+S+1			J=N-S+2... ...J=N+S+2		
	J'=N'-S	X	Z	Z				SS		
N'	....	Z	X	Z						
	J'=N'+S	Z	Z	X						
	J'=N'-S+1				X	Z	Z			
N'+1	....				Z	X	Z			
	J'=N'+S+1				Z	Z	X			
	J'=N'-S+2	SS						X	Z	Z
N'+2	....							Z	X	Z
	J'=N'+S+2							Z	Z	X

X is the total diagonal energy equal to the sum of the rotational, spin-rotation, Zeeman, and for S>0.5, the (diagonal portion) of the spin-spin interactions; Z is the off diagonal *J*-mixing Zeeman interaction contribution; SS stands for the off-diagonal spin-spin interaction.

sub-blocks to one-another with the selection rule $\Delta N = \pm 2$ When the spin-spin interaction exists ($S \geq 1$) each matrix for each value of M_J is truly infinite dimensional and does not factor into independently treatable sub-blocks of finite size! For S = ½, (a doublet state), there is no spin-spin interaction. For doublet states, each M_J-matrix conveniently factors into unconnected sub-blocks of dimension 2 x 2. These small matrices can be handled easily, and we analyze the most important aspects of the Hund's case (b) MR effect through them. Later, computer diagonalization of truncated matrices can be used to illustrate examples of higher multiplicity $S \geq 1$ states.

We would like to obtain a closed form expression for the eigenvalues of the Hamiltonian matrix of a $^2\Sigma$ state. Rather than work out the necessary summation formula for the matrix elements in equation (A.25), we rederive the desired result by another route, fully expecting $\Delta J \neq 0$ matrix elements.

A.8.2 *Spherical tensor algebraic methods*

By applying a special case of the Wigner-Eckart theorem (Zare 1988, 195) for finding the matrix elements of an operator that acts only a subspace rather than the entire contracted coupled-space, we can immediately write down the Zeeman matrix elements (Hirota 1985, 65). In this case the subspace is **S**, the contracted

coupled space is $\mathbf{J} = \mathbf{N} + \mathbf{S}$, and the operator is $\mathbf{S}_z$,

$$\langle N\,S\,J'M_J|\mathbf{S}_z|N\,S\,J''M_J\rangle = (-1)^{J'-M_J}\begin{pmatrix} J' & 1 & J'' \\ -M_J & 0 & M_J \end{pmatrix}\langle J'\|\mathbf{S}_z\|J''\rangle, \qquad \text{A.26}$$

The reduced matrix element $\langle J'\|\mathbf{S}_z\|J''\rangle$ contains one Wigner 6-J symbol,

$$\langle J'\|\mathbf{S}_z\|J''\rangle = (-1)^{N+S+J+1}\sqrt{(2J'+1)(2J''+1)S(S+1)(2S+1)}\begin{Bmatrix} S & J' & N \\ J'' & S & 1 \end{Bmatrix}. \qquad \text{A.27}$$

The independent 2 x 2 sub-blocks of the matrices for a $^2\Sigma$ state are filled using equation A.27. For $|M_J| < (N + 1/2)$, the two eigenvalues of the sub-blocks are (Hirota 1985, 68),

$$E_\pm = -\gamma/4 \pm 1/2\sqrt{\gamma^2(N+1/2)^2 + 2\gamma\mathbf{g}_S\beta B_z M_J + (\mathbf{g}_S\beta B_z)^2}. \qquad \text{A.28}$$

For the extreme M_J levels with $|M_J| = (N + 1/2)$, the eigenvalues are

$$E_\pm = \frac{\gamma N}{2} \pm \frac{\mathbf{g}_S\beta B_z}{2}. \qquad \text{A.29}$$

For both equation A.28 and A.29, the energies in common to both eigenvalues has been neglected including the electronic, vibrational and rotational contributions. At *zero magnetic field,* the "+" eigenvalue subscript denotes $J = N + 1/2$ and the "-" subscript $J = N - 1/2$. The tuning of the M_J-levels of a $^2\Sigma$ state in a magnetic field is shown in figure A.5. The change of slope (slope=

tuning rate) of the curves is the molecular analogue of the atomic Paschen-Back effect. It is a general feature of the Zeeman effect for *all* Hund's case (b) states.

The tuning rate of the non-extreme $|M_J| < (N + 1/2)$ levels varies proportional to the square root of B_z at small fields. Yet, at large fields, the tuning rate is linear with B_z! A the smallest fields, the pattern of Hund's case (b) levels primarily depends on the M_J value. For Hund's case (a) states, the pattern always was determined by the M_J value.

Hund's case (b) molecules with small fine structure splittings quickly show splitting patterns according to the value of $M_S = M_J - M_N$. For the doublet states there are two possible values of M_S. At any field strength, the ± subscript labels on the eigenvalues in equations A.28 and A.29 indicate M_S. At large enough fields, the tuning rate of a doublet state becomes independent of the fine structure constant γ. In fact, at high fields, the Zeeman energy level pattern for any Hund's case (b) state will appear similar to the pattern from any other same multiplicity state regardless of the the fine structure constants: the pattern will consist of $2S + 1$ groups of lines with constant M_S for each N. In other words, the Zeeman effect becomes independent of the particular molecular model. This situation has been described as the spin uncoupling from the molecular framework and recoupling to the external laboratory field (Herzberg 1989, 303).

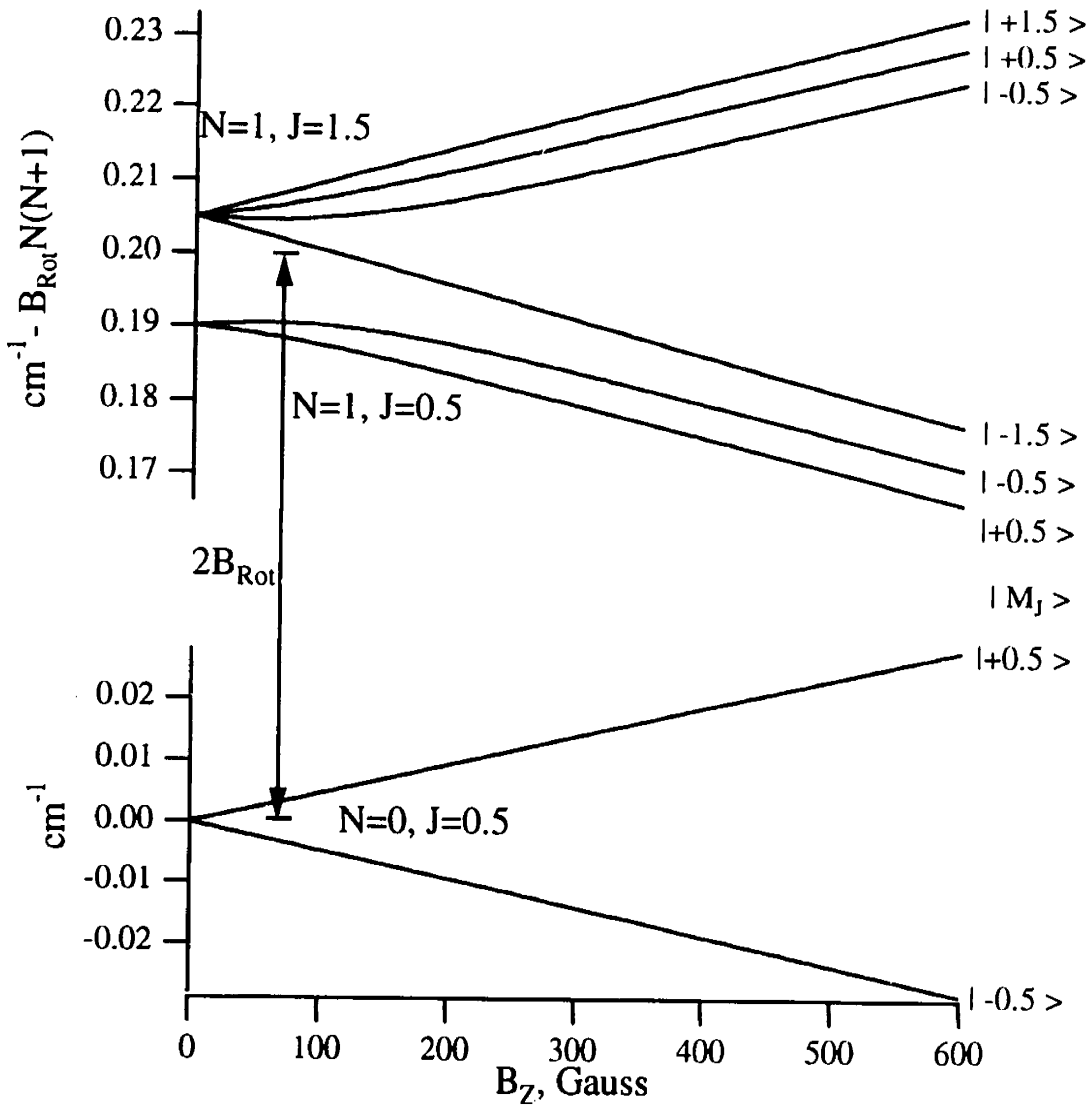

Figure A.5:Energy level diagram for $N = 0$ and $N = 1$ of a $^2\Sigma$ state in a magnetic field. Although the spin-rotation constant $\gamma = 0.01\ \text{cm}^{-1}$ is only one hundredth of the rotational constant, $B_{Rot} = 1.0\ \text{cm}^{-1}$, J-mixing nevertheless occurs rapidly for the $N = 1$, $|M_J| < N$ levels.

The patterns of Zeeman energy levels for $^4\Sigma$ states are shown in figures A.6 (small λ) and A.7 (large λ). These levels are calculated using the computer diagonalization of (the truncated) matrices for higher multiplicity states (see appendix C).

In these figures for the $^4\Sigma$ states, the patterns of levels are more complicated than those for $^2\Sigma$ states owing to the presence of four values of M_S and both the spin-rotation and spin-spin interactions. In figure A.8 , the spin-spin constant is large enough (0.10 cm^{-1}) that no perceptible spin-uncoupling occurs at typical MRS field strengths. Thus we expect Hund's case (b) states possessing large enough fine structure splittings (*at any multiplicity*) to have energy level patterns and MR spectra somewhat similar to Hund's case (a) states[23].

A.8.3 *Hund's case (b)-case(b) MR transitions*

Electric dipole transitions between Zeeman components of different Hund's case (b) states in the spin-uncoupled limit are still, *in principle*, allowed, even though this fact may not be immediately obvious. Consider the possible transitions between two $^2\Sigma$ states originating from the non-extreme $|M_J| < (N + 1/2)$ levels as an example. The energies of these levels is given in

[23]This will be shown later by considering the transitions from a rotationless level, which cannot spin-uncouple regardless of field or fine structure.

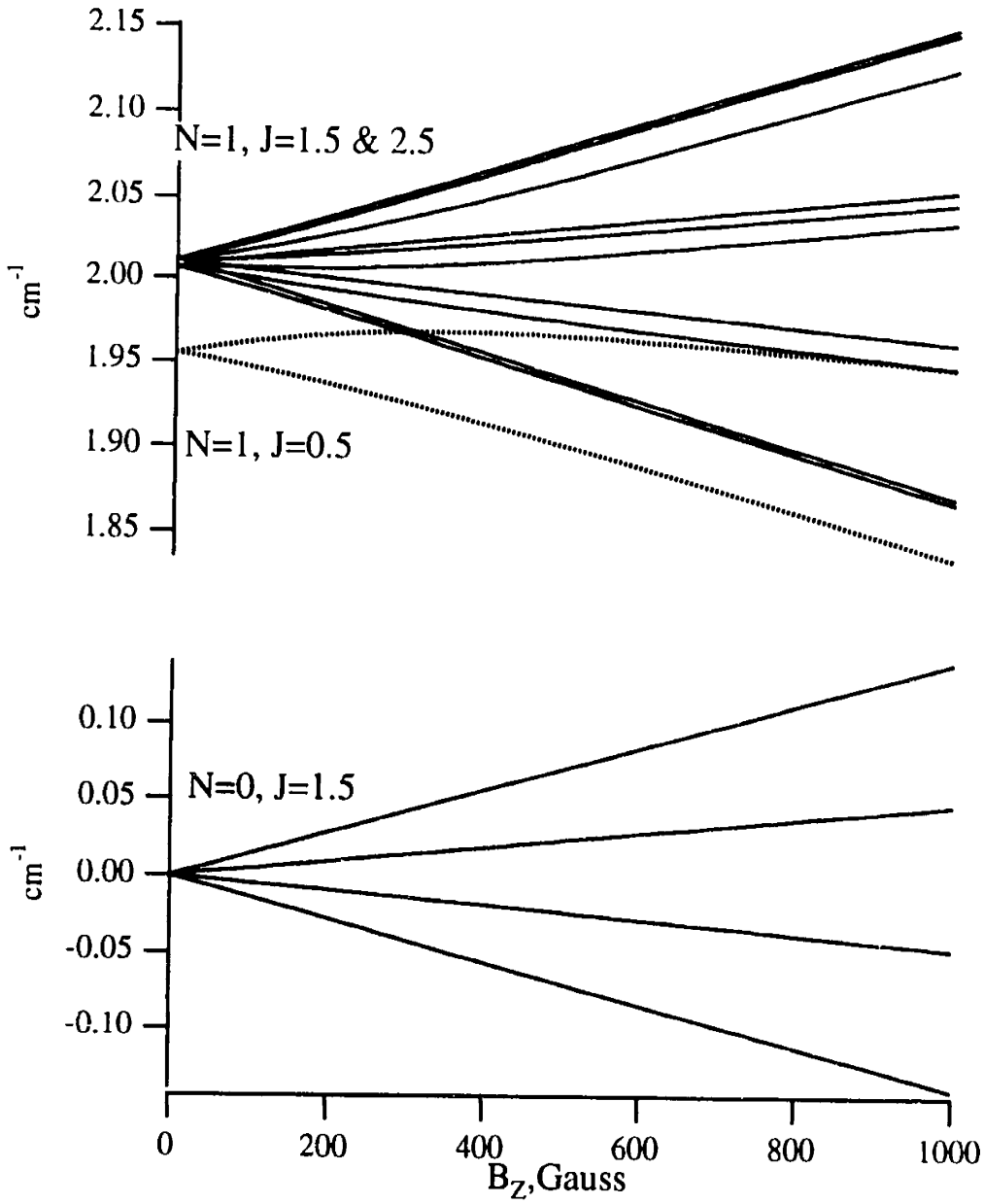

Figure A.6: Energy level diagram for $N = 0$ and $N = 1$ of a $^4\Sigma$ state in a magnetic field, with $B_{Rot} = 1.0\ cm^{-1}$, $\gamma = 0.01\ cm^{-1}$, and the spin-spin constant, $\lambda = 0.01\ cm^{-1}$. With higher multiplicity, spin-uncoupling occurs more rapidly even in the presence of a small spin-spin splitting.

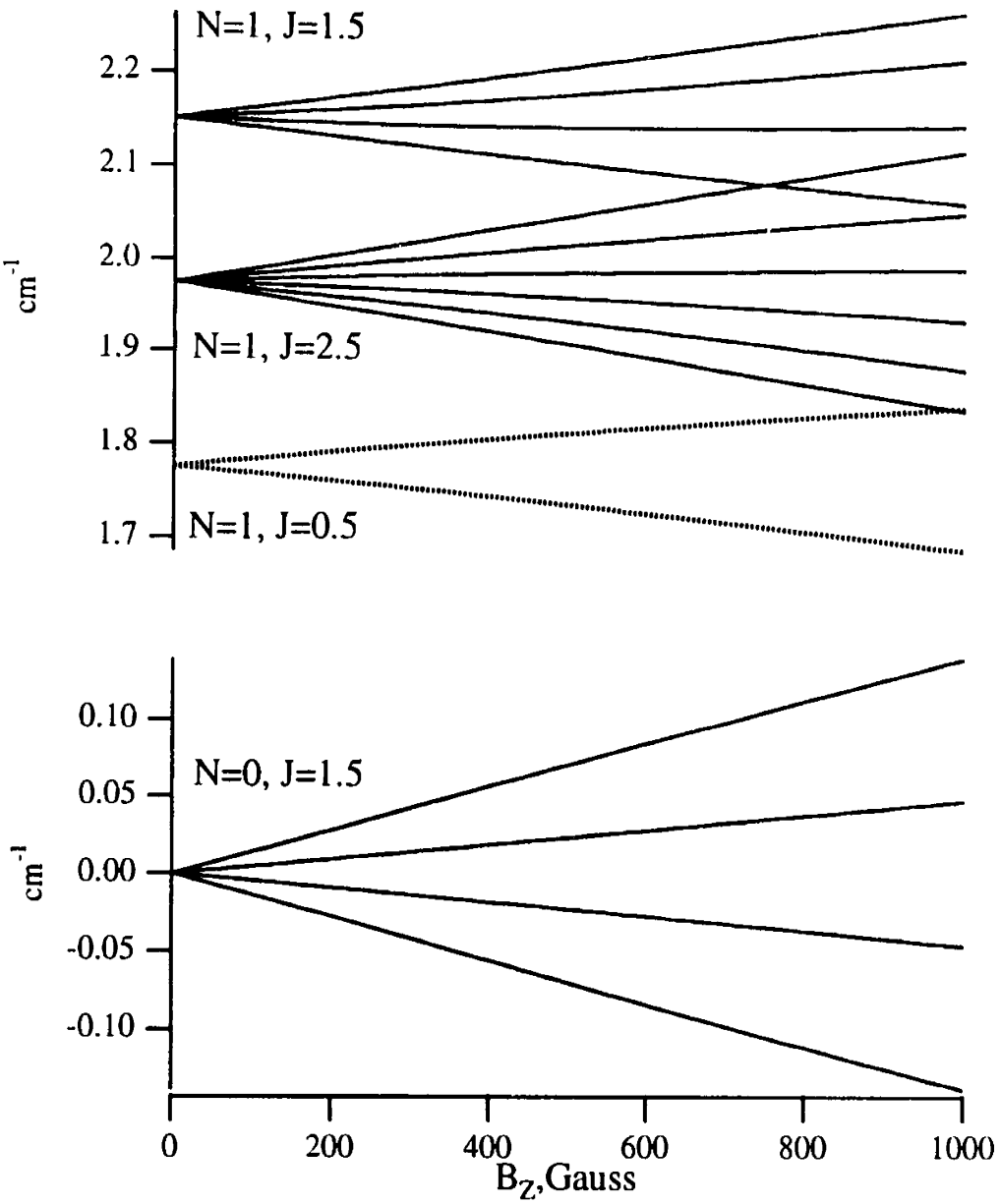

Figure A.7: Energy level diagram for $N = 0$ and $N = 1$ of a $^4\Sigma$ state in a magnetic field, with $B_{Rot} = 1.0\,cm^{-1}$, $\gamma = 0.01\,cm^{-1}$, and the spin-spin constant, $\lambda = 0.1\,cm^{-1}$. With a larger spin-spin interaction, spin uncoupling occurs more slowly than in figure A.6 and the various J-levels become easily identifiable.

equation A.28. As soon as the field is turned on, these non-extreme $|M_J| < (N + 1/2)$ levels become J- mixed, although M_S and M_J remain good quantum labels. Each of the two J- mixed eigenstates is a linear combination of two pure-J basis functions,

$$\psi_{\pm} = c_{1\pm} |N S J_1 M_J\rangle \pm c_{2\pm} |N S J_2 M_J\rangle \qquad \text{A.30}$$

The rigorous selection rule[24] is still $\Delta M_J \pm 1$. Therefore, the total MR electronic dipole transition intensity to-and-from such mixed-J eigenstates is now the *square of the sum* of four individual transition *amplitudes* involving the pure-J levels. The evaluation of the four individual transition *amplitudes* is still governed by the selection rule $\Delta J = \pm 1$ *or* 0. There is no mechanism to force the individual transition amplitudes to be zero, or to force interference to completely cancel their combined amplitudes. Therefore the total MR electronic dipole transition intensity will not be *a priori* zero. Similar qualitative arguments can be made for higher multiplicity states. Therefore one expects transitions even in the spin-uncoupled limit regardless of the states multiplicity. A reduction of MRS signal in the spin-uncoupled limit will not in general be caused by a loss of transition intensity, but rather by the field induced energy levels shifts that cause

[24]Some authors (such as Herzberg 1989) claim that the only useful selection rule is $\Delta M_S = 0$.

complicated interference of the individual dispersion curves (as was seen earlier for the P(5.5) Hund's case (a) transition).

A.8.4 *Analysis of Hund's Case (b) MR spectra*

The MRS spectra arising from a transition between two Hund's case (b) states are calculated using the same procedures that were used for Hund's case (a) state transitions earlier. In general, the peak MR signal for allowed transitions between two Hund's case (b) states will be somewhat *smaller* than for the same ΔJ and J'' transition between two Hund's case (a) states. This reduction occurs because certain Hund's case (b) M_J *transitions* will not tune at all with the magnetic field, although the energies of the individual *levels* involved do tune. If the individual transition energy does not tune, it will not contribute to the overall MRS signal for the line. The reduction is greatest at the lowest N (or J'') levels. The smallest reduction occurs for Hund's case (b) forbidden transitions and high N.

Consider the transitions from the lowest N-level of an arbitrary Hund's case (b) state $^2\Sigma$. Two sets of transitions are possible (use figure A.5 as a guide); a Q(0.5) line from the $N=0$, $J=\frac{1}{2}$ lower level to a $N=1$, $J=\frac{1}{2}$ upper level and a R(0.5) line from the $N=0$, $J=\frac{1}{2}$ lower level to a $N=1$, $J=\frac{3}{2}$ upper level[25].

For the Q(0.5) transition only two individual Zeeman transitions occur in the usual MR geometry (with the magnetic field along the laser propagation direction). At fields small enough so that the upper level has not spin-uncoupled, this case is identical to the Hund's case (a) situation, where we found enhancement. But unfortunately, Q branch transitions are forbidden between Σ states of the same multiplicity and hence their MRS signal will be weak (Kaledin 1996), and any enhancement will be likely undetectable.

For the R(0.5) line, there are *four* possible Zeeman transitions that can occur, although only *two* can contribute to the MRS signal at any field![26] This arises because the transitions involving the extreme M_J-components of each J-level originate and terminate at M_J-levels that tune at identical rates. Since they tune at identical rates, their associated opposite-phased dispersion curves always destructively interfere. In other words, no net circular birefringence can ever be created by two of the four possible Zeeman transitions. Therefore only half of the possible transitions contribute to the MR signal at this lowest-J level. A similar effect occurs for higher-J rotational transitions of this type. For the next higher-J transition, rather than half of the individual transitions, only one quarter of the the individual transitions do not contribute to the total MR signal.

[25]These are of course, zero-field J-values.

[26]This is the origin of the pseudo-selection rule $\Delta M_S = 0$, mentioned in an earlier note.

Effectively this erodes the lowest-J intensity enhancement we saw for Hund's case (a)- case (a) transitions.

If, however, the Hund's case (b) states are sufficiently perturbed so that Q lines are no longer "forbidden", their low-J level MRS signal can be enhanced (Yan 1985). This would be the only possible mechanism for a Hund's case (b)-case (b) selectively low-N or low-J enhanced MR effect. For Hund's case (b)-case (b) transitions, the MR effect enhancement should not be *a priori* expected to aid in spectral assignment of unperturbed transitions.

A.8.5 *Simulation of Hund's Case (b)-Case (a) MR spectra and analysis*

Many molecules that posses Hund's case (b)-like lower states, posses excited electronic states with rotational level structure that *closely* resembles typical Hund's case (a) states. This situation arises often since excited electronic states are often so "mixed" with the many neighboring excited states that they experience large spin-orbit like interactions. For the purpose of simulating MR spectra, we can think of these excited Hund's case (a) states as a Hund's case (b) state with infinitely large (diagonal) fine structure constants[27] arising from this "mixing".

[27]This is not technically correct, but rather just a useful approximation so that we can maintain the quantum number N, neglect Ω, and retain the simplicity of a pure basis state picture. This approximation does not noticeably reduce the quantitative accuracy of our treatment.

MR transitions between the two different types of states should not be assumed to be weak simply because they are "forbidden" in the pure-state limits (Yan 1985; Herzberg 1989) . The situation is complicated so we must consider the specific fine structure of the case (b) state involved. This posses a fundamental problem; without *a priori* knowledge of the exact values of the Hund's case (b) fine structure constants the MRS spectrum for these mixed type transitions cannot be accurately predicted.

In the earlier treatment of Hund's case(a) - case (a) transitions this difficulty does not arise because the Zeeman effect for these states depends on the almost integer (and often known) g-factors and Ω-values, but with Hund's case (b) states, the energy level structure is *very* sensitive to the fine structure splitting.

Since we cannot accurately predict the MR spectrum, accurate quantitative determination of the transition strengths or line positions can not be directly extracted from observed MRS spectra[28] (Yan 1985). Nevertheless, we can learn something by considering particular simple test cases.

The simplest case of interest concerns the transitions between a lower Hund's case (b) doublet state to an upper Hund's case (a) state. For further simplicity, we ignore all rotational, vibrational, and electronic contributions to the transition

[28]The problem arises because we do not know *a priori* what the observed MR line shapes will be. We should not expect a simple second derivative of a Gaussian like profile, but as demonstrated later, *something* else!

energy. For ${}^2\Sigma - {}^2\Sigma$ transitions, four main branches, ${}^RR_{11}$, ${}^RR_{22}$, ${}^PP_{11}$, ${}^PP_{22}$ and two satellite branches ${}^RQ_{21}$ and ${}^PQ_{12}$ are allowed where the prescript signifies the value of $\Delta N = N' - N''$ and the main letter denotes the value of $\Delta J = J' - J''$, *at zero magnetic field* (Herzberg 1989, 249). The subscripts on the labels define the *zero-field* relationship of N to J for the upper and lower states (in that order), with a "1" indicating $J = N + 0.5$ and a "2", $J = N - 0.5$. The satellite branches with $\Delta N \neq \Delta J$ are expected to have less intensity than the main branches with $\Delta N = \Delta J$ as observed by absorption spectroscopy at zero-field.

Figures A.8-11 portray the results of MR line shape calculations on all possible ${}^2\Sigma - {}^2\Sigma$ transitions from the $N = 0$ and $N = 1$ lower levels. Since the lowest-J ${}^PP_{22}$ line originates at $N = 2$, only five of the possible six branches are considered. The most striking feature of the figures is that the typical line shape looks more like a first-derivative of a Gaussian than a second derivative! In fact, only transitions originating at the lowest level appear with the naively expected second derivative line shape. This arises because the lowest *rotationless* level does not spin-uncouple at any field strength, so that the pattern of its energy levels is similar to the Hund's case (a) patterns. This is an example of a general rule about MR line shapes: typical second derivative of a Gaussian-like line shapes occur whenever spin-uncoupling hasn't occurred in the Hund's case (b)

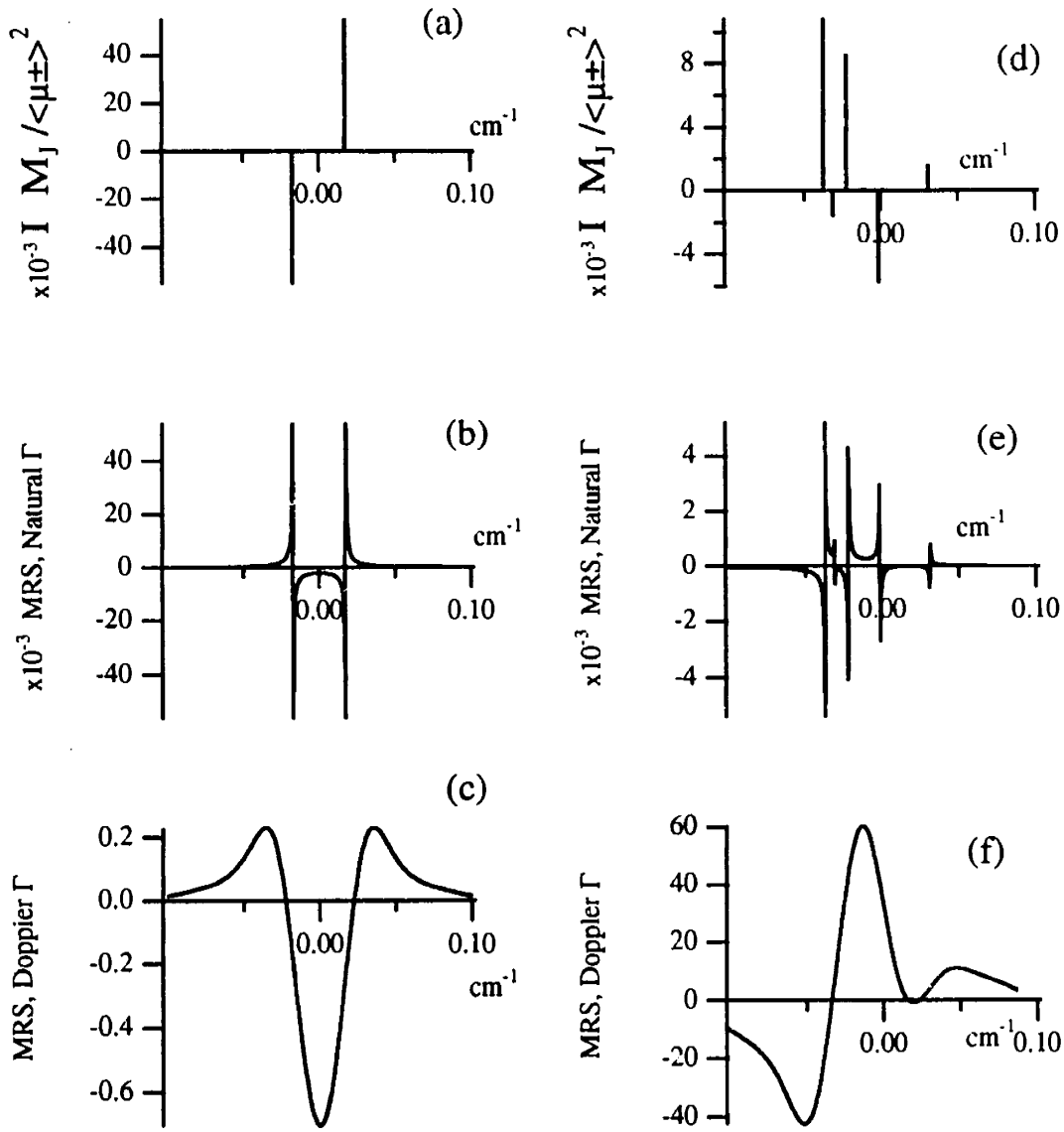

Figure A.8: Calculated MR Spectra for $^2\Sigma$ Hund's case (b) - Hund's case (a) transitions at 100 G with $\gamma = 0.01\ cm^{-1}$. Panels (a), (b) and (c) are for a $^RQ_{21}(0.5)$ transition (named at zero-field). Panels (d), (e) and (f) are for a $^RQ_{21}(1.5)$ transition. Other parameters and details given in figures A.2-4.

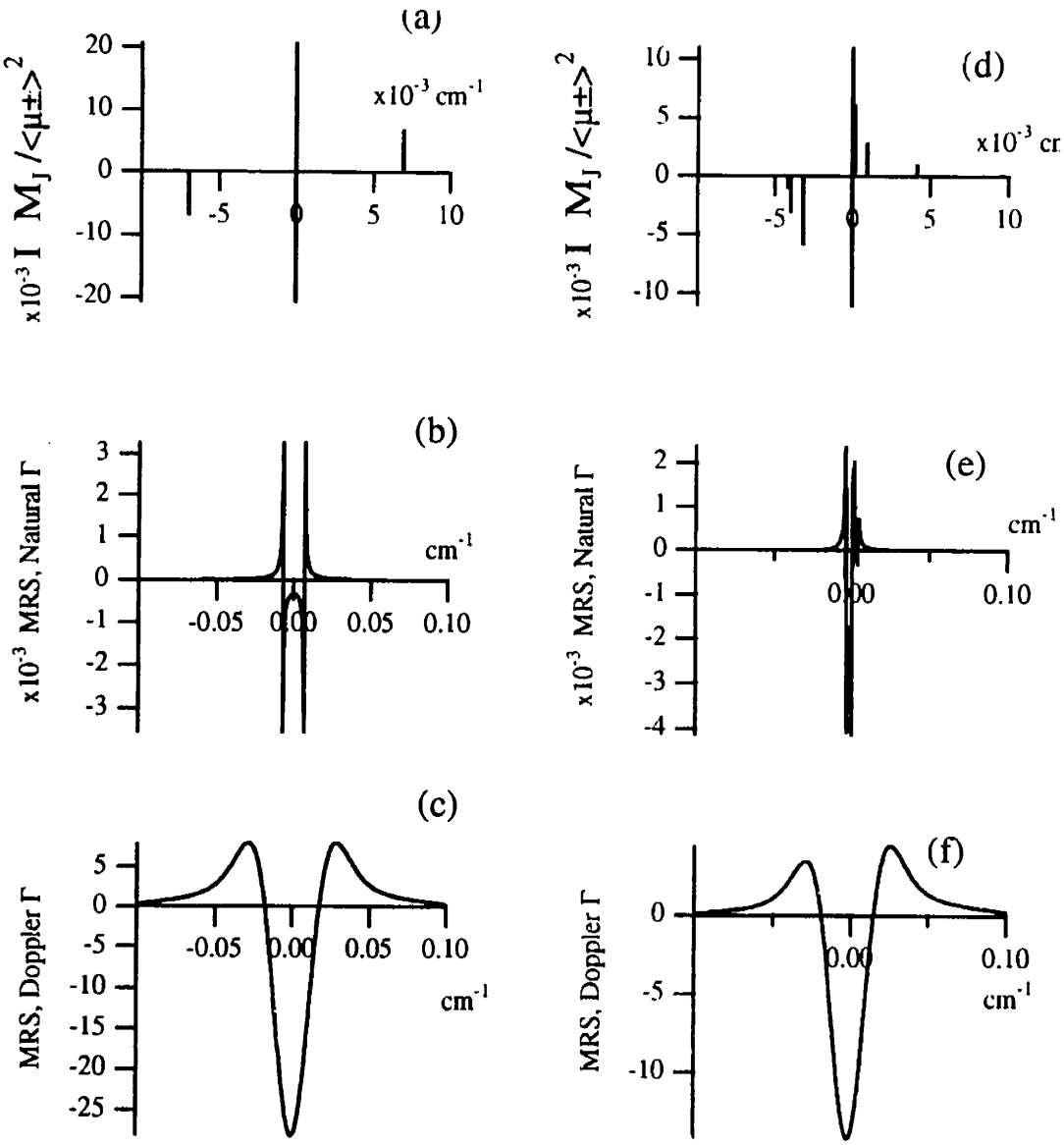

Figure A.9: Calculated MR Spectra for $^2\Sigma$ Hund's case (b) - Hund's case (a) transitions at 100 G with $\gamma = 0.01\ \mathrm{cm}^{-1}$. Panels (a), (b) and (c) are for a $^{R}R_{11}(0.5)$ transition (named at zero-field). Panels (d), (e) and (f) are for a $^{R}R_{11}(1.5)$ transition. Other parameters and details given in figures A.2-4.

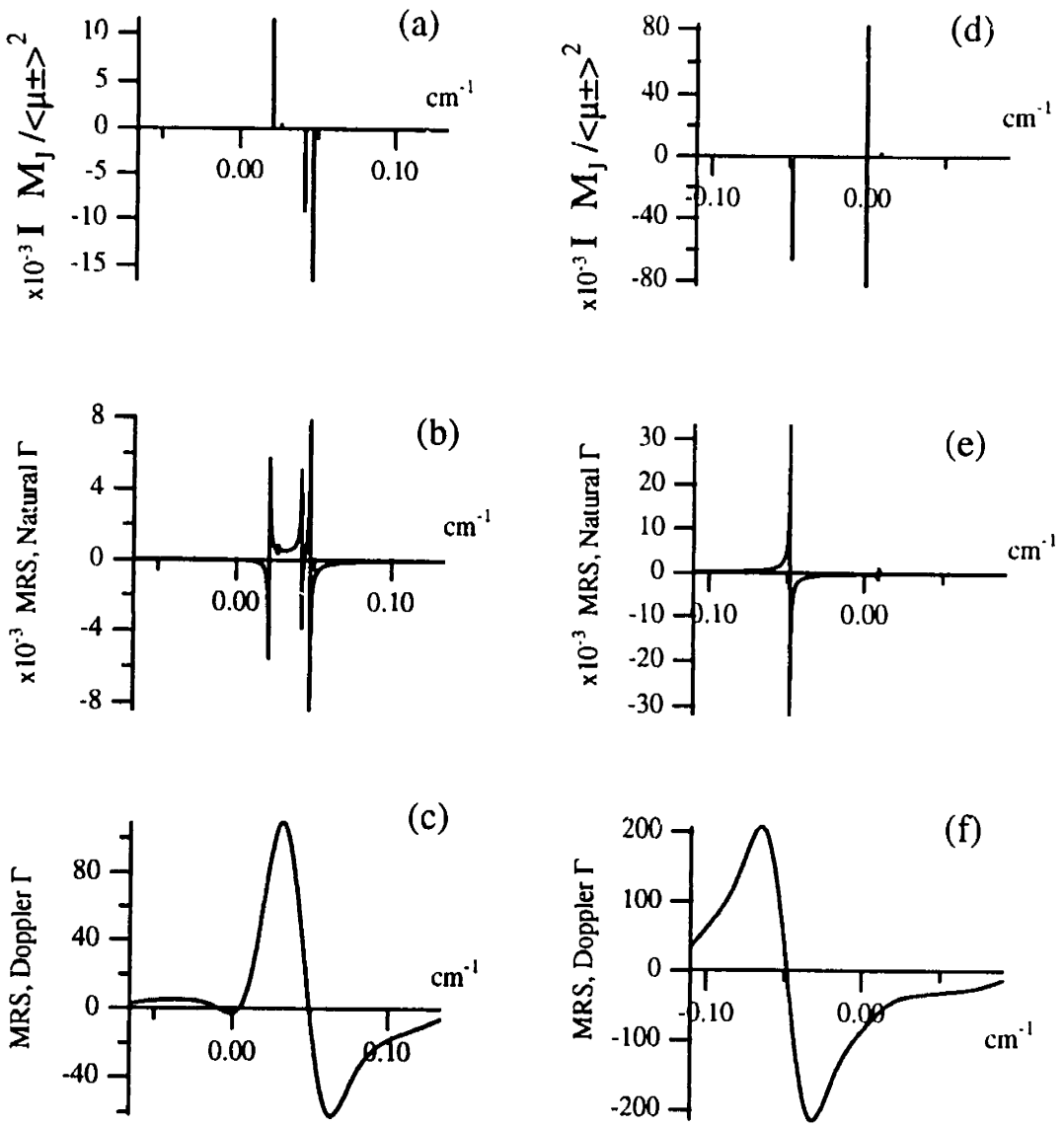

Figure A.10: Calculated MR Spectra for $^2\Sigma$ Hund's case (b) - Hund's case (a) transitions at 100 G with $\gamma = 0.01\ cm^{-1}$. Panels (a), (b) and (c) are for a $^{R}R_{22}(0.5)$ transition (named at zero-field). Panels (d), (e) and (f) are for a $^{P}P_{11}(0.5)$ transition. Other parameters and details given in figures A.2-4.

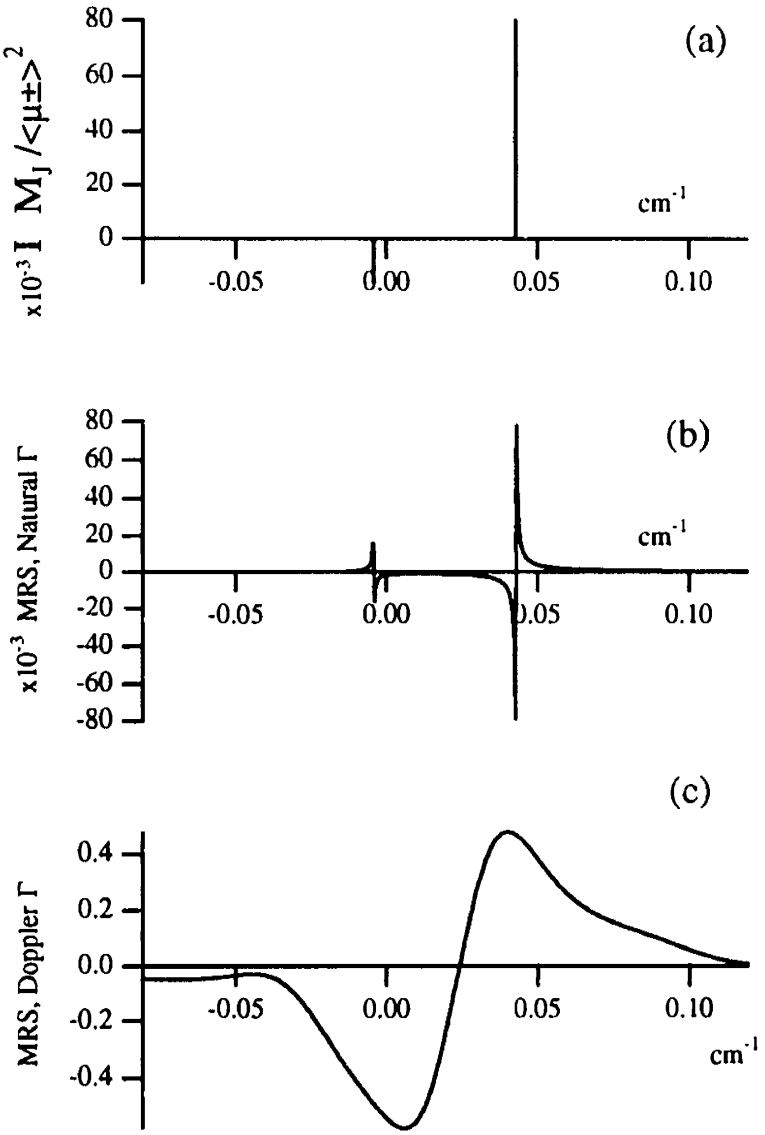

Figure A.11: Calculated MR Spectra for $^2\Sigma$ Hund's case (b) - Hund's case (a) transitions at 100 G with $\gamma = 0.01\ cm^{-1}$. Panels (a), (b) and (c) are for a $^PQ_{12}(1.5)$ transition (named at zero-field). Other parameters and details given in figures A.2-4.

state and when spin-uncoupling has occurred, the line shape will be complicated, field dependent, and difficult to analyze. When spin-uncoupling is expected to occur immediately (at small fields because the fine structure splittings are small), the presence of a second derivative-like line shape identifies a transition involving rotationless (lowest possible J) levels.

Look now at the relative intensities of the MR spectra in the figures. The ${}^{R}Q_{21}(0.5)$ transition with the second derivative line shape is ten times stronger than the other lines with a similar lineshape, ${}^{R}R_{11}(0.5)$ and ${}^{R}R_{11}(1.5)$. This occurs because the most intense components of the weaker lines do not contribute to the MR effect (as explained earlier for Hund's case (b)- Hund's case (b) transitions). The most intense of these second-derivative-like lines for these mixed-type transitions will be a lowest-J satellite transition. Yet, the MR signal intensity alone should not be used to identify the transition, since other transitions will have comparable have MRS intensity even though they have different line shapes. Regardless of the multiplicity of the state, there will always be many more of these lines than there are of the intense second-derivative-like lowest-J satellite transitions. The strong non-second derivative-like lines occur in close proximity to the satellite lines, often interfering with the satellite lines' observation, precisely when the fine structure splittings are small and the enhancement is most needed to help assign the spectra.

In conclusion, MR spectra from Hund's case (b)-case (a) transitions are complex because the gross features of the line shapes vary with the specific transition involved. Because the lineshapes vary considerably, observed MR spectra do not yield accurate line positions or absorption-line strengths without the aid of a computer simulation. Some general feature of MR spectra are expected that may, in some cases, provide identification of specific spectral features. Interestingly, the MR signal is usually strongest for satellite lines. Unfortunately, when the manifold of Hund's case (b) levels is very dense and the fine structure splittings constants are small, these strong MR satellite lines may be overlapped with strong first-derivative like MR main lines.

A.9 *References*

1978 Brown, J. M. , M. Kaise, C. M. L. Kerr, and D. J. Milton, *Mol. Phys.*, **36**, 553.

1979 Bunker, P. R., *Molecular Symmetry and Spectroscopy*, Boston: Academic Press.

1967 Carrington, A. and A. D. McLachlan, *Introduction To Magnetic Resonance*, New York: Harper & Row.

1969 Carrington, A., G. N. Currie, T. A. Miller, and D. H. Levy, *J. Chem.*

Phys., **50**, 2726.

1970 Carrington, A. and N. J. D. Lucas, *Proc. R. Soc. A*, **314**, 567.

1932 Carroll, T., *Phys. Rev.*, **41**, 489.

1977 Cohen-Tannoudji, C., D. Diu, and I. Laloë, *Quantum Mechanics*, Vol 1 & 2, New York: John Wiley & Sons.

1960 Edmonds, A. R., *Angular Momentum in Quantum Mechanics*, Princeton: Princeton University Press.

1961 Fried, B. D., and S. D. Conte, *The Plasma Dispersion Function*, New York: Academic Press.

1989 Herzberg, G., *Molecular Spectra and Molecular Structure, I. Spectra of Diatomic Molecules*, reprint edition, Malabar: Krieger Publishing.

1985 Hirota, E., *High-Resolution Spectroscopy of Transient Molecules*,New York: Springer-Verlag

1962 Hougen, J. T., *J. Chem. Phys.*, **45**, 4214.

1970 Hougen, J. T., *Nat. Bur. Stand. (U.S.)*, Monogr. 115

1996 Kaledin, L, J. C. Bloch, M. C. McCarthy, and R. W. Field, *J. Mol. Spect.*,**000**,000

1986 Lefebvre-Brion, H. and R. W. Field, *Perturbations in the Spectra of Diatomic Molecules*, Boston: Academic Press.

1992a McCarthy, M. C. and R. W. Field, *J. Chem. Phys.*, **96**, 7237.

1992b McCarthy, M. C., PhD Thesis, MIT.

1994 McCarthy, M. C. and R. W. Field, *J. Chem. Phys.*, **100**, 6347.

1985 McDonald, S. A., PhD Thesis, MIT

1898 Righi, A., *Comptes Rendus*, **127**, p. 216 and **128**, 45.

1986 Seigman, A. E., *Lasers*, 2 Ed, Mill Valley: University Science Books.

1985 Steinfeld, J. I., *Molecules and Radiation*, Cambridge: MIT Press.

1975 Townes, C. H. and A. L. Schawlow, *Microwave Spectroscopy*, New York: Dover Publications.

1978 Weissbluth, M., *Atoms and Molecules, Student Edition*, Boston: Academic Press.

1985 Yan, W., R. F. Curl, A. J. Merer, and P. G. Carrick, *J. Mol. Spec.*, **112**, 436

1988 Zare, R. N., *Angular Momentum*, New York: John Wiley and Sons.

B.1 *Introduction*

Often, the need arises to calculate the matrix elements of a *laboratory* fixed operator other than **J**, the total angular momentum, or one of its components, when the wavefunction is specified in the *molecular* frame[1]. Two cases have arisen already in this thesis, concerning the Zeeman effect and electric-dipole transition intensity calculations. In the calculation of an experimental (or laboratory) observable of a molecular system, one cannot avoid using angular momentum vectors with components specified in the laboratory or space-fixed reference frame. If the molecular wavefunctions are specified using the often preferred Hund's case(a) basis set (Lefebvre-Brion 1986, 41), the difficulty of the calculation is confounded by the fact that *only* the laboratory-fixed projection of **J** is known, while those of **L** and **S** are not. In the following sections of this appendix, an expression is developed that solves such a problem. As we shall see, one of the consequences of imposing an arbitrary laboratory reference on the molecular frame is the possibility of $\Delta J \neq 0$ matrix elements!

B.2 *From Hund's case (a) to the laboratory*

[1]Boldface type is used for vectors.

The eigenfunctions of a Hund's case (a) basis set are written,

$$|L\,\Lambda;\,S\,\Sigma;\,\Omega\,J\,M_J\rangle, \qquad \text{B.1}$$

where J is the total angular momentum quantum number with space-fixed projection M_J and Λ, Σ, Ω, are the molecule fixed projections of L, S, and J respectively[2]. In many other presentations L is not specified. All other labels necessary for the complete description of the functions have been suppressed for clarity. We are interested in calculating the matrix elements χ,

$$\chi = \langle L'\,\Lambda';\,S'\,\Sigma';\,\Omega'\,J'\,M'_J|A_p|\,L\,\Lambda;\,S\,\Sigma;\,\Omega\,J\,M_J\rangle, \qquad \text{B.2}$$

where $\mathbf{A}_p$ is the p^{th} component of a laboratory referenced vector operator. Therefore $\mathbf{A}$ is a first rank irreducible tensor operator (either spherical or Cartesian), $\mathrm{T}^1{}_{1p}(\mathbf{A})$ with $\mathbf{A}_0 = \mathbf{A}_Z$ (Rose 1957, 76).

Using the Wigner D^{k*}_{pq} *functions*, $\mathrm{T}^I{}_{1p}(\mathbf{A})$ is expressed as a sum over molecule fixed[3] components $\mathrm{T}^I{}_{1q}(\mathbf{A})$ (Zare 1988, 179)[4],

---

[2]These quantities are function labels and not vectors; they do not appear in boldface.

[3]The subscript p refers to the sPace fixed components, while the subscript q refers to the moleCUle-fixed components.

[4] As recommended by Brown 1976, to circumvent the *potential* problems caused by the anomalous commutation rules of **J**, if **A** is a compound operator involving **J**, **A** must be first evaluated in a space-fixed system *before* rotation into the molecular frame. See Freed 1966, or Femenias 1974, for other less obvious methods. Note that also, the phase convention here, although not clearly specified, is consistent with that of Brown.

$$T^{l}{}_{lp}(\mathbf{A}) = \sum_{q} D^{l*}_{pq}\, T^{l}{}_{lq}(\mathbf{A}). \qquad \text{B.3}$$

Since the Wigner D^{k*}_{pq} functions[5] act only on the rotational $|\Omega J M_J\rangle$ part of the wavefunction, we assume that $\mathbf{A}_p$ does not also operate on $|\Omega J M_J\rangle$ and rewrite equation B.1,

$$\chi = \sum_{q} \langle L' \Lambda'; S' \Sigma' | T^{l}{}_{lq}(\mathbf{A}) | L \Lambda; S \Sigma \rangle \langle \Omega' J' M'_J | D^{l*}_{pq} | \Omega J M_J \rangle. \qquad \text{B.4}$$

By replacing $T^{l}{}_{lq}(\mathbf{A})$ in equation B.4 with the molecule-fixed operator $\mathbf{A}_q$, and the Wigner D^{k*}_{pq} function with the Wigner $\mathbf{D}^{(kk)}_{p,-q}$ *double tensor* (Judd 1975, 10),

$$\mathbf{D}^{(kk)}_{p,-q} = (-1)^{k-q}\sqrt{2k+1}\, D^{k*}_{pq}, \qquad \text{B.5}$$

we find that χ can be expressed as,

$$\chi = 3^{-1/2} \sum_{q} (-1)^{1-q} \langle L' \Lambda'; S' \Sigma' | \mathbf{A}_q | L \Lambda; S \Sigma \rangle \langle \Omega' J' M'_J | \mathbf{D}^{(11)}_{p,-q} | \Omega J M_J \rangle, \qquad \text{B.6}$$

which can be immediately evaluated using the well known Wigner-Eckart theorem (Zare 1988, 180) twice. This yields,

[5]The Wigner D^{k*}_{pq} functions are assumed to be functions of the three Euler angles.

$$\chi = 3^{-1/2}\sum_q (-1)^{2J'+1-q-M'_J-\Omega'}\langle L'\,\Lambda';\,S'\,\Sigma'\,|\mathbf{A}_q|\,L\,\Lambda;\,S\,\Sigma\rangle\times \begin{pmatrix} J' & 1 & J \\ -M'_J & p & M_J \end{pmatrix}\begin{pmatrix} J' & 1 & J \\ -\Omega' & q & \Omega \end{pmatrix}\langle J'\,\|\mathbf{D}^{(11)}\|\,J\rangle \qquad \text{B.7}$$

where the (doubly) reduced matrix element $\langle J'\,\|\mathbf{D}^{(11)}\|\,J\rangle$ of the Wigner double tensor is (Judd 1975, 50),

$$\langle J'\,\|\mathbf{D}^{(11)}\|\,J\rangle = \sqrt{3(2J'+1)(2J+1)}. \qquad \text{B.8}$$

This leads directly to the desired result, where the to-be-evaluated matrix elements of space-fixed $\mathbf{A}_p$, $\langle \mathbf{A}_p\rangle$, are expressed neatly in terms of the (simplified) matrix elements of molecule fixed $\mathbf{A}_q$, $\langle \mathbf{A}_q\rangle$,

$$\langle \mathbf{A}_p\rangle = \sqrt{(2J'+1)(2J+1)}\begin{pmatrix} J' & 1 & J \\ -M'_J & p & M_J \end{pmatrix}\times \sum_q (-1)^{2J'+1-q-M'_J-\Omega'}\langle \mathbf{A}_q\rangle\begin{pmatrix} J' & 1 & J \\ -\Omega' & q & \Omega \end{pmatrix}. \qquad \text{B.9}$$

One could have also arrived at this result without using the Wigner double tensor by exploiting the well known correspondence[6] between the D^{k*}_{pq} functions and the rigid-rotor wavefunctions,

$$|J\,\Omega\,M\rangle = \left[\frac{2J+1}{8\pi^2}\right]^{1/2} D^{J*}_{M\Omega}(\alpha,\beta,\gamma), \qquad \text{B.10}$$

and using subsequent integration of the product of three[7] Wigner D^{k*}_{pq} functions over the three Euler angles α,β,γ[8] . This is in fact how equation B.8 is derived

[6]For example, see Zare 1988, 105.

[7]One function arises for the ket, one for the bra, and one for the operator.

(Judd 1975).

B.3 *Using equation B.7*

Notice that the first 3-J symbol in equation B.9 is a function of the laboratory fixed projection M_J and p, while the second 3-J symbol is a function of the molecule fixed projection Ω and q. Three selection rules immediately apply, *regardless* of the specific problem:

$$J' - J = 0, +1, \text{or} -1, \qquad \text{B.11}$$

$$\Omega' - \Omega = 0, +1, \text{or} -1, \qquad \text{B.12}$$

and,

$$M'_J - M_J = 0, +1, \text{or} -1. \qquad \text{B.13}$$

A special, yet common case, requires the evaluation of $\langle \mathbf{A}_q \rangle = \langle L' \Lambda'; S' \Sigma' | \mathbf{A}_q | L \Lambda; S \Sigma \rangle$ when $\Lambda' - \Lambda = \Sigma - \Sigma'$. By noting that $\Omega = \Lambda + \Sigma$, and applying the triangle-rule (Lefebvre-Brion 1986, 110) to the second 3-J symbol in equation B.9, we find that the sum in equation B.9 reduces to a single term, $q = 0$. This occurs for electric-dipole allowed transitions.

Furthermore, when $J' = J$, which occurs for electric dipole allowed Q

[8]See Zare 1988, 285; Femenias 1974 and references therein.

branches, the 3-J symbols in equation B.9 simplify using (Edmonds 1960, 125)[9]. In this case with $J' = J$, when p or q is zero, we have,

$$\begin{pmatrix} J & 1 & J \\ M & 0 & -M \end{pmatrix} = (-1)^{J-M}(-1)^{2J+1}\frac{M}{\sqrt{J(J+1)(2J+1)}} \qquad \text{B.14}$$

and when $p \text{ or } q = \pm 1$,

$$\begin{pmatrix} J & 1 & J \\ M & 1 & -M-1 \end{pmatrix} = (-1)^{J-M}(-1)^{2J+1}\sqrt{\frac{(J-M)(J+M+1)}{(2J+2)(2J+1)J}}. \qquad \text{B.15}$$

And finally when $J' = J \pm 1$, (occurring for a P or R branch), we use,

$$\begin{pmatrix} J+1 & J & 1 \\ M & -M & 0 \end{pmatrix} = (-1)^{J-M-1}\sqrt{\frac{2(J+M+1)(J-M+1)}{(2J+3)(2J+2)(2J+1)}} \qquad \text{B.16}$$

and likewise,

$$\begin{pmatrix} J+1 & J & 1 \\ M & -M-1 & 1 \end{pmatrix} = (-1)^{J-M-1}\sqrt{\frac{(J-M)(J-M+1)}{(2J+3)(2J+2)(2J+1)}}. \qquad \text{B.17}$$

With these relationships and equation B.9, all allowed electric and magnetic dipole transition amplitudes and all Zeeman effect matrix elements may be calculated.

[9]Edmond's (1960) tables of 3-J and 6-J symbols (for angular momentum arguments up to 2) are the most useful found in the "common" short-texts available on angular momentum. Zare (1988, 65) gives references for closed form expressions involving larger arguments. See also appendix C for a computer algorithm.

B.4 *References*

1976 Brown, J. M. and B. J. Howard, *Molecular Physics*, **31**, 1517.

1960 Edmonds, A. R., *Angular Momentum in Quantum Mechanics*, Princeton: Princeton University Press.

1974 Féménias, J. L., C. Anthénour, R. Stringat., *Can. J. Phys.*, **52**, 361.

1966 Freed, K. F., *J. Chem. Phys.*, **45**, 4214.

1975 Judd, B. R., *Angular Momentum Theory for Diatomic Molecules*, New York: Academic Press.

1986 Lefebvre-Brion, H. and R. W. Field, *Perturbations in the Spectra of Diatomic Molecules*, Boston: Academic Press.

1957 Rose. M. E., *Elementary Theory Of Angular Momentum*, New York: John Wiley and Sons.

1988 Zare, R. N., *Angular Momentum*, New York: John Wiley and Sons.

C.1 *Computer Code for chapter 4*

C.1.1 *Program MeshBk.for*

```
*  Program MeshBk.for
*
*  VMS FORTRAN
*
*       By Jonathan C. Bloch March 22,1992
*       (Original written by Tom Varberg, October 25, 1989.)
*
*       MeshBk.for reads the output file from the Herman-Skillman SCF program
*       extracts only the radial wavefunction, and outputs the wave
*       function in an X-Y ASCII format useful for calculating integrals
*
*       The output file of MeshBk.for is the input file for Bkcalc.for
*
*       "file" is name mad of Molecule+Configuration; i.e., "EuIII(4f7)"
*
*       To use this program:
*       (1) Run Herman-Skillman program
*             name the input "file.HSin" and output file "file.HSout"
*       (2) Run MeshBk program: follow directions
*             output file of MeshBk is: "file.BKIn"
*
*       Then, to calculate Bk integrals
*       (3) Run Bocalc.for
*             output will be file.BKOut
*

        character  wave*13,file*45,outfile*45,infile*45,Mol*6

      character  title*45,Config*10,path*30

     character orbname*6,nname*8,waver*14

    real Q(200,5), P(1000), X, R, delta,zz

     integer KKK, nblock, npoint,nlines,num,n,l,c,nnlz,numorb,orb,nc,z

   integer charge, pos1,pos2

                print   *,   '-----------------------------------------------'
```

```
      print *, 'Enter Molecule (as EuIII, etc.): '
      read(*,6000) mol
      print *, 'Enter name of Orbital file (configuaration): '
      read(*,6000) Config
* make sure to get rid of blanks before adding prefix/suffix
      pos1=index(Mol,' ')
         path='[bloch.orbitals.'//Mol(:pos1-1)//']'
      pos2=index(path,' ')
         file=path(:pos2-1)//Mol(:pos1-1)//config
      pos=index(file,' ')
       infile=file(:pos-1)//'.HSOut'
       outfile=file(:pos-1)//'.BkIn'
                    print    *,'-------------------------------------------------'
      print *,'   input file: ',infile
      print *,'  output file: ',outfile
                    print    *,'-------------------------------------------------'
    orbname='spdfgh'
     nname='01234567'
6000   format(a20)
      open(5,file=infile,status='old')
      open(7,file=outfile,status='new')
* read in charge from first line of file
6020   format(15x,i1)
     read(5,6020) charge
* read in Z and card number (NC) from infile
* read until (& including) 90th card
* see HS book for details of file format
```

```
6010     format(73x,i3,i4)
100    read (5,6010) Z,NC
       if (nc.ne.90) goto 100
       print *,' Z = ',z
       print *,' Charge = ',charge
       print *,' Processing ....'
         ZZ = 1.0 /(float(Z))**0.3333333333
* write out title and Z (needed for the CF calculation)
       pos2=index(config,' ')
            title=Mol(:pos1-1)//'('//config(:pos2-1)//')'
        write(7,1009) title,z,charge
1009        format(1x,a15,2x,'Z=',i3,2x,'Charge= ',i1)
* Now we are up to the first orbital:
* read in nnlz (see below) and KKK (# mesh points)
500         read (5,1001,end=9999) nnlz, KKK
* n = principle quantum # ; l = angular momentum; c = labeling constant
* (c is for expansion purposes)
        n = nnlz/100
          l =  (nnlz-n*100)/10
         c = nnlz - n*100 - l*10
* Now, read in all the rR(r) wavefunction data
1001        format(i4,t47,i4)
        nlines = (KKK-1)/5 + 1
       do 10 J = 1,nlines
            read (5,1000) (Q(J,K),K=1,5)
1000         format(1x,5f14.7)
```

```
      do 20 K = 1,5
20        P(5*(J-1)+K) = Q(J,K)              ! convert to single index
10    continue
* Now write the output in an X-Y format.
* Note that X is the radial distance in the scaled coordinate.
*  According to Herman & Skillman, R = 0.88534138*Z**-(1/3) * X
* where R is in atomic units.
* wave is name of orbital
        wave = nname(n+1:n+1)//orbname(l+1:l+1)
204       format(a2,1x,i1,i1,1x,i3)
       write (7,204) wave,n,l,kkk
      print *,'   ',wave, ' orbital'
* calculate  R for  P(num) = amplitude at R(num) * R
     do 30 num = 1,KKK
        nblock = int((num-1)/40) + 1
       npoint = mod(num-1,40)
         delta = 0.0025*2.0**(nblock-1) * 0.88534138*ZZ  ! delta is in a.u.
           X = 0.1*2.0**(nblock-1) - 0.1 + npoint*0.0025*2.0**(nblock-1)
      R = 0.88534138*ZZ * X                    ! in a.u.
        write (7,1002) num,delta, R,P(num)
1002        format(1x,i4,3(2x,f12.8))
30    continue
* go read next orbital
    goto 500
* on end-of-file error, we come here
9999  close(5)
    close(7)
     print *,'..... Finally Done'
```

```
      end
```

C.1.2 *Program BkCalc.For*

```
*
*  Program  BkCalc.For
*
*        VMS FORTRAN
*
*        by Jonathan C. Bloch 4/20/92
*
*        REQUIRES External Subrutine Bkn
*
*        This program calculates all Bk Crystal field parameters
*        from the "converted" output of the Herman Skillman program
*
*        Steps to use :
*
*                Calculate radial wavefunctions ( use Hermin Skillman program)
*                Run "MeshBk" program to convert output of HS program
*                to input for BkCalc.  See MeshBk.For for Details
*                Run BkCalc program
*
*        Running BkCalc:
*
*                Enter standard name of atom/ion [=Mol]: enter GdIII for Gd2+
*                Enter configuaration [=config]:  i.e.,  4f76s2
*                BkCalc finds data file in file Mol(Config).Bkin
*                        i.e.,    "GdIII(4f76s2).BkIn"
*                BkCalc looks only in directory Mol: i.e., "GdIII"
*                Enter Re in angstroms.  Value is converted to A.U.
*
*        Output File:
*
*                 Output is written to file Mol(Config).BkOut

       CHARACTER file*45, title*45, orb*2, infile*40, outfile*40

      CHARACTER config*10, path*30, mol*6

       REAL*8     delta(500), X(500), PX(500)

      REAL*8    Bk(0:6), Bo, Re, R, Norm

     INTEGER   number, n, l, z, nummax, num
     INTEGER   charge, pos1, pos2, pos

6000  FORMAT (a15)
```

```
      PRINT      *,'-----------------------------------------------'
      PRINT  *,' Enter Molecule (as EuIII, etc.):'
      READ  (*,6000) Mol
      PRINT  *,' Enter name of Orbital File (configuaration):'
      READ  (*,6000) Config
*  Remove blanks, concat. and form filenames:
      pos1= INDEX(Mol, ' ')
         path= '[Bloch.Orbitals.'//Mol(:pos1-1)//']'
      pos2= INDEX(path, ' ')
         file=  path(:pos2-1)//Mol(:pos1-1)//Config
      pos= INDEX(file, ' ')
        infile=  file(:pos-1)//'.BkIn'
       outfile=  file(:pos-1)//'.BkOut'
      OPEN (1, FILE=infile, STATUS='old')
      OPEN (7, FILE=outfile, STATUS='new')
*  Read in Re from keyboard
      PRINT *, 'Please type Re (in Angstroms):'
     READ *,Re

*  Get title line, Z (atomic number) and charge from infile
*     write out this information to outfile
      READ (1,1010) title, Z, Charge
      WRITE (7,1050)
      WRITE (7,1030)
      WRITE (7,1009) title,Re
      WRITE (7,1030)
      WRITE (7,1040) (pos,pos=0,6,2)
```

```
*   and put information on the terminal

                    PRINT       *,'-------------------------------------------------'

     PRINT  *,'    Input file: ', InFile

     PRINT  *,'   Output file: ', OutFile

                    PRINT       *,'-------------------------------------------------'

     PRINT  *,' Z= ',Z

     PRINT  *,' Charge = ',Charge

     PRINT  *,' Processing . . .'

1010  FORMAT  (1x, a15, 4x, i3, 10x, i1)

1009  FORMAT  (' Bk(in Cm-1) CF parameters for: ',a15,5x,'Re= ',f5.3,
    &       ' Angstroms')

1030          FORMAT(1x,'-----------------------------------------
                &-------------------------------')

1040  FORMAT  (8x, 'Norm', 5x, ' k= ', 4x, i1, 3(12x, I1))

1050  FORMAT  (25x, 'BkCalc (Revision 4/20/92)')

* Put Re into Atomic Units for calculation

      R=re/0.529177

* Now do calculation, one orbital at a time

*   Read in 1st orbital:
*     Gets its name and number of points for its wavefunction

10    READ  (1, 1008, END=9999) orb, n, l, nummax

* Read in the nummax points of the nl wavefunction
*   number is point number
*   delta is difference between x-coordinates of two successive points
*   X(num) is X coordinate, here in A.U.
*   PX(num) is amplitude at X, here rR(X) in A.U.

1008    FORMAT  (a2, 1x, i1, i1, 1x, i3)

      DO 300 num= 1, nummax

         READ (1,*) number, delta(num), X(num), PX(num)
```

```
300   CONTINUE

* Call Bkn subroutine to calculate all Bk terms (and Overlaps)

      DO 400 k= 0, 2*l, 2

      Bo= 0.

      Norm= 0.

       Call Bkn(R, K, Nummax, X, PX, PX, Delta, Bo, Norm)
         Bk(k)= float(charge) * 2. * 109737.311 * Bo

400   CONTINUE

* Write results to outfile

        WRITE(7,1003) Orb, Norm, (Bk(k), k=0, 2*l, 2)

1003    FORMAT  (1x, a2, 4x, f12.8, 4f12.0)

* Show progress on terminal

      PRINT  *,'    ',orb,' orbital'

* Go get next orbital

   GOTO 10

* We come here at end-of-file error

9999  CLOSE(1)

    CLOSE(7)

     PRINT  *,' . . . finally done'

   END
```

C.1.2.1 *Subrutine Bkn.for*

```
*
* SUBRUTINE Bkn.for
*
* VMS FORTRAN
*
*       by Jonathan Bloch March 22, 1992
*       (original by C.GITTINS 30-OCT-89)

*       Bkn.for calculates B[K0] integrals for Ligand field theory
```

```
*       from radial wavefunctions.  Input data MUST be in atomic units.
      SUBROUTINE BKN(RE,K,N,X,PX1,PX2,DELTA,BK,Norm)
     INTEGER I,K,N
          REAL*8  DELTA(500),X(500),PX1(500),PX2(500)
      REAL*8 RE,BK,XL,XG,GRID,Norm
      BK = 0.
      Norm=0.
      DO 110, I=1,N
        IF (X(I) .LT. RE) THEN
          XL = X(I)
        XG = RE
       ELSE
          XL = RE
          XG = X(I)
       END IF
       IF (XL .EQ. 0) THEN
         GRID = 0
       ELSE
              GRID = (XL**K)/(XG**(K+1))
       ENDIF
          BK = BK + DELTA(I+1) * PX1(I) * PX2(I) * GRID
          Norm = Norm + DELTA(I+1) * PX1(I) * PX2(I)
110   CONTINUE
     RETURN
     END
```

C.1.2.2 *Output of BkCalc*

Example of output file for BkCalc, above:

BkCalc (Revision 4/20/92)

Bk(in Cm-1) CF parameters for: TbII(4f85d6s) Re= 1.960 Angstroms

	Norm	k= 0	2	4	6
1s	1.02716970	60866.			
2s	1.02684550	60846.			
2p	1.02719135	60867.	38.		
3s	1.02598480	60795.			
3p	1.02656569	60830.	306.		
3d	1.02714874	60864.	242.	2.	
4s	1.02569189	60778.			
4p	1.02654418	60828.	1719.		
4d	1.02730517	60874.	1931.	99.	
4f	1.02734372	60875.	3210.	410.	106.
5s	1.02746527	60882.			
5p	1.02762229	60883.	11641.		
5d	1.02722009	60019.	22742.	12208.	
6s	1.02722792	54290.			

C.2. Computer code for appendix A

C.2.1 *Function Hrb*

```
*       FORTRAN Function Hrb(N,B,D)
*
*       Jonathan C. Bloch      09/01/95
*
*       • Calculates Rotational Matrix elements for Hund's case (b) Σ states
*
*         in a coupled representation,
*
*                 <N S J MJ |Hr| N S J MJ>
*
*       • Note: elements are simple and diagonal ∂(NN')∂(SS')∂(JJ')....
*
*               <Hr> = B N(N+1) - D [N(N+1)]^2
*

        FUNCTION Hrb(N, B, D)

        IMPLICIT NONE
```

```
      REAL*8 Hrb, N, B, D, X

      X  =  N*(N+1.0)

      Hrb = B*X - D*X*X

      RETURN

      END
```

C.2.2 *Function Hsrb*

```
*     FORTRAN Function Hsrb(N,S,J,G)
*
*     Jonathan C. Bloch      09/01/95
*
*     • Calculates Spin-Rotation Matrix elements for Hund's case (b) Σ
*
*     states in a coupled representation
*
*           <N S J |Hsr| N S J>
*
*     • Algorithm:
*
*           in coupled case (b) all spin-rotation elements are diagonal,
*
*           <Hsrb> = 0.5 * G [ - N(N+1) - S(S+1) + J(J+1)] * ∂NN' ∂JJ' ∂SS'
*
*     • G (= gamma) is the effective coupling constant
*
      FUNCTION Hsrb(N, S, J, G)

      IMPLICIT NONE

      REAL*8 Hsrb, N, S, J, G

      Hsrb = 0.0

      Hsrb =  0.5 * G * ( J*(J+1.0) - N*(N+1.0) - S*(S+1.0) )

      RETURN

      END
```

```
*       FORTRAN Function Hssb(N,S,J,Np,L)
*
*       Jonathan C. Bloch      09/01/95
*
*       • Calculates Spin-Spin Matrix elements for Hund's case (b) Σ states
*
*         in a coupled representation  <N SJ MJ |Hss| Np S J MJ>
*
*       • NEEDS an (external) 3-J  & 6-J routine !          uses COS(xπ) = (-1)^x
*
*       • Algorithm:
*
*       (1)  calculate using 3J and 6J symbols
*
*       (2) Normalize so that constant factors do to value of S are
*
*         incorporated into L=Lambda effective coupling constant
*
        FUNCTION Hssb(N, S, J, Np, L)

        IMPLICIT NONE

        REAL*8 Hssb, N, S, J, Np, L, E, TJ, SJ

        External TJ, SJ

        Hssb = 0.0

        E = N + Np + S + J

        Hssb = DCOS(E*DBLEQ(PI)) * sqrt((2*N+1.0) * (2*Np+1.0))
&       * SJ(N,S,J,S,Np,2.0) * TJ(N,2.0,Np,0.0,0.0,0.0) * L

        Hssb = Hssb * 4.0 * sqrt (S*(2.0 * S-1)*(2.*S+1.0)*(S+1.0) *
&       (2.0*S+3.0)) / 6.0

        RETURN

        END
```

C.2.3 *Function Hzb*

```
*       FORTRAN Function Hzb(N,S,J,MJ,Jp,C)
*
*       Jonathan C. Bloch      09/01/95
*
*       • Calculates Zeeman Matrix elements for Hund's case (b) Σ states
*
*         in a coupled representation  <N S J MJ |Hz| N S Jp MJ>
```

```
*
*       • NEEDS a (external) 3-J routine, uses COS(xπ) = (-1)^x
*
*       • Algorithm:
*
*       (1) Uncouple each IN S J MJ> into the 2S+1 IN MN>IS MS>
*
*            using 3-J coefficients.
*
*       (2) Calculated <N SJ MJ IHzI N S Jp MJ> in the uncoupled
*
*            representation by summing over MS, noting:
*
*              <Hz> = c MS ∂(MSMS' ∂(MJMJ') ∂(MNMN') ∂(NN')
*
*       • C is the effective coupling constant, C=-μGB
*
      FUNCTION Hzb(N, S, J, Mj, Jp, C)

      IMPLICIT NONE

      REAL*8 Hzb, N, S, J, Mj, Jp, C, Ms, Mn, TJ

      EXTERNAL TJ

      Hzb = 0.0

      DO Ms = -S, S, 1

            Mn = Mj - Ms

            Hzb = Hzb + TJ(N,S,Jp,Mn,Ms,-Mj) * TJ(N,S,J,Mn,Ms,-Mj) * MS

      END DO

      Hzb = Hzb * DSQRT((2*J+1.0) * (2.0*Jp+1.0)) * c *
     &  DCOS(2.0*(N-S-Mj)*DBLEQ(PI))

      RETURN

      END
```

C.2.4 *Function Mueb*

```
*       FORTRAN Function Mueb(NN,S,J,MJ,Jp,C)
*
*       Jonathan C. Bloch      09/01/95
*
*       PPC COMPILER OPTIONS SHOULD BE: -u -noimplicit -ov -r -double
*
*       • Calculates transition amplitude of hund's case (b) Σ states by
*
*          projecting onto case (a) Σ states assuming that radiation is not
*
*          along internuclear axis z (perpendicular ΔMj=±1 only !)
*
*       • the helicity of light is a parameter, RCP or LCP, chosen by setting
*
*          RL=±1 corresponding to ΔMj=±1
*
*       • input is case (b) coupled representation, with ΔS=0 !
*
*                <N S J MJ |μe| Np S Jp Mjp>
*
*       • NEEDS an (external) 3-J routine,  uses COS(xπ) = (-1)^x
*
*          and Function M1(x)=(-1)^x
*
*       • Algorithm:
*
*       (1)  Expand each Hund's case (b) |N S J MJ>  state into the 2S+1
*
*            Hund's case (a) |S Σ >|J Mj Ω> case (a) states, with Ω=Σ,
*
*            using 3-J coefficients.
*
*       (2) Calculate the  case(a) matrix elements of the molecule fixed
*
*           components of μe by rotating the lab-fixed components using
*
*            wigner D symbols, etc...(leading to 3-J's)
*

      FUNCTION  Mueb(N,S,J,Mj,Np,Jp,Mjp,RL)
      IMPLICIT NONE
      REAL*8 Mueb, N, S, J, Mj, Jp, Np, MjP, TJ, sigma, Cb, Cbp, RL, M1
      EXTERNAL TJ
```

```
      Mueb = 0.0

      DO Sigma = -S, S,1

* Cb and Cbp are the "amplitudes" or projection coefficients of the
* Hund's case(a) functions with Σ=sigma for the two levels

            Cb= M1(N-S+sigma) * DSQRT(2.*N+1.)  *
&             TJ(J,S,N,sigma,-sigma,0.)

            Cbp=M1(Np-S+sigma)*DSQRT(2.*Np+1.)  *
&             TJ(Jp,S,Np,sigma,-sigma,0.)

* we have sigma states of the same multipicty (2S+1), use Ω=Σ and ΔΩ=0
*       the first 3-J symbol (below) contains selection rule for ΔΩ
*       the second 3-J contains the ΔMj rule
*       the results are always purely real since in an intermediate step
*       (assumed, not shown) the wignar D functions are expressed as
*       clebsh-gordan coefficients with a phase-choice made to make them
*       purely real. The CB's lead to the 3-J's which then are also purely real
*       NOTE: the signs though may be + or - which leads to interferences !

            Mueb=Mueb+Cb*Cbp*DSQRT((2.*Jp+1.)/(2.*J+1.))  *
&             M1(-J-Jp+sigma+Mj)  *  TJ(Jp,1.,J,sigma,0.,-sigma)  *
&             TJ(Jp,1.,J,Mjp,RL,-Mj)

      END DO

      RETURN

      END

*     FORTRAN Function M1
*
*     calculate  (-1)^q
*
      FUNCTION M1(q)

      IMPLICIT NONE

      REAL*8 M1,q

      M1=DCOS(q*DBLEQ(PI))

      RETURN

      END
```

C.2.5 *Subroutine H8b*

```
* FORTRAN Subroutine H8b
*
*       Jonathan C. Bloch and Leonid Kaledin
*
*       Compatible with Field group's non-linear least squares fitter
*
*       Fills a 8Σ effective Hamiltonian in Hund's case (b)
*               DOES NOT INCLUDE HIGHER-ORDER EFFECTS THAN Hsr and Hss
*
SUBROUTINE H8b(IP,P,H,J,MAXP)
     PARAMETER(NNPAR=9,NNDATA=1500,NNHSIZE=4,NNBLOCK=4,NNJMAX=90)

c       P(1)=B"
c       P(2)=D"
c       P(3)=Lambda"
c       P(4)=Gamma"
c         P(5)=T'(v)
c       P(6)=B'
c       P(7)=D'
c       P(8)=Lambda'
c       P(9)=Gamma'

      REAL*8 H(NNHSIZE,NNHSIZE), P(NNPAR)

     INTEGER MAXP(NNBLOCK)

      REAL*8 J,Z,E,N

     INTEGER IP,W

     do k1=1,NNHSIZE

         do k2=1,NNHSIZE

                 H(k1,k2)=0.0

         enddo

    enddo

         e=-1000000000000.

       if(IP.eq.1.or.IP.eq.2) then
        W=0
     end if

       if(IP.eq.3.or.IP.eq.4) then
        W=5
     end if

      if((IP.EQ.2).OR.(IP.EQ.4)) GO TO 110
```

```
c  e-parity
c F5
      N=J+0.5
                H(2,2)=P(1+W)*N*(N+1)-P(2+W)*N*N*(N+1)*(N+1)+5*P(3+W)*(1-12./
&       (2*N-1)+9./(2*N+3))-0.5*P(4+W)*(N+16)
      if(N.LT.2.0) then
                 H(2,2)=e
     endif

c F3
      N=J-1.5
                H(3,3)=P(1+W)*N*(N+1)-P(2+W)*N*N*(N+1)*(N+1)+3*P(3+W)*(1-7./
&       (2*N-1)+20./(2*N+3))+0.5*P(4+W)*(3*N-12)
      if(N.LT.1.0) then
              H(3,3)=e
     endif

c F7
      N=J+2.5
                H(1,1)=P(1+W)*N*(N+1)-P(2+W)*N*N*(N+1)*(N+1)-P(3+W)*(1+45./
&       (2*N-1))-0.5*P(4+W)*(5*N+12)
      if(N.LT.3.0) then
         H(1,1)=e
     endif

c F1
      N=J-3.5
                H(4,4)=P(1+W)*N*(N+1)-P(2+W)*N*N*(N+1)*(N+1)-7*P(3+W)*(1-3./
 &      (2*N+3))+3.5*P(4+W)*N
      if(N+1.0.LT.1.0) then
         H(4,4)=e
     endif

C off-diagonal elements
C  F7-F5
      N=J+2.5
      if(N.LT.4.0) GO TO 100
                Z=(N+J+4.5)*(N+J+3.5)*(N+J-4.5)*(N+J-3.5)*(N-J+3.5)*(N-J+2.5)*
&       (J-N+4.5)*(J-N+5.5)/((2*N-1)*(2*N-1)*(2*N-3)*(2*N+1))
        H(1,2)=0.5*P(3+W)*DSQRT(Z)
       H(2,1)=H(1,2)

C  F5-F3
      N=J+0.5
      if(N.LT.3.0) GO TO 100
                Z=(N+J+4.5)*(N+J+3.5)*(N+J-4.5)*(N+J-3.5)*(N-J+3.5)*(N-J+2.5)*
&       (J-N+4.5)*(J-N+5.5)/((2*N-1)*(2*N-1)*(2*N-3)*(2*N+1))
        H(2,3)=0.5*P(3+W)*DSQRT(Z)
       H(3,2)=H(2,3)

C  F3-F1
```

```
      N=J-1.5
      if(N.LT.2.0) GO TO 100
                Z=(N+J+4.5)*(N+J+3.5)*(N+J-4.5)*(N+J-3.5)*(N-J+3.5)*(N-J+2.5)*
     &    (J-N+4.5)*(J-N+5.5)/((2*N-1)*(2*N-1)*(2*N-3)*(2*N+1))
          H(3,4)=0.5*P(3+W)*DSQRT(Z)
          H(4,3)=H(3,4)

  100 CONTINUE
      if(IP.EQ.3) then
          H(1,1)=H(1,1)+P(5)
          H(2,2)=H(2,2)+P(5)
          H(3,3)=H(3,3)+P(5)
        H(4,4)=H(4,4)+P(5)
      end if
      go to 999

C  f-parity
  110 CONTINUE

C F4
      N=J-0.5
                H(3,3)=P(1+W)*N*(N+1)-P(2+W)*N*N*(N+1)*(N+1)+5*P(3+W)*(1-9./
     &    (2*N-1)+12./(2*N+3))+0.5*P(4+W)*(N-15)
      if(N.LT.2.0) then
          H(3,3)=e
      endif

C F6
      N=J+1.5
                H(2,2)=P(1+W)*N*(N+1)-P(2+W)*N*N*(N+1)*(N+1)+3*P(3+W)*(1-20./
     &    (2*N-1)+7./(2*N+3))-0.5*P(4+W)*(3*N+15)
      if(N.LT.3.0) then
          H(2,2)=e
      endif

C F2
      N=J-2.5
                H(4,4)=P(1+W)*N*(N+1)-P(2+W)*N*N*(N+1)*(N+1)-P(3+W)*(1-45./
     &    (2*N+3))+0.5*P(4+W)*(5*N-7)
      IF(N.LT.1.0) then
          H(4,4)=e
      endif

C F8
      N=J+3.5
                H(1,1)=P(1+W)*N*(N+1)-P(2+W)*N*N*(N+1)*(N+1)-7*P(3+W)*(1+3./
     &    (2*N-1))-3.5*P(4+W)*(N+1)
      IF(N.LT.4.0) then
          H(1,1)=e
      endif
```

```
C off-diagonal

C  F8-F6
       N=J+3.5
       if(N.LT.4.0) GO TO 200
                Z=(N+J+4.5)*(N+J+3.5)*(N+J-4.5)*(N+J-3.5)*(N-J+3.5)*(N-J+2.5)*
&       (J-N+4.5)*(J-N+5.5)/((2*N-1)*(2*N-1)*(2*N-3)*(2*N+1))
         H(2,1)=0.5*P(3+W)*DSQRT(Z)
        H(1,2)=H(2,1)

C  F6-F4
       N=J+1.5
       if(N.LT.3.0) GO TO 200
                Z=(N+J+4.5)*(N+J+3.5)*(N+J-4.5)*(N+J-3.5)*(N-J+3.5)*(N-J+2.5)*
&       (J-N+4.5)*(J-N+5.5)/((2*N-1)*(2*N-1)*(2*N-3)*(2*N+1))
         H(3,2)=0.5*P(3+W)*DSQRT(Z)
        H(2,3)=H(3,2)

C  F4-F2
       N=J-0.5
       if(N.LT.2.0) GO TO 200
                Z=(N+J+4.5)*(N+J+3.5)*(N+J-4.5)*(N+J-3.5)*(N-J+3.5)*(N-J+2.5)*
 &      (J-N+4.5)*(J-N+5.5)/((2*N-1)*(2*N-1)*(2*N-3)*(2*N+1))
         H(4,3)=0.5*P(3+W)*DSQRT(Z)
        H(3,4)=H(4,3)

 200  CONTINUE
      if(IP.EQ.4) THEN
        H(1,1)=H(1,1)+P(5)
        H(2,2)=H(2,2)+P(5)
        H(3,3)=H(3,3)+P(5)
        H(4,4)=H(4,4)+P(5)
      end if

 999    continue
      return
     end
```

C.2.6 *Subroutine H8a*

```
* FORTRAN Subroutine H8a
*
*       Jonathan C. Bloch
*
*       Compatible with Field group's non-linear least squares fitter
*
*       Fills a 8Σ effective Hamiltonian in Hund's case (a)
*               DOES NOT INCLUDE HIGHER-ORDER EFFECTS THAN Hsr and Hss
*
SUBROUTINE H8a(IP,P,H,J,MAXP)
    PARAMETER(NNPAR=9,NNDATA=1500,NNHSIZE=4,NNBLOCK=4,NNJMAX=90)
```

```
c       P(1)=B"
c       P(2)=D"
c       P(3)=Lambda"
c       P(4)=Gamma"
c         P(5)=T'(v)
c       P(6)=B'
c       P(7)=D'
c       P(8)=Lambda'
c       P(9)=Gamma'

      REAL*8 H(NNHSIZE,NNHSIZE), P(NNPAR)
     INTEGER MAXP(NNBLOCK)
      REAL*8 J,DNE,Br,Dr,L,G,T,X
     REAL*8 A,B,C,D,ES,FS,GS,HS
     INTEGER IP,W

* Clean out the entire Hamiltonian block, fill it with zeroes
      do k1=1,NNHSIZE
       do k2=1,NNHSIZE
          H(k1,k2)=0.0
       enddo
     enddo

* If a diagonal element does not exist, it will be assigned this #,
         DNE=-1000000000000.

* Block (=IP) 1 & 2 are for the Ground state, while Block 3 & 4 are
* for the upperstate
      W=0
       if(IP.eq.3.or.IP.eq.4) then
        W=5
      end if

* For simplifying the matrix elements the parameters have been reassigned * as follows:

        Br=P(1+W)
        Dr=P(2+W)
       L=P(3+W)
       G=P(4+W)
       T=P(5)

* ef is used to designate e/f parity in the wang symmtrized basis set.
* From RWF's book, I know that e-parity is formed from the - combination
* and f-parity is formed from the + combination of signed omega states

      ef=1.
       if((IP.EQ.2).OR.(IP.EQ.4)) then
        ef=-1.
      end if

       X = J*(J+1.)
```

```
* These are the diagonal R2 matrix elements:
      A = X - 8.75
      B = X + 3.25
      C = X + 11.25
      D = X + 15.25

* These are the off-diagonal R2 matrix elements squared.
* Note, however that the actual elements are negative.
* Thus, the actual elements are -1*DSQRT('variable below').
       ES =  7.*(X-8.75)
       FS = 12.*(X-3.75)
       GS = 15.*(X-0.75)
       HS = 16.*(X+0.25)
* All matrix elements below are expressed in terms of the above
* variable assignments
*
* Diagonal elements of block IP
*
* F1 (e, ef=1) or F2 (f, ef=-1)
        H(4,4)= Br*A - Dr*(    (A*A)+ES)  -3.5*G + 14.*L
      if(J.LT.3.5) then
       H(4,4)=DNE
     endif

* F3 or F4
        H(3,3)= Br*B - Dr*(ES+(B*B)+FS)  -9.5*G +  2.*L
      if(J.LT.2.5) then
       H(3,3)=DNE
     endif

* F5 or F6
        H(2,2)= Br*C - Dr*(FS+(C*C)+GS) -13.5*G    -6.*L
      if(J.LT.1.5) then
       H(2,2)=DNE
     endif

* F7 or F8
        H(1,1)= Br*D - Dr*(GS+(D*D)+HS) -15.5*G  -10.*L
&       -   ef*DSQRT(HS)*(Br - 2*Dr*D -0.5*G)
      if(J.LT.0.5) then
       H(1,1)=DNE
     endif

*  elements next to the diagonal (delta omega = +1 or -1)

* F7-F5 or F8-F6
     if(J.LT.1.5) GO TO 100
       H(1,2)= -DSQRT(GS) * (Br - Dr*(C+D - ef*DSQRT(HS)) - 0.5*G)
       H(2,1)=H(1,2)

* F5-F3 or F6-F4
```

```
      if(J.LT.2.5) GO TO 100
        H(2,3)= -DSQRT(FS) * (Br - Dr*(B+C) - 0.5*G)
        H(3,2)=H(2,3)

*  F3-F1  or  F2-F4
      if(J.LT.3.5) GO TO 100
        H(3,4)= -DSQRT(ES) * (Br - Dr*(A+B) - 0.5*G)
        H(4,3)=H(3,4)

 100  CONTINUE

*  elements where delta omega = +2 or -2

*  F7-F3  or  F8-F4
      if (J.LT.2.5) GO TO 200
       H(3,1)= -Dr * DSQRT(GS*FS)
        H(1,3)=H(3,1)

*  F5-F1  or  F6-F2
      if (J.LT.3.5) GO TO 200
       H(4,2)= -Dr * DSQRT(FS*ES)
        H(2,4)=H(4,2)
 200   Continue

      if (IP.GT.2) then
         H(1,1)=H(1,1)+ T
         H(2,2)=H(2,2)+ T
         H(3,3)=H(3,3)+ T
         H(4,4)=H(4,4)+ T
     end if

     go to 999
 999   continue
      return
     end
```

C.2.7 *Program ZS*

```
*       FORTRAN Program ZS
*       Jonathan C. Bloch      October 1995
*       Σ state MR effect simulator !
*       with output auto-read by IGOR PRO
*
*       lower Σ state -> Hund's case (b)
*       upper state -> Hund's case (a)-like

   PROGRAM ZS

        IMPLICIT NONE

         INTEGER*4  Points,iJL,iJH,iNmax,iDmax,iS,iJmax,HJ,
```

```
x iMult,iSL,iSH,iDNE,idNmax,idJmax

      REAL*8 Hrb,Hsrb,Hssb,Hzb,RS,T,Mueb

      CHARACTER*2 SN
*
*     TO USE ZS:
*           (1) Change THESE PARAMETERS in statements below
*           (2) Change #'s in format statements 2XX and 3XX
*           (3) Re-compile all source code
*
*     For integer J and S:
*           set:    iS = S and HJ = 0
*
*     For half-integer J and S
*           set:    iS = S-0.5 and HJ = 1
*
*     Also set:
*
*           iNmax= largest N to calculate, should be ≥ S
*           idNmax = largest abs(ΔN) considered for transitions
*           idJmax = largest abs(ΔJ) considered for transitions
*
*           Points = # number of grid points for magnetic field values
*           T = arbitrary Energy in cm-1 of isolated upper-state level
*
*     WARNING!
*           Due to format statements, dimension of matrix is limited to ≤ 9 x 9 !
*           If Nmax so that all levels exits, we are limited to quartet states.
*           (for sextet states, we want Nmax=3, hence Dmax=4*5 - 10 = 10 !)
*           this can all be fixed by using 2 places for output of array indices
*           and extending 'logicals' in definition of iDNE !
*           (in other words, only minor changes needed!)
*

      PARAMETER( iS=0 , HJ=1 , iNmax=1 , idNmax=1 ,idJmax=1 ,Points=10 , T=1000 )

*
*     DO NOT CHANGE  PARAMETERS BELOW ---> these are calculated from above !
*
*           iMult  = 'Multiplicity' = 2S+1 = 2*iS+1+HJ
*           iDNE   = '# of levels for S, that do not exist assuming correct iNmax'
*           iDmax= 'full Dimension of H'
*           = (# of N levels)*(Multiplicity)-(#level that DNE)=(iNmax+1)*imult-iDNE
*           iJmax= 'largest J level - lowest J level' = iNmax+iS
*           iJL    = 'most negative Mj value - lowest J level' = -iJmax-HJ
*           iJH    = 'most positive Mj value - lowest J level' = iJmax


* WARNING !
*     Logical Assignments in PARAMETER statement are MACHINE DEPENDANT!
```

```
*       For PPC MAC, logical (1=1) evaluates to -1, not +1

        PARAMETER(iMult=(2*iS+1+HJ), iJmax=iNmax+iS , iJL=-iJmax-HJ, iJH=iJmax )
       PARAMETER(iDNE=(imult-1)-(imult-3)*(imult>3)-(imult-5)*(imult>5)-
     x(imult-7)*(imult>7))

         PARAMETER( iDmax=(iNmax+1)*imult-iDNE )

         PARAMETER( iSL=-iS-HJ,iSH=-is-HJ+iMult-1)

        REAL*8 N,J,Np,Jp,B,D,L,G,Gs,Mu,Mj, Bmin,Bmax,Sd,Si,Sp,dNmax,dJmax,EU

* LOWER STATE full HAMILTONIAN MATRIX H(i,k) where i and k are both functions of J and N

         REAL*8 H(iDmax,iDmax)

* LOWER STATE ENERGY = EL(Bfield, Mj ,x=f(N,J)        )

        REAL*8 EL(points,iJL:iJH,iDmax)


* Transition ENERGY = TE(Bfield,ΔN,ΔJ,x"=f(N,J),Mj",ΔMj)
*       note: Nominal J",N" from X=f(N",J") and N'(nom)=Nmax+dNmax.....

         REAL*8 TE(points,-idNmax:idNmax,-idJmax:idJmax, iDmax ,iJL:iJH ,-1:1)

* Transition INTENSITY = TE(Bfield,ΔN,ΔJ,x"=f(N,J),Mj",ΔMj)

         REAL*8 TI(points,-idNmax:idNmax,-idJmax:idJmax, iDmax ,iJL:iJH ,-1:1),TTi

*       H eigen-values = W, H eigen vectors = Z, index is the usual X=f(N,J)

          REAL*8 W(iDmax),Z(iDmax,iDmax),fv1(iDmax),fv2(iDmax)

        REAL*8 DNE,DD,MJi,ZC

         REAL*8 Bfield,Bstep

         REAL*8 Nmax,S,Dmax,Jmin,Jmax,Ju,MJu,Nu

           INTEGER*4 ierr,x,y,Bpoint,iMj,iN,iNp,iJ,iJP,i,k,i2J(iDmax),
     x   i2N(iDmax),iJu,iMJu,iNu,idMj,idN,idJ

* NOTICE all needed externals below !!!!!!!!

        EXTERNAL Hrb,Hsrb,Hssb,RS,Hzb,Mueb,SN

* Take care of half-integer J and S: Smallest J=Jmin is either 0 or 0.5
*       HJ true indicates half-integer, HJ false indicates integer
*       set: Jmax (real) =iJmax(integer)+Jmin(real)
*            and S (real)=Jmin(real)+iS(integer)
```

```
      Jmin=0.0
      IF (HJ .eq. 1) THEN
            Jmin=0.5
      END IF
      Jmax = Jmin + DFLOTI(IJmax)
      S = Jmin + DFLOTI(iS)
      Nmax=DFLOTI(iNMAX)
      Dmax=DFLOTI(iDMAX)
* set-up conversion from Matrix (i,k) to J,N for all J,N
* save i <-> J,N as look up table for later
* levels that do not exist do to N<S are auto-skipped !
* largest matrix index must be still a single digit, hence max. is 9x9
      i=0
      DO iN=0,iNmax
            N=DFLOTI(in)
            Do   iJ=iN+iS-JMIN0(imult,2*iN+1)+1,(iN+iS)
                  J=DFLOTI(iJ)+Jmin
                  i=i+1
                  IF( iDmax .LT. i ) THEN
                        WRITE(6,1000)' Matrix Size Error !'
                        WRITE(6,1000)' You changed wrong parameter statement !'
                        WRITE(6,1000)'  Bye !'
                        GO TO 10000
                  END IF
                  i2J(i)=  iJ
                  i2N(i)=  iN
            END DO
      END DO
```

```
* the Matrix H has two indices i,k -- each an arbitrary function of J and N
*       We fill H in this order: all J for N;  all J for N+1; etc...
*       Mathematically, we have i= N(2S+1) + Sp + S +1
*       where J-N=Si and Jp-Np=Sp.
*       the results were already stored in arrays iJ(i)=J-Jmin and iN(i)=N for lookup
*
*       e.g., given S=0.5, Nmax=2 and DMax=5, iDNE=1  --> H is 5x5 , and looks like this:
*
*
*
*                       i       1       2       3       4       5
*       Mj              N       0       1       1       2       2
*       H(i,k)          Si      0.5     -0.5    0.5     -0.5    0.5
*                       J       0.5     0.5     1.5     1.5     2.5
*                       ------------------------------
* K Np  Sp    J         |
* 1 0    0.5   0.5      |
* 2 1   -0.5   0.5      |
* 3 1    0.5   1.5      |
* 4 2   -0.5   1.5      |
* 5 2    0.5   2.5      |
*

* NOW, write to screen, not to file: TELL USER ABOUT PROGRAM AS COMPILED !

      WRITE(6,1000)'*---- Σ state simulator, by Jon Bloch ----*'
      WRITE(6,1000)' Compiled for:'
      WRITE(6,5000)'            S =',S
      WRITE(6,5000)'       up to N =',Nmax
      WRITE(6,5000)'         and J =',JMax
      WRITE(6,5000)'      Smallest J =',Jmin
      WRITE(6,5000)'Matrix  Dimension =',Dmax
      WRITE(6,1000)'*----      Check FORMAT statements      ----*'
      WRITE(6,1000)' '
      WRITE(6,1000)' Conversion Table: Matrix Index to J,N '
      WRITE(6,50)'X  ==>  (  J,  N  ) ',(X,dfloti(i2J(x))+Jmin,i2N(x),x=1,Dmax)
50    Format(' ',a,4(' : ',I1, ' ==> ( ' ,F3.1 , ', ' , I1, ' )'))

      WRITE(6,1000)' '

* Get constants from keyboard, On MAC PPC, monitor is pre-assigned unit=6

      WRITE (6,1000)'Choose B,D,lamda,gamma in cm-1'

      READ *,B,D,L,G

      WRITE (6,1000)'Choose Bmin, Bmax in Gauss'

      READ *,Bmin,Bmax
```

```
      Bstep=((Bmax-Bmin)/DFLOAT(points-1))

* Setup Output FILE

      CALL F_SetDefaultFileName ('ZS.awav')
      OPEN(10,File="'Choose ouput file (for IGOR
PRO)',Status='New',CREATOR='IGR0',FILETYPE='IGTX')

*     Above file can only be opened by IGOR PRO ! Use next line for standard TEXT file output
*     OPEN(10,File="'Choose ouput file (formatted for IGOR)',Status='New')

* Constants for Hz
*     G-value const Mu as 1.4 MHZ/GAUSS or in cm-1/Gauss, below

      Mu=4.67D-05

      Gs=2.002

* When H is firts set up or filled, diagonal Energies (that do not yet exist)
* are assigned DNE, while all off diagonal elements are assigned zero

      DNE=-1000000000000.

***** Calculate the LOWER STATE (and while doing so calculate needed upperstate levels *****
* Here we consider all N=0..Nmax, J=Jmin...Jmax
* for any value of Lambda and gamma and B. Hence the zeeman effect mixes J
* and the spin-spin interaction mixes N, and we must consider Mj the good quantum #
* and so we FILL MATRICES organized by Mj and diagonalize them, saving the Eigen Values
* we then use them to calculate transition frequencies
* and the e-vectors (projected or expanded in a case (a) bases set) to calc. intensities
* noting that we already calc. everything we need for the 'isolated' J,N pure upper-state
*
* We do everything (points) times, each iteration of Bpoint at a new field value.....

      Do  Bpoint=1,points,1

            Bfield = Bstep * DFLOTI(Bpoint-1) + Bmin

            write(6,5000) 'LOWER STATE: Working on B-field = ',Bfield

* Mj and S are constants for each matrix, so elements are < Np Jp IHI N J >
* first loop though all Mj's

            Do  iMj=iJL,iJH

                  Mj=DFLOTI(iMj)+Jmin

* clean out and set-up matrix (for each Mj !). Set all diagonal elements to DNE

      DO x=1,iDmax
            DO y=1,iDmax
                  H(x,y)=0.
```

```
                IF (x .eq. y) then
                    H(x,y)=DNE
                END IF
            END DO
        END DO
```

* We will loop through each element in the matrix, for the smallest abs(Mj) everything exists!
* We look up N and J from table

```
                DO i=1,iDmax

                    iN=i2N(i)

                    iJ=i2J(i)

                    N=DFLOTI(in)

                    J=DFLOTI(iJ)+Jmin
```

* always make sure that this Mj exists for this J

```
                    IF (Dabs(Mj) .LE. J) THEN

                        DO k=1,iDmax

                            iNp=i2N(k)

                            iJp=i2J(k)

                            Np=DFLOTI(iNp)

                            Jp=DFLOTI(iJp)+Jmin
```

* and check this Mj for Jp

```
                            IF (Dabs(Mj) .LE. Jp) THEN
```

* ΔJ=0,ΔN=0 --> calculate the completely diagonal elements <N S J Mj IHI N S J Mj>

```
                                IF (i .eq. k)  THEN

                    H(i,k)=Hrb(N,B,D)+Hsrb(N,S,J,G)+Hssb(N,S,J,N,L)

                                END IF
```

* S≥1 and ΔN=±2,ΔJ=0 --> add in the off-diagonal spin-spin elements

```
                IF  ((S .GE. 1.) .AND. (labs(iN-iNp) .eq. 2) .AND. (iJ .eq. iJp) ) THEN

                                    H(i,k)=Hssb(N,S,J,Np,L)
```

```
                                        END IF
* and for all ΔN=0, we must ADD the zeeman interaction contribution:

                                        IF (iN .eq. iNp) THEN
                                            Zc=Bfield*Gs*Mu
                                        H(i,k)=H(i,k)+Hzb(N,S,J,Mj,Jp,Zc)

                                        END IF

                                    END IF
* next k
                                END DO

                            END IF
* next i
                        END DO
*
* DONE FILLING H: variables free now are iJ,J,iJp,Jp,iN,N,iNp,Np,i,k
*
*                               iMj , Mj and Bpoint are still in use !
*
* diagonalize, getting BOTH e-values and e-vectors
                        call  RS(iDmax,iDmax,H,w,1,z,fv1,fv2,ierr)

* the plan:     (1) loop through eigen-values, saving E-values
*               (2) clear out array for storing transition E and Int's
*               (3) If LOWER LEVEL actually exists, calculate all transitions from it

*       although J is mixed by the field, N still has defined parity
*       and we still have the selection rule that ΔN is odd
*       a parameter statement sets the bounds on abs(ΔN) and (ΔJ)
*       since J is mixed we can have even ΔJ  even for Σ-Σ transitions !

                        Do i=1,iDmax

* Save E
                            EL(Bpoint,iMj,i)=w(i)
```

```
* first, clear out all arrays:  idN is always odd !

                        DO idN=-idNmax,idNmax,2

                            DO idJ=-idJmax,idJmax,1
*   ΔMj=-1
                                TE(Bpoint,idN,idJ,i,iMj,-1)=DNE
                                TI(Bpoint,idN,idJ,i,iMj,-1)=DNE

*   ΔMj=+1
                                TE(Bpoint,idN,idJ,i,iMj,+1)=DNE
                                TI(Bpoint,idN,idJ,i,iMj,+1)=DNE

                            END DO

                        END DO

*  IF LOWER LEVEL exists continue to calculate all the stuff

                        IF( EL(1,iMj,i) .NE. DNE) THEN

* now try and calculate transitions:
* we don't know N and J downstairs exactly, we must organize by upperstate
* the branch labels will be based on zero field values of J,N downstairs !
* the PARITY of N downstairs is known
* so depending on i, we need only check odd or even N upstairs !

* zero-field lower state nominal J and N:

                            iN=i2N(i)

                            N=DFLOTI(iN)

                            iJ=i2J(i)

                            J=DFLOTI(iJ)+Jmin

* try all values of ΔN, ΔJ allowed checking that J' exists for N' and Mj' is possible for that J'


                            DO idN=-idNmax,idNmax,2

* calculate N upstairs, based on zero field downstairs

                                iNu=iN+idN

                                Nu=DFLOTI(iNu)

                                IF (iNu .GE. 0) THEN

                                    DO idJ=-idJmax,idJmax,1
```

```
* calculate J upstairs, based on zero field downstairs

                                                    iJu=iJ+idJ

                                                    Ju=DFLOTI(iJu) + Jmin

* 2 constraints on Ju: J≥ N-S (except at N<S !)    and Ju≤N+S

      IF ((iJu .GE. iJmax-JMIN0(imult,2*iNmax+1)+1) .and. (iJu .LE. iNu+iS)) THEN

                                                          DO idMJ=-1,1,2

* now get Mj upstairs , this is exact, since we know Mj downstairs

                                                               iMju=iMj+idMj

                                                          Mju=DFLOTI(iMju)+Jmin

                                                    IF (DABS(Mju) .LE. JU) THEN

* the upper level exists, so calculate its energy.
*       ignoring Spin-Rotation,Spin-Spin, we have only rotation, T and the Zeeman Interaction!
*       think of T as a case (b) pseudo spin-orbit constant !

*       used to spread out upperstate:
*             EU = HrB( Nu,B,D) + T*(1.+(Ju-Nu)/100.) + Hzb(Nu,S,Ju,Mju,Ju,Zc)
*
* this line doesn't use T and doesn't spread out states....

            EU = Hrb(N,B,D)+Hsrb(N,S,J,G)+Hssb(N,S,J,N,L)+Hzb(Nu,S,Ju,Mju,Ju,Zc)

*Now we calculate the transition Energy,

                                          TE(Bpoint,idN,idJ,i,iMj,idMj)=Eu-EL(Bpoint,iMj,i)

*and using Eigen-Vectors Z(k,i), calculate Transition Intensity TI
*external function Mueb takes care of case(b)-case(a) problems...returns signed Transition
Amplitude !
* by using e-vectors we are finally expressing "i" in terms of pure J and N levels !
                                                               TTI=0.0

      DO k=1,Dmax

* look up actual J and N for each lower state bases vector now, and make them real*8

            J=DFLOTI(i2J(k))+Jmin

            N=DFLOTI(i2N(k))

* now, call μeb function for each pure-case(b) lower J,N-level and upper Ju,Nmax-level
```

```
                TTI=TTI+Z(k,i)*Mueb(Nu,S,Ju,Mju,N,J,Mj,DFLOTI(idMj))

        END DO

* notice, transition intensity as a signed quantity facilitates MRS lineshape calc.

                TI(Bpoint,idN,idJ,i,iMj,idMj)=TTI*TTI*DFLOTI(idMj)

                                                                ENDIF
* ΔMj loop
                                                            END DO

                                                        ENDIF

* ΔJ loop
                                                    END DO

                                                END IF
* ΔN loop

                                            END DO

                                        END IF

* next "i" in eigen value assignment loop

                            END DO

* done with everything for this Mj,
* next Mj

                    END DO

* next Bstep

        END DO

* all done with calculations.....
*
*       OUTPUT section for reading and processing by IGOR PRO.....
*               See IgorPro Manual
*

        WRITE(10,1000)'IGOR'

* First write-out look-up table !

        WRITE(10,1000)'X I Conversion Table:  X ==> J , N'
        WRITE(10,1000)'Waves/o/d  i2J,i2N'
        WRITE(10,1000)'Begin'
        DO i=1,Dmax
                WRITE(10,190)   DFLOTI(i2J(i))+Jmin,DFLOTI(i2N(i))
```

```
      ENDDO
      WRITE(10,1000)'END'

* LOWER STATE results:
*       write out all levels, even if they do not exist
*       so that we have nice blocks of data.
*       then tell IGOR to delete the levels that DNE
*       Organization:  Blocks of Mj, columns of all x=1,Dmax (recall x=f(N,J)
*       Label levels by index in H, not J,N---you lookup later

      DO  iMj=iJL,iJH

            MJ=DFLOTI(iMj)+Jmin

            WRITE(10,1000)'X  I  '
            WRITE(10,200)   'X  ILower-state:  Mj=',MJ
            WRITE(10,1000)'X  I  '

* column NAMES are based on the value of MJ and H index since J and N are nominal !
*       even at zero field, N and J are "nominal"
*       because we organized the levels by Mj, not J --
*       the USUAL NAMING convention is based on energy ordering of levels with same J NOT Mj
!
*       also, with non- zero field J,N are mixed....

* the column name must not have "+" , "-" ,  or "." characters (see IGOR manual)
*       so we write only POSITIVE integer labels out to the file, integer=ABS(real Mj -Jmin)
*       and indicate the sign of the integer with either a 'p' for (REAL MJ -Jmin) >0 or 'm' for
<0

* write COLUMN LABELS for this Mj, uses function SN to deal with sign of iMJ

            WRITE(10,210)   (i,SN(iMJ),JIabs(iMJ),i=1,iDmax)

            WRITE(10,1000)'Begin'

* write all ENERGY levels across by x, down by Bpoint

            DO Bpoint=1,Points
                  x=0
                  WRITE(10,230)   (EL(Bpoint,iMj,x),x=1,iDmax)
            ENDDO

            WRITE(10,1000)'END'

* tell IGOR  horizontal axis (or Bfield) scale information

            WRITE(10,240)   (Bmin,Bmax,(i,SN(iMj),JIabs(iMj),i=1,iDmax))

* now if wave does not exist (DNE), tell IGOR to KILL IT
```

```
            DO i=1,iDmax
                  IF(  EL(1,iMj,i) .eq. DNE ) THEN
                        WRITE(10,270)   (i,SN(iMj),Jlabs(iMj))
                  END IF
            ENDDO

*  Mj loop
      ENDDO


* FORMAT STATEMENTS FOR LOWER STATE OUPUT
*       the #'s here in format statements must be set properly !
*       set the # in #('N',I1,'J',I1,'Mjp',I1,',')) to the value of Dmax !
*       if unsure check status output when program runs....
 190  format(1x,g,g)
 200  format(1x,a,g)
 210  format('  Waves/D/O  ',3('X',I1,'Mj',A1,I1,','))
 230  format(3(  1x,g))
 240  format(' X SetScale/I  X  ',g,',',g,', "G",  ',3('X',I1,'Mj',A1,I1,','))
 270  format(' X  Killwaves/Z  ','X',I1,'Mj',A1,I1,',')

* now output TRANSITION ENERGIES and INTENSITIES
*             ΔJ and ΔN are nominal, as is N",J" but N' and J' are rigorous
*

* Organize in BLOCKS of Mj, SUB-BLOCKS of ΔMj,ΔN,ΔJ and columns are of x=1,Dmax where
*   x=f(N,J)

* column names are initially C1,C2....Cn
* if data exists, they are renamed... otherwise they will be overwritten by IGOR, and hence
*  killed

      DO  iMj=iJL,iJH

            Mj=DFLOTI(iMj)+Jmin

            WRITE(10,1000)'X      I-------------------------------------'
            WRITE(10,200) 'X ITransition info: Mj   =',Mj
            WRITE(10,1000)'X  I'

            DO  idMj=-1,1,2

                  WRITE(10,200)  'X  I  rigorous          ΔMj =',DFLOTI(idMj)

                  DO  idN=-idNmax,idNmax,2

                              WRITE(10,1000)'X  I'
                              WRITE(10,200)   'X  I  nominal          ΔN =',DFLOTI(idN)
                              WRITE(10,1000)'X  I'

                        DO  idJ=-idJmax,idJmax,1
```

```
                        WRITE(10,1000)'X  I'
                        WRITE(10,200)  'X I nominal          ΔJ =',DFLOTI(idJ)
                        WRITE(10,1000)'X  I'
```

* before we do anything, check to see if entire block DNE's , since many will not exist !

```
                        k=0

                        DO i=1,iDmax

                        IF(  TE(1,idN,idJ,i,iMj,idMj) .eq. DNE  ) THEN

                              k=k+1

                        END IF

                        ENDDO

                        IF (K .eq. iDmax) THEN

                              WRITE(10,1000)'X I  Block does not exist at all!'
                              WRITE(10,1000)'X I   '

                        ELSE

                              WRITE(10,1000)'X  I'
                              WRITE(10,1000)'X I ....Energies....'
                              WRITE(10,1000)'X  I'
```

* do TRANSITION ENERGY

* now WRITE provisional column names

```
                              WRITE(10,405)  (i,i=1,iDMAX)

                              WRITE(10,1000)'Begin'
```

* ouput ENERGY

```
                              DO Bpoint=1,Points

                  WRITE(10,430)  (TE(Bpoint,idN,idJ,i,iMj,idMj),i=1,Dmax)

                              ENDDO

                              WRITE(10,1000)'END'
```

* now RENAME and Xscale waves that exist

```
                              DO i=1,iDmax

                                    IF(  TE(1,idN,idJ,i,iMj,idMj) .NE. DNE )
```

```
THEN
                                        WRITE(10,450)  (Bmin,Bmax,i)
            WRITE(10,470)  i,  i2N(i)+idN,i2J(i)+idJ,i,SN(iMJ),ABS(iMJ),SN(idMj)
                                          END IF
                                       ENDDO
*now deal with INTENSITY
                                       WRITE(10,1000)'X  I'
                                       WRITE(10,1000)'X  I  Intensities....'
                                       WRITE(10,1000)'X  I'
* provisional Column Names
                                       WRITE(10,405)  (i,i=1,iDMAX)
                                       WRITE(10,1000)'Begin'
*  Intensities
                                       DO Bpoint=1,Points
                          WRITE(10,430)  (TI(Bpoint,idN,idJ,i,iMj,idMj),i=1,iDmax)
                                       ENDDO
                                       WRITE(10,1000)'END'
* now RENAME and X-SCALE waves when TE exists
                                       DO i=1,iDmax
                                  IF(  TE(1,idN,idJ,i,iMj,idMj) .NE. DNE ) THEN
                                                 WRITE(10,460)  (Bmin,Bmax,i)
            WRITE(10,480)  i,  i2N(i)+idN,i2J(i)+idJ,i,SN(iMJ),ABS(iMJ),SN(idMj)
                                          END IF
                                       ENDDO
*                          skip-block end if
                                  END IF
* next ΔJ,
                                  ENDDO
* next ΔN
                       End DO
```

```
* next ΔMj

            END DO

* next lower state Mj

      END DO

* DONE, DONE, DONE, FINALLY DONE WITH ZS!
* format statements for transition stuff
* again YOU MUST change #'s below in #(...) to value of Dmax
 405   format(' Waves/D/O  ',3('C',I1,',') )
 430   format(3(  1x,g))

 * statements below are OK for all Dmax...
 450   format(' X SetScale/I X ',g,',',g,', "G", C',I1 )
 460   format(' X SetScale/I X ',g,',',g,', "G", C',I1)
 470   format(' X RENAME C',I1,', TEN',I1,'J',I1,'X',I1,'Mj',A1,I1,A1)
 480   format(' X RENAME C',I1,', TIN',I1,'J',I1,'X',I1,'Mj',A1,I1,A1)

* other FORMAT statements .... for monitor output
 1000  format(1x,a)
 5000  format(' ',a,g)

10000Continue
      END

* FORTRAN Function SN
*       used in OUTPUT for IGOR
*       returns a string of length 1, based on sign of arg

      Function SN(Arg)

            CHARACTER*1 SN

            Integer*4 ARG

            IF (ARG .LT. 0) THEN

                  SN='m'

            ELSE

                  SN='p'

            ENDIF

            RETURN

      END
```

C.3 *A sampling of utility programs for the Coherent 699-29 laser*

C.3.1 **.SCN loader*

This program reads the IBM binary files by a Coherent 699-29 laser on a Macintosh computer running the graphing software IGORPRO by Wavemetrics.

```
*.SCN loader        by Jonathan C. Bloch

    *.SCN loader loads the IBM binary files created by a Coherent autoscan laser. The routine is a
simple Proc (or Macro) compatible with IGOR PRO (power PC and otherwise). It can be easily modified
for your specific use. After installation, a new menu, "Load_SCN", is added to the IGOR toolbar, with
2 new commands, "Load *.SCN SP" and "Load *.SCN DP".
    Load *.SCN DP loades all sensors from a  *.SCN file as double-precision waves, calculates double-
precision GHz and wavenumber waves, and prints the results in the history. Wave names are formed
from the file name by removing the .SCN suffix; for example, the first channel from file Test.SCN
would become Test_0 with Test_GHz and Test_Cm calculated.  Creates wavenote summary. Caution:
Existing waves (with same names as new waves) are always overwritten !
    Load *.SCN SP loades all sensors from a  *.SCN file as double-precision waves, calculates double-
precision GHz and wavenumber waves, but then redimensions only the sensor waves as single precision
before printing the results in the history.  Since the Autoscan only records 12-bits, this results in
substantial memory (and disk space) savings without any loss of accuracy. However, do to limitations
in the way IGOR performs some commands, having the data waves as SP and the wavenumber waves as
DP may be inappropriate. For example, some curve fitting will not work on mixed wave types !  The
GHz and wavenumber waves must be kept as double precision. Also Creates wavenote summary

Installing*.STN loader for general use (allowing no modification):

    (0) make sure that the file *.SCN loader is somewhere inside the USER PROCEDURES folder in your
        IGOR folder
    (1) from any procedure window in IGOR PRO type the following line, and then compile.
        #include "*.SCN loader"

Installing *.SCN loader for modification:

    (1) open the file *.SCN loader as a procedure in IGOR PRO and compile.
    (2) modify and save as with a new file name....

IGOR CODE:

Menu "Load_SCN"
    "Load *.SCN ...SP",LoadSCN(1)
    help={"Loads 1 binary file (*.SCN) created by Coherent 699 Or 899 -29 laser.  Jonathan C. Bloch
        8/23/95"}
    "Load *.SCN ...DP",LoadSCN(0)
```

```
    help={"Loads 1 binary file (*.SCN) created by Coherent 699 Or 899 -29 laser.  Jonathan C. Bloch
        8/23/95"}
end

Proc LoadSCN(SP)                        | loads 1 Binary File created by Coherent 699 Or 899 -29 laser
    variable SP
    silent 1
    String file
    string ScanDate,ScanTime,name
    variable/d  refNum,NumLoaded,totalfileBytes,dataBytes,MemAlocBytes,infoBytes,filepos
    variable/d  scanNum,StartGhz,  IntMhz,segSec,lenGHz,f
    variable/d  pointsperarray,pointspersegment
    string  NoteStr,doit
        | file to open
            Open/D/M="Choose *.SCN file to load "/R refNum      | dialog only.. BUT gets full file
                                                                | name with path !
            file=S_filename
    if  (cmpstr(file[strlen(file)-4,strlen(file)-1],".SCN")==0)      |make sure its *.SCN
            | get info about the file we just opened (refNum)
            Open/R refNum file      | open the file
            Fstatus refNum
            name=S_filename[0,strlen(S_filename)-5]+"_"          | filename only( no path) - .SCN
            totalFileBytes=V_logEOF                             | S_path is now path name here
            | calc. size of areas in file, see Coherent manual
            infoBytes=10+10+2+8+8+8+8+2+2+24+24+24
            MemAlocBytes=26
            dataBytes=totalfileBytes-infoBytes-2*memalocBytes
            | skip over memory allocation area & data arrays,  read in information about this data set:
            | read in STRING containing scan date -> ScanDate
                filePos=memalocBytes+databytes                  |correct file pos
                FSetPos refNum, filepos
                Freadline/N=10/T="" refNum,  ScanDate           | at most 10 ascii characters
            | read in STRING containing scan time -> ScanTime
                filePos+=10                                     | next area (forced !)
                FSetPos refNum, filepos
                Freadline/N=10/T="" refNum,scanTime             | at most 10 ascii characters
            | read in Unsigned INTEGER containing scan number ->scanNum
                filePos+=10                                     | move to end of string
                FSetPos refNum, filepos
                FBinRead/f=2/b refNum,scanNum                   | 2 byte unsigned int (forced)

            notestr="Data Set #" + num2str(scanNum) + ":\t( *.SCN Load by Jonathan C. Bloch
                        8/23/95)\r    " + ScanDate[0,strlen(scandate)-2] + " "
            notestr+=  ScanTime[0,strlen(scantime)-2]
            | read in DP FP (intel or swapped) containg starting wavelength, in Ghz ->StartGhz
                filePos+=2
                f=5                                             | f=5 means 64 bit floating point
                IFSetPos refNum, filepos                        | no need to move in file, all ready there
                FBinRead/f=(f)/b refNum,startGhz
                | double precision floating point, 8 Bytes, /b==swapped !!!!
                | read in DP FP# containing data collection interval in MHz -> IntMHz
```

```
            IFSetPos refNum, filepos                    I see above
            FBinRead/b/f=(f)  refNum,IntMhz             I DP FP, 8 Bytes, swapped !!!!
            I read in DP FP# containing scan time in seconds per 10GHz segment ->segSec
            filePos+=8
            IFSetPos refNum, filepos                    I see above
            FBinRead/f=(f)/b  refNum,segSec             I DP FP, 8 Bytes, swapped !!!!
            I read in DP FP# containing scan distance in GHz -> lenGHz
            filePos+=8
            IFSetPos refNum, filepos
            FBinRead/f=(f)/b  refNum,lenGHz             I DP FP, 8 Bytes, swapped !!!!
            I done with (all manually read) info that we need, so close (all) file (s)
        close/a
    notestr=notestr+"\r    Starting wavelength "+num2str(StartGhz)+" (GHz)\r    Data interval" +
        num2str(IntMHZ)+" MHz"
    notestr=notestr+"\r    Scan time per segment "+num2str(segsec)+" seconds\r  Scan distance "
        + num2str(lenGhz)+"  GHz"
        I calculate points (not bytes)  that will be read into 1 or more waves automatically
        pointspersegment=ceil(10200/IntMhz)+1           I why need +1  ? Manual Error?
        pointsperarray=(lenGHz/10)*pointspersegment
        I now go load all data.....  (using path and file name!)
        I wave names are automatically chosen.....
        doit="GBLoadWave/Q/O/D/B/N="+name+"/F=2/L=16/S=26/U="  +
            num2str(pointsperarray)  +  "\""+file+"\""
    execute doit
    I make x scaling waves, Ghz, BUT do not forget about overlap !
        duplicate/o  $(name+"0"),$(name+"GHz"),$(name+"CM")
        $(name+"GHz")=StartGhz+P*IntMhz/1000-floor(p/pointspersegment)*IntMhz*3/1000
        $(name+"CM")=    $(name+"GHz")/29.9792458
        SetScale y 0,0,"GHz", $(name+"GHz")
        SetScale y 0,0,"K", $(name+"CM")
        notestr+="\r loaded WAVES"
        if(SP)
            notestr+="/S   "
        else
            notestr+="/D   "
        endif
        iterate(V_flag)
            if(SP)
                redimension/s  $(name+num2str(i))
            endif
            notestr+=name+num2str(i)+",  "
        loop
        notestr=notestr[0,strlen(notestr)-3]+"\rcalculated  WAVES/D "+ name  +
            "GHz, "+name+"CM"
        print  notestr
else
    DoAlert 0,"Please Choose Only *.SCN file !"
endif
End
```

C.3.2 *Load & Print*

These routines load, process, display, and print on a Macintosh computer, spectra recorded using a Coherent 699-29 Autoscan laser. One color panel (shown in black and white below) controls all of these routines. Balloon help is also included. The spectral data can can be either in ascii or IBM binary format.

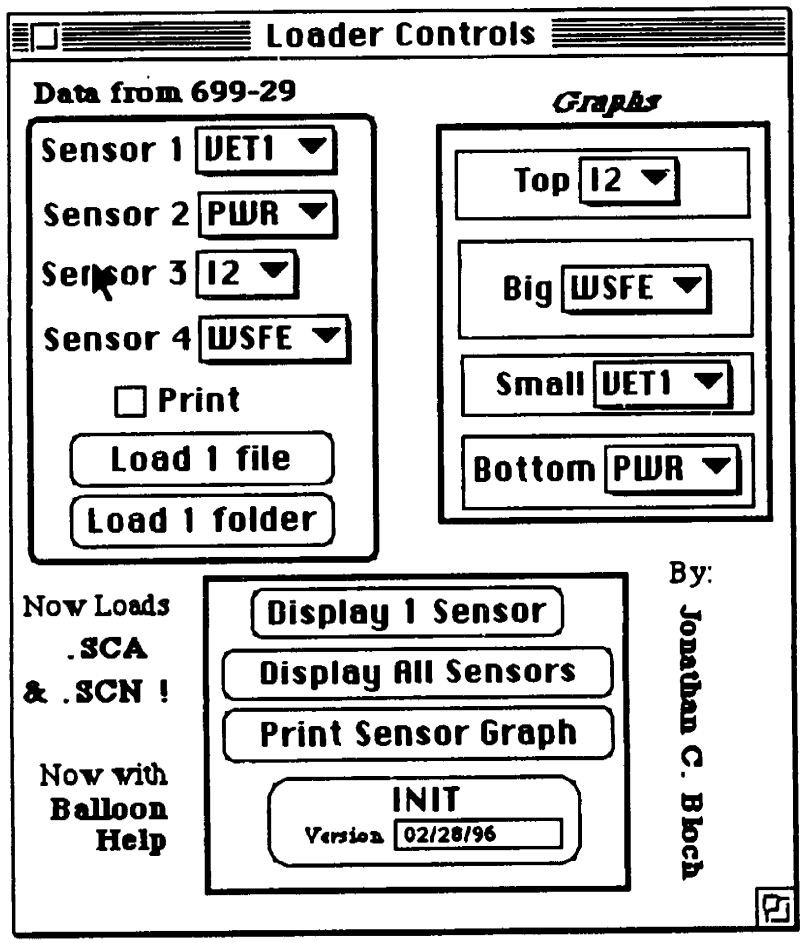

intro, description

```
|**********************************
|   INSTALL FILE LIST                |
|                                    |
|   to automatically load and install current    |
|   procedures for the AutoScan Laser,           |
|   simply "un-comment" the appropriate line     |
|   by deleting the "I" character.  When this    |
|   window compiles, procedures will be loaded   |
|   (or removed) according to this list.         |
| CAVEAT EMPTOR:                     |
|   some files require other files               |
|   Quick assign needs QuickCommands and         |
|       Master List                  |
#include <Strings as Lists> menus=0
#include ":AutoScan:Load & Print 02/28/96"  menus=0
|#include ":AutoScan:I2_assign 02/28/96"
|#include ":AutoScan:FindPeaks 05/18/95"
|#include ":AutoScan:Data_assign 02/28/96"
|#include ":AutoScan:QuickCommands 08/18/95"
|#include ":AutoScan:Quick_assign 02/28/96"
|#include ":AutoScan:Master List 08/04/95"



LOAD & PRINT BELOW:

-----
| set VERSION HERE
Function/S fVersion()
    return("02/28/96")
end


| This function is never called, but when compiled creates the global variables
|   hence compilation errors are avoided
|   this function can not (and will not) set initial values to variables
Function CREATE_GLOBALS()
    String/G  typelist
    string/g  sen1,sen2,sen3,sen4,gra1,gra2,gra3,gra4
    variable/g  ms1,ms2,ms3,ms4,mg1,mg2,mg3,mg4
    variable/g  printYesNO,BinaryFile
    String/G  Version
end
|---
| Re-init of LOADER STUFF:  sets possibilities and DEFAULTS
| kills old panel, makes new panel
|
Macro Init()
    | possibilities for data types: last entry must be DNE for Does Not Exist !
        typelist="GHz;LES;I2;VET1;PWR;90MRS;45MRS;FM;90FMMRS;45FMMRS;SOODR"
        typelist+=";Abs;GHz;WSFE;PulseFM;Pulse;PulseFMI;PulseFMQ;DNE"
```

```
    I when loading data, print if  printYesNO=1:
        printYesNO=0
    I default: loaded data is of these types:
        sen1="VET1";sen2="PWR";sen3="I2";sen4="WSFE"
    I default: graphed data is of these types:
        gra1="I2";gra2="WSFE";gra3="VET1";gra4="PWR"
    I for default popup menus to work properly, the numeric variables below must be set correctly
    I numbers refer to item placement in typelist (GHz=0, VET1=3, etc...)
    I    these specify default TYPES LOADED:
            mg1=3;mg2=14;mg3=4;mg4=5
    I    these specify default  TYPES GRAPHED:
            ms1=4;ms2=5;ms3=3;ms4=14

    I kill old panel, make new panel
        dowindow/k  Loader_Panel
        Loader_Panel()
End
I
I Buttons on panel call routines below:

Macro  Process1File()
    Load1File("")
End
Macro  Process1Folder()
    LoadFolder()
End

I routines called to do loading
Macro Load1File(File)                          I loads 1 file and processes it
    String  file                               I if file is empty string, get name via dialog
    Silent  1                                  I file is full name, including path !!
    string  NoteStr,DateString,BaseName
    variable F1,NumLoaded
        if  (cmpstr(File,"")==0)
            Open/D/R/M="Choose file to load (*.SCA  or *.SCN only)" F1
            I gets full file name, including path
            File=S_filename
        endif
        I now determine if this file is binary (.SCN) or ascii (.SCA)
            Binaryfile=-1
            if  (cmpstr(File[strlen(file)-3,strlen(file)],"SCN")==0)
                BinaryFile=1
            endif
            if  (cmpstr(File[strlen(file)-3,strlen(file)],"SCA")==0)
                BinaryFile=0
            endif
        I Basename is string from last : to . in file name
        BaseNAme=File[last(File,":"),last(File,".")-2]
        if  (BinaryFile==0)                            I ascii file, so just load as general text
            Notestr=Fileinfo(File)
            LoadWave/Q/O/G/D/N=T699_  File
```

```
        NumLoaded=V_flag
    endif
    if (BinaryFile==1)                  | binary file, load special format via Bload1file()
        NoteStr=BLoad1File(file)        | need to return info string
        NumLoaded=V_flag
    endif
    if (BinaryFile>=0)                  | some file was loaded o.k., so go process new waves
        Notestr+=Sensorinfo(Numloaded/(2-Binaryfile))
        Print "Successfully Loaded AutoScan data from:   ",File
        Print NoteStr
        ConvertLoadedWaves(NumLoaded,NoteStr,BaseName)
        if(printYesNO)
            Graph4Sensors(Basename)
            PrintSensorGraph(Basename)
        endif
        DoWindow/K     $(Basename)
    else
        DoAlert 0,"Not a data file from Coherent AutoScan laser" | wrong FILE type selected !
    endif
    close/a

End
Function/S BLoad1File(file)                         | loads 1 Binary File
    String file
    silent 1
    string ScanDate,ScanTime
    variable/d refNum,NumLoaded,totalfileBytes,dataBytes,MemAlocBytes,infoBytes,filepos
    variable/d scanNum,StartGhz, IntMhz,segSec,lenGHz,f
    variable/d pointsperarray,pointspersegment
    make/o/d/n=2 T699_0
    string NoteStr,doit
        if (cmpstr(FIle,"")==0)         | dialog only
            Open/D/M="File to load "/R refNum        | gets file name
            file=S_filename
        endif
        | get info about the file we just opened (refNum)
            Open/R refNum file      | open the file
            Fstatus refNum
            lFile=S_filenam
            totalFileBytes=V_logEOF             | S_path is now path name here
        | calc. size of areas in file, see Coherent manual
            infoBytes=10+10+2+8+8+8+8+2+2+24+24+24
            MemAlocBytes=26
            dataBytes=totalfileBytes-infoBytes-2*memalocBytes
        | skip over memory allocation area & data arrays, read in information about this data set:
            | read in STRING containing scan date -> ScanDate
                filePos=memalocBytes+databytes          |correct file pos
                FSetPos refNum, filepos
                Freadline/N=10/T="" refNum, ScanDate    | at most 10 ascii characters
            | read in STRING containing scan time -> ScanTime
                filePos+=10                             | next area (forced !)
                FSetPos refNum, filepos
```

```
            Freadline/N=10/T="" refNum,scanTime     | at most 10 ascii characters
        | read in Unsigned INTEGER containg scan number ->scanNum
            filePos+=10                             | move to end of string
            FSetPos refNum, filepos
            FBinRead/f=2/b  refNum,scanNum          | 2 byte unsigned int (forced)

        notestr="Data Set #" + num2str(scanNum) + ":\t ".SCN Load\r    " +
ScanDate[0,strlen(scandate)-2] + " " + ScanTime[0,strlen(scantime)-2]

        | read in DP FP# (intel or swapped) containg starting wavelength, in Ghz ->StartGhz
            filePos+=2
            f=5                                     | f=5 means 64 bit floating point
            IFSetPos refNum, filepos                | no need to move in file, all ready there
            FBinRead/f=(f)/b  refNum,startGhz       | DP FP#, 8 Bytes, /b==swapped !!!!
            | read in DP FP# containing data collection interval in MHz -> IntMHz
            IFSetPos refNum, filepos                | see above
            FBinRead/b/f=(f)  refNum,IntMhz         | DP FP#, 8 Bytes, /b==swapped !!!!
            | read in DP FP# containing scan time in seconds per 10GHz segment ->segSec
            filePos+=8
            IFSetPos refNum, filepos                | see above
            FBinRead/f=(f)/b  refNum,segSec         | DP FP#, 8 Bytes, /b==swapped !!!!
            | read in DP FP# containing scan distance in GHz -> lenGHz
            filePos+=8
            IFSetPos refNum, filepos
            FBinRead/f=(f)/b  refNum,lenGHz         | DP FP#, 8 Bytes, /b==swapped !!!!
        | done with (all manually read) info that we need, so close (all) file (s)
        close/a
    notestr=notestr+"\r    Starting wavelength "+num2str(StartGhz)+" (GHz)\r    Data interval
"+num2str(IntMHZ)+" MHz"
    notestr=notestr+"\r    Scan time per segment "+num2str(segsec)+" seconds\r    Scan distance
"+num2str(lenGhz)+"   GHz\r"
        | calculate points (not bytes)  that will be read into 1 or more waves automatically
        pointspersegment=ceil(10200/IntMhz)+1          | why need +1  ? Manual Error?
        pointsperarray=(lenGHz/10)*pointspersegment
        | now go load all data.....  (using path and file name!)
        | wave names are automatically chosen.....
        doit="GBLoadWave/Q/O/D/B/N=T699_/F=2/L=16/S=26/U="+num2str(pointsperarray)+
"\""+file+"\""
    Iexecute("GBLoadWave/O/D/B/N=wave/F=2/L=16/S=26/U=(pointsperarray)  (file)")
    execute doit
    | make x scaling waves, Ghz, BUT do not forget about overlap !
        duplicate/o  T699_0,$("T699_"+num2str(V_flag))
        wave/d  Ghz=$("T699_"+num2str(V_flag))
        Ghz=StartGhz+P*IntMhz/1000-floor(p/pointspersegment)*IntMhz*3/1000
return(notestr)
End

Macro LoadFolder()
    String File
    variable F1,NumLoaded,index
    silent 1
```

```
            NewPath/O Pathname
            index=0
            Do
                File=IndexedFile(pathname,index,"TEXT")
                if  ((cmpstr(File[strlen(file)-3,strlen(file)],"SCA")==0)+(cmpstr(File[strlen(file)-
3,strlen(file)],"SCN")==0))
                print " Loading ",file
                    Open/Z/R/p=pathname F1 as file
                    If (V_flag==0)
                        Pathinfo Pathname
                        Load1file(S_path+File)
                    endif
                endif
                Close/A
                index+=1
            While (strlen(File)>0)
end

| ******* Routines for conditioning loaded data
 MAcro ConvertLoadedWaves(NumWaves,NewNote,NewBAseName)
    Variable NumWaves
    String NewNote,NewBAseNAme
    string Results="New Waves: ",S1="",S2=""
    variable wave,zero
    | set up string variables with new wave names, and kill old if exists (always overwite)
        S1=NewBasename+"_GHz"
        Killwaves/Z $S1
    if (BinaryFile)
        | Ghz wave is last wave only ! (Numwaves)
        Rename $("T699_"+num2str(Numwaves)), $S1
    else
        |(ascii)
        | Ghz info is in first and all even waves, T699_0,T699_2, etc...
        Rename T699_0, $S1
        Iterate(Numwaves/2-2)           | kill other even waves !
            wave=2*(i+1)                |start at T699_2

            killwaves $("T699_"+num2str(wave))
        Loop
    endif
        Note $S1,NewNote                | wavenote for Ghz wave
        Results+=S1                     | and text for report string
        S2=NewBasename+"_Cm"            | name of cm wave
        Duplicate/o $S1,$S2
        $S2/=29.97925                   | scale using c
        Results+=", "+S2
        setscale y 0,0,"Hz" $S1             | Ghz is actually in Hz, relative !
        $S1*=1e9
        zero=$S1[0]
        $S1-=zero
    | now process all other loaded waves
    | if ascii, data is in odd waves (2*i+1), if binary, data in all waves (i)
```

```
    Iterate(Numwaves/(2-BinaryFile))          | always iterate same number of times !
        wave=i*binaryfile+(2*i+1)*(!BinaryFile)
        S1=NewBasename+"_" +SensName(i+1)
        Killwaves/Z $S1
        rename $("T699_"+num2str(wave)),$s1
        Results+=", "+s1
        Redimension/S $s1                     | data need only be single precision
    Loop
    Print Results
End
Function/s SensName(w)
    variable w
    if (w==1)
        return (sen1)
    endif
    if (w==2)
        return(sen2)
    endif
    if (w==3)
        return(sen3)
    endif
    return(sen4)
end

|********* for getting information from original *.SCA data file
Function/S FileInfo(FileName)                          | get text from 699 data file
    string Filename
    string Datestring="",FormattedText="",DataSet=""
    variable F
        Open/R F Filename
    Datestring="      "+ReadNextline(F)
    DataSet=ReadNextline(F)
    DataSet=DataSet[0,strlen(DataSet)-2]
    FormattedText+=DataSet+":\t *.SCA load\r"+Datestring+"      "+ReadNLines(F,4,"      ")
    Close F
    Return(FormattedText)
End
Function/S SensorInfo(NumSensors)
    variable NumSensors
    string FormattedText="      "+num2str(NumSensors)+" Sensors: "
    variable Sensor=1
    Do
        FormattedText+=" _"+SensNAme(Sensor)+", "
        Sensor+=1
    While(Sensor<=NumSensors)
    FormattedText=FormattedText[0,strlen(FormattedText)-3]
    Return(FormattedText)
End
Function Last(Str,Chr)              | Return Location+1 of last chr in string
    string Str,chr
    Variable Loc,lastloc
    Loc=-1
```

```
    do
        lastloc=loc+1
        loc=strsearch(str,chr,lastloc)
    while(loc>=0)
    Return(lastloc)
End

Function/s ReadNextLine(FileNum)                    | Reads 1 line of text from file spec'ed by
    variable Filenum                                | Filenum.  Returns edited string
    string line=""                                  | where bad char's have been replaced
    variable Loc
    Freadline FileNum,Line
    Loc=strsearch("  ")        | not a space, but an unprintable character from IBM filed, copy from file
    Line[Loc,Loc]=" "
    Return(Line)
End
Function/S ReadNlines(Filenum,N,Str)                | Reads next N lines of text from file
    variable Filenum,N                              | reads each line using ReadNextLine(Filenum)
    string str
    variable Not_first=0                                | reads each line using ReadNextLine(Filenum)
    string Nlines=""                                | str is appended between lines
    do
        if  (not_First)
            Nlines+=str
        endif
        Nlines+=ReadNextLine(Filenum)
        N-=1
        Not_First=1
    while (N>0)                 | as long as condition is true
    Return(Nlines)
End


|***************      Display  stuff  here
| 3 ways:  graph a list, 4 sensor graph, or graph 1 sensor

Macro GraphSensors(Basename)                | graphs 4 sensors belonging to basename
    string basename
    prompt basename, "Choose basename", popup,BasenameList()
        silent 1
        string botaxis=basename+"_Cm",topaxis=basename+"_Ghz", list
        list=wavelist(basename+"_*",";","")
        Graph4(list,botaxis,topaxis,basename)
End
Macro Graph1Sensor(basename,sensorname)             | graphs1 sensor of a basename (uses graphlist)
    string basename,sensorname
    prompt basename, "Choose basename", popup,BasenameList()
    prompt sensorname, "Choose sensor", popup,TypeList
        silent 1
        string list=basename+"_"+sensorname
        string botaxis=basename+"_Cm",topaxis=basename+"_Ghz"
```

```
        print list
        if (exists(list)!=1)
            abort "No such sensor for: "+basename
        endif
        list=botaxis+";"+topaxis+";"+list
        GraphList(list,botaxis,topaxis,basename+"_"+Sensorname+"_G")
End
Macro GraphList (list,botaxis,topaxis,basename)        | graphs List of waves on 1 graph
    string list,botaxis,topaxis,basename
        silent 1
        string cm=botaxis,Ghz=topaxis,Ywave
        string/g axis
        variable sensor=1,index=0,numsensors
            pauseupdate
            numsensors=numitemsinlist(list,";")-2
            do
                Ywave=GetStrFromList(list,index,";")
                if (cmpstr(Ywave,cm)==0+cmpstr(Ywave,GHz)==0)
                    index+=1
                else                                    |graph a wave
                    axis="L"+num2str(sensor)
                    if (sensor==1)
                        Display/W=(70,52,548,444)/L=$(axis) $Ywave vs $CM as Basename
                        Dowindow/C $(Basename)
                        AppendToGraph/L=$axis/T $Ywave vs $GHz
                        ModifyGraph manTick(bottom)={0,0.4,0,2},manMinor(bottom)={19,5}
                        ModifyGraph margin(left)=14
                        ModifyGraph grid(top)=2
                        ModifyGraph nticks(top)=3
                        Label bottom "cm\\S-1
                        ModifyGraph standoff(top)=0
                    else            | not first sensor
                        Append/L=$axis $Ywave vs $CM
                    endif
                    | now clean up graph, for all sensors
                    ModifyGraph freePos($axis)=0
                    | give each sensor a different size plot area or scale
                    ModifyGraph
axisEnab($axis)={axisstart(sensor,numsensors),axisend(sensor,numsensors)}
                    ModifyGraph mirror($axis)=1
                    Label $axis ("\\Z18"+Ywave[Strsearch(Ywave,"_",0),strlen(Ywave)])
                    ModifyGraph lblRot($Axis)=-90
                    ModifyGraph lblLatPos($axis)=-10;ModifyGraph lblPos($axis)=130
                    SetAxis/A/N=2 $axis
                    Index+=1
                    Sensor+=1
                endif
            While(Sensor<=NumSensors)
End

|******** for graphing list of waves
```

```
Function AxisStart(Sensor,NumSensors)        ICalculates axis start for Total of Numsensor
    variable sensor,numsensors                    I spacing between each axis is blankspace
        variable blankspace=0.05
        variable axisspace=(1-(blankspace*(Numsensors-1)))/numsensors
        Return((BlankSpace+AxisSpace)*(Sensor-1))
End
Function AxisEnd(Sensor,NumSensors)          I calcilates axis end for above
    variable sensor,numsensors
        variable blankspace=0.05
        variable axisspace=(1-(blankspace*(Numsensors-1)))/numsensors
        Return((BlankSpace*(Sensor-1)+(AxisSpace*Sensor)))
End

I**********

Macro Graph4Sensors(Basename)            I graphs 4 sensors belonging to basename  (graphs a list)
    string basename                           I graphs only sensors as chosen in panel
    prompt basename, "Choose basename", popup,BasenameList()
        silent 1
        string botaxis=basename+"_Cm",topaxis=basename+"_Ghz", list
        list=wavelist(basename+"_*",";","")
        Graph4(list,botaxis,topaxis,basename)
End

Macro Graph4 (list,botaxis,topaxis,basename)      I graphs List of waves on 1 graph
    string list,botaxis,topaxis,basename
    I Top should be for I2, then big for data (WSFE, ETC), then VET1, then PWR  !
    string Pwr_Wave, I2_wave, Vet_Wave, DATA_Wave, DNE_wave="dummy"
    variable scanlen
    PauseUpdate; Silent 1       I building window...
        I2_Wave=basename+"_"+GRA1
        DATA_Wave=basename+"_"+ GRA2
        Pwr_Wave=basename+"_"+GRA4
        Vet_Wave=basename+"_"+GRA3
        scanlen=round($botaxis(rightx($botaxis))-$botaxis[0])
        duplicate/o $DATA_wave,$DNE_wave ; $DNE_wave=nan       I data_wave must exist !!!
        if  (exists(pwr_wave)==0)      I if waves do not exist, make a dummy wave to plot
            pwr_wave=DNE_wave
        endif
        if  (exists(I2_wave)==0)
            I2_wave=DNE_wave
        endif
        if  (exists(Vet_wave)==0)
            vet_wave=DNE_wave
        endif
    Display /W=(70,52,694,493)/L=L1  $PWR_wave vs $botaxis as basename
    Dowindow/C $(Basename)
    Append/L=L1/T $PWR_wave vs $topaxis
    Append/L=L2 $Vet_Wave vs$botaxis
    Append/L=L3 $Data_Wave vs $botaxis
    Append/L=L4 $I2_Wave vs $botaxis
```

```
    ModifyGraph margin(left)=144
    ModifyGraph lSize=0.5
    ModifyGraph grid(top)=2
    ModifyGraph  mirror(L1)=1,mirror(L2)=1,mirror(L3)=1,mirror(L4)=1
    ModifyGraph nticks(top)=3,nticks(L2)=3
    ModifyGraph fSize(L1)=9,fSize(L2)=9
    ModifyGraph standoff(top)=0
    ModifyGraph lblPos(L1)=129,lblPos(L2)=130,lblPos(L3)=135,lblPos(L4)=121
    ModifyGraph lblLatPos(L2)=1,lblLatPos(L3)=-8,lblLatPos(L4)=-3
    ModifyGraph lblRot(L1)=-90,lblRot(L2)=-90,lblRot(L3)=-90,lblRot(L4)=-90
    ModifyGraph freePos(L1)=0
    ModifyGraph freePos(L2)=0
    ModifyGraph freePos(L3)=0
    ModifyGraph freePos(L4)=0
    ModifyGraph axisEnab(L1)={0,0.1}
    ModifyGraph axisEnab(L2)={0.15,0.25}
    ModifyGraph axisEnab(L3)={0.3,0.7375}
    ModifyGraph axisEnab(L4)={0.7875,1}
    ModifyGraph  manTick(bottom)={0,(0.4*scanlen),0,2},manMinor(bottom)={19,5}
    ModifyGraph  manTick(L2)={0,200,0,0},manMinor(L2)={0,50}
    Label L1 "\\Z18_"+GRA4
    Label bottom "cm\\S-1"
    Label L2 "\\Z18_"+GRA3
    Label L3 "\\Z18_"+GRA2
    Label/Z L4 "\\Z18_"+GRA1
    SetAxis L1 240,255
    SetAxis/A/N=1 L2
    SetAxis/A/N=2 L3
    SetAxis/A/N=2 L4
EndMacro

Macro PrintsensorGraph(Name)
    string Name
    prompt Name,"Choose Graph Name", popup,BasenameList()
    string Box=note($(Name+"_GHZ"))
        if (strlen(winlist(Name,";","Win:1"))==0)
            abort "No Such Graph Exists Now !"
        endif
        Layout/W=(5,42,506,618) $Name as "L3graph"
        Dowindow/C $(Name+"_Layout")
        ModifyLayout left=67,top=72,width=581-67,height=652-72,Frame=0,mag=.5
        Textbox/N=text0/F=0/S=3/A=MT/X=7.45/Y=0.41      "\\Z24\\f01"+name
        Textbox/N=text1/A=MB/X=-0.91/Y=1.51   "\\Z09"+Box
        Textbox/N=text2/A=RB/X=8.73/Y=5.77  "\\Z07  Macros:"+Version+"\r  Now:  "+DATE()+"\r
Jonathan C. Bloch"
        PrintLayout $(Name+"_Layout")
        DoWindow/K      $(Name+"_Layout")
End
Function/S BasenameList()
    string  allcmwaves="",list=""
    variable Loc,lastloc
        allcmwaves=WaveList("*_Cm",";","")
```

```
        do
            lastloc=loc+1
            loc=strsearch(allcmwaves,";",lastloc)
            list+=allcmwaves[lastloc-1,loc-4]
        while(loc>=0)
    Return(list)
End


Function NumItemsInList(List,sep)
    string list,sep
        variable loc=-1,lastloc,numitems=-1
            Do
                LastLoc=Loc+1
                NumItems+=1
                Loc=StrSearch(List,Sep,LastLoc)
                if (loc==0)                                    |don't count first char
                    numitems-=1
                endif
            While(Loc>=0)
            if  (cmpstr(list[strlen(list)-1,strlen(list)],sep)==0)     | don't count last char
                Return(numitems)
            else
                Return(numitems+1)
            endif
End



|********** Control PAnel for Loader !!!

Macro InitS()
String/G  sen1,sen2,sen3,sen4,gra1,gra2,gra3,gra4
end

Function PPS1(ctrlName,popNum,popStr) : PopupMenuControl
    String ctrlName ;Variable popNum; String popStr
    Sen1=popstr
End
Function PPS2(ctrlName,popNum,popStr) : PopupMenuControl
    String ctrlName ;Variable popNum; String popStr
    Sen2=popstr
End
Function PPS3(ctrlName,popNum,popStr) : PopupMenuControl
    String ctrlName ;Variable popNum; String popStr
    Sen3=popstr
End
Function PPS4(ctrlName,popNum,popStr) : PopupMenuControl
    String ctrlName ;Variable popNum; String popStr
    Sen4=popstr
End
```

```
Function PPG1(ctrlName,popNum,popStr) : PopupMenuControl
    String ctrlName ;Variable popNum; String popStr
    Gra1=popstr
End
Function PPG2(ctrlName,popNum,popStr) : PopupMenuControl
    String ctrlName ;Variable popNum; String popStr
    Gra2=popstr
End
Function PPG3(ctrlName,popNum,popStr) : PopupMenuControl
    String ctrlName ;Variable popNum; String popStr
    Gra3=popstr
End
Function PPG4(ctrlName,popNum,popStr) : PopupMenuControl
    String ctrlName ;Variable popNum; String popStr
    Gra4=popstr
End
Macro Load1Proc(ctrlName) : ButtonControl
    String ctrlName
    Process1file()
End

Macro LoadallProc(ctrlName) : ButtonControl
    String ctrlName
    Process1folder()
End

Function CheckProc(ctrlName,checked) : CheckBoxControl
    String ctrlName
    Variable checked
    variable/g printYesNO=0
        printYESNO=0
    if (checked==1)
        printYESNO=1
    endif
End
Macro Disp1(ctrlName) : ButtonControl
    String ctrlName
    Graph1sensor()
End
MAcro DispAll(ctrlName) : ButtonControl
    String ctrlName
    GraphSensors()
End
Macro GoInit(ctrlName) : ButtonControl
    String ctrlName
    Init()
End
Function SetVarProc(ctrlName,varNum,varStr,varName) : SetVariableControl
    String ctrlName
    Variable varNum
    String varStr
    String varName
```

```
        Version=fVersion()
End
Macro GoPrint(ctrlName) : ButtonControl
    String ctrlName
    PrintSensorGraph()
End
Window Loader_Panel() : Panel
    PauseUpdate; Silent 1       | building window...
    Version=fVersion()
    NewPanel /W=(198,39,496,372) as "Loader Controls"
    ModifyPanel cbRGB=(32769,65535,32768)
    SetDrawLayer ProgBack
    SetDrawEnv fillpat= 0
    SetDrawEnv save
    SetDrawLayer UserBack
    SetDrawLayer UserBack
    SetDrawEnv linethick= 2
    DrawRRect 6,192,139,21
    SetDrawEnv linethick= 2
    DrawRect 162,178,291,25
    DrawRect 169,35,283,62
    DrawRect 284,70,170,108
    DrawRect 284,114,171,138
    DrawRect 171,145,284,173
    SetDrawEnv fstyle= 1,textrgb= (1,4,52428)
    DrawText 9,19,"Data from 699-29"
    SetDrawEnv fstyle= 3,textrgb= (1,4,52428)
    DrawText 205,24,"Graphs"
    SetDrawEnv linethick= 2,rounding= 40
    SetDrawEnv fillfgc= (49151,65535,65535)
    DrawRect 72,197,235,319
        SetDrawEnv fstyle= 1,textrgb= (26214,17479,0),textrot= -90
    DrawText 252,315,"Jonathan C. Bloch"
    SetDrawEnv textrgb= (65535,0,0)
    DrawText 4,215,"Now Loads"
    SetDrawEnv fstyle= 1,textrgb= (65535,0,0)
    DrawText 20,232,".SCA"
    SetDrawEnv fstyle= 1,textrgb= (65535,0,0)
    DrawText 4,249,"& .SCN !"
    SetDrawEnv textrgb= (0,0,65535)
    DrawText 10,280,"Now with"
    SetDrawEnv fstyle= 1,textrgb= (0,0,65535)
    DrawText 14,293,"Balloon"
    SetDrawEnv fstyle= 1,textrgb= (0,0,65535)
    DrawText 31,305,"Help"
    SetDrawEnv textrgb= (26214,17479,0)
    DrawText 251,204,"By:"
    PopupMenu popupS1,pos={8,25},size={116,19},proc=PPS1,title="Sensor 1"
    PopupMenu popupS2,pos={9,50},size={120,19},proc=PPS2,title="Sonsor 2"
    PopupMenu popupS3,pos={8,73},size={101,19},proc=PPS3,title="Sensor 3"
    PopupMenu popupS4,pos={9,98},size={115,19},proc=PPS4,title="Sensor 4"
    PopupMenu popupG1,pos={189,38},size={67,19},proc=PPG1,title="Top"
```

```
    PopupMenu popupG2,pos={184,80},size={84,19},proc=PPG2,title="Big"
    PopupMenu popupG3,pos={181,117},size={95,19},proc=PPG3,title="Small"
    PopupMenu popupG4,pos={172,149},size={107,19},proc=PPG4,title="Bottom"
    PopupMenu popupS1,mode=ms1,value= #"typelist"
    PopupMenu popupS2,mode=ms2,value= #"typelist"
    PopupMenu popupS3,mode=ms3,value= #"typelist"
    PopupMenu popupS4,mode=ms4,value= #"typelist"
    PopupMenu popupG1,mode=mg1,value= #"typelist"
    PopupMenu popupG2,mode=mg2,value= #"typelist"
    PopupMenu popupG3,mode=mg3,value= #"typelist"
    PopupMenu popupG4,mode=mg4,value= #"typelist"
    Button Load1,pos={22,143},size={100,20},proc=Load1Proc,title="Load 1 file"
    Button LoadAll,pos={22,166},size={100,20},proc=LoadAllProc,title="Load 1 folder"
    CheckBox check0,pos={37,121},size={50,20},proc=CheckProc,title="Print"
    Button button0,pos={90,202},size={120,20},proc=Disp1,title="Display 1 Sensor"
    Button button1,pos={79,226},size={150,20},proc=DispAll,title="Display All Sensors"
    Button button2,pos={79,249},size={150,20},proc=GoPrint,title="Print Sensor Graph"
    SetVariable setvar0,pos={110,291},size={100,14},proc=SetVarProc,title="Version"
    SetVariable setvar0,fSize=9,limits={-INF,INF,1},value=Version
    Button button3,pos={96,275},size={120,34},proc=GoInit,title="INIT\r"
IBaloon Help
Button LoadAll help={"Load all the *.SCA or *.SCN files contained in 1 folder. Works best when file is
on a Mac Disk. See Load 1 File."}
Button Load1 help={"Load the contents of a *.SCA or *.SCN file. Works best when file is on a Mac
disk. The file is assumed to contain 1 to 4 sensors. Waves are created with names formed by the
filename and the appendix chosen above. _GHz and _cm waves are always created."}
PopupMenu popupS1 help={"Type of data that was recorded for first sensor."}
PopupMenu popupS2 help={"Type of data that was recorded for second sensor."}
PopupMenu popupS3 help={"Type of data that was recorded for third sensor."}
PopupMenu popupS4 help={"Type of data that was recorded for forth sensor."}
CheckBox check0 help={"When this box is checked, Loading files will print 1 page for each file loaded,
with formated graphs of each sensor. Page layout is assigned by choosing the type of data for each
graph."}
PopupMenu popupG1 help={"Type of data to be displayed in top graph of printed page. Format is best for
I2"}
PopupMenu popupG2 help={"Type of data to be displayed in bigest graph of printed page. Format is best
for actual data."}
PopupMenu popupG3 help={"Type of data to be displayed in small graph of printed page. Format is best
for VET1 or VET2."}
PopupMenu popupG4 help={"Type of data to be displayed in bottom graph of printed page. Format is best
for PWR."}
Button button0 help={"For 1 file (scan), displays 1 chosen sensor (1 data type) graphed vs cm and
GHz."}
Button button1 help={"For 1 file (scan), displays all 4 sensors (data types) vs cm and GHz on 1 page.
Format is chosen by popups above."}
Button button2 help={"Prints the All Sensors graph if it is displayed (See above)."}
Button button3 help={"Re-Initialization of this panel. Use this in case of trouble."}
EndMacro
```

1994 McCarthy, M. C., J. C. Bloch and R. W. Field, "Frequency-modulation enhanced magnetic rotation spectroscopy: a sensitive and selective absorption scheme for paramagnetic molecules", *J. Chem. Phys.*, **100**, 6331.

1994 Bloch, J. C., R. W. Field, G. E. Hall, and T. J. Sears, "Time -resolved frequency modulation spectroscopy of photochemical transients", *J. Chem. Phys.*, **101**, 1717.

1994 Sears, T. J., M. Wu, G. E. Hall, B. Chang, G. Hansford, J. C. Bloch, and R. W. Field, "Infrared and near infrared transient absorption spectroscopy of molecular free radicals", in *Laser Techniques for State-Selected and State-State Chemistry*, SPIE Proceeding Series No. **2124**, SPIE Press, Washington.

1994 Kaledin, L. A., J. C. Bloch, M. C. McCarthy, L. V. Gurvich, and R. W. Field, "Laser spectroscopic study of terbium monofluoride: ligand field assignments of some $f^8[^7F]sp$-$f^8[^7F]s^2$ transitions", *Mol. Phys.*, **83**, 881.

1995 Smith, J. M., J. C. Bloch, R. W. Field, and J. I. Steinfeld, "Trace

detection of NO_2 by frequency modulation enhanced magnetic rotation spectroscopy", *J. Opt. Soc. Am.* B, **6**, 964.

1996 Kaledin, L. A., J. C. Bloch, M. C. McCarthy, E. A. Shenyavskaya, and R. W. Field, "Laser Spectroscopy of Gadolinium Monofluoride: Ligand Field Assignments of States in the 0-3 eV Range", *J. Mol. Spec.*, **176**, 148.

1996 Eyler, E. E., S. Gangopadhyay, N. Melikechi, J. C. Bloch, and R. W. Field, "FM spectroscopy with transform-limited nanosecond laser pulses", *Opt. Lett.*, **21**, 225.

1996 Bloch, J. C., L. A. Kaledin, M. C. McCarthy, C. Linton, and R. W. Field, "Laser spectroscopic study of DyF: observation of three low-lying superconfigurations", *J. Mol. Spec.*,**000**, 000.

1996 Bloch, J. C., L. A. Kaledin, M. C. McCarthy, and R. W. Field, "Observation and assignment of low-lying CeF states using laser excitation and frequency modulation enhanced magnetic rotation spectroscopy", *J. Mol. Spec.*, **000**, 000.

1996 Bahns, J. T., C. C. Tsai, B. Ji, J. T. Kim, G. Zhao, W. C. Stwalley, J. C. Bloch, and R. W. Field, "Laser frequency modulated spectroscopy of a laser-guided plasma in sodium vapor: line positions for NaH ($A^1\Sigma+$-$X^1\Sigma^+$), Na (0-13 d and 11-14 s), and Ar (5p-4s)," in preparation.